

UCSF

UC San Francisco Electronic Theses and Dissertations

Title

Mechanisms of water and solute transport at the ocular surface

Permalink

<https://escholarship.org/uc/item/8dj783v7>

Author

Levin, Marc Harris

Publication Date

2006

Peer reviewed|Thesis/dissertation

Mechanisms of Water and Solute Transport at the Ocular Surface

by

Marc Harris Levin

DISSERTATION

Submitted in partial satisfaction of the requirements for the degree of

DOCTOR OF PHILOSOPHY

in

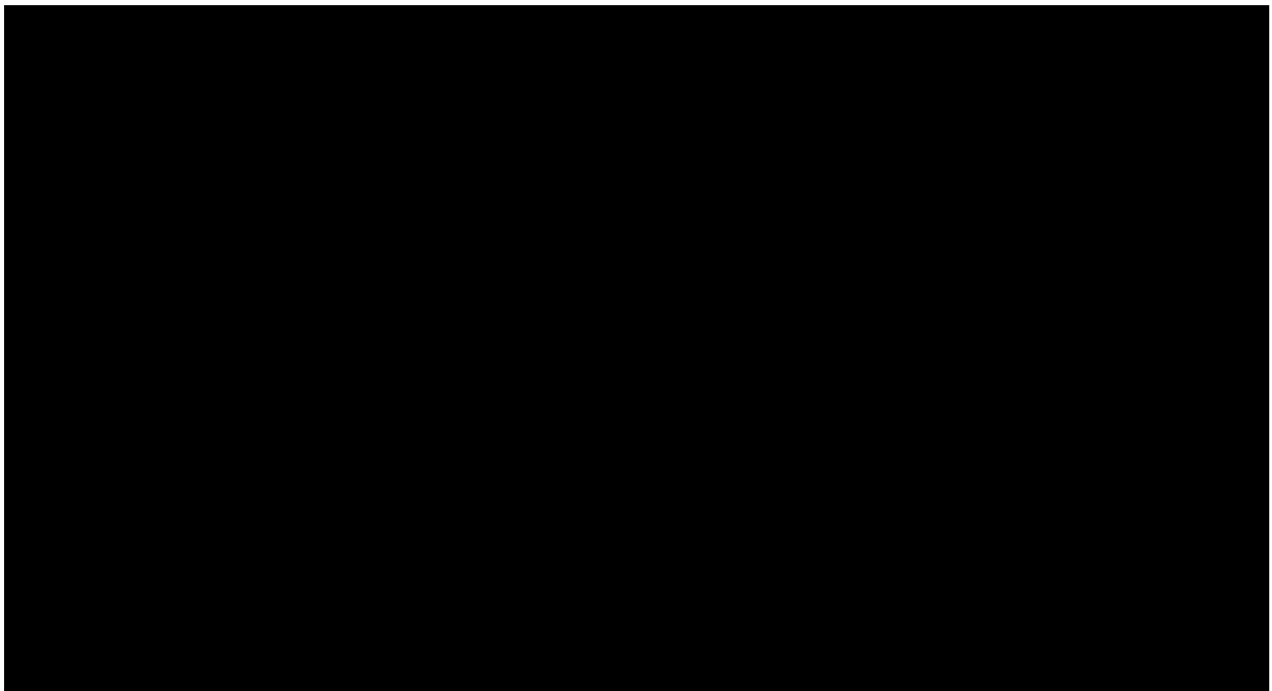
the Graduate Group in Biophysics

in the

GRADUATE DIVISION

of the

UNIVERSITY OF CALIFORNIA, SAN FRANCISCO



Copyright 2006

by

Marc Harris Levin

Dedication

To Patricia Levin and Janice Pivnick,
my mother and grandmother, with all my love and appreciation.

Acknowledgments

I thank my family for the encouragement and support they have given me from the very start. Gary and Patricia Levin, my father and mother, raised me to embrace learning and academic achievement, and most importantly to act out of care and compassion for others. Jonathan and Diana Levin, my brother and sister, are my best friends and greatest confidants. Charles and Janice Pivnick, my maternal grandparents, have supported me with love and wisdom, and have served as examples of hard work and fortitude. Barri and Hayley Lucero, my aunt and cousin, have brought an exciting energy to our family. The memory of my loving paternal grandmother, Virginia Levin, will remain with me always. Sydney Levin, my paternal grandfather, has supported me at every step of my journey, doing everything possible to make the road seem much shorter. Peggy Levin, his wife, has embraced my family as her own. So many members of my extended family, as well as numerous friends and colleagues, have my deep respect and appreciation for the integral roles they have played in my life.

Dr. Alan Verkman of the University of California, San Francisco, was most directly responsible for the direction and quality of my graduate work. As my graduate advisor, he provided me with personal attention in the form of daily feedback and

encouragement. He was particularly supportive of my personal and career goals and invested his time, intellect, and enthusiasm in my graduate work. With Dr. Verkman as my mentor, I was fortunate to develop professional skills as an experimentalist, scribe, orator, and thinker.

The Verkman laboratory afforded endless resources that enabled me to address a wide range of scientific questions. The laboratory environment facilitated learning by providing access to a diverse group of scientists with expertise in the fields of biophysics, chemistry, physiology, computation, and clinical medicine. Many laboratory members and collaborators, past and present, supported me intellectually and otherwise. As a lab member I have also benefited from National Institutes of Health laboratory grants DK35124, EB00415, HL73856, HL59198, and EY13574, and Research and Translational Core Center grant DK72517, as well as a Research Development and Drug Discovery Program grant from the Cystic Fibrosis Foundation. Other sources of financial support include three conference travel grants, two awarded by the Tear Film and Ocular Surface Society and one awarded by the National Eye Institute. I was also fortunate to receive financial support from a UCSF Biophysics training grant.

I greatly appreciate the financial and institutional backing provided by the Medical Scientist Training Program (MSTP) at UCSF. I will always consider it an honor to have been chosen to take part in such an outstanding program. NIH support throughout my years as a medical/graduate student has made the learning experience a comfortable one. The past and current UCSF MSTP directors, Drs. Tris Parslow and Arthur Weiss, have steered the ship in positive directions, and I remain in constant awe of what M.D.-

Ph.D. students accomplish while training at UCSF. A special acknowledgment goes to Jana Toutolmin and Catherine Norton, who have made the navigating much easier for us all. The UCSF School of Medicine deserves mention for valuing the training of physician scientists and for providing me with a superior medical education.

Thank you to the Graduate Group in Biophysics at UCSF, especially Julie Ransom, for welcoming me into the program as an MSTP student. Julie and others understood the challenges of completing a dual degree program and of working in a lab that was geographically isolated from the graduate school community. My oral qualifying and thesis committees have been vitally important in helping direct my approach to scientific problem solving. Drs. Todd Margolis, Roger Cooke, Stephen McLeod, and Daniel Minor comprised my oral qualifying committee. Drs. Alan Verkman, Todd Margolis, Roger Cooke, and David Sretavan were the members of my thesis committee. Finally, Claire Herriot, my graduate-student colleague in the Verkman laboratory, taught me more than words could possibly describe.

Long before I enrolled at UCSF, a series of research experiences played a notable role in developing my affinity for medical research, thus contributing to my “indoctrination.” I thank my past advisors, in chronological order: Dr. Ken Aldape (UCSF), Dr. Alan Launer (Stanford University), Cheryl Pearson-Carey (Palo Alto VA), Dr. Richard Zare (Stanford University), and Dr. Erin O’Shea (UCSF) for exposing me to exciting scientific endeavors and piquing my interest in academic research. A great many UCSF faculty in the School of Medicine, and specifically in the Department of Ophthalmology, have most recently helped me focus my career goals within clinical

the treatment of ocular disorders. I am most grateful to these dedicated individuals, all of whom have been exceptional mentors and role models for me.

The text of this dissertation includes material that has been published at the time of dissertation submission in *Investigative Ophthalmology & Visual Sciences* and in *Journal of Membrane Biology*. Copyright permission for reproduction of these publications was granted by the Association for Research in Vision & Ophthalmology and by Springer Science and Business Media, respectively. Citations for all published articles and articles submitted or in press are listed below:

CHAPTER 1.

Levin MH, Verkman AS. Aquaporins and CFTR in ocular epithelial fluid transport. *J Membr Biol*. 2006;210:105–115.

CHAPTER 2.

Levin MH, Verkman AS. Aquaporin-dependent water permeation at the mouse ocular surface: in vivo microfluorimetric measurements in cornea and conjunctiva. *Invest Ophthalmol Vis Sci*. 2004;45:4423–4432.

CHAPTER 3.

Levin MH, Verkman AS. Aquaporin-3-dependent cell migration and proliferation during corneal re-epithelialization. *Invest Ophthalmol Vis Sci*. In Press.

CHAPTER 4.

Levin MH, Verkman AS. CFTR-regulated chloride transport at the ocular surface in living mice measured by potential differences. *Invest Ophthalmol Vis Sci*. 2005;46:1428–1434.

CHAPTER 5.

Levin MH, Kim JK, Hu J, Verkman AS. Potential difference measurements of ocular surface Na⁺ absorption analyzed using an electrokinetic model. *Invest Ophthalmol Vis Sci*. 2006;47:306–316.

CHAPTER 7.

Levin MH, Sullivan S, Nielson D, Yang B, Finkbeiner WE, Verkman AS. Hypertonic saline therapy in cystic fibrosis: evidence against the proposed mechanism involving aquaporins. Submitted.

CHAPTER 8.

Levin MH, de la Fuente R, Verkman AS. Nanomolar potency small-molecule inhibitors of urea transporter UT-B identified by high-throughput screening. Submitted.

The coauthor listed in each of these publications (A.S. Verkman) directed and supervised the research that forms the basis for this dissertation:

Statement from Dr. Verkman: “Marc Levin describes accurately below the contributions of coauthors and others on each of the chapters/papers. As first author, Marc led each project in its conception, execution, and presentation. The work described in **this** thesis is comparable in scope to that of a standard Ph.D. thesis or dissertation.”

Special acknowledgment is extended to those colleagues from the Verkman laboratory and others who have aided in specific aspects of my thesis. For all studies, Dr. Alan Verkman contributed substantially to the quality of both experimental design and writing. Liman Qian deserves special thanks for mouse breeding and genotype analysis. Other notable contributions are organized and contributors listed by chapter, in numerical order:

CHAPTER 1.

Dr. Jay Thiagarajah, for providing parts of Figure 5.

CHAPTER 2.

Drs. Marios Papadopoulos, Yaunlin Song, and Tong Da, for help with microsurgical technique; Greg Friedland, for assistance with computer modeling.

CHAPTER 3.

Vibeke Pederson, for processing and imaging tissue for electron microscopy; Dr. Mariko Hara-Chikuma, for valuable input on AQP3 biology; Dr. Jie Hu, for advice on cell culture studies.

CHAPTER 4.

Drs. Luis Galiotta, Yaunlin Song, and Danieli Salinas, for advice on electrophysiology.

CHAPTER 5.

Coauthor Jung Kyung Kim, for collaborating to produce the useful electrokinetic model; coauthor Dr. Jie Hu, for contributing various PD measurements that appear in figures throughout the manuscript; Dr. Oscar Candia, for advice on model parameter selection.

CHAPTER 6.

Dr. Yaunlin Song, for technical advice on in vivo fluorescence measurements.

CHAPTER 7.

Coauthor Dr. Shannon Sullivan, for completing the experiments summarized in Figure 6; coauthor Dr. Baoxue Yang, for completing the AQP expression analysis presented in Figure 4; coauthor Dr. Walter Finkbeiner, for providing cultures of human airway epithelia. All coauthors, including Dr. Dennis Nielson, contributed to aspects of manuscript preparation. Lorna Zlock and Jean Davidson, for preparing cultures of human airway epithelia; Dr. Michael Matthay, for assistance in the acquisition of lung specimens; Dr. Dan Zhao, for assistance with RT-PCR analysis; Dr. Yaunlin Song, for technical advice on mouse lung perfusion.

CHAPTER 8.

Coauthor Dr. Ricardo de la Fuente, for substantial intellectual discourse throughout high-throughput assay optimization, for writing the software to carry

out screening, and for carrying out primary screening and analogue optimization in collaboration with me. Dr. Nitin Sonawane, for helping with analogue selection and structure-activity presentations; Dr. Baoxue Yang, for valuable advice on urea transport throughout the study; Drs. Shannon Sullivan and Dennis Nielson, for venipuncture; Dr. Jung Kyung Kim, for assistance with computer modeling.

Copyright by the
Association for Research in Vision & Ophthalmology
TX 6-093-760
2004

Copyright by the
Association for Research in Vision & Ophthalmology
TX 6-187-411
2005

Copyright by the
Association for Research in Vision & Ophthalmology
TX 6-312-593
2006

Abstract

Mechanisms of Water and Solute Transport

At the Ocular Surface

by Marc Harris Levin

Fluid transport across corneal and conjunctival epithelia involves secondary active chloride and sodium transport, which establishes the osmotic gradient to drive net water secretion. Aquaporins (AQPs), the cystic fibrosis transmembrane conductance regulator (CFTR), and the epithelial sodium channel (ENaC) provide molecular routes for transport of water, chloride, and sodium, respectively, through many epithelial tissues. The studies here define quantitatively contributions of these transporters to water and solute movement at the ocular surface, thus establishing new regulation mechanisms. Fluorescence and electrophysiological techniques were introduced to measure corneal/conjunctival transport properties in living mouse tissue. Comparative measurements were made between wild-type mice and transgenic mice deficient in various transporters, and using small-molecule modulators of transporter function. Supported by mathematical modeling, the data implicate AQPs, CFTR, and ENaC in ocular surface fluid balance, and as attractive targets for pharmacological treatment of disorders such as dry eye syndromes and corneal erosions.

Actions of and interactions among AQPs, CFTR, and ENaC are also of central importance to airway surface liquid (ASL) function and dysfunction, and have been considered with regard to both the etiology and possible treatment of cystic fibrosis (CF) lung disease. Recent data indicated clinical benefit of nebulized hypertonic saline in CF. The proposed mechanism of increased ASL volume relies on purported inhibition of lung AQPs by the ENaC inhibitor amiloride. Sensitive fluorescence methods indicated that amiloride does not inhibit AQP-mediated airway water permeability, indicating the need to identify alternate mechanisms for clinical benefit of hypertonic saline.

Another therapeutic strategy considered here is inhibition of urea transporters (UTs). Functional studies in knock-out mice indicate a critical role for UTs in renal urinary concentration and urea clearance. We performed high-throughput screening using a human erythrocyte lysis assay to discover the first high-affinity small-molecule UT-B inhibitors. Compounds were identified with EC_{50} approaching 10 nM, belonging to phenylsulfoxyoxazole, benzenesulfonamide, phthalazinamine, and aminobenzimidazole chemical classes. UT-B inhibitors will be evaluated for their application as a new class of diuretics ('urearetics') to increase renal water and solute clearance in water-retaining states, hypertension, and azotemia.

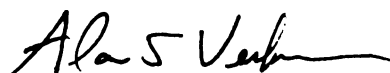


Table of Contents

CHAPTER 1.	1
Aquaporins and CFTR in Ocular Epithelial Fluid Transport	
CHAPTER 2.	34
Aquaporin-Dependent Water Permeation at the Mouse Ocular Surface: In Vivo Microfluorimetric Measurements in Cornea and Conjunctiva	
CHAPTER 3.	74
Aquaporin-3-Dependent Cell Migration and Proliferation During Corneal Re-epithelialization	
CHAPTER 4.	109
CFTR-Regulated Chloride Transport at the Ocular Surface in Living Mice Measured by Potential Differences	
CHAPTER 5.	136
Potential Difference Measurements of Ocular Surface Na ⁺ Absorption Analyzed Using an Electrokinetic Model	
CHAPTER 6.	184
Non-Invasive Measurements of Mouse Tear Film Ionic Composition	
CHAPTER 7.	198
Hypertonic Saline Therapy in Cystic Fibrosis: Evidence Against the Proposed Mechanism Involving Aquaporins	
CHAPTER 8.	234
Nanomolar Potency Small-Molecule Inhibitors of Urea Transporter UT-B Identified by High-Throughput Screening	

CHAPTER 1.

Aquaporins and CFTR

in Ocular Epithelial Fluid Transport

Abstract

Aquaporins (AQPs) and the cystic fibrosis transmembrane conductance regulator (CFTR) provide the molecular routes for transport of water and chloride, respectively, through many epithelial tissues. In ocular epithelia, fluid transport generally involves secondary active chloride transport, which creates the osmotic gradient to drive transepithelial water transport. This chapter examines roles for AQPs and CFTR in water and ion transport across corneal/conjunctival epithelia, corneal endothelium, ciliary epithelium, and retinal pigment epithelium. The potential relevance of water and chloride transport to common disorders of ocular fluid balance is also introduced. Recent data suggest AQPs and CFTR as attractive targets for drug development for therapy of keratoconjunctivitis sicca, recurrent corneal erosions, corneal edema, glaucoma, retinal detachment, and retinal ischemia.

The eye contains specialized fluid compartments and tissues that are avascular and low in protein so as to meet the needs of optical transparency, as in the cornea, and to maintain a suitable ionic environment for neural signal transduction, as in the retina. Regulated transfer of fluid and metabolites between extravascular spaces and adjacent

tissues or the systemic circulation supports these highly specialized functions (reviewed in Ref ¹). It is now appreciated that Cl⁻ secretion provides a primary driving force for active near-isosmolar water transport across the principal ocular epithelia: corneal/conjunctival epithelia, corneal 'endothelium,' ciliary epithelium, and retinal pigment epithelium. HCO₃⁻ transport often plays a crucial, though indirect role in promoting Cl⁻ uptake across membranous barriers. AQPs and CFTR have been identified as the principal molecular pathways for water and chloride transport, respectively, across a variety of epithelial tissues. The roles of these channels in mammalian physiology have been elucidated from phenotype analysis of transgenic mice and/or humans with absent or mutated channels, and in the case of CFTR, from the use of small-molecule inhibitors.

AQP-type water channels make up a family of small (~30 kDa) proteins with six alpha-helical membrane-spanning domains that facilitate bidirectional osmotic water transport across cell plasma membranes (reviewed in Ref ^{2,3}). A cell membrane osmotic water permeability coefficient of greater than ~0.01 cm/s generally indicates the presence of AQP water channels. Analysis of AQP knock-out mice has established the involvement of AQPs in extraocular epithelia in osmotically driven and near-isosmolar fluid transport, as in the urinary concentrating mechanism and glandular fluid secretion.³ Additionally, AQPs are involved in a growing list of less predictable epithelial cell functions, including cell migration and proliferation.^{4,5} This introductory chapter examines the roles of AQPs in ocular epithelial fluid absorption and secretion with special consideration of their relevance to common human disorders of ocular fluid balance such as dry eye syndrome, corneal swelling, and glaucoma.

CFTR, one of a growing list of Cl⁻ channels (reviewed in Ref. ⁶), is expressed in many fluid-transporting epithelia in the airways, pancreas, and intestine (reviewed in Refs. ^{7,8}). CFTR is a large (~180 kDa) cAMP-stimulated Cl⁻ channel comprised of 12 transmembrane domains, two cytoplasm-facing nucleotide-binding domains, and a cytoplasm-facing regulatory domain. CFTR is the only member of the ATP-binding-cassette (ABC) transporter superfamily known to conduct ions. Mutations in CFTR cause cystic fibrosis (CF), a relatively common life-shortening human genetic disease. Though CF is not commonly associated with overt eye diseases such as keratoconjunctivitis sicca (KCS, or dry eye), corneal edema, or retinal detachment, various subtle derangements have been reported in the eyes of CF subjects, including altered ocular surface hydration, corneal thickness, and vision transduction.^{9,10,11,12} However, though reduced CFTR function produces only minor effects on ocular functions, increasing CFTR activity could be useful in the treatment of several important eye diseases, as discussed below.

AQP and CFTR Expression in Ocular Epithelia

Figure 1 depicts the sites of AQP and CFTR expression in the eye. The AQP/CFTR expression patterns in corneal/conjunctival epithelium, corneal endothelium, ciliary epithelium, and retinal pigment epithelium suggest their involvement in regulation of tear film volume, corneal hydration and transparency, aqueous fluid volume and intraocular pressure, and subretinal compartment size and ionic composition. Indeed, functional significance for several AQPs in ocular tissues has been confirmed in AQP-deficient mice, including AQP1 in corneal endothelium and ciliary epithelium, AQP3 in conjunctival and corneal epithelium, AQP4 in ciliary epithelium and retinal Müller cells,

and AQP5 in corneal.^{5,13,14,15,16,17} Also, recent studies have reported altered AQP expression in association with various human corneal disease states associated with fluid imbalance.^{18,19,20} CFTR is functionally expressed in corneal and conjunctival epithelium, corneal endothelium, and retinal pigment epithelium.^{21,22,23,24,25,26}

Ocular Surface Epithelia

The ocular surface is lined by stratified corneal and conjunctival epithelia, which lie in contact with the tear film. The water permeability of the ocular surface, together with the rates of evaporative water loss and tear fluid production and drainage, determine tear film volume and osmolality,²⁷ as well as corneal stromal water content.²⁸ Active Cl⁻ secretion and Na⁺ absorption drive net water secretion into tears across both corneal and conjunctival epithelia (reviewed in Refs. ^{29,30}). The ocular surface, and the conjunctival epithelium in particular (covering 17 times more area than the cornea in humans),³¹ contributes to active tear fluid secretion under basal conditions, and even more so upon stimulation.^{32,33} Keratoconjunctivitis sicca is a heterogeneous group of conditions with the common features of reduced tear volume and tear hyperosmolarity, which lead to inflammatory damage to the ocular surface.³⁴ A computational model of tear film balance demonstrated the sensitivity of tear film osmolality to both excessive tear evaporation and inadequate tear secretion, the two general causes of dry eye syndrome (Fig. 2).¹⁶ In this model, tear fluid generated by osmotic flux (J_v) and isosmolar active secretion (J_s) is removed by evaporation (J_e) and isotonic drainage (J_d), such that in the steady-state, $J_s + J_v = J_e + J_d$. Computed tear film osmolality depended strongly on both passive water

permeation and active fluid secretion, which are influenced by AQPs and CFTR, respectively.

AQPs and the Ocular Surface

The stratified corneal epithelium of mouse, rat, and human expresses a water-selective aquaporin, AQP5, and at relatively lower levels, a water- and glycerol-transporting aquaglyceroporin, AQP3. AQP3 is more highly expressed throughout the neighboring conjunctival epithelium.^{5,16,35,36} Kang et al. demonstrated mercurial-sensitive water transport in cultured bovine corneal epithelial cells, which was attributed to AQP5 based on siRNA knock-down.³⁷ Subsequent studies in AQP5-null mice revealed that AQP5-deficient corneas were thicker than wild-type corneas by ~20%, exhibiting both inter- and intraepithelial fluid accumulation at the ultrastructural level (Fig. 3A).¹⁵ Functional measurements on living mice demonstrated AQP5 to be a significant epithelial pathway for stromal water uptake and extrusion. The rate of corneal swelling upon exposure of the epithelial surface to hypotonic saline was reduced 2-fold in AQP5-null compared to wild-type mice. Osmotically induced net fluid flux across the intact corneal barrier, measured by a steady-state dye-dilution method, indicated a 5-fold slowing of transcorneal water movement in AQP5 deficiency.

Plasma membrane osmotic water permeability of corneal epithelial cells (P_f^{mem}) was determined in mice utilizing an ocular surface perfusion method (Fig. 3B) involving microfluorimetric measurement of calcein quenching in surface cells. The high P_f^{mem} (0.045 cm/s) measured in wild-type mice was in agreement with conclusions from the older literature that the cornea is highly water permeable.^{38,39} P_f^{mem} was reduced 2-fold in AQP5 deficiency (Fig. 3C). The modest dependence of P_f^{mem} on AQP5 was likely

accounted for by the ~5-fold upregulation of AQP3 in AQP5-null versus wild-type mouse corneas. Yet despite this compensation, AQP5-null corneas are grossly edematous, highlighting the exquisite sensitivity of corneal water balance to altered water permeation across multiple membrane barriers in series.

Recent studies have suggested a novel role for AQP3 in basal cells of the corneal epithelium that is unrelated to transepithelial corneal fluid transport.⁵ AQP3-null mice had ~2-fold decreased P_f^{mem} compared to that of wild-type mice, and greatly reduced (>10-fold) glycerol transport. AQP3 deletion significantly delayed re-epithelialization following removal of the corneal epithelium by scraping. Tissue and cell culture studies suggested the involvement of AQP3 in corneal epithelial cell migration and proliferation, though the cellular mechanisms linking these functions to AQP3-dependent water and/or glycerol transport require further investigation.

CFTR and the Ocular Surface

Cl⁻-dependent fluid secretion has been found across ocular surface epithelia in several species. Electrophysiological measurements on rabbit cornea and conjunctiva, as well as in cultured cells, have demonstrated Ca⁺⁺- and cAMP-sensitive outward apical Cl⁻ currents, the latter likely due to activation of CFTR and other cAMP-sensitive channels, such as basolateral membrane K⁺ channels, that establish the electrochemical driving force for Cl⁻ efflux.^{13,40,41,42,43,44,45} CFTR is expressed in apical superficial cell membranes of corneal and conjunctival epithelia,^{13,21} where it may participate in tear film homeostasis. Studies on CF subjects have shown mild ocular surface abnormalities suggestive of defective fluid secretion, including decreased tear production, increased

corneal fluorescein staining, corneal and conjunctival metaplasia, and reduced tear film Na^+ content.^{10,11,46}

In recent experiments from our laboratory, CFTR function at the mouse ocular surface was demonstrated directly using an open-circuit potential difference (PD) technique, which involved perfusion of solutions over the ocular surface of anesthetized and immobilized mice (Fig. 4A).²⁵ Electrogenic Cl^- secretion and Na^+ absorption across superficial cell apical membranes of corneal and conjunctival epithelia contribute to generate sizable steady-state transepithelial potentials (-23 mV on average, tear film with respect to the body), as measured with Ag/AgCl electrodes and a high-impedance voltmeter. These voltages were sensitive to imposed transepithelial Cl^- gradients and various Cl^- channel modulators, including CFTR activators and inhibitors. Comparative measurements were made on wild-type mice and transgenic mice lacking functional CFTR (representative PD tracings shown in Fig. 4B). CFTR Cl^- conductance was stimulated in wild-type mice by the cAMP agonist forskolin or by a selective activator (not shown), and this conductance was inhibited by CFTR_{inh}-172. The substantial and sustained activation of CFTR-mediated Cl^- secretion by CFTR-selective activators provides a rational basis for their evaluation as therapy for KCS. Indeed, the phosphodiesterase inhibitor isobutylmethylxanthine reduced tear osmolarity in a rabbit model of KCS and in humans with KCS.^{47,48} INS365, a long-acting UTP agonist that stimulates mucus and calcium-sensitive Cl^- -driven fluid secretion,⁴⁹ is in phase III clinical trials for treatment of KCS. Direct measurement of CFTR-dependent ocular surface fluid secretion will be important in establishing the utility of CFTR activators as clinically useful secretagogues.

Corneal Endothelium

Maintenance of corneal stromal transparency requires precise regulation of extracellular water content.^{50,51} The aqueous-facing corneal endothelium, a misnamed leaky (low-resistance) monolayer epithelium, permits passive hydrostatic flux of water and ions from the aqueous compartment to the stroma. The endothelium also establishes opposing ion gradients by secondary active Cl^- and HCO_3^- transport, driving water movement to yield a relatively dehydrated stromal matrix of regularly spaced collagen fibrils. However, the corneal endothelial cell population is gradually depleted due to little or no cell proliferation in vivo (reviewed in Ref. ⁵²). Corneal dystrophies and iatrogenic damage from ocular surgeries such as cataract extraction accelerate this age-related cell loss.⁵³ Decreased total endothelial cell surface area results in reduced barrier and pump functions, potentially leading to corneal edema and opacity requiring corneal transplantation. Stimulation of stroma-to-aqueous fluid transport might reduce corneal swelling.

AQPs and Corneal Endothelium

AQP1 is expressed in mouse, rat, and human corneal endothelial cells.^{16,35,36} Corneal thickness is ~20% reduced in AQP1 deficiency (Fig. 5A), though baseline corneal transparency is normal.¹⁵ AQP1 water transport function in corneal endothelium in vivo was demonstrated by slowed corneal swelling upon hypotonic challenge at the endothelial surface utilizing an anterior chamber microperfusion method (Fig. 5B). An important role for AQP1 in maintenance of corneal transparency was demonstrated in an experimental model of corneal edema produced by transient exposure of the corneal

surface to hypotonic solution, in which AQP1 deficiency was associated with impaired recovery of corneal transparency and thickness (Fig. 5C). In primary corneal endothelial cell cultures, AQP1 deficiency reduced osmotically driven cell membrane osmotic water permeability, but did not impair active near-isosmolar transcellular fluid transport.⁵⁴ The commonly invoked mechanism of transcellular, AQP-facilitated fluid transport has been questioned in relation to the corneal endothelium, with Fischbarg and colleagues proposing a central role for electro-osmotic coupling of fluid transport to recirculating currents at the level of the intercellular junctions.^{55,56} This model posits that AQP1 contributes primarily to cell volume regulation, a role that remains difficult to reconcile with the dramatic corneal swelling phenotype of AQP1-null mice and with the substantially slower rate of cell volume regulation vs. osmotic equilibration.

AQP1 is also highly expressed in stromal keratocytes, where its function is not known.^{16,36,57} Keratocytes, the primary resident stromal cells, perform many fibroblast-like functions including extracellular matrix deposition during development and enhanced motility and signaling during inflammation and wound healing. AQP1 might be involved in keratocyte biosynthetic and/or cell migratory functions, and possibly in the regulation of stromal extracellular water content. The role for keratocyte/endothelial AQP1 in stromal dehydration may be revealed with an improved understanding of the evolution of the relatively thin AQP1-null corneas during development, similar to what was done for the lumican-deficient mouse.⁵⁸ Primary cultures of mouse keratocytes⁵⁹ may also prove informative in elucidating AQP1 function.

CFTR and Corneal Endothelium

Cl^- and HCO_3^- are important for stroma-to-aqueous fluid transport (reviewed in Ref. ⁶⁰). HCO_3^- is taken up at the stromal-facing (basolateral) membrane by an electrogenic $\text{Na}^+/\text{HCO}_3^-$ co-transporter with 1:2 stoichiometry. Cl^- enters basolaterally via the NKCC co-transporter and across the aqueous-facing (apical) membrane via a $\text{Cl}^-/\text{HCO}_3^-$ exchanger. CFTR was localized to the apical membrane in bovine corneal endothelial cell cultures, where efflux of Cl^- and HCO_3^- are cAMP-dependent.²³ As found in other cell types,^{61,62} CFTR is probably permeable to both Cl^- and HCO_3^- in corneal endothelium. Recent studies provide evidence for indirect HCO_3^- activation of CFTR-dependent Cl^- transport involving stimulation and upregulation of soluble adenylyl cyclase.^{63,64} One study on CF subjects reported increased endothelial permeability and cell density, and slightly (4%) thicker corneas compared to control subjects.⁶⁵ While these data support the possibility of CFTR activation to treat corneal edema, direct measurements of anion and fluid secretion in response to CFTR activators/inhibitors are needed to prove a role for CFTR in corneal endothelial fluid transport.

Ciliary Epithelium

The ciliary epithelium is a bilayered tissue consisting of pigmented ciliary epithelia (PCE) and nonpigmented ciliary epithelia (NCE), whose apical surfaces are juxtaposed and basolateral surfaces face the ciliary body and aqueous humor, respectively. Aqueous fluid production involves near-isosmolar water secretion across the ciliary epithelium into the posterior aqueous chamber. Aqueous secretion is crucial for providing nutrients to avascular ocular tissues of the anterior segment and for inflating

the globe to maintain intraocular pressure (IOP). IOP is also influenced by aqueous drainage, which occurs by pressure-driven bulk fluid flow into the canal of Schlemm and across the sclera. Elevated IOP is associated with glaucoma, a disorder of progressive visual loss and a major cause of blindness worldwide.⁶⁶ Reduction of ciliary secretion is the primary pharmacologic strategy for treatment of elevated IOP in glaucoma, warranting examination of AQP- and CFTR-facilitated ciliary fluid transport as possible targets for inhibition.

AQPs and Ciliary Epithelium

NCE cells co-express AQP1 and AQP4,^{36,67,68,69} suggesting their involvement in maintaining a high NCE cell water permeability for aqueous fluid production. An initial study on human NCE cultures reported AQP1 protein expression and a partial sensitivity of fluid transport to Hg²⁺ and AQP1 siRNA, suggesting AQP1-dependent aqueous inflow.⁷⁰ Measurements of IOP in mice using a fluid-filled microneedle inserted into the anterior chamber showed a modest reduction in IOP by 2–3 mm Hg in mice lacking AQP1 and/or AQP4 compared to wild-type mice.¹³ AQP1 is also expressed in trabecular meshwork endothelium in the canal of Schlemm, where a role in cell volume regulation had been proposed.⁷¹ However, direct measurement of aqueous fluid outflow in mice by a pulsed infusion method showed no effect of AQP1 deletion.¹³ Together with measurements of aqueous fluid production by a fluorescein iontophoresis-confocal detection method, it was concluded that reduced IOP in AQP-deficient mice was due to reduced ciliary aqueous fluid production. It will be important to investigate the role of AQPs in IOP regulation in mouse models of glaucoma, such as an episcleral vein

cauterization model developed recently by our lab,⁷² and when selective AQP inhibitors are available, in large animal models.

CFTR and Ciliary Epithelium

The clinical utility of acetazolamide in reducing aqueous fluid secretion had focused the bulk of attention regarding ciliary epithelial ion transport on HCO_3^- - rather than Cl^- -driven fluid secretion. However, Cl^- but not HCO_3^- was found to concentrate within ciliary epithelial cells, leading to the realization that HCO_3^- plays a critical though secondary role in supporting Cl^- secretion (reviewed in Ref. ⁷³). The NKCC co-transporter and Na^+/H^+ exchanger at the basolateral membrane of PCE cells have been shown to promote Cl^- uptake, with inhibition of cytoplasmic carbonic anhydrase by acetazolamide reducing aqueous fluid secretion by interfering with this secretion mechanism. Following Cl^- accumulation in PCE cells and subsequent spread through gap junctions to NCE cells, Cl^- release occurs through channel(s) of unknown molecular identity. There is no evidence for CFTR-dependent secretion across the ciliary epithelium. Aqueous fluid production in CF subjects was equivalent to that in non-CF controls.⁷⁴ While cAMP was shown to enhance NKCC symport, thereby increasing net Cl^- flux, forskolin-induced cAMP production was reported to, if anything, reduce aqueous fluid secretion.⁷⁵ More likely candidates for the basolateral NPE Cl^- channels include the swelling-activated ClCa-3 and pCl_n channels, though their roles remain controversial.

Retinal Pigment Epithelium

The retinal pigment epithelium (RPE) is a monolayer epithelium separating the neural retina from the capillaries of the choroid. The RPE lines the outer blood-retinal barrier (BRB), preventing leak between compartments; the inner BRB consists of tight-junction-laden endothelial cells that line retinal blood vessels. Functionally, the RPE supplies the retina with nutrients critical for the visual cycle, phagocytoses photoreceptor outer segment discs, and absorbs fluid from the subretinal space in the outer retina. Fluid absorption from the subretinal space is important to maintain the volume and ionic composition of the extracellular space surrounding photoreceptor segments within a range that supports phototransduction. Passive forces, including IOP-driven bulk flow and choroidal osmotic pressure, prevent the build-up of subretinal fluid. However, in disease states when the BRB is disrupted and protein aberrantly enters the subretinal space, active RPE transport is crucial to oppose oncotic water accumulation.⁷⁶

Modulation of RPE absorptive function thus represents a logical strategy for treatment of retinal detachment.⁷⁷ A distinct retinal extracellular space, located in the inner retina, is maintained by the dehydrating actions of the glial-like Müller cells. Ischemic disorders caused by retinal artery occlusion, diabetes, and hypertension, are associated with fluid accumulation in this second compartment.⁷⁸

AQPs and Retinal Pigment Epithelium

The presence and function of AQPs in the RPE remain in question. In one study, AQP1 was localized to human RPE in situ using an ultra-sensitive cell-surface biotinylation method and in cell culture by immunofluorescence using an affinity-purified

AQP1 antibody.⁷⁹ AQP1 mRNA had been previously detected in cultured fetal RPE cells.⁸⁰ However, other studies on rat and human tissue have failed to identify AQP1 protein in RPE (Ref. ⁶⁰, and our own unpublished data). AQP1 localization to photoreceptor, glyceric amacrine, and Müller cells has also been reported without demonstrated function.^{81,82,83}

AQP4 is strongly expressed in Müller cells, especially in perivascular and end-feet processes (facing the retinal capillaries and vitreous body), where it is thought to form multiprotein complexes involving the inwardly rectifying Kir4.1 K⁺ channel.^{84,85,86} Analogous to its roles in brain astroglial cells and cochlear supportive cells,^{87,88} AQP4 in Müller cells has been proposed to maintain extracellular space volume and K⁺ concentration during bipolar cell neural activity. AQP4-null mice exhibited mildly defective retinal signal transduction as evidenced by reduced short full-field electroretinogram (ERG) b-wave amplitude and latency,¹⁴ suggesting functional coupling between water and K⁺ clearance. AQP4 deletion in Müller cells also protected against edema and ganglion cell death following retinal ischemia.¹⁷ These results implicate AQP4 in both neuronal and glial cell swelling. AQP4 inhibitors might therefore limit inner retinal pathology following vascular occlusive and other ischemic diseases causing cytotoxic (cellular) edema.⁷⁸

CFTR and Retinal Pigment Epithelium

Cl⁻ is transported into RPE cells across the retinal (apical) membrane against a concentration gradient through the NKCC co-transporter, and across the choroidal (basolateral) membrane via a Cl⁻/HCO₃⁻ exchanger. Choroidal Cl⁻ exit takes place largely through a Ca⁺⁺-sensitive channel. Linkage of mutations in the Best1 gene to Best disease

(autosomal dominant Best vitelliform macular dystrophy) led to the discovery of bestrophins, which now appear to be the Ca^{++} -dependent Cl^- channels of the RPE and other epithelia.⁸⁹ Interestingly, aspects of Best disease resemble the much more common disorder, age-related macular degeneration (reviewed in Ref. ⁹⁰). Basolateral Cl^- secretion is controlled by endogenously generated ATP, which initiates purinergic signaling at the P2Y_2 receptor on the apical membrane. In addition to expressing anion channels ClC-2 , ClC-3 , ClC-5 , and the pCLCA1 Cl^- regulator,⁹¹ the RPE also expresses CFTR. In human cell culture and bovine organ culture models, CFTR was proposed to enhance RPE fluid transport indirectly by ATP release and autocrine purinergic signaling.²⁶ In two studies, Vitamin A-corrected CF subjects exhibited decreased contrast sensitivity in visual testing, but this phenotype more likely reflects a defect in optic nerve rather than retinal neural processing.^{10,11} Pharmacologic studies on non-CF human fetal retinal explants provided evidence for cAMP regulation of the fast oscillatory component of the ERG,²⁴ which can be generated by Cl^- transport. However, in isolated frog retinal preparation, cAMP elevation dissipated solute gradients across the RPE, thereby inhibiting rather than stimulating fluid transport.⁹² With only this conflicting data available, the precise role for CFTR in RPE transport is unclear. Nonetheless, modulation of net RPE Cl^- transport had considerable therapeutic promise, as demonstrated by reduced subretinal fluid bleb size in rat and rabbit following stimulation of purinergic receptors by INS37217.^{93,94} CFTR activators may similarly enhance RPE fluid absorption.

Additional work is needed to establish roles for AQP1 and CFTR in RPE function. Recent advances in non-invasive measurement of slow potentials in mice allow for study of electrical activity derived from non-neuronal components of the visual

cycle.⁹⁵ Differences in Müller cell-generated slow potentials have been identified in Kir4.1 heterozygous mice compared to wild-type mice.⁹⁶ Careful study of AQP-deficient mouse slow ERG components might reveal similar abnormalities. The slow light peak in the electrooculogram also reflects RPE basolateral membrane Cl⁻ conductance,⁹⁷ and is decreased as a diagnostic feature of Best disease. Advances in mouse ERG measurements have recently been applied to evaluate the electrophysiological consequences of CFTR channel gene disruption, demonstrating contributions of CFTR to RPE-driven ERG components.⁹⁸

Summary and Perspective

Ocular epithelia have the capacity for high rates of fluid transport, which often depends on active Cl⁻ secretion or absorption, producing near-isosmolar fluid transport. From a variety of approaches, including analysis of AQP- and CFTR-deficient mice, there is now compelling evidence for involvement of AQPs and CFTR in ocular epithelial fluid transport. Small-molecule modulators of ocular AQP and CFTR function or expression might thus be exploited clinically, as summarized in Table 1. At the ocular surface, AQP3 or AQP5 upregulation could accelerate wound healing and reduce corneal edema, while CFTR activators are predicted to stimulate tear secretion. Corneal endothelial AQP1 and CFTR activators/inducers might also reduce corneal edema and associated opacity. AQP1/AQP4 inhibition represents a promising strategy in reducing IOP associated with glaucoma. In the retina, AQP4 inhibitors might be neuroprotective following retinal ischemia, and activation of RPE CFTR might be useful in treating retinal detachment. Potent small-molecule CFTR activators and inhibitors have already

been identified, and the therapeutic potential of CFTR inhibitors has been demonstrated in rodent models of CFTR-dependent secretory diarrhea.^{99,100,101} When available, non-toxic AQP inhibitors will prove useful in confirming analyses of knock-out mice, and may provide new approaches for treatment of eye diseases associated with abnormalities in fluid balance.

References

1. Hamann S. Molecular mechanisms of water transport in the eye. *Int Rev Cytol.* 2002;215:395–431.
2. Agre P, Kozono D. Aquaporin water channels: molecular mechanisms for human diseases. *FEBS Lett.* 2003;27:72-78.
3. Verkman AS. More than just water channels: unexpected cellular roles of aquaporins. *J Cell Sci.* 2005;118:3225–3232.
4. Hara-Chikuma M, Verkman A S. Aquaporin-1 facilitates epithelial cell migration in kidney proximal tubule. *J Am Soc Nephrol.* 2006;17:39–45.
5. Levin MH, Verkman AS. Aquaporin-3 dependent cell migration and proliferation during corneal re-epithelialization. *Invest Ophthalmol Vis Sci.* In press.
6. Jentsch TJ, Stein V, Weinreich F, Zdebik AA. Molecular structure and physiologic function of chloride channels. *Physiol Rev.* 2002;82:503–568.
7. Pilewsky JM, Frizzell RA. Role of CFTR in airway disease. *Physiol Rev.* 1999;79:S215–S255.
8. Sheppard DM, Welsh MJ. Structure and function of the CFTR chloride channel. *Physiol Rev.* 1999;79:S23–S45.
9. Sheppard JD, Orenstein DM, Chao C, Butala S, Kowalski RP. The ocular surface in cystic fibrosis. *Ophthalmology.* 1989;96:1624–1630.
10. Morkeberg JC, Edmund C, Prause JU, Lanng S, Koch C, Michaelsen KF. Ocular findings in cystic fibrosis patients receiving vitamin A supplementation. *Graëfes Arch Clin Exp Ophthalmol.* 1995;233:709–713.
11. Ansari EA, Sahni K, Etherington C, et al. Ocular signs and symptoms and vitamin A status in patients with cystic fibrosis treated with daily vitamin A supplements. *Br J Ophthalmol.* 1999;83:688–691.
12. Mrugacz M, Minarowska A. Eye symptoms of cystic fibrosis. *Klin Oczna.* 2002;104:418–420.
13. Zhang D, Vetrivel L, Verkman AS. Aquaporin deletion in mice reduces intraocular pressure and aqueous fluid production. *J Gen Physiol.* 2002;119:561–569.

14. Li J, Patil RV, Verkman AS. Mildly abnormal retinal function in transgenic mice without Müller cell aquaporin-4 water channels. *Invest Ophthalmol Vis Sci.* 2002;43:573–579.
15. Thiagarajah JR, Verkman AS. Aquaporin deletion in mice reduces corneal water permeability and delays restoration of transparency after swelling. *J Biol Chem.* 2002;277:19139–19144.
16. Levin MH, Verkman AS. Aquaporin-dependent water permeation at the mouse ocular surface: in vivo microfluorimetric measurements in cornea and conjunctiva. *Invest Ophthalmol Vis Sci.* 2004;45:1428-1434.
17. Da T, Verkman AS. Aquaporin-4 gene disruption in mice protects against impaired retinal function and cell death after ischemia. *Invest Ophthalmol Vis Sci.* 2004;45:4477–4483.
18. Kenney MC, Atilano SR, Zorapapel N, Holguin B, Gaster RN, Ljubimov AV. Altered expression of aquaporins in bullous keratopathy and Fuchs' dystrophy corneas. *J Histochem Cytochem.* 2004;52:1341–1340.
19. Macnamara E, Sams GW, Smith K, Ambati J, Singh N, Ambati BK. Aquaporin-1 expression is decreased in human and mouse corneal endothelial dysfunction. *Mol Vis.* 2004;10:51–56.
20. Rabinowitz YS, Dong L, Wistow G. Gene expression studies of human keratoconus cornea for NEIBank: a novel cornea-expressed gene and the absence of transcripts for aquaporin 5. *Invest Ophthalmol Vis Sci.* 2005;46:1239–1246.
21. Turner HC, Bernstein A, Candia OA. Presence of CFTR in the conjunctival epithelium. *Curr Eye Res.* 2002;24:182–187.
22. Shiue MH, Gukasyan HJ, Kim K, Loo DD, Lee VHL. Characterization of cyclic AMP-regulated chloride conductance in the pigmented rabbit conjunctival epithelial cells. *Can J Physiol Pharmacol.* 2003;80:533–540.
23. Sun XC, Bonanno JA. Expression, localization, and functional evaluation of CFTR in bovine corneal endothelial cells. *Am J Physiol.* 2002;282:C673–C683.
24. Blaug S, Quinn R, Quong J, Jalickee S, Miller SS. Retinal pigment epithelial function: a role for CFTR? *Doc Ophthalmol.* 2003;106:43–50.
25. Levin MH, Verkman AS. CFTR-regulated chloride transport at the ocular surface in living mice measured by potential differences. *Invest. Ophthalmol. Vis. Sci.* 2005;46:4423–4432.

26. Reigada D, Mitchell CH. Release of ATP from retinal pigment epithelial cells involves both CFTR and vesicular transport. *Am J Physiol*. 2004;288:C132–C140.
27. Mathers WD, Lane JA, Sutphin JE, Zimmerman MB. Model for ocular tear film function. *Cornea*. 1996;15:110–119.
28. Mandell RB, Fatt I. Thinning of the human cornea on awakening. *Nature*. 1965;208:292–293.
29. Candia OA. Electrolyte and fluid transport across corneal, conjunctival, and lens epithelia. *Exp Eye Res*. 2004;78:527–535.
30. Dartt DA. Regulation of mucin and fluid secretion by conjunctival epithelial cells. *Prog Retin Eye Res*. 2002;21:555–576.
31. Watsky MA, Jablonski MM, Edelhauser HF. Comparison of conjunctival and corneal surface area in rabbit and human. *Curr Eye Res*. 1988;7:483–486.
32. Murakami T, Fujihara T, Nakamura M, Nakata K. P2Y(2) receptor stimulation increases tear fluid secretion in rabbits. *Curr Eye Res*. 2002;21:782–787.
33. Yang H, Reinach PS, Koniarek JP, Wang Z, Iserovich P, Fischbarg J. Fluid transport by cultured corneal epithelial cell layers. *Br J Ophthalmol*. 2000;84:199–204.
34. Lemp MA. Report of the National Eye Institute/Industry Workshop on clinical trials for dry eyes. *CLAO J*. 1995;21:221–232.
35. Patil RV, Saito I, Yang X, Wax MB. Expression of aquaporins in the rat ocular tissue. *Exp Eye Res*. 1997;64:203–209.
36. Hamann S, Zeuthen T, La Cour M, et al. Aquaporins in complex tissues: distribution of aquaporins 1–5 in human and rat eye. *Am J Physiol*. 1998;274:C1332–1345.
37. Kang F, Kuang K, Li J, Fischbarg J. Cultured bovine corneal epithelial cells express a functional aquaporin water channel. *Invest Ophthalmol Vis Sci*. 1999;40:253–257.
38. Mishima S, Hedbys BO. The permeability of the corneal epithelium and endothelium to water. *Exp Eye Res*. 1967;6:10–32.
39. Fischbarg J, Motoreano R. Osmotic permeabilities across corneal endothelium and antidiuretic hormone-stimulated toad urinary bladder structure. *Biochim Biophys Acta*. 1982;690:207–214.

40. Klyce SD, Neufeld AH, Zadunaisky JA. The activation of chloride transport by epinephrine and DB cyclic-AMP in the cornea of the rabbit. *Invest Ophthalmol.* 1973;12:127–139.
41. Klyce SD, Wong RKS. Site and mode of adrenaline action on chloride transport across the rabbit corneal epithelium. *J Physiol.* 1977;266:777–799.
42. Wolosin JM, Candia OA. Cl⁻ secretagogues increase basolateral K⁺ conductance of frog corneal epithelium. *Am J Physiol.* 1987;253:C555–C560.
43. Kompella UB, Kim KJ, Lee VH. Active chloride transport in the pigmented rabbit conjunctiva. *Curr Eye Res.* 1993;12:1041–1048.
44. Turner HC, Alvarez LJ, Candia OA. Cyclic AMP-dependent stimulation of basolateral K⁺ conductance in the rabbit conjunctival epithelium. *Exp Eye Res.* 2000;70:295–305.
45. Al-Nakkash L, Reinach PS. Activation of a CFTR-mediated chloride current in a rabbit corneal epithelial cell line. *Invest Ophthalmol Vis Sci.* 2001;42:2364–2370.
46. Botelho SY, Goldstein AM, Rosenlund ML. Tear sodium, potassium, chloride, and calcium at various flow rates: children with cystic fibrosis and unaffected siblings with and without corneal staining. 1973. *J Pediatr.* 1973;83:601–606.
47. Gilbard JP, Rossi SR, Heyda KG, Dartt DA. Stimulation of tear secretion and treatment of dry-eye disease with 3-isobutyl-1-methylxanthine. *Arch Ophthalmol.* 1991;109:672–676.
48. Gilbard JP. Treatment of keratoconjunctivitis sicca in rabbits with 3-isobutyl-1-methylxanthine. *Arch Ophthalmol.* 1994;112:1614–1616.
49. Li Y, Kuang K, Yerxa B, Wen Q, Rosskothan H, Fischbarg J. Rabbit conjunctival epithelium transports fluid and P2Y₂(2) receptor agonists stimulate Cl⁻ and fluid secretion. *Am J Physiol.* 2001;281:C595–C602.
50. Maurice DM. The structure and transparency of the cornea. *J Physiol.* 1957;136:263–286.
51. Freegard TJ. The physical basis of transparency of the normal cornea. *Eye.* 1997;11:465–471.
52. Joyce NC. Proliferative capacity of the corneal endothelium. *Prog Retin Eye Res.* 2003;22:359–389.
53. Yi DH, Dana MR. Corneal edema after cataract surgery: incidence and etiology. *Semin Ophthalmol.* 2002;17:110–114.

54. Kuang K, Yiming M, Wen Q, et al. Fluid transport across cultured layers of corneal endothelium from aquaporin-1 null mice. *Exp Eye Res.* 2004;78:791–798.
55. Fischbarg J. On the mechanism of fluid transport across corneal endothelium and epithelia in general. *J Exp Zool A Comp Exp Biol.* 2003;300:30–40.
56. Fischbarg J, Diecke FP. A mathematical model of electrolyte and fluid transport across corneal endothelium. *J Membr Biol.* 2005;203:41–56.
57. Wen Q, Diecke FP, Iserovich P, Kurang K, Sparrow J, Fischbarg J. Immunocytochemical localization of aquaporin-1 in bovine corneal endothelial cells and keratocytes. *Exp Biol Med (Maywood).* 2001;226:463–467.
58. Song J, Lee YG, Houston J, et al. Neonatal corneal stromal development in the normal and lumican-deficient mouse. *Invest Ophthalmol Vis Sci.* 2003;44:548–557.
59. Chakravarti S, Wu F, Vij N, Roberts L, Joyce S. Microarray studies reveal macrophage-like function of stromal keratocytes in the cornea. *Invest Ophthalmol Vis Sci.* 2004;45:3475–3484.
60. Bonanno JA. Identity and regulation of ion transport mechanisms in the corneal endothelium. *Prog Retin Eye Res.* 2003;22:69–94.
61. Paradiso AM, Coakley RD, Boucher RC. Polarized distribution of HCO_3^- transport in normal and cystic fibrosis nasal epithelia. *J Physiol.* 2003;548:203–218.
62. Welsh MJ, Smith JJ. cAMP stimulation of HCO_3^- secretion across airway epithelia. *JOP.* 2001;2:291–293.
63. Sun XC, Zhai CB, Cui M, et al. HCO_3^- -dependent soluble adenylyl cyclase activates cystic fibrosis transmembrane conductance regulator in corneal endothelium. *Am J Physiol.* 2003;284:C1114–C1122.
64. Sun XC, Cui M, Bonanno JA. $[\text{HCO}_3^-]$ -regulated expression and activity of soluble adenylyl cyclase in corneal endothelial and Calu-3 cells. *BMC Physiol.* 2004.4:8.
65. Lass JH, Spurney RV, Dutt RM, et al. A morphologic and fluorophometric analysis of the corneal endothelium in type I diabetes mellitus and cystic fibrosis. *Am J Ophthalmol.* 1995;100:783–788.
66. Weinreb RN, Khaw PT. Primary open-angle glaucoma. *Lancet.* 2004;363:1711–1720.

67. Nielsen S, Smith BI, Christensen EI, Agre PA. Distribution of the aquaporin CHIP in secretory and resorptive epithelia and capillary endothelia. *Proc Natl Acad Sci USA*. 1993;90:7275–7279.
68. Hasegawa H, Lian SC, Finkbeiner, WB, Verkman AS. Extrarenal tissue distribution of CHIP28 water channels by in situ hybridization and antibody staining. *Am J Physiol*. 1994;266:C893–C903.
69. Frigeri A, Gropper M, Turck CW, Verkman AS. Immunolocalization of the mercurial-insensitive water channel and glycerol intrinsic protein in epithelial cell plasma membranes. *Proc Natl Acad Sci USA*. 1995;92:4328–4331.
70. Patil RV, Han Z, Yiming M, et al. Fluid transport by human nonpigmented ciliary epithelial layers in culture: a homeostatic role for aquaporin-1. *Am J Physiol*. 2001;281:C1139–C1145.
71. Stamer WD, Peppel K, O'Donnell ME, Roberts BC, Wu F, Epstein DS. Expression of aquaporin-1 in human trabecular meshwork cells: role in resting cell volume. *Invest Ophthalmol Vis Sci*. 2001;42:1803–1811.
72. Ruiz-Ederra J, Verkman AS. Mouse model of sustained elevation in intraocular pressure produced by episcleral vein occlusion. *Exp Eye Res*. 2006;82:879–884.
73. Do CW, Civan MM. Basis of chloride transport in ciliary epithelium. *J Membr Biol*. 2004;200:1–13.
74. McCannel CA, Scanlon PD, Thibodeau S, Brubaker RF. A study of aqueous humor formation in patients with cystic fibrosis. *Invest Ophthalmol Vis Sci*. 1992;33:160–164.
75. Do CW, Kong CW, To CH. cAMP inhibits transepithelial chloride secretion across bovine ciliary body epithelium. *Invest Ophthalmol Vis Sci*. 2004;45:3638–3643.
76. Marmor MF. Mechanisms of fluid accumulation in retinal edema. *Doc Ophthalmol*. 1999;97:239–249.
77. Marmor MF. Control of subretinal fluid: experimental and clinical studies. *Eye*. 1990;4:340–344.
78. Bringmann A, Uckermann O, Pannicke T, Iandiev I, Reichenbach A, Wiedemann P. Neuronal versus glial cell swelling in the ischaemic retina. *Acta Ophth Scand*. 2005;83:528–538.

79. Stamer WD, Bok D, Hu J, Jaffe GJ, McKay BS. Aquaporin-1 channels in the human retinal pigment epithelium: role in transepithelial water movement. *Invest Ophthalmol Vis Sci.* 2003;44:2803–2808.
80. Ruiz A, Rok D. Characterization of the 3' UTR sequence encoded by the AQP-1 gene in human retinal pigment epithelium. *Biochim Biophys Acta.* 1996;1282:174–178.
81. Kim IB, Oh SJ, Nielsen S, Chun MH. Immunocytochemical localization of aquaporin 1 in the rat retina. *Neuroscience Letters.* 1998;244:52–54.
82. Kim IB, Lee EJ, Oh SJ, Park CB, Pow DV, Chun MH. Light and electron microscopic analysis of aquaporin 1-like-immunoreactive amacrine cells in the rat retina. *J Comp Neurol.* 2002;452:178–191.
83. Iandiev I, Pannicke T, Reichel MB, Wiedemann P, Reichenbach A, Bringmann A. Expression of aquaporin-1 immunoreactivity by photoreceptor cells in the mouse retina. *Neurosci Lett.* 2005;388:96–99.
84. Nagelhus EA, Veruki ML, Torp R, et al. Aquaporin-4 water channel protein in the rat retina and optic nerve: polarized expression in Müller cells and fibrous astrocytes. *J Neuroscience.* 1998;18:2506–2519.
85. Nagelhus EA, Horio A, Inanobe AI, et al. Immunogold evidence suggests that coupling of K⁺ siphoning and water transport in rat retinal Müller cells is mediated by a coenrichment of Kir4.1 and AQP4 in specific membrane domains. *Glia.* 1999;26:47–54.
86. Connors NC, Kofuji P. Potassium channel Kir4.1 macromolecular complex in retinal glial cells. *Glia.* 2005;53:124–131.
87. Manley GT, Fujimura M, Ma T, et al. Aquaporin-4 deletion in mice reduces brain edema following acute water intoxication and ischemic stroke. *Nature Medicine.* 2000;6:159–163.
88. Li J, Verkman AS. Impaired hearing in mice lacking aquaporin-4 water channels. *J Biol Chem.* 2001;276:31233–31237.
89. Marmorstein AD, Marmorstein LY, Royborn M, Wang X, Holyfield JG, Petrukhin K. Bestrophin, the product of the Best vitelliform macular dystrophy gene (VMD2), localizes to the basolateral membrane of the retinal pigment epithelium. *Proc Natl Acad Sci USA.* 2000;97:12758–12763.
90. Hartzell C, Qu Z, Putzier I, Artinian L, Chien L, Cui Y. Looking chloride channels straight in the eye: bestrophins, lipofuscinosis, and retinal degeneration. *Physiology.* 2005;20:292–302.

91. Loewen ME, Smith NK, Hamilton DL, Grahn BH, Forsyth GW. CLCA protein and chloride transport in canine retinal pigment epithelium. *Am J Physiol.* 2003;285:C1314–1321.
92. Miller SS, Hughes BA, Machen TE. Fluid transport across retinal pigment epithelium is inhibited by cyclic AMP. *Proc Natl Acad Sci USA.* 1982;79:2111–2115.
93. Meyer CH, Hotta K, Peterson WM, Toth CA, Jaffe GJ. Effect of INS38717, a P2Y(2) agonist, on experimental retinal detachment and electroretinogram in adult rabbits. *Invest. Ophthalmol Vis Sci.* 2002;43:3567–3574.
94. Maminishkis A, Jalickee S, Blaug SA, et al. The P2Y(2) receptor agonist INS37217 stimulates RPE fluid transport in vitro and retinal reattachment in rat. *Invest Ophthalmol Vis Sci.* 2002;43:3555–3566.
95. Wu J, Peachey NS, Marmorstein AD. Light-evoked response of the mouse retinal pigment epithelium. *J Neurophysiol.* 2004;91:1134–1142.
96. Wu J, Marmorstein AD, Kofuji P, Peachey NS. Contribution of Kir4.1 to the mouse electroretinogram. *Mol Vis.* 2004;10:650–654.
97. Gallemore RP, Hughes BA, Miller SS. Retinal pigment epithelial transport mechanisms and their contribution to the electroretinogram. *Prog Retinal Eye Res.* 1997;16:609–566.
98. Wu J, Marmorstein AD, Peachey NS. Functional abnormalities in the retinal pigment epithelium of CFTR mutant mice. *Exp Eye Res.* 2006;83:424–428.
99. Ma T, Vetrivel L, Yang H, et al. High-affinity activators of cystic fibrosis transmembrane conductance regulator (CFTR) chloride conductance identified by high-throughput screening. *J Biol Chem.* 2002;277:37235–37241.
100. Ma T, Thiagarajah JR, Yang H, et al. Thiazolidinone CFTR inhibitor identified by high-throughput screening blocks cholera toxin-induced intestinal fluid secretion. *J Clin Invest.* 2002;110:1651–1658.
101. Muanprasat C, Sonawane ND, Salinas DB, Taddei A, Galiotta LJ, Verkman AS. 2004. Discovery of glycine hydrazide pore-occluding CFTR inhibitors: mechanism, structure-activity analysis and in vivo efficacy. *J Gen Physiol.* 2004;124:125–137.

Table 1

Proposed AQP- and CFTR-based therapies for common ocular disorders.

Clinical Disorder	Treatment Strategy	Intervention
Keratoconjunctivitis Sicca (Tear film deficiency)	↑ Corneal and conjunctival fluid secretion	↑ CFTR
Corneal Edema/Opacity (Dystrophy, trauma)	↑ Endothelial and epithelial fluid transport	↑ CFTR, AQP1, AQP5
Recurrent Corneal Erosions (Persistent abrasions)	↑ Epithelial migration and proliferation	↑ AQP3
Glaucoma (Elevated IOP)	↓ Ciliary epithelial aqueous humor secretion	↓ AQP1, AQP4
Retinal Detachment (BRB break-down & outer retinal edema)	↑ Retinal pigment epithelial fluid absorption	↑ CFTR
Retinal Ischemia (Vascular occlusion & inner retinal edema)	↓ Neuronal and Müller swelling	↓ AQP4

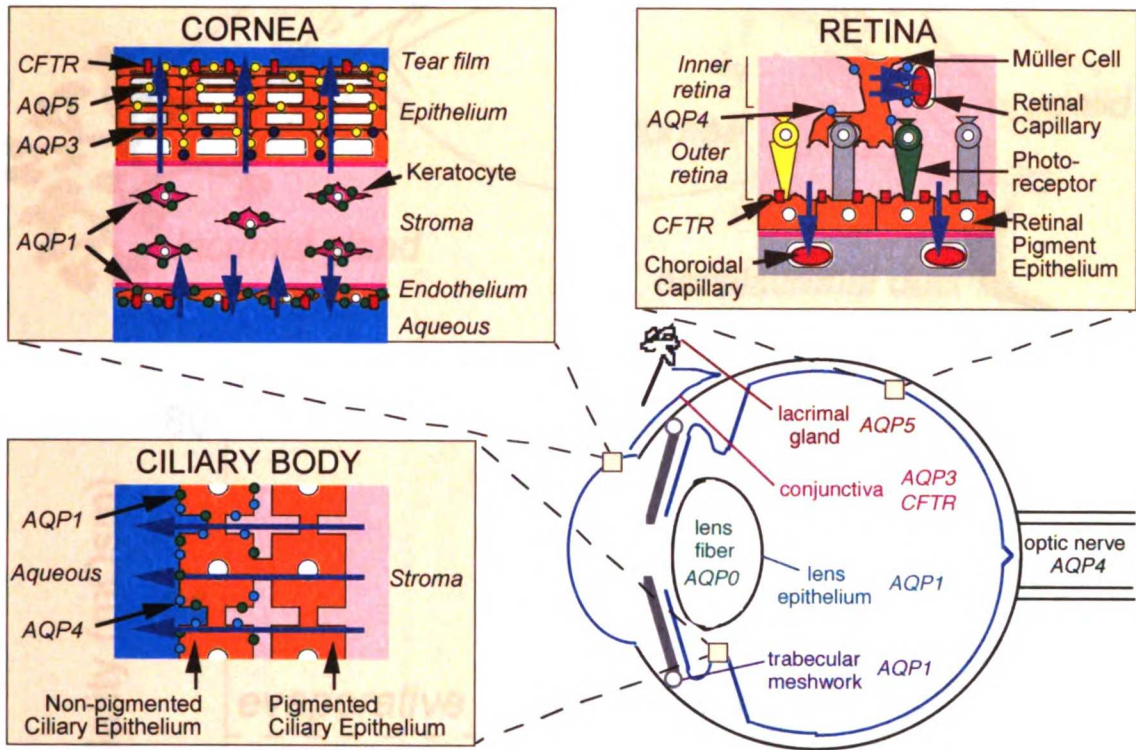


Figure 1

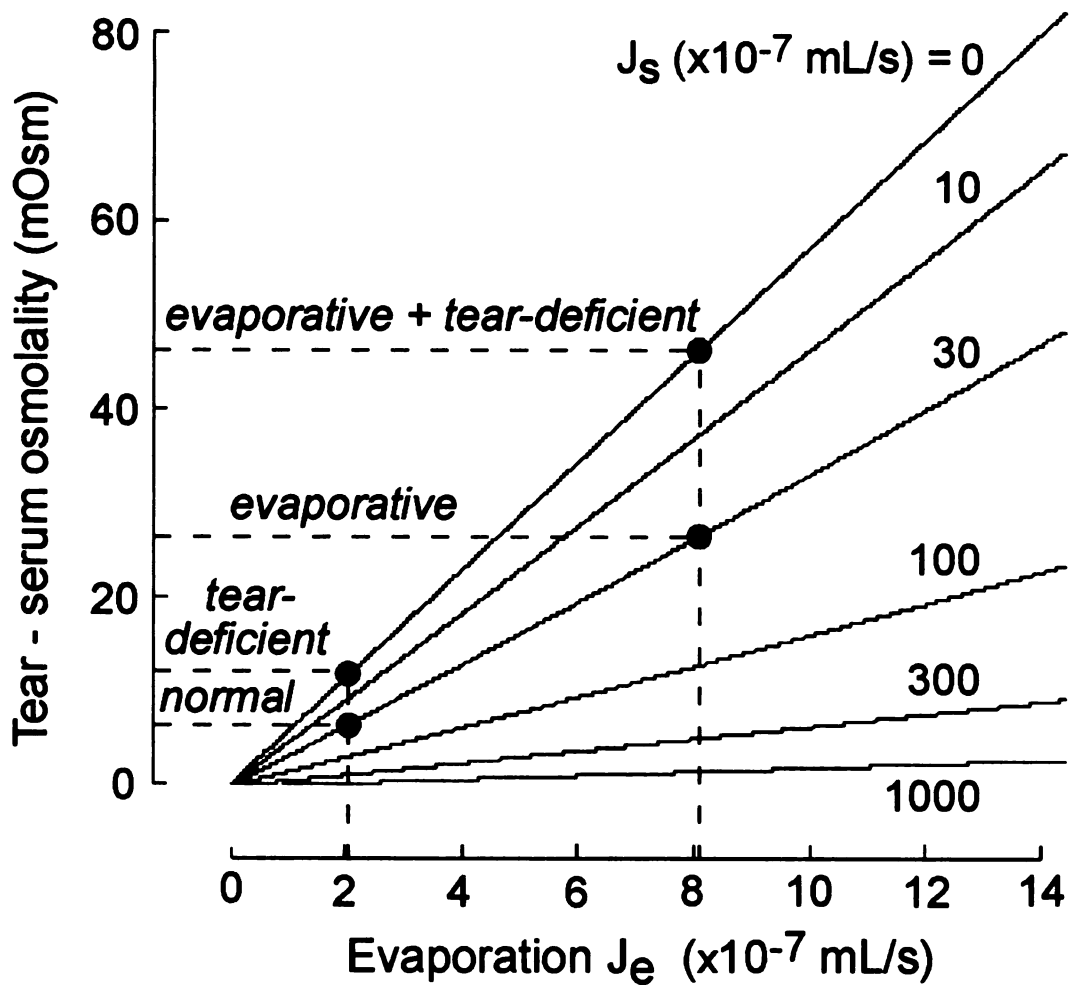
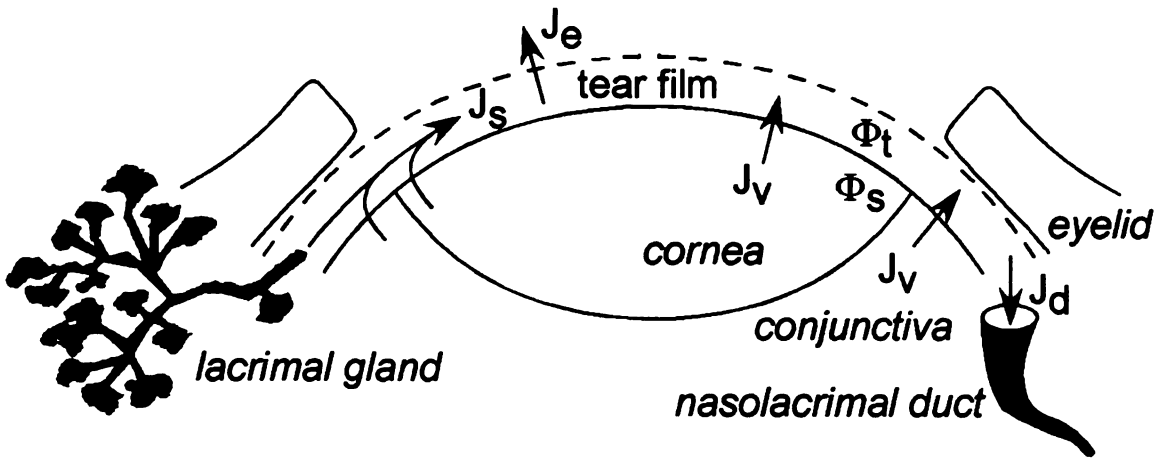


Figure 2

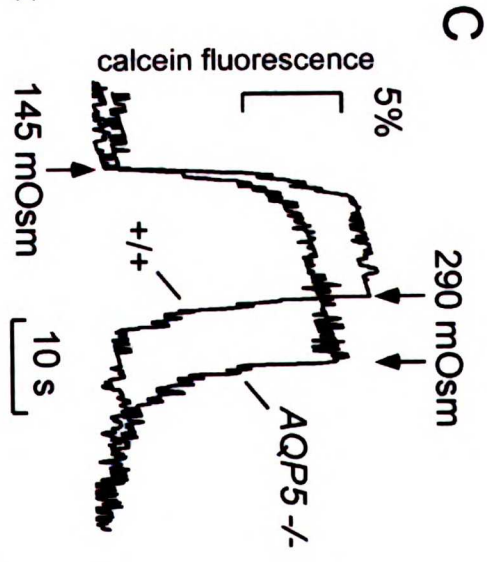
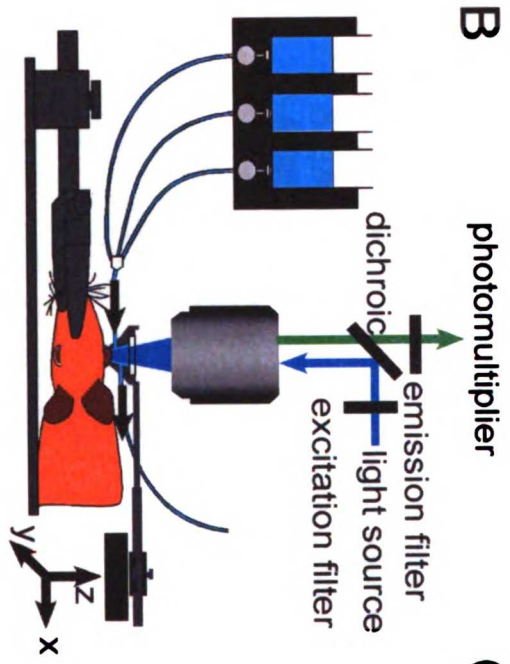
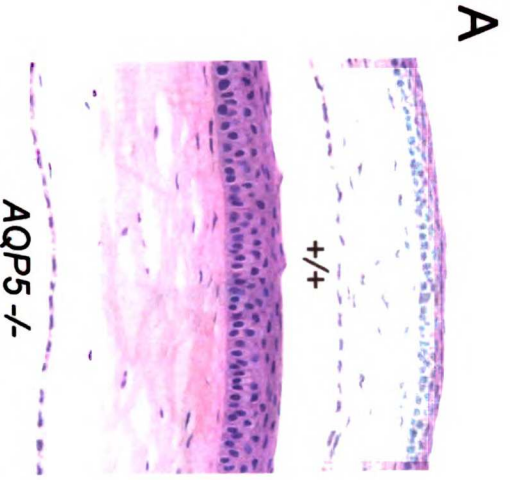


Figure 3

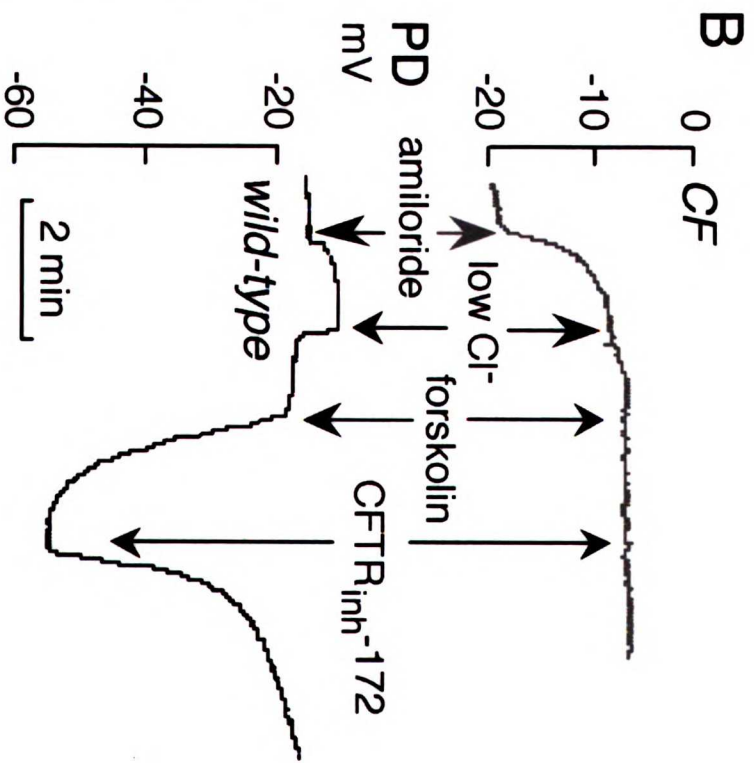
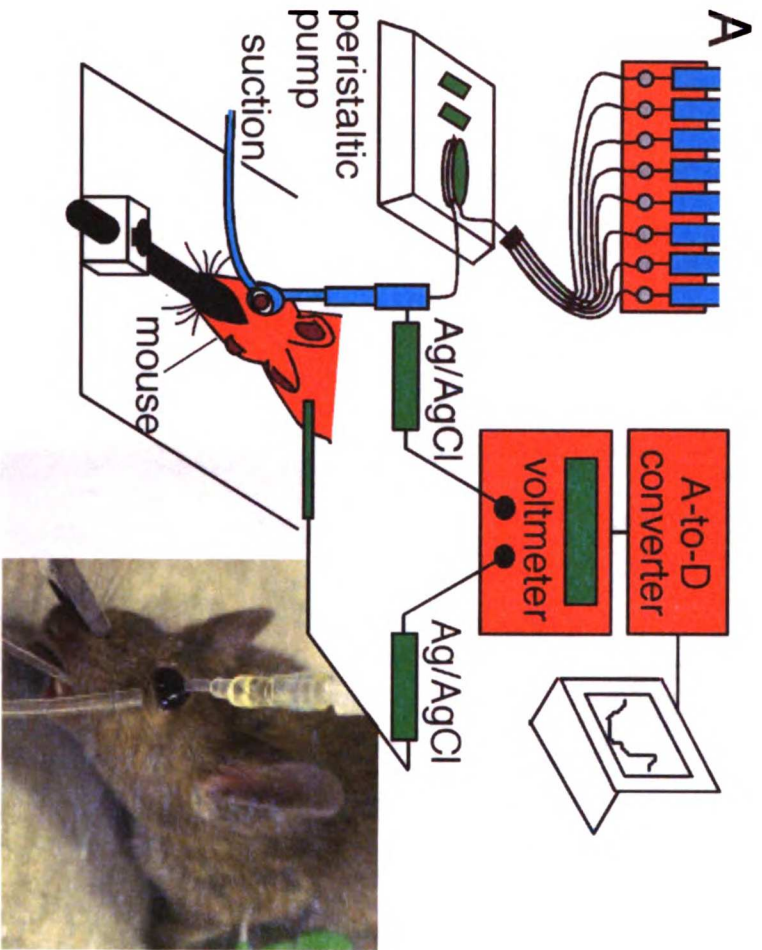


Figure 4

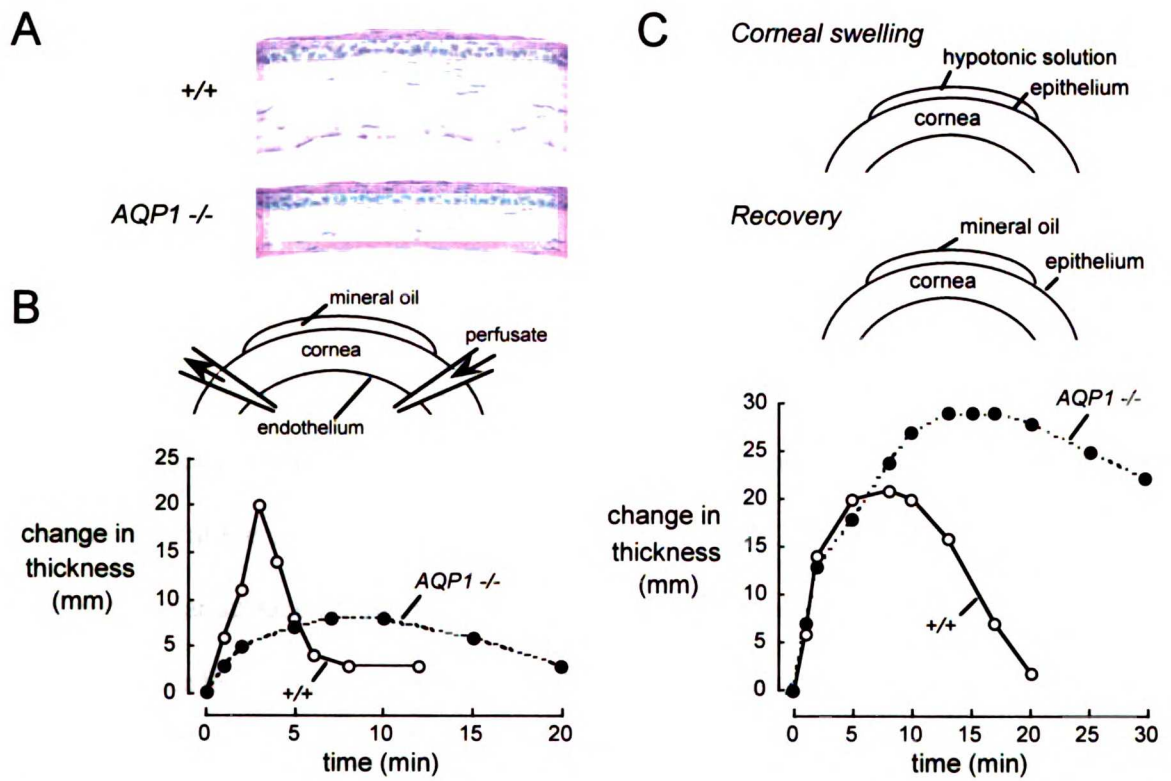


Figure 5

Figure Legends

FIGURE 1. AQP- and CFTR-dependent fluid transport across ocular epithelia. *Top left:* water balance in the corneal stroma, showing passive influx through the leaky endothelium and active efflux across endothelium and epithelium. *Bottom left:* aqueous fluid secretion across non-pigmented ciliary epithelium, involving transfer of water and solutes from pigmented ciliary epithelium via gap junctions. *Top right:* modulation of outer retinal fluid by retinal pigment epithelium and inner retinal fluid by astroglial Müller cells. Locations of confirmed AQP- and CFTR-facilitated transport indicated. See text for explanations.

FIGURE 2. Theoretical role of ocular surface water permeability in tear film dynamics. *Top:* schematic of ocular surface geometry and contributors of tear fluid balance. J_e , rate of evaporation at the exposed corneal surface; J_s , rate of fluid secretion by the lacrimal gland and ocular surface epithelia; J_v , osmotic volume flow across the corneal and conjunctival surfaces; J_d , tear fluid removal by nasolacrimal drainage; Φ_t and Φ_s , osmolarities of tear film and surface tissue, respectively. *Bottom:* theoretical dependence of tear film osmolarity on tear evaporation and secretion rates, computed from the model and plotted as the extent of hyperosmolarity ($\Phi_t - \Phi_s$). Adapted from Ref¹⁶.

FIGURE 3. AQP5 function at the ocular surface. (A) Increased stromal and epithelial thicknesses in AQP5-deficiency in paraffin-embedded central corneal sections. (B) Schematic of ocular surface perfusion for fluorescence measurements of cell volume changes. The instrumentation consisted of a microchamber positioned on the corneal

surface, optical elements for calcein fluorescence measurement, rapid exchange perfusion system, and stereotaxic platform. (C) Representative time courses of corneal epithelial cell calcein fluorescence in response to a hypoosmolar osmotic gradient in wild-type and AQP5-deficient mice. Adapted from Ref ¹⁶.

FIGURE 4. CFTR function at the ocular surface. (A) Diagram of ocular surface perfusion and PD recording methods. Anesthetized mouse immobilized in a stereotaxic platform, with perfusion tubing attached to an electrical recording system and in contact with a droplet of constant size on the ocular surface. *Inset:* photograph of perfused ocular surface. (B) Ocular surface PDs in wild-type vs. CF mice in response sequentially to amiloride (10 μ M), low Cl⁻, forskolin (10 μ M), and CFTR_{inh}-172 (10 μ M). Adapted from Ref ²⁵.

FIGURE 5. AQP1 function in corneal endothelium. (A) Reduced corneal thickness in AQP1-deficient corneas in paraffin-embedded central corneal sections. (B) Osmotic water transport across the corneal endothelium. *Top:* schematic showing micropipette placement for anterior chamber perfusion. *Bottom:* time courses of corneal thickness following corneal endothelial exposure to hypotonic saline in wild-type (*open circles*) and AQP1-null (*filled circles*) mice. (C) Restoration of corneal thickness after osmotic swelling. *Top:* procedure to induce corneal swelling and follow recovery of thickness. *Bottom:* representative time courses of corneal thickness after exposure of the corneal surface to hypotonic saline. Corneal thicknesses measured by in vivo by z-scanning confocal microscopy. Adapted from Ref ¹⁵.

CHAPTER 2.

Aquaporin-Dependent Water Permeation at the Mouse Ocular Surface: In Vivo Microfluorimetric Measurements in Cornea and Conjunctiva

Abstract

PURPOSE. Fluorescence methods were developed to quantify membrane and tissue water permeabilities at the ocular surface and to compare water transport in wild-type mice versus transgenic mice lacking each of the water channels, aquaporin (AQP)-1, -3, and -5, normally expressed in cornea or conjunctiva.

METHODS. Membrane water permeabilities (P_f^{mem}) of calcein-stained surface epithelial cells were measured from the kinetics of fluorescence quenching in response to rapid (<0.2 seconds) changes in extraocular fluid osmolarity. Tissue water permeabilities (P_f^{tiss}) across intact cornea and conjunctiva—the relevant parameters describing water movement into the hyperosmolar tear film in vivo—were determined by a dye-dilution method from the fluorescence of Texas red-dextran in an anisosmolar solution in a microchamber at the ocular surface.

RESULTS. Osmotic equilibration occurred with an exponential time constant (τ) of 1.3 ± 0.2 seconds ($P_f^{\text{mem}} = 0.045$ cm/s) in calcein-loaded corneal epithelial cells of wild-type mice, slowing 2.1 ± 0.4 -fold in AQP5-deficient mice; τ was 2.4 ± 0.1 seconds in conjunctiva

($P_f^{\text{mem}} = 0.025$ cm/s), slowing 3.6 ± 0.7 -fold in AQP3-deficient mice. In dye-dilution experiments, P_f^{tiss} of cornea was 0.0017 cm/s and decreased by greater than fivefold in AQP5-deficient mice. P_f^{tiss} in AQP5-null mice was restored to 0.0015 cm/s after removal of the epithelium. P_f^{tiss} of conjunctiva was 0.0011 cm/s and was not sensitive to AQP3 deletion.

CONCLUSIONS. These results define for the first time the water-transporting properties of the two principal ocular surface barriers in vivo. The permeability data were incorporated into a mathematical model of tear film osmolarity, providing insights into the pathophysiology of dry eye disorders.

The ocular surface consists of the cornea and conjunctiva, which make contact with the tear film. The corneal stroma is covered externally by a stratified squamous epithelium and internally by a single-layered endothelium. Maintenance of stromal transparency requires precise regulation of extracellular water content. The conjunctiva, which covers more of the ocular surface than the cornea (17 times more area in humans),¹ consists of a superficial stratified epithelium interspersed with goblet cells and a deeper stroma with arterial and lymphatic networks. The palpebral and bulbar conjunctivae cover the posterior lid and the anterior scleral surfaces, respectively.

The ocular surface plays a role in regulation of tear film volume and composition. Near-isosmolar tear fluid is secreted actively by lacrimal and ocular surface tissues, dispersed by blinking, and drained through the nasolacrimal duct. Fluid secretion measurements across the cornea and conjunctiva in several species provide evidence that

ocular surface epithelia contribute significantly to tear fluid under basal conditions and may be particularly important in lacrimal gland dysfunction.^{2,3,4} Indeed, new therapies for dry eye, or keratoconjunctivitis sicca (KCS), target signaling pathways involved in corneal and conjunctival chloride-driven fluid secretion.^{5,6,7}

Ocular surface water transport plays an additional role in maintenance of tear volume and osmolarity by replacing evaporative water losses. Although under normal conditions, evaporation is retarded by a thin outer lipid tear layer secreted by meibomian glands,^{8,9,10} it is still responsible for at least 10% to 25% of tear turnover,¹¹ driving transcellular osmotic water transport across ocular surface tissues. Evaporative water loss is an important determinant of tear film ionic content and is primarily responsible for the elevated tear film osmolarity and ocular surface changes common to all forms of dry eye disease.¹² Transepithelial osmosis is also an important determinant of corneal hydration. Hypoxia from contact lens wear generates lactate osmoles in the cornea,¹³ inducing stromal swelling, which is reversed mainly by evaporation from tears rather than endothelium pump function.¹⁴ Transepithelial osmosis is responsible for the diurnal 4% thinning of corneas during the first few waking hours of each day.¹⁵ Though these phenomena are well described, little information is available about water permeability properties of ocular surface tissues, particularly in vivo. High water permeability at the ocular surface is thought to facilitate fluid secretion into the tear film in response to active ion secretion and to minimize tear film hyperosmolarity during evaporation.

Aquaporin (AQP)-type water channels make up a family of small transmembrane proteins that facilitate osmotically driven water transport across cell plasma membranes,

providing the major molecular pathway for water movement. Three AQP proteins are strongly expressed at plasma membranes in cornea and conjunctiva, including AQP1 in corneal endothelium and keratocytes, AQP5 in corneal epithelium, and AQP3 in conjunctival epithelium.^{16,17,18,19} Transgenic knock-out mice have been informative in elucidating the role of AQPs in mammalian physiology, manifesting a variety of phenotypes such as defective urinary concentrating ability in mice lacking AQP1 or AQP3,^{20,21} altered cerebral fluid balance and neural signal transduction in mice lacking AQP4,^{22,23} and defective salivary and submucosal gland secretion in mice lacking AQP5.^{24,25} In the eye, mice lacking AQP1 and AQP4 (expressed in ciliary epithelium) have reduced intraocular pressure and aqueous fluid production,²⁶ mice lacking AQP4 (expressed in retinal Müller cells) have reduced flash-induced retinal potentials,²⁷ and mice lacking AQP1 show delayed restoration of corneal transparency after experimental swelling.²⁸ The presence of AQPs in ocular surface tissues suggests that they have a role in fluid transport and tear film homeostasis.

The goals of this study were to measure osmotic water permeability of the two principal ocular surface barriers—the cornea and conjunctiva—in mice *in vivo* and to investigate the role of AQPs as the molecular pathway of water permeation. Mice were chosen because of the availability of transgenic mice lacking each of the major ocular surface AQPs, permitting quantitative analysis of the role of each AQP by comparative permeability measurements in wild-type versus AQP knock-out mice. Measurements were made *in vivo*, with vascular supply intact, to minimize concerns about altered tissue architecture, regulatory mechanisms, and AQP expression in isolated or cultured ocular tissues. In addition, *in vivo* measurements have direct relevance in relating tear-stromal

osmotic driving forces to induced water flow into the tear film layer. Novel microfluorimetric methods were developed to measure water permeability in ocular surface cells and intact ocular tissues. Several experimental challenges required the design of custom microperfusion chambers for in vivo optical measurements, including the rapid osmotic equilibration of surface cells, slow net water transport across intact ocular surfaces, and physical constraints imposed by the mouse orbit. The new methods were applied to characterize water permeation mechanisms and the roles of AQPs in cornea and conjunctiva. The results were incorporated into a quantitative model of tear film osmolarity with relevance to clinical dry eye syndromes.

Methods

Transgenic Mice

Transgenic mice deficient in AQP1, -3, and -5 in a CD1 genetic background were generated by targeted gene disruption, as described previously.^{20,21,24} Wild-type and knock-out mice were matched by age and weight (ages 6–8 weeks, 22–25 g).

Investigators were blinded to mouse genotype in all functional studies until completion of data analysis. Protocols were approved by the University of California at San Francisco Committee on Animal Research and are in compliance with the ARVO Statement for the Use of Animals in Ophthalmic and Vision Research.

Fluorescence Microscopy

Fluorescence was measured with a stereo epifluorescence microscope (SMZ1500; Nikon, Tokyo, Japan) equipped with a 1.6x objective lens (working distance, 24 mm; numerical aperture, 0.21), adjustable zoom set to 6x, and custom filter sets for Texas red and FITC (Chroma, Rockingham, VT). The illumination source was a 100-W tungsten-halogen lamp powered by a stabilized direct current source. Fluorescence was detected with a 14-dynode photomultiplier, amplifier, and analog-to-digital converter, and recorded with custom-written software (written in LabView; National Instruments, Austin, TX). In some studies, fluorescence was imaged with a cooled charge-coupled device (CCD) camera (CoolSnap HQ; Photometrics, Tucson, AZ).

Ocular Surface Perfusion

Two stainless-steel perfusion microchambers (volumes, ~4 and 33 μ L) were constructed to measure cell and tissue water permeabilities at the ocular surface *in vivo*. Scaled drawings with chamber dimensions are provided in Figure 1A . The upper (lens-facing) surfaces were bounded by sapphire windows (Edmund Optics; Barrington, NJ) fixed to the chambers with optical cement. The bottom (ocular surface-facing) surfaces were beveled to the contour of the mouse globe (~3.2-mm diameter sphere). The 2-mm diameter bottom dimension was chosen to isolate corneal tissue from the limbus and conjunctiva. The same beveled contact surface achieved an airtight seal with the conjunctiva. Inlets and outlets were made from 21-gauge steel needles. Solutions were perfused using PE-90 tubing and a gravity pinch valve system (ALA Scientific

Instruments, Westbury, NY). Chambers were positioned with an *x-y-z* micromanipulator (World Precision Instruments, Sarasota, FL) as depicted in Figure 1B.

Mouse Preparation

Mice were anesthetized intraperitoneally with ketamine (40 mg/kg) and xylazine (20 mg/kg). Corneas were treated with topical proparacaine (0.5%) and kept hydrated with PBS supplemented with NaCl to 320 mOsM to match mouse serum osmolarity. Mice were immobilized for optical measurements with a custom-built stereotaxic device with a rotating jaw clamp, and the eye under study facing upward (Fig. 1C). Body temperature was maintained at $37 \pm 1^\circ\text{C}$ with a heating pad and rectal temperature probe. A wire clip applied gentle upward pressure to present the globe to the chamber for corneal permeability measurements without inducing trauma or corneal edema. In some experiments, much of the corneal epithelium was mechanically removed without trauma to the stroma using a Beaver blade (BD Biosciences, Mountain View, CA) and a standard scraping procedure.²⁹ For measurements on conjunctiva, a flat area of tissue consisting of portions of the upper tarsus and fornix was exposed with a pair of hook retractors threaded through the upper eyelid with sutures and fixed to posts with elastic bands. The globe was depressed into the orbit with surgical sponges (Medtronic, Jacksonville, FL; Fig. 1C).

Cell Membrane Water Permeability In Vivo

A calcein-quenching method developed previously for water permeability measurement in brain astrocyte cell cultures³⁰ was adapted to the mouse eye. Surface

epithelial cells were loaded with calcein by exposure of the cornea or conjunctiva for 30 minutes to 25 μ L PBS containing 10 μ M calcein-AM (Molecular Probes, Eugene, OR). The solution remained in place by surface tension, and, if necessary, solution was added during the incubation. After 30 minutes, the loading solution was rinsed from the eye surface with PBS. The 33- μ L microchamber was then positioned over the cornea or conjunctiva for continuous measurement of cell calcein fluorescence during perfusion with solutions of specified osmolarities. Complete solution exchange time was <50 ms at a perfusion rate of 55 mL/min achieved with the outlet under vacuum (Fig. 3A, bottom). The chamber was designed with its inlet close to the ocular surface, to establish a flow pattern with even faster exchange at the surface of the eye. For water permeability measurements, superficial cell loss was minimized by slowing perfusion approximately threefold with an adjustable valve on the outlet tubing. Solutions were exchanged between PBS (290 mOsM) and hypoosmolar (145 mOsM, PBS diluted with distilled water) or hyperosmolar (590 mOsM, PBS with added D-mannitol) saline. Solution osmolarities were measured with a freezing point–depression osmometer (Precision Systems, Natick, MA). The time course of fluorescence in response to solution osmolarity changes, $F(t)$, was fitted to a single exponential time constant, τ : $F(t) = A + B e^{-t/\tau}$, where A and B are related to system sensitivity and background signal. P_f^{mem} was computed with a mathematical model of osmosis through a multilayer tissue, as described in the Chapter 1 Appendix.

Transcorneal and Transconjunctival Water Permeabilities In Vivo

Water permeability across intact cornea and conjunctiva was measured by a dye-dilution method in which a cell-impermeant, photostable dye (Texas red-dextran, 3 kDa; Molecular Probes) was used as an inert marker of water flux. Texas red-dextran (0.05 mg/mL) was dissolved in hypoosmolar (~150 mOsM), isosmolar (~310 mOsM), or hyperosmolar (~580 mOsM) saline and infused into the microchamber positioned over the cornea or conjunctiva. Flow was stopped after solution exchange, and Texas red fluorescence was monitored continuously over 4 minutes. In some experiments, the solution was supplemented with 10% (wt/vol) 500-kDa dextran to increase viscosity 10-fold. Solute-free water movement across the corneal surface produced linear changes in Texas-red concentration and measured fluorescence. Water flux, J_v (in cubic centimeters per second), was computed from the product of chamber volume, V_c , and the rate of fluorescence change (after background subtraction), $d(F/F_0)/dt$. V_c was determined to be 3.8 μL when in contact with the curved corneal surface and 5.4 μL when in contact with the flat conjunctiva. With the assumption that unstirred layer effects are negligible, the osmotic water permeability coefficient, P_f^{tiss} (in centimeters per second), is defined from the relation: $J_v = P_f^{\text{tiss}} S v_w (\Phi_1 - \Phi_2)$, where S is the tissue surface area assuming a smooth surface, v_w is the partial molar volume of water (18 cm^3/mol), and $(\Phi_1 - \Phi_2)$ is the osmotic gradient, giving: $P_f^{\text{tiss}} = V_c [d(F/F_0)/dt] / [S v_w (\Phi_1 - \Phi_2)]$.

Corneal Thickness Measurement by Confocal Microscopy

Corneal thickness changes were measured after removal of the epithelium and exposure to solutions of various osmolarities, according to a method described previously.²⁸ After removal of the epithelium, corneas in living mice were exposed to hypoosmolar, isosmolar, or hyperosmolar solutions for specified times. Corneas were dried rapidly by blotting, and thickness was determined by scanning bright-field confocal microscopy, with an upright Nipkow wheel-type confocal microscope with a confocal/coaxial module (Technical Instrument Co., San Francisco, CA) and 20x air objective (working distance, 20.5 mm; numerical aperture, 0.35; Nikon). Images were acquired in the reflectance mode every 5 μm with a cooled CCD camera.

Immunocytochemistry

After mouse sacrifice, globes were enucleated and embedded in Tissue-Tek OCT compound, and 7- μm cryostat sections were cut. Immunocytochemistry was performed on acetone-fixed sections by using polyclonal anti-AQP1, -3, and -5 antibodies (Chemicon, Temecula, CA) and secondary Cy3-conjugated anti-rabbit IgG (Sigma-Aldrich, St. Louis, MO). Fluorescence micrographs were obtained using a Leica upright fluorescence microscope with 20x air objective and 3-color cooled Spot CCD camera (Diagnostic Instruments, Sterling Heights, MI).

Results

AQP Expression in Ocular Surface Tissues in Mice

Immunocytochemistry showed AQP1 in corneal endothelium and stromal keratocytes, and AQP5 in corneal epithelium, with no specific staining in corresponding knock-out mice (Fig. 2). AQP3 was expressed in conjunctival and corneal epithelia. RT-PCR analysis of whole mouse corneas with AQP-specific primers confirmed expression of transcripts encoding AQP1, -3, and -5, with no detectable transcripts encoding AQP0, -2, -4, -6, -7, -8, and -9 (not shown).

Water Permeability of Cells Lining the Ocular Surface

Measurement of cell membrane water permeability involved loading ocular surface cells of anesthetized mice with a membrane-permeant, nonfluorescent calcein derivative, which when de-esterified in the cytoplasm becomes fluorescent and membrane impermeant. Figure 3A (top) shows calcein staining of most superficial epithelial cells across the entire cornea, as visualized by epifluorescence stereomicroscopy through the 33- μ L microperfusion chamber (Fig. 1A, top). Initial calcein-quenching experiments at the maximum perfusion rate indicated osmotic equilibration in \sim 1 to 2 seconds in cornea and conjunctiva of wild-type mice. Because cell exfoliation often occurred, in most studies flow was slowed approximately threefold (exchange time, <150 ms) to minimize cell loss. A slight downward force was applied to the chamber with a three-axis micromanipulator to achieve an airtight seal over corneal and conjunctival tissues.

A calcein fluorescence-quenching method was adapted to the mouse eye to compare *in vivo* osmotic water permeability in wild-type versus AQP-deficient ocular surface cells. As found in other cell types,³⁰ calcein fluorescence in ocular surface cells was sensitive to the size and direction of the imposed osmotic gradient (Fig. 3B). Nearly twofold changes in relative superficial cell volume produced by changing perfusate osmolarity from 290 mOsM to 145 or 590 mOsM yielded a 5% to 8% change in fluorescence signal. Signal changes were independent of magnification, as expected with a cytoplasmic quenching mechanism (not shown). Figure 3C shows representative kinetics of reversible corneal (left) and conjunctival (right) cell swelling in response to serial perfusion with solutions of osmolarities 290, 145, and 290 mOsM. AQP5 deletion in cornea slowed osmotic equilibration, as did AQP3 deletion in conjunctiva. Figure 3D summarizes exponential time constants (τ) for a series of mice, which are inversely proportional to swelling rates. Osmotic equilibration was slowed 2.1 ± 0.4 -fold in AQP5-deficient corneal epithelium ($P < 0.05$) and 3.6 ± 0.7 -fold in AQP3-deficient conjunctiva ($P < 0.01$). Also, corneal epithelial cell membrane water permeability in AQP1-deficient mice was similar to that in wild-type mice (Fig. 3D), as expected, since AQP1 is expressed in corneal endothelium and keratocytes but not in corneal epithelium.

The osmotic water permeability coefficients (P_f^{mem}) of corneal and conjunctival epithelial cell membranes were computed from the time course of fluorescence change in response to osmotic challenge, assuming multilayered epithelia containing five (cornea) or four (conjunctiva) cell layers of increasing thickness from superficial to basal layer, as estimated from histologic sections (see the Chapter 1 Appendix).³¹ Deduced P_f^{mem} (in centimeters per second) were: 0.045 (wild-type) and 0.020 (AQP5-null) for cornea, and

0.025 (wild-type) and 0.007 (AQP3-null) for conjunctiva. The high P_f^{mem} of corneal epithelium in wild-type mice may be important in facilitating rapid water transport across the multilayered corneal epithelium, which contains ~10 membranous barriers in series.

Water Permeability Across Intact Cornea and Conjunctiva

A different fluorescence approach was developed to measure steady state, osmotically driven water transport across intact cornea and conjunctiva. A very small 4- μL chamber (Fig. 1A, bottom) was constructed to measure changes in dye concentration in anisomolar solutions contacting ocular surface epithelia, where submicroliter net osmotic water fluxes are predicted over several minutes. Texas red-dextran (3 kDa) was found to be a useful volume marker because of its photostability, membrane impermeability, and, compared with other dyes tested, minimal binding to the microchamber and ocular surfaces. The experimental procedure involved measurement of dye fluorescence in isosmolar saline for 4 minutes to establish a baseline signal. In some experiments there was slow signal loss (generally $<1\%/min$) over this time, possibly due to reflex tearing from eye irritation and/or dye binding to the chamber walls, which was corrected for in osmotic water permeability studies. The isosmolar solution was then changed to a hyperosmolar (~580 mOsM) or hypoosmolar (~150 mOsM) solution for 4 minutes, returned to the control isosmolar solution, and then changed to hypoosmolar or hyperosmolar solutions, respectively. Figure 4A shows approximately linear kinetics of the increase in fluorescence with hypoosmolar solutions (water entering tissue resulting in increased dye concentration) and decrease in fluorescence with hyperosmolar solutions (water exiting tissue resulting in dye dilution). The fluorescence signal changed by only a

few percent over 4 minutes in the 4- μ L chamber because of the small ocular surface area available for steady state osmosis. In control experiments, there was no appreciable signal change when the 33- μ L chamber was used, as expected, because of the correspondingly smaller fractional changes in dye concentration caused by osmotic water transport. Figure 4A also shows reduced changes in fluorescence for water transport across corneas from AQP5- but not AQP1-null mice. Similar slopes were produced when conjunctivae of wild-type were compared with AQP3-null mice.

One concern in this approach was the potential for error in deduced P_f^{tiss} due to dye diffusion between the small chamber and the 21-gauge inlet and outlet ports over the 4-minute measurement time. To rule out significant diffusional effects, experiments were done in corneas of wild-type mice as in Figure 4A (top), except that the viscosity of bathing solutions was increased 10-fold by addition of an inert, high-molecular-weight dextran. There were no significant differences in water permeability with the viscous solutions (for example, $d(F/F_0)/dt \times 10^{-4} \text{ s}^{-1} = -1.7 \pm 0.3$ for nonviscous versus -1.4 ± 0.2 for viscous hyperosmolar solutions in same eyes), indicating the absence of significant diffusional effects.

Figure 4B summarizes averaged slopes for many experiments as in 4A, including data from corneas in which the epithelium was removed by a scraping procedure. Figure 4C summarizes the corresponding P_f^{tiss} values. AQP5 deletion reduced P_f^{tiss} significantly in intact cornea, as measured with both hypo- and hyperosmolar solutions. Removal of the epithelium had no significant effect on P_f^{tiss} in cornea from wild-type mice, though it restored P_f^{tiss} in cornea from AQP5-null mice to the level in wild-type mice. These results

implicate the involvement of AQP5 in water movement across the intact corneal epithelium and show that the epithelium can be the rate-limiting barrier in osmosis across the intact cornea in the absence of AQP5. Corneal P_f^{tiss} was reduced to a lesser extent by AQP1 deletion and only for hypoosmolar challenge after removal of the epithelium. P_f^{tiss} was lower in conjunctiva than cornea. Despite the reduced water permeability of surface conjunctival cells in AQP3-null mice, as shown in Figure 3D, AQP3 deletion did not affect osmosis across intact conjunctiva, indicating that AQP3 is not the rate-limiting barrier for osmosis across intact conjunctiva.

Corneal Thickness Measurements

Measurements of corneal thickness were made after removal of the corneal epithelium by scraping to investigate possible differences in stromal properties in AQP deficiency and to determine whether an osmotically sensitive, semipermeable barrier remained on the stromal surface. Baseline and serial corneal thickness measurements were made by z-scanning bright-field confocal microscopy as described previously.²⁸ Figure 5A shows an example of serial confocal images used to determine corneal thickness, with outer and inner corneal surfaces producing characteristic morphologic features. Figure 5A (bottom, right) summarizes baseline thicknesses for undisturbed corneas (in micrometers): 130 ± 1 (wild-type), 139 ± 2 (AQP5-null), and 100 ± 1 (AQP1-null), in agreement with previous results.

As expected, exposure of intact corneas to isosmolar solution produced no change in thickness (not shown). After removal of the epithelium, corneal thickness increased when the surface was bathed in hypoosmolar (150 mOsM) or isosmolar solutions, and

decreased in hyperosmolar (580 mOsM) solution (Fig. 5B). Swelling of de-epithelialized corneas in hypoosmolar solution was markedly greater in corneas from AQP1-null mice than in wild-type and AQP5-null mice. Swelling also occurred when de-epithelialized corneas were bathed in isosmolar solution, reflecting the imbibition pressure of the dehydrated stroma. For all mice, hyperosmolar challenge produced corneal thinning that was lower in absolute magnitude than was the swelling measured under hypoosmolar challenge. Hyperosmolar-induced corneal thinning was slowest in AQP1-deficient mice. In each case, results were similar for wild-type and AQP5-null mice, suggesting that AQP5 deletion does not affect stromal properties.

Model of Tear Film Osmolarity

Based on the ocular surface water permeabilities measured in this study, a simple model was constructed to predict tear film osmolarity under normal physiological conditions and for two traditionally distinct classes of dry eye syndrome—secretory dysfunction and excessive evaporation. As depicted in Figure 6 (top), tear fluid is generated by active secretion (J_s) and osmotic flux (J_v), and removed by evaporation (J_e) and drainage (J_d). In the steady state

$$J_s + J_v = J_e + J_d \quad (1)$$

Near-isotonic fluid (serum osmolarity, Φ_s) is actively secreted (J_s) by various ocular tissues, including the main and accessory lacrimal glands, conjunctiva, and cornea. Evaporation from the air-exposed surface of the eye (primarily from cornea in mouse, with surface area $S_{\text{cornea}} \sim 0.09 \text{ cm}^2$) concentrates the preocular film uniformly and rapidly.

Osmosis (J_v) across the entire corneal and conjunctival surfaces ($S_{\text{cornea}} + S_{\text{conjunctiva}}$) drives water into the tears, partially reducing tear film osmolarity (Φ_t). J_v is defined by the relation

$$J_v = [P_{f(\text{cornea})} S_{\text{cornea}} + P_{f(\text{conjunctiva})} S_{\text{conjunctiva}}] \nu_w (\Phi_t - \Phi_s) = P_f' \nu_w (\Phi_t - \Phi_s) \quad (2)$$

where, for simplicity, P_f denotes P_f^{tiss} . $P_{f(\text{cornea})} = 0.0017$ cm/s, and $P_{f(\text{conjunctiva})} = 0.0011$ cm/s as measured in this case, and P_f' represents a single weighted value of ocular surface whole-tissue permeability. Because nasolacrimal drainage is assumed to be the only route for solute removal, $J_d = J_s(\Phi_s/\Phi_t)$. Combining this relation with equations 1 and 2, and solving for Φ_t

$$\Phi_t = \left[\frac{((P_f' \nu_w \Phi_s - J_s + J_e)^2 + (4 P_f' \nu_w J_s \Phi_s))^{1/2}}{(2 P_f' \nu_w)^{-1}} - \frac{((J_s - P_f' \nu_w \Phi_s - J_e)(2 P_f' \nu_w)^{-1}}{(2 P_f' \nu_w)^{-1}} \right] \quad (3)$$

$\Phi_t - \Phi_s$ is plotted in Figure 6 (bottom) over the range of J_e measured in rabbits and humans at 30% to 40% humidity,³² and a range of plausible J_s based on measured mouse tear production rates.³³ Φ_s for mice was taken as 320 mOsM and $S_{\text{conjunctiva}}/S_{\text{cornea}}$ as 5 based on microdissection measurements, somewhat lower than $S_{\text{conjunctiva}}/S_{\text{cornea}}$ of 17 in humans and 9 in rabbits.¹ Figure 6 (bottom) shows that for a physiological evaporative rate of 1.5×10^{-6} g/cm² per second and J_s of 3×10^{-6} mL/s, tear film osmolarity is predicted to be mildly elevated over serum osmolarity ($\Phi_t - \Phi_s$ is ~6.5 mOsM). If J_s is zero at a normal evaporative rate, $\Phi_t - \Phi_s$ increases to 12 mOsM. In contrast, if J_e is elevated fourfold as in meibomian gland dysfunction,¹⁰ $\Phi_t - \Phi_s$ becomes 26 mOsM. If J_s

UCSF LIBRARY

is zero and J_e is increased fourfold, $\Phi_t - \Phi_s$ becomes 46 mOsM. The relationship between Φ_t and J_e and J_s has relevance to understanding dry eye syndromes (see the Discussion section).

Discussion

Novel microfluorimetric methods were applied to measure water permeability of the two principal ocular surface tissues, the cornea and conjunctiva, at the cell membrane and whole tissue levels. Measurements were made in living mice with selective AQP deletions to assess the contributions of AQP1, -3, and -5 to osmotic fluid transport across intact surface tissues. As discussed in the introduction, the motivation for this work was the recognition of the role of the ocular surface in tear film homeostasis and as a promising target for development of therapies for dry eye syndromes. Approximately one half of middle-aged women report dry eye symptoms, with KCS affecting 10% to 15% of the elderly population.³² Dry eye symptoms are also a common side effect of contact lens wear and laser refractive surgery in all age groups.

Water permeability of ocular surface cells was measured by a calcein fluorescence-quenching method, which is based on rapid changes in cytoplasmic calcein fluorescence in response to changes in concentration of cytoplasmic anionic proteins and hence to changes in cell volume.³⁰ The wide-field fluorescence detection method used for calcein fluorescence measurement is insensitive to small pulsatile and perfusion-related eye movements, which precludes water permeability measurement by confocal detection methods. Osmotic equilibration in corneal and conjunctival epithelial cells was very fast

in wild-type mice, ~1 to 2 seconds, requiring the development of an ocular surface perfusion chamber capable of fluid exchange on a much faster time scale. A model relating induced cell volume changes to osmotic water permeability (P_f^{mem}) was developed for a stratified epithelium, in which the kinetics of thickness of calcein-containing surface cells was computed after a change in osmolarity of solution bathing the ocular surface. P_f^{mem} is the single most informative parameter characterizing the water-transporting capacity of a membrane barrier, particularly in assessing the potential role of water transport by molecular pores. Mishima and Hedbys³⁴ and Fischbarg and Motoreano³⁵ estimated water permeability of ~0.01 cm/s in full thickness corneal epithelium from osmotically induced changes in corneal thickness in living rabbits and mounted tissues. This value is lower than the P_f^{mem} of 0.045 cm/s determined in the present study for plasma membrane in mouse cornea, probably because of the presence of multiple barriers and possible unstirred layers in full-thickness rabbit corneal epithelium. A P_f^{mem} of greater than ~0.01 cm/s provides evidence of the presence of molecular water channels.

Water permeability across the intact corneal and conjunctival barriers was measured by a steady state dye-dilution method in which the concentration of an inert, membrane-impermeant fluorescent dye was measured at the external ocular surface in response to a sustained osmotic gradient. The detection of appreciable changes in dye concentration required the design of a microchamber with <4- μ L solution volume and the selection of a fluorescent dye with minimal surface binding and excellent photostability. Dye fluorescence signal changed by ~1%/min for a ~200 mOsM osmotic gradient in cornea and conjunctiva. The direction of signal changes depended on the direction of the

osmotic gradient, as expected, with linearly decreasing signal for a hyperosmolar solution driving water into the external solution. The deduced P_f^{tiss} for cornea and conjunctiva was independent of the direction of the osmotic gradient, and substantially lower than P_f^{mem} because of the multiple layers of epithelial cell membranes and other barriers in series.

Mechanical removal of the entire stratified epithelial layer of the cornea did not enhance osmotically driven water transport in corneas of wild-type mice. Of the corneal tissues, the epithelium has been considered rate limiting to water movement. However, in this study the normal epithelium did not impede osmotically induced transcorneal fluid movement in vivo. Indeed, the P_f^{tiss} of ~ 0.002 cm/s for whole cornea measured was approximately five times lower than water permeability of full-thickness corneal epithelium of ~ 0.01 cm/s, as mentioned earlier. Although the corneal epithelium in wild-type mice was not rate-limiting for transcorneal osmosis, reducing epithelial water permeability by AQP5 deletion caused a marked ~ 5 -fold slowing of transcorneal water flux in intact cornea, which was restored by removal of the epithelium to the level in wild-type mice. These results indicate that AQP5 provides the principal route for osmotically driven water flux across the intact corneal epithelium and that most water moves from corneal stroma to the tear film layer by a transcellular route.

Osmotic water movement across intact corneas of AQP1-deficient mice was similar to that in wild-type mice under both hypoosmolar and hyperosmolar conditions, suggesting that AQP1 is not a rate-limiting barrier for transcorneal osmosis. Unexpectedly, there was apparent asymmetry in water transport in corneas of AQP1-null mice after removal of the epithelium, where transcorneal osmosis was reduced ~ 2.5 -fold

UCSF LIBRARY

only after hypoosmolar challenge. Measurements of stromal thickness by bright-field confocal microscopy were obtained to investigate possible differences in stromal properties in corneas from AQP1-null mice that might account for this result. Thickness measurements indicated corneal swelling and thinning after exposure of the denuded corneal surface to hypoosmolar and hyperosmolar solutions, respectively. Because salt gradients are not thought to induce osmosis across exposed stromal tissue, it is likely that one or more membranes remained at the stromal surface after the denudation procedure. Grossly, corneas from AQP1-null mice scattered more light throughout the swelling process than did corneas from wild-type or AQP5-null mice. Both hypoosmolar and isosmolar swelling was increased in AQP1-null mice compared with wild-type and AQP5-null mice, which may be related to impaired endothelial fluid pump function and/or differential stromal properties of the relative thin corneas in AQP1-null mice. AQP1 thus plays an important role in the removal of excess fluid from the corneal stroma after experimental corneal edema, rather than in osmotically driven water movement from the aqueous to tear film compartments.

Immunostaining revealed AQP3 expression at the plasma membranes of conjunctival epithelia, in agreement with data in rat.¹⁸ Cell water permeability in AQP3-deficient mice was substantially reduced (3.6-fold) compared with that in wild-type mice, although osmotically induced water movement across the intact conjunctiva was not AQP3 dependent. Therefore, the AQP3-containing conjunctival epithelial cell layer is not the rate-limiting barrier for osmosis in full-thickness conjunctiva, and thus AQP3-facilitated water transport does not play a role in transconjunctival fluid movement. Water movement across complex tissues such as conjunctiva could be impeded by rate-limiting

obstacles other than plasma membranes. A similar conclusion was reported for AQP3 in skin, which has a structure similar to that of conjunctiva and other mucous membranes, except for the presence in skin of a superficial watertight layer of stratum corneum consisting of lipidic, cornified cell envelopes. Although water permeability was reduced after AQP3 deletion in epidermal cells, measurements of skin hydration in response to altered rates of evaporative water loss indicated that the AQP3 water transport function was not responsible for the reduced hydration and other abnormalities in AQP3-deficient mice.^{36,37} Decreased epidermal and stratum corneum glycerol content was found in the AQP3-null mice, which, when normalized by systemic glycerol administration, resulted in correction of the skin phenotype abnormalities.³⁸ It was concluded that the glycerol-, rather than the water-transporting function of AQP3, was responsible for the abnormal skin phenotype. As in skin, we speculate that AQP3-facilitated glycerol transport in conjunctiva and other mucous membranes plays a functional, but at present unknown, physiological role.

Osmotic water permeation across the corneal and conjunctival barriers is important for replacement of evaporative water loss in the tear film when the ocular surface is exposed to ambient humidity, and for preventing significant tear film hyperosmolarity. The model of tear film osmolarity presented in Figure 6 provides a quantitative prediction of tear fluid hyperosmolarity under physiological and pathologic conditions. Measurements on human and rabbit tear samples by freezing-point depression osmometry have shown normal tears to be mildly hyperosmolar ($\Phi_t - \Phi_s \sim 10-14$ mOsM),^{10,39,40,41} slightly higher than the ~ 7 mOsM predicted in our model for the mouse

UCSF
LIBRARY

tear film. In our model, tear secretions are assumed to be isosmolar, whereas the lacrimal component of tear fluid secretions may be slightly hyperosmolar.⁴²

Tear film osmolarity is increased in both evaporative (caused by excessive tear evaporation rates) and tear-deficient (caused by inadequate tear fluid secretion) dry eye. Tear fluid osmolarity has been established as an objective, quantitative index of KCS severity.³⁹ Mathers et al.⁴³ found both diminished tear flow and increased evaporative rates to correlate with osmolarity. The model presented in this study makes predictions for tear film osmolarity in evaporative and tear-deficient states of varying severities alone and in combination. The $\Phi_t - \Phi_s$ of ~ 26 mOsM predicted for pure meibomian gland dysfunction recapitulates the $\Phi_t - \Phi_s$ of 20 to 30 mOsM measured in a rabbit model.⁴⁴ In pure tear deficiency, decreased tear turnover and consequent greater evaporation time accounts qualitatively for the hyperosmolarity in KCS, even at normal evaporation rate. However, this effect $\Phi_t - \Phi_s \sim 12$ mOsM is smaller than that measured in tear-deficient KCS ($\Phi_t - \Phi_s > 22$ mOsM).^{41,45} Possible explanations for this quantitative difference include changes in tear film evaporation at low secretion rates (due to abnormal tear composition),^{41,46} and/or increased osmolarity of lacrimal secretions at very low secretion rates.⁴² However, the latter mechanism probably would not substantially increase tear film osmolarity because of the low lacrimal secretion rate compared with secretion from ocular surface tissues. The quantitative difference in predicted versus measured tear film osmolarity in tear-deficient dry eye syndrome emphasizes the need for further investigation into the complex interplay of aqueous and meibomian secretions in retarding tear film evaporation in dry eye syndromes.

Appendix

Computation of Corneal Epithelial P_f^{mem}

Plasma membrane permeability in corneal epithelial cells was computed from the kinetics of cell volume change in response to changing the osmolarity of fluid bathing the cornea according to the model shown in Figure 7A. An approximately linear dependence of calcein fluorescence on cell volume was assumed, as reported previously.³⁰ Only the outermost corneal cell layer was loaded with calcein-AM under the conditions of our experiments as seen by confocal microscopy, consistent with ex vivo experiments using esterified dyes,^{47,48} dye injection experiments,⁴⁹ and ultrastructural studies,⁵⁰ providing evidence against gap-junctional coupling among superficial cells and between superficial and deeper wing cell layers. P_f is defined, for simplicity, as the intrinsic plasma membrane water permeability (P_f^{mem}), assumed to be the same throughout the corneal epithelium. For model computations, apparent water permeability at the outermost surface was taken as $2 \cdot P_f$, to account for microvillar surface convolutions^{51,52} and apparent water permeability of interfaces between two layers (containing two membrane barriers) was taken as $P_f/2$. Unstirred layer effects were considered insignificant.

Water flux (J_i) across each membrane barrier is: $J_i = P_f^i \cdot S \cdot v_w \cdot (\Phi_{i+1} - \Phi_i)$, where $dV_i(t)/dt = J_{i-1} - J_i$. Because osmotic equilibration occurs much faster than ionic equilibration, the product of cell volume (V_i) and osmolarity (Φ_i) remains constant over the time course of the measurement: $\Phi_i(0) \cdot V_i(0) = \Phi_i(t) \cdot V_i(t)$. Combining these equations and expressing as the ratio of volume-to-surface area, $h_i(t)$

$$\begin{aligned}
dh_i(t)/dt = P_f^{i-1} \cdot v_w [\Phi_i(0) \cdot V_i(0)/V_i(t) - \Phi_{i-1}(0) \cdot V_{i-1}(0)/V_{i-1}(t)] - \\
P_f^i \cdot v_w [\Phi_{i+1}(0) \cdot V_{i+1}(0)/V_{i+1}(t) - \Phi_i(0) \cdot V_i(0)/V_i(t)].
\end{aligned}
\tag{A1}$$

The five coupled differential equations were numerically integrated by using the forward Euler method (time-step, 0.01 ms) to obtain $h_i(t)$. Computed $h_i(t)/h_i(0)$ are shown in Figure 7B for the best fitted P_f , along with a comparison of an experimental curve with computed $h_1(t)$.

References

1. Watsky MA, Jablonski MM, Edelhauser HF. Comparison of conjunctival and corneal surface area in rabbit and human. *Curr Eye Res.* 1988;7:483–486.
2. Candia OA, Zamudio AD. Chloride-activated water permeability in the frog corneal epithelium. *J Membr Biol.* 1995;143:259–266.
3. Murakami T, Fujihara T, Nakamura M, Nakata K. P2Y(2) receptor stimulation increases tear fluid secretion in rabbits. *Curr Eye Res.* 2000;21:782–787.
4. Yang H, Reinach PS, Koniarek JP, Wang Z, Iserovich P, Fischbarg J. Fluid transport by cultured corneal epithelial cell layers. *Br J Ophthalmol.* 2000;84:199–204.
5. Li Y, Kuang K, Yerxa B, Wen Q, Rosskothan H, Fischbarg J. Rabbit conjunctival epithelium transports fluid and P2Y2(2) receptor agonists stimulate Cl⁻ and fluid secretion. *Am J Physiol.* 2001;281:C595–C602.
6. Murakami T, Fujihara T, Horibe Y, Nakamura M. Diquafosol elicits increases in net Cl⁻ transport through P2Y2 receptor stimulation in rabbit conjunctiva. *Ophthalmic Res.* 2004;36:89–93.
7. Fujihara T, Murakami T, Fujita H, Nakamura M, Nakata K. Improvement of corneal barrier function by the P2Y(2) agonist INS365 in a rat dry eye model. *Invest Ophthalmol Vis Sci.* 2001;42:96–100.
8. Mishima S, Maurice DM. The oily layer of the tear film and evaporation from the corneal surface. *Exp Eye Res.* 1961;1:39–45.
9. Iwata S, Lemp M, Holly FJ, Dohlman CH. Evaporation rate of water from the precorneal tear film and cornea in the rabbit. *Invest Ophthalmol.* 1969;8:613–619.
10. Mathers WD. Ocular evaporation in meibomian gland dysfunction and dry eye. *Ophthalmol.* 1993;100:347–351.
11. Mishima S. Some physiologic aspects of the precorneal tear film. *Arch Ophthalmol.* 1965;73:233–241.
12. Lemp MA. Report of the National Eye Institute/Industry Workshop on clinical trials for dry eyes. *CLAO J.* 1995;21:221–232.
13. Klyce SD. Stromal lactate accumulation can account for corneal oedema osmotically following epithelial hypoxia in the rabbit. *J Physiol.* 1981;321:49–64.

14. O'Neal MR, Polse KA. In vivo assessment of mechanisms controlling corneal hydration. *Invest Ophthalmol Vis Sci*. 1985;26:849–856.
15. Mandell RB, Fatt I. Thinning of the human cornea on awakening. *Nature*. 1965;208:292–293.
16. Frigeri A, Gropper M, Turck CW, Verkman AS. Immunolocalization of the mercurial-insensitive water channel and glycerol intrinsic protein in epithelial cell plasma membranes. *Proc Natl Acad Sci USA*. 1995;92:4328–4331.
17. Patil RV, Saito I, Yang X, Wax MB. Expression of aquaporins in the rat ocular tissue. *Exp Eye Res*. 1997;64:203–209.
18. Hamman S, Zeuthen T, La Cour M, et al. Aquaporins in complex tissues: distribution of aquaporins 1–5 in human and rat eye. *Am J Physiol*. 1998;274:C1332–C1345.
19. Wen Q, Diecke FPJ, Iserovich P, Kuang K, Sparrow J, Fischbarg J. Immunocytochemical localization of aquaporin-1 in bovine corneal endothelial cells and keratocytes. *Exp Biol Med (Maywood)*. 2001;226:463–467.
20. Ma T, Song Y, Yang B, et al. Nephrogenic diabetes insipidus in mice deficient in aquaporin-3 water channels. *Proc Natl Acad Sci USA*. 2000;97:4386–4391.
21. Ma T, Yang B, Gillespie A, Carlson EJ, Epstein CJ, Verkman AS. Severely impaired urinary concentrating ability in transgenic mice lacking aquaporin-1 water channels. *J Biol Chem*. 1998;273:4296–4299.
22. Manley GT, Fujimura M, Ma T, et al. Aquaporin-4 deletion in mice reduces brain edema following acute water intoxication and ischemic stroke. *Nat Med*. 2000;6:159–163.
23. Li J, Verkman AS. Impaired hearing in mice lacking aquaporin-4 water channels. *J Biol Chem*. 2001;276:31233–31237.
24. Ma T, Song Y, Gillespie A, Carlson EJ, Epstein CJ, Verkman AS. Defective secretion of saliva in transgenic mice lacking aquaporin-5 water channels. *J Biol Chem*. 1999;274:20071–20074.
25. Song Y, Verkman AS. Aquaporin-5 dependent fluid secretion in airway submucosal glands. *J Biol Chem*. 2001;276:41288–41292.
26. Zhang D, Vetrivel L, Verkman AS. Aquaporin deletion in mice reduces intraocular pressure and aqueous fluid production. *J Gen Physiol*. 2002;119:561–569.

27. Li J, Patil RV, Verkman AS. Mildly abnormal retinal function in transgenic mice without Müller cell aquaporin-4 water channels. *Invest Ophthalmol Vis Sci.* 2002;43:573–579.
28. Thiagarajah JR, Verkman AS. Aquaporin deletion in mice reduces corneal water permeability and delays restoration of transparency after swelling. *J Biol Chem.* 2002;277:19139–19144.
29. Kao WW, Kao CW, Kaufman AH, et al. Healing of corneal epithelial defects in plasminogen- and fibrinogen-deficient mice. *Invest Ophthalmol Vis Sci.* 1999;39:502–508.
30. Solenov E, Watanabe H, Manley GT, Verkman AS. Sevenfold-reduced osmotic water permeability in primary astrocyte culture from AQP-4-deficient mice, measured by a fluorescence quenching method. *Am J Physiol.* 2004;286:C426–C432.
31. Smith RS, Sundberg JP, John SWM. The anterior segment and ocular adnexae. Smith RS eds. *Systemetic Evaluation of the Mouse Eye: Anatomy, Pathology, and Biomethods.* 2002;3–23. CRC Press Boca Raton, FL.
32. Mathers WD. Evaporation from the ocular surface. *Exp Eye Res.* 2004;78:389–394.
33. Moore M, Ma T, Yang B, Verkman AS. Tear secretion by lacrimal glands in transgenic mice lacking water channels AQP1, AQP3, AQP4, and AQP5. *Exp Eye Res.* 2000;70:557–562.
34. Mishima S, Hedbys BO. The permeability of the corneal epithelium and endothelium to water. *Exp Eye Res.* 1967;6:10–32.
35. Fischbarg J, Motoreano R. Osmotic permeabilities across corneal endothelium and antidiuretic hormone-stimulated toad urinary bladder structure. *Biochim Biophys Acta.* 1982;690:207–214.
36. Ma T, Hara M, Sougrat R, Verbavatz JM, Verkman AS. Impaired stratum corneum hydration in mice lacking epidermal water channel aquaporin-3. *J Biol Chem.* 2002;277:17147–17153.
37. Hara M, Ma T, Verkman AS. Selectively reduced glycerol in skin of aquaporin-3-deficient mice may account for impaired skin hydration, elasticity, and barrier recovery. *J Biol Chem.* 2002;277:46616–46621.
38. Hara M, Verkman AS. Glycerol replacement corrects defective skin hydration, elasticity, and barrier function in aquaporin-3-deficient mice. *Proc Natl Acad Sci USA.* 2003;100:7360–7365.

39. Gilbard JP, Farris RL, Santamaria J. Osmolarity of tear microvolumes in keratoconjunctivitis sicca. *Arch Ophthalmol*. 1978;96:677–681.
40. Gilbard JP, Rossi SR, Gray KL. A new rabbit model for keratoconjunctivitis sicca. *Invest Ophthalmol Vis Sci*. 1987;28:225–228.
41. Craig JP, Signh I, Tomlinson A, Morgan PB, Efron N. The role of tear physiology in ocular surface temperature. *Eye*. 2000;14:635–641.
42. Gilbard JP, Dartt DA. Changes in rabbit lacrimal gland fluid osmolarity with flow rate. *Invest Ophthalmol Vis Sci*. 1982;23:804–806.
43. Mathers WD, Lane JA, Sutphin JE, Zimmerman MB. Model for ocular tear film function. *Cornea*. 1996;15:110–119.
44. Gilbard JP, Rossi SR, Gray KL. Tear film and ocular surface changes after closure of the Meibomian gland orifices in the rabbit. *Ophthalmology*. 1989;96:1180–1186.
45. Gilbard JP, Gray KL, Rossi SR. A proposed mechanism for increased tear-film osmolarity in contact lens wearers. *Am J Ophthalmol*. 1986;102:505–507.
46. Rolando M, Refojo MF, Kenyon KR. Increased tear evaporation in eyes with keratoconjunctivitis sicca. *Arch Ophthalmol*. 1983;101:557–558.
47. Wolosin JM. Gap junctions in rabbit corneal epithelium: limited permeability and inhibition by cAMP. *Am J Physiol*. 1991;261:C857–C864.
48. Jester JV, Li H, Petroll WM, R, et al. Area and depth of surfactant-induced corneal injury correlates with cell death. *Invest Ophthalmol Vis Sci*. 1998;39:922–936.
49. Williams KK, Watsky MA. Dye spread through gap junctions in the corneal epithelium of the rabbit. *Curr Eye Res*. 1997;16:445–452.
50. McLaughlin BJ, Caldwell RB, Sasaki Y, Wood TO. Freeze-fracture quantitative comparison of rabbit corneal epithelial and endothelial membranes. *Curr Eye Res*. 1985;9:951–961.
51. Nichols B, Dawson CR, Togni B. Surface features of the conjunctiva and cornea. *Invest Ophthalmol Vis Sci*. 1983;24:570–576.
52. Gipson IK. Distribution of mucins at the ocular surface. *Exp Eye Res*. 2004;78:379–388.

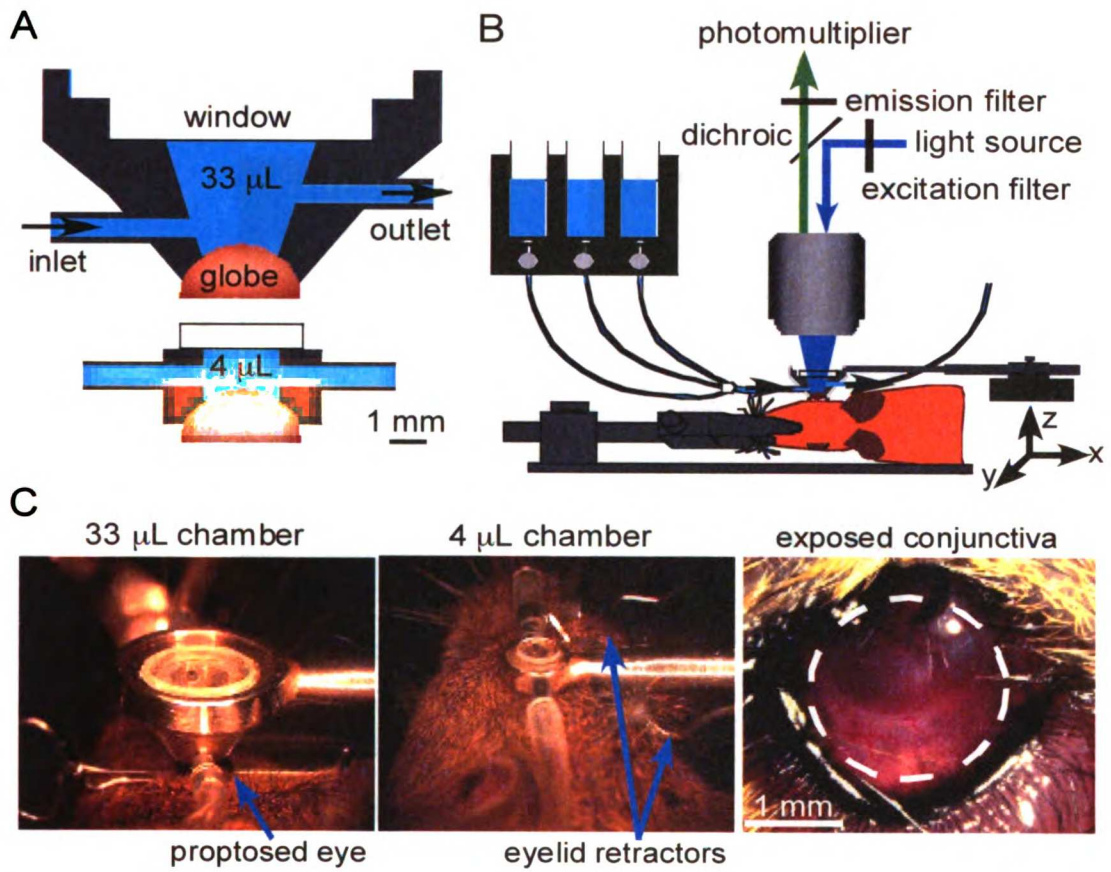


Figure 1

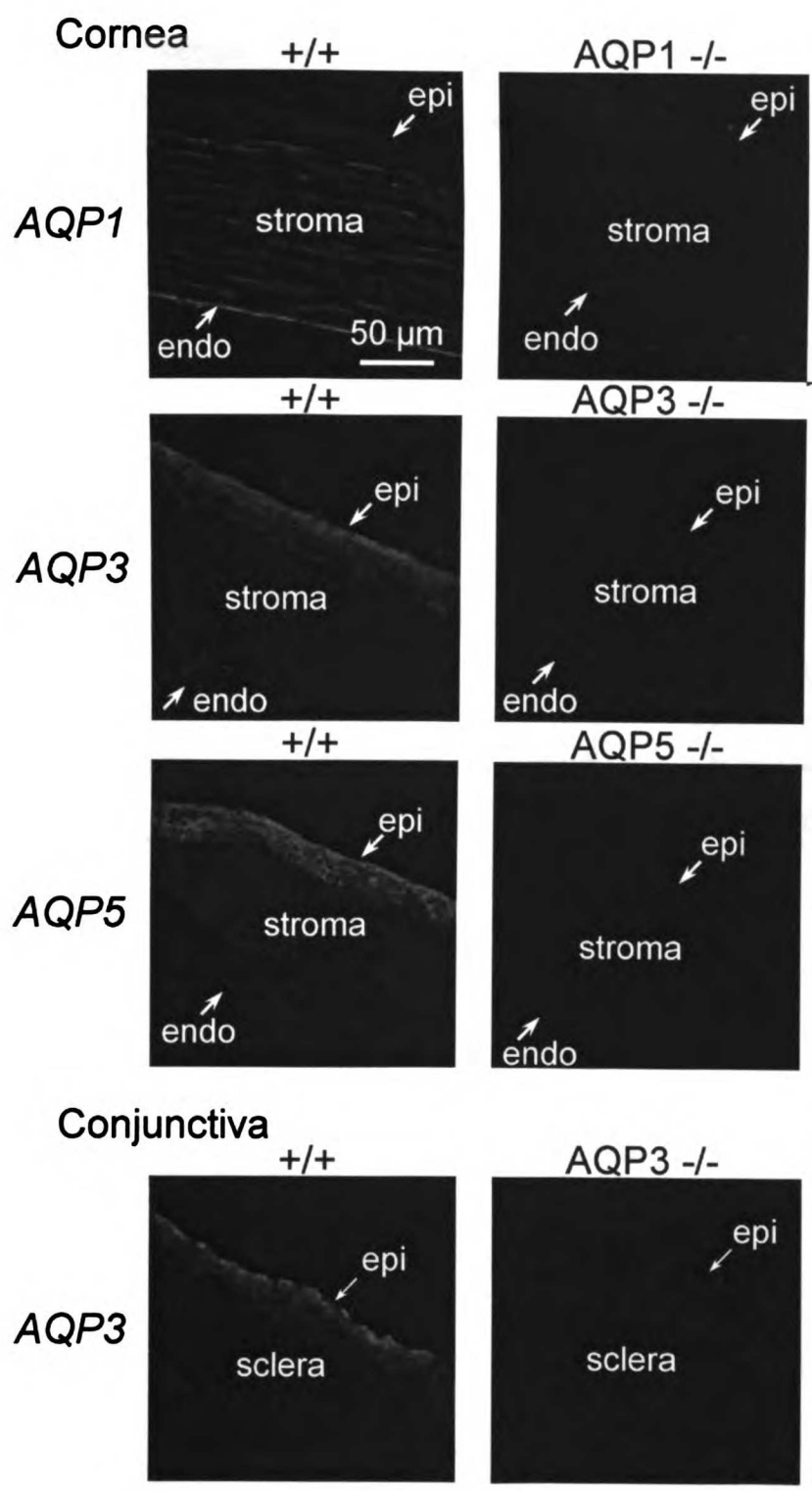


Figure 2

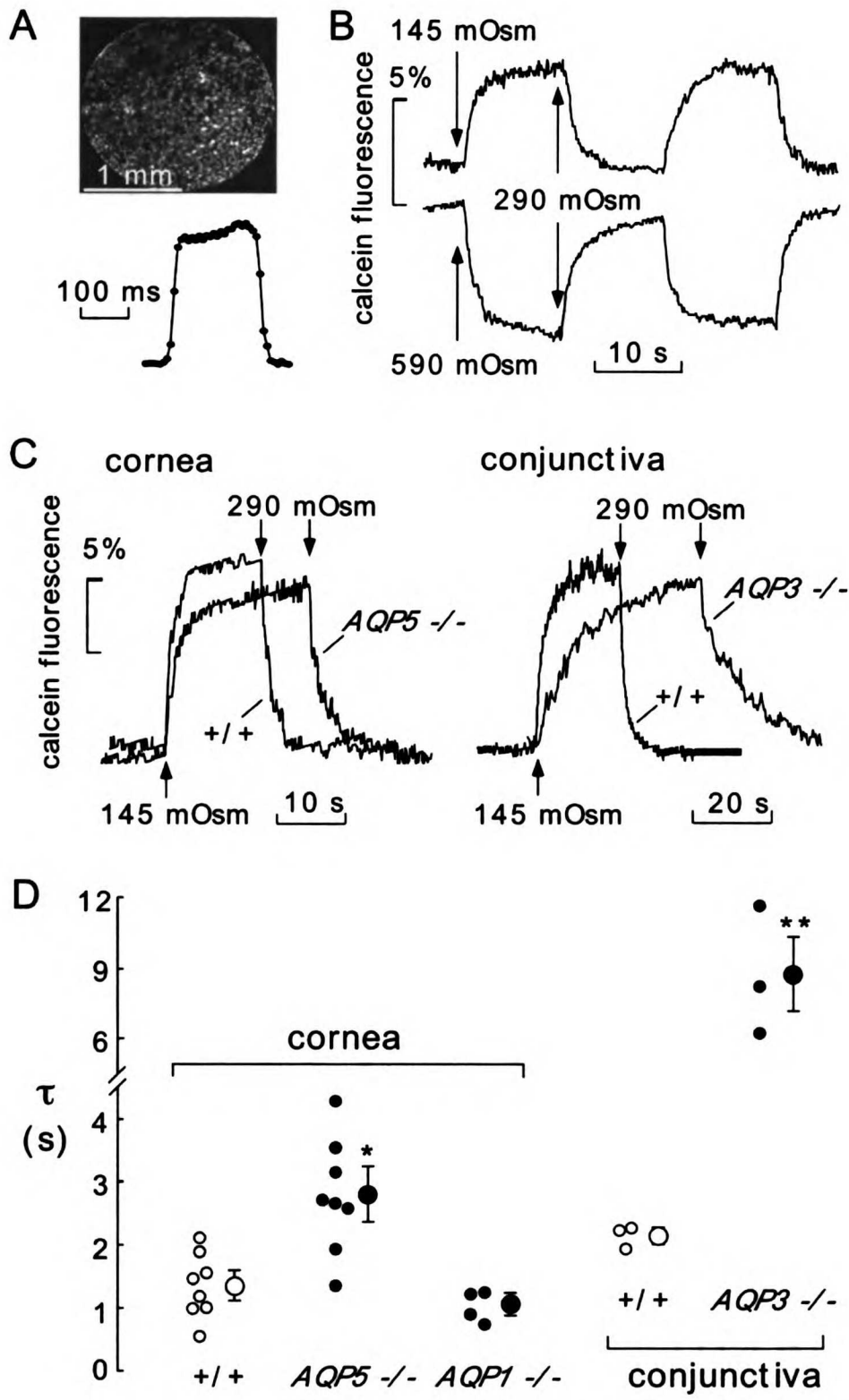


Figure 3

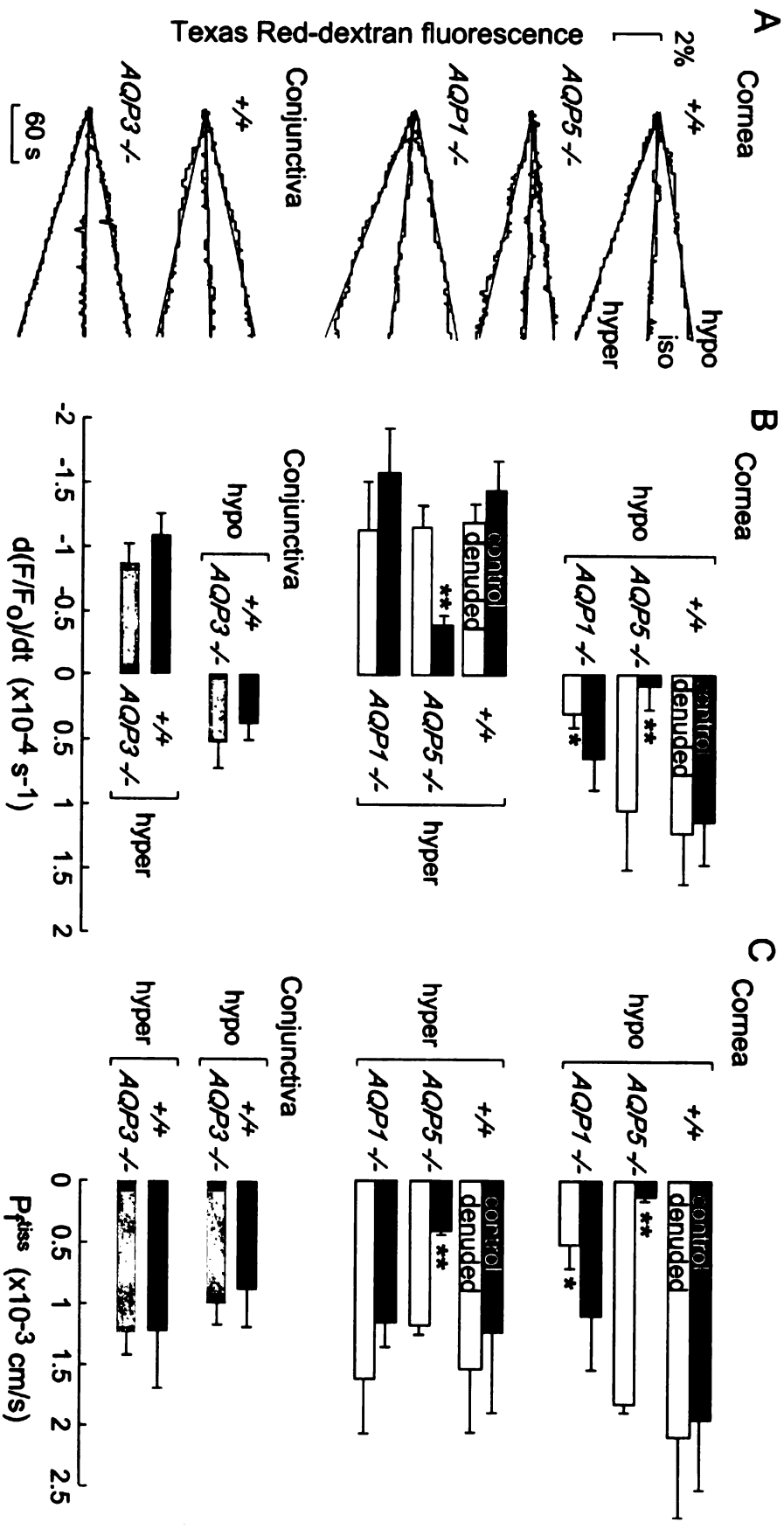


Figure 4

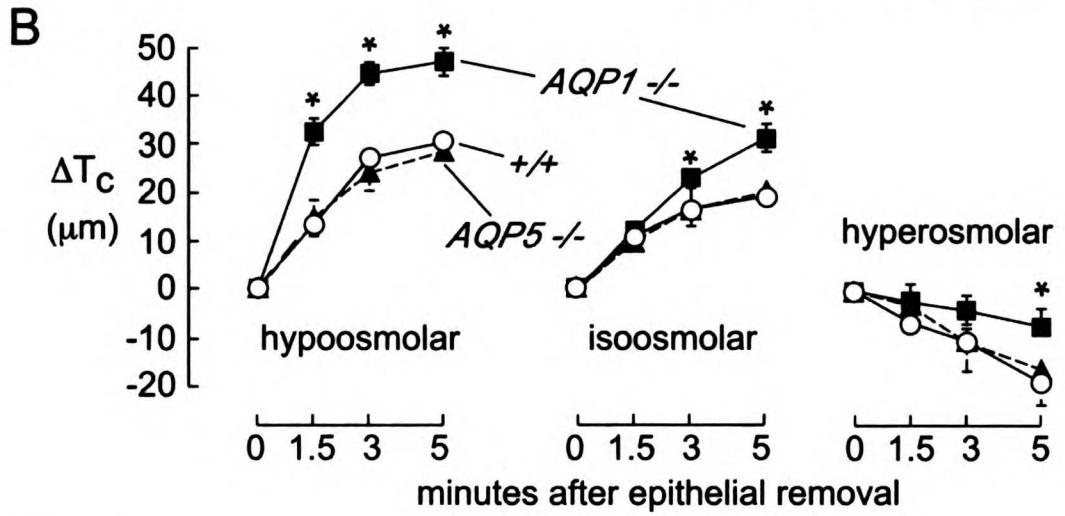
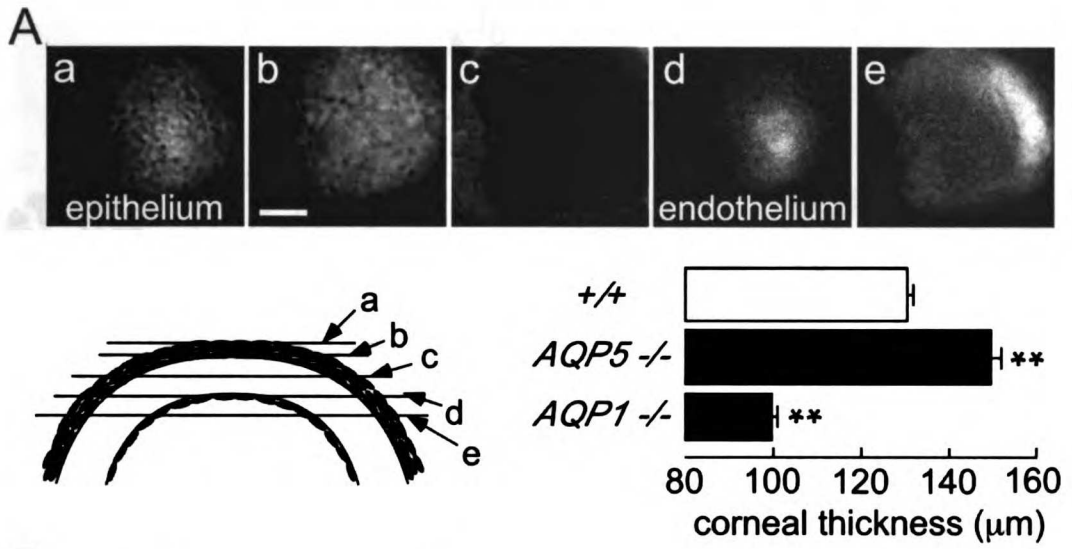


Figure 5

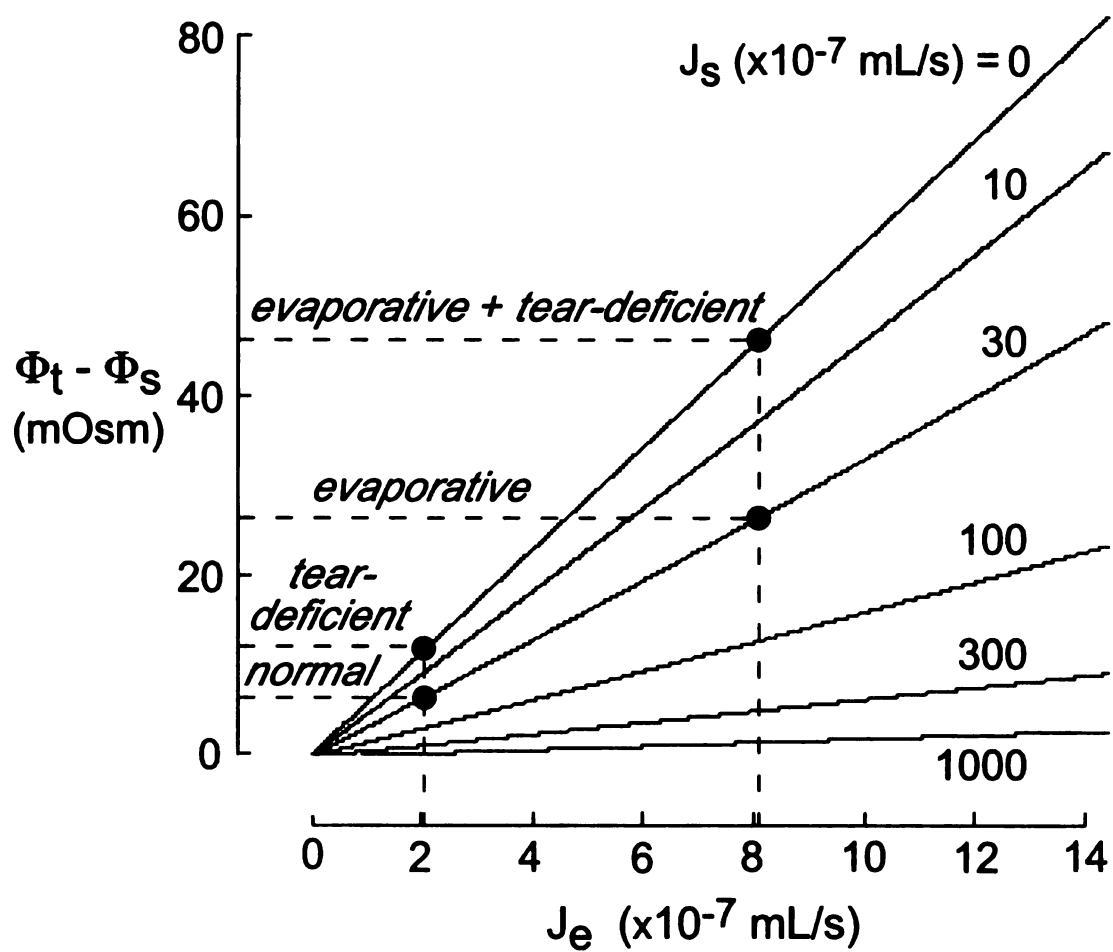
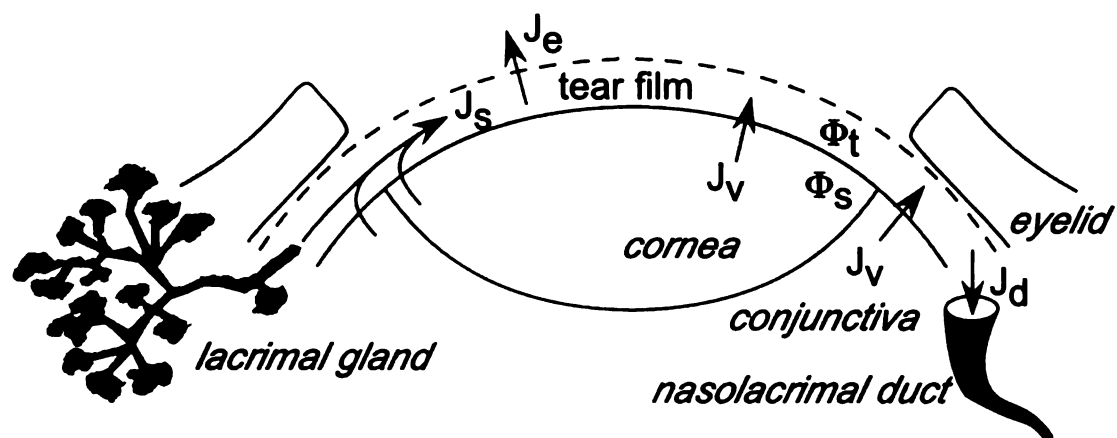


Figure 6

UCSF LIBRARY

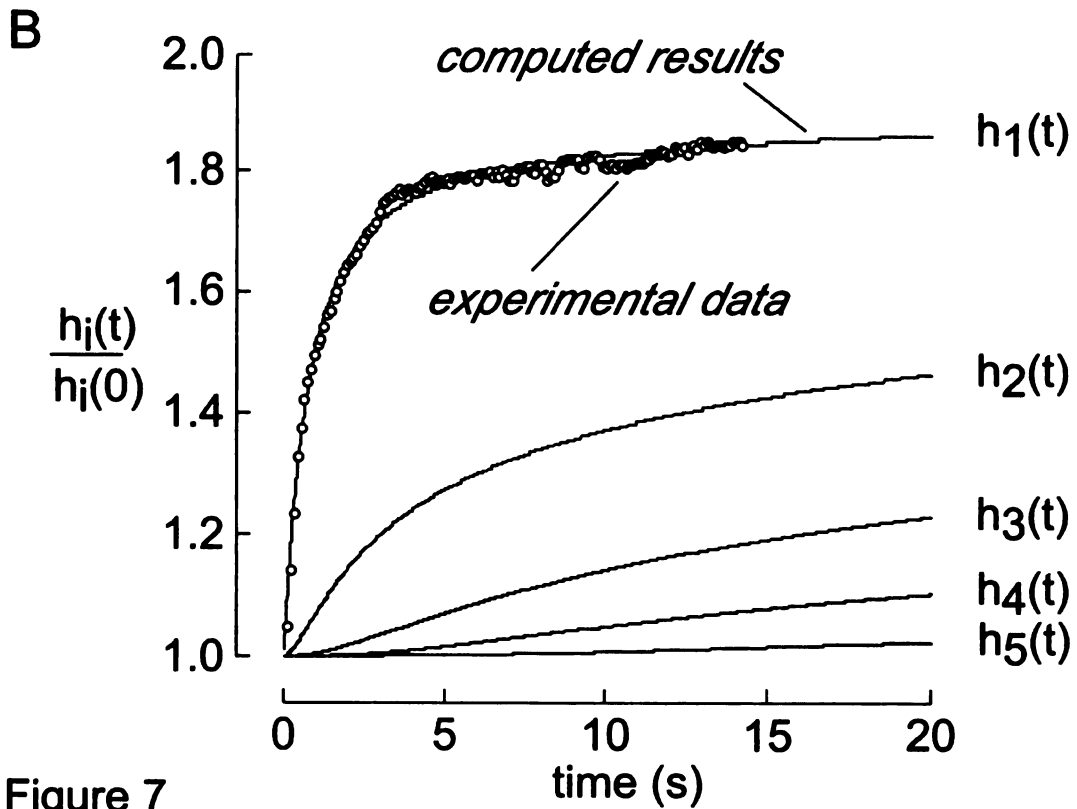
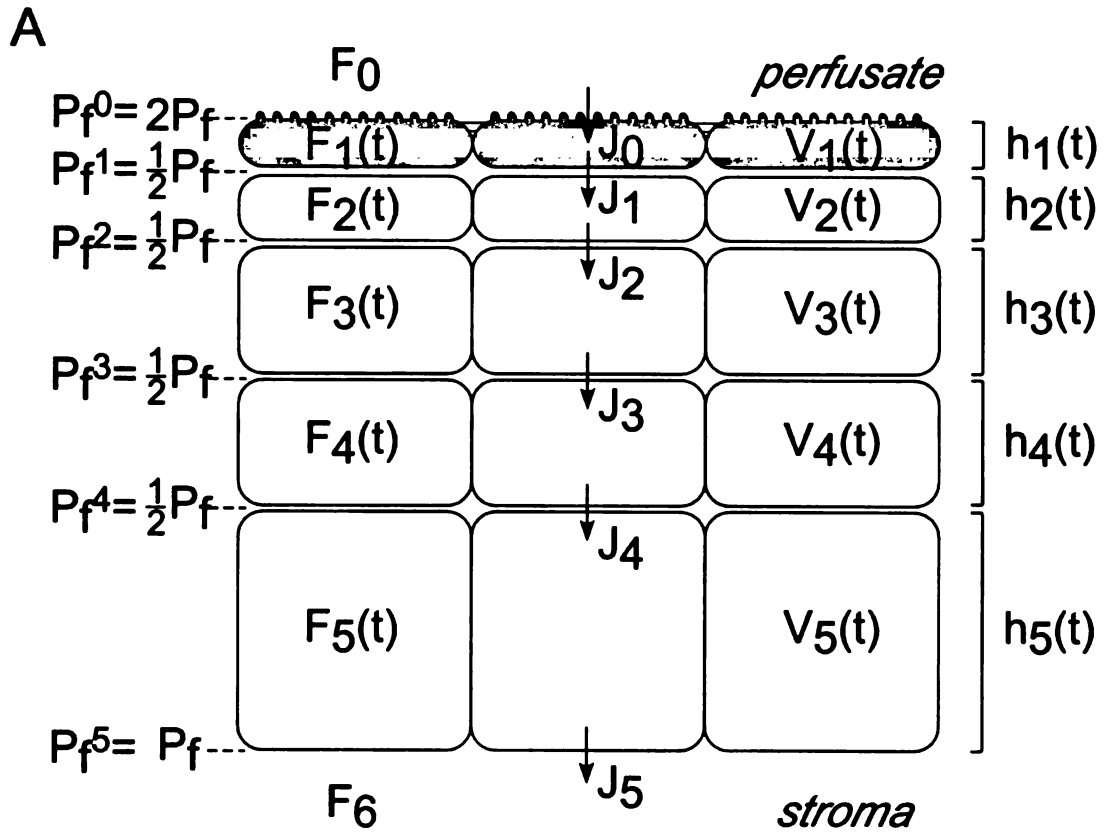


Figure 7

Figure Legends

FIGURE 1. Methods for ocular surface perfusion. (A) Microchambers for measurement of rapid changes in ocular surface cell volume (*top*) and steady state water flux (*bottom*) across the cornea and conjunctiva. Chambers are drawn to scale. (B) Schematic of experimental setup for measurement of cell volume changes with the 33- μ L chamber positioned on the mouse cornea by using a three-axis micromanipulator. Optical elements for fluorescence measurements are depicted, along with the perfusion system and stereotaxic platform. (C) Photographs of the 33- μ L chamber in contact with the cornea of a proptosed globe (*left*), the 4- μ L chamber forming a seal with the exposed conjunctival surface (*middle*), and an area of conjunctiva exposed by retracting the upper lid and depressing the globe into the orbit (*right*).

FIGURE 2. AQP expression at the mouse ocular surface. Immunofluorescence of cornea (*top*) and bulbar conjunctiva (*bottom*) from wild-type (*left*) and indicated AQP-null (*right*) mice, stained for AQPs 1, 3, or 5.

FIGURE 3. AQP-dependent water permeability in ocular surface cells measured by a calcein fluorescence-quenching method. (A, *top*) Fluorescence micrograph of calcein-stained corneal epithelial cells. *Bottom*: solution exchange time measurement in 33- μ L chamber perfused with saline and fluorescein-containing saline. (B) Representative calcein fluorescence in cornea of wild-type mouse showing changes in response to hypoosmolar (*top*) and hyperosmolar (*bottom*) challenge. (C) Time course of corneal (*left*) and conjunctival (*right*) calcein fluorescence in response to hypoosmolar osmotic

gradient in wild-type and indicated AQP-deficient mice. (D) Summary of exponential time constants for swelling response. Each point represents average data for 8 to 15 curves in individual mice, with means \pm SE for each genotype shown. * $P < 0.05$, ** $P < 0.01$.

FIGURE 4. Osmotic water transport across intact cornea and conjunctiva. The ocular surface was covered by a 4- μ L microchamber containing Texas-red dextran in hypo-, iso-, or hyperosmolar solutions. (A) Representative kinetics of fluorescence intensities for measurements on cornea (*top*) or conjunctiva (*bottom*) of mice of indicated genotype. Osmotic gradients induced water movement into (hyperosmolar) or out of (hypoosmolar) the chamber, producing dye dilution (decreasing fluorescence) or concentration (increasing fluorescence), respectively. (B) Averaged rates of relative fluorescence signal change, $d(F/F_0)/dt$ (\pm SE, 4–6 eyes per condition, multiple measurements done on each eye). Where indicated (*open bars*), the corneal epithelium was removed by scraping. (C) Whole-tissue osmotic water permeability coefficients P_f^{tiss} (\pm SE) computed from data in (B). * $P < 0.05$, ** $P < 0.01$.

FIGURE 5. Corneal thickness changes after removal of the epithelium measured by z-scanning bright-field confocal microscopy. (A, *top*) Bright-field confocal images of cornea from wild-type mouse taken at various z-positions (a–e), where corneal epithelial and endothelial surfaces are identified by characteristic morphometric features as depicted (*bottom, left*). Averaged baseline corneal thickness with epithelium intact (*bottom, right*; \pm SE, 10–12 eyes per group). ** $P < 0.01$ compared with wild-type. Scale bar = 1 mm. (B) The time course of corneal thickness (T_c) after removal of the epithelium

and exposure of stromal surface to either hypoosmolar (*left*), isosmolar (*middle*), or hyperosmolar (*right*) saline (\pm SE, 3–4 corneas per condition per genotype) * $P < 0.05$ compared with wild-type.

FIGURE 6. Theoretical dependence of tear film osmolarity on rates of evaporation (J_e) and tear fluid secretion (J_s). *Top*: schematic of ocular surface geometry. J_v , osmotic volume flow across the corneal and conjunctival surfaces; J_d , tear fluid removal by nasolacrimal drainage; Φ_t and Φ_s , osmolarities of tear film and surface tissue, respectively. *Bottom*: $\Phi_t - \Phi_s$, computed from the model described in the text (equation 3). See text for explanations.

FIGURE 7. Model for computation of corneal epithelial cell plasma membrane water permeability from calcein fluorescence quenching experiments. (A) Schematic of multilayered corneal epithelium. An osmotic gradient is imposed at the most superficial cell layer (apical osmolarity, Φ_0). Depicted are layer thicknesses, $h_i(t)$; osmolarities, $\Phi_i(t)$; and interlayer water fluxes J_i . Tissue osmolarity, Φ_6 , is fixed at serum osmolarity. P_f represents the intrinsic osmotic water permeability of the epithelial cell plasma membrane (P_f^{mem}), assumed to be the same in each layer. (B) Time course of relative corneal epithelial cell thicknesses, $h_i(t)/h_i(0)$, in response to a sudden decrease in Φ_0 from 300 to 150 mOsM. Parameters: $P_f^{mem} = 0.045$ cm/s, $\Phi_i(0) = 300$ mOsM, $h_1(0) = 2$ μ m, $h_2(0) = 3$ μ m, $h_3(0) = 7$ μ m, $h_4(0) = 7$ μ m, $h_5(0) = 21$ μ m. Experimental data are shown overlying $h_1(t)$. The same model was implemented for the thinner conjunctival epithelium, except that four layers were included, with $h_1(0) = 2$ μ m, $h_2(0) = 3$ μ m, $h_3(0)$

= 5 μm , $h_4(0) = 10 \mu\text{m}$, giving a P_f^{mem} of 0.025 cm/s for conjunctiva of wild-type mice (not shown).

CHAPTER 3.

Aquaporin-3-Dependent Cell Migration and Proliferation During Corneal Re-epithelialization

Abstract

PURPOSE. To determine a role for the water- and glycerol-transporting protein aquaporin-3 (AQP3) in mammalian corneal epithelium, where it is expressed but has no known function.

METHODS. Corneal epithelial water and glycerol permeabilities were measured in living wild-type and AQP3-null mice using calcein fluorescence quenching and ^{14}C -glycerol uptake assays, respectively. Following removal of the corneal epithelium by scraping, re-epithelialization was followed by fluorescein staining. The contribution of AQP3-facilitated cell migration to corneal re-epithelialization was assessed using an organ culture model, in which initial resurfacing results from epithelial cell migration, as shown by BrdU analysis and 5-fluorouracil insensitivity, and by scratch wound assay using primary cultures of corneal epithelial cells from wild-type vs. AQP3-null mice.

Involvement of AQP3 in epithelial cell proliferation was investigated by morphometric and BrdU analysis of histologic sections, and by measurement of ^3H -thymidine uptake in primary cultures of corneal epithelial cells.

RESULTS. AQP3 deficiency did not alter corneal epithelial thickness, morphology, or glycerol content, though both water and glycerol permeabilities were reduced. Time to corneal re-epithelialization in vivo was significantly delayed in AQP3-null mice compared to wild-type mice. A delay was also found in organ and primary cultures, demonstrating a distinct defect in cell migration arising from AQP3 deletion. Delayed restoration of full-thickness epithelia of AQP3-null mice over days following scraping suggested a separate defect in epithelial cell proliferation, which was confirmed by reduction in proliferating BrdU-positive cells in AQP3-deficient mice, and by reduced proliferation in primary cultures of corneal epithelial cells from AQP3-null mice.

CONCLUSIONS. The significant impairment in corneal re-epithelialization in AQP3-deficient mice results from distinct defects in corneal epithelial cell migration and proliferation. Our results provide the first evidence for involvement of an aquaporin in cell proliferation, and suggest AQP3 induction as a possible therapy to accelerate the resurfacing of corneal defects.

Aquaporins (AQPs) comprise a family of small transmembrane proteins that transport water, and in some cases, both water and small solutes such as glycerol. Functional studies on AQP knock-out mice have revealed the importance of high transcellular water permeability in facilitating osmotically driven epithelial fluid transport, as with AQP1 and AQP3 in the kidney,^{1,2} and in rapid near-isosmolar transport, as with AQP5 in salivary and submucosal glands, AQP1 in choroid plexus, and AQP1 and AQP4 in ciliary epithelium.^{3,4,5,6} In addition to these classical functions of AQPs, recent phenotype analysis of knock-out mice has revealed several unexpected cellular

roles. For example, AQP1 facilitates tumor angiogenesis by enhancing cell motility by a mechanism that may involve facilitated water transport at the leading edge of migrating cells.⁷ AQPs that transport both water and glycerol are involved in skin hydration and biosynthesis (AQP3) and fat metabolism (AQP7) by regulation of cellular glycerol content.^{8,9} In skin, AQP3 deletion also slowed wound healing and recovery of barrier function after stratum corneum removal.¹⁰

The stratified corneal epithelia of mouse, rat, and human express the water-selective aquaporin AQP5, and the water- and glycerol-transporting aquaglyceroporin AQP3.^{11,12,13} We previously found reduced transcorneal water permeability in mice lacking AQP5.¹³ The function of AQP3 in cornea is unknown. Maintenance of the corneal epithelial layer is crucial to providing a smooth and transparent refractive surface and a barrier to infection, requiring continued regeneration to replace normal epithelial cell loss from the surface.¹⁴ Limbal stem cells located between the cornea and conjunctiva give rise to a single layer of centripetally migrating, mitotically active columnar basal cells that adhere to a basement membrane. These transient amplifying cells undergo several rounds of cell division before producing an intermediate layer of suprabasal wing cells one to three cells thick, and finally a superficial layer of terminally differentiated squamous cells two to four layers thick.

Corneal epithelial cell renewal is greatly increased during wound healing. Whereas suprabasal and basal epithelia of normal mouse cornea migrate centripetally at an average linear rate of 0.7–1.0 mm/hr,^{15,16} the marginal cells bordering a defect can migrate at 30–60 mm/hr.¹⁷ There is an body of extensive literature on the biology of

corneal epithelial regeneration based on wound-closure models (reviewed in Ref. ¹⁸). Corneal epithelial replacement involves three distinct phases: the latent phase, when cells clear debris at the wound edge and alter their metabolic status (~6 hr); the cell migration/adhesion phase, involving increased protein and macromolecule synthesis and glycogen utilization (up to 24 hr); and the cell proliferation phase (days). Recurrent or persistent corneal erosions in humans generally arise from trauma or various forms of epithelial basement membrane dystrophy, and may result in ulceration or perforation of the underlying stroma with associated pain and visual impairment.^{19,20}

We hypothesized that aquaporins might be involved in one or several aspects of corneal epithelial regeneration. Here, we first demonstrate the functional expression of AQP3 in corneal epithelium of mice. Significant impairment in corneal re-epithelialization was found in AQP3-null mice using an established mouse model of corneal epithelial removal, which was evaluated mechanistically by studies of corneal epithelial cell migration and proliferation in organ and primary cell cultures. Our results implicate AQP3 in the two processes fundamental to wound healing: cell migration and proliferation.

Methods

Mouse Preparation

Transgenic mice deficient in AQP3 and AQP5 in a CD1 genetic background were generated by targeted gene disruption as described.^{2,3} Mice were bred and cared for at the University of California, San Francisco, Animal Facility. For each experiment, wild-type

WEST LIBRARY

and knock-out mice were matched by age and weight (6–9 weeks, 22–30 grams).

Investigators were blinded to mouse genotype in all functional studies until completion of data analysis. Protocols were approved by the University of California, San Francisco, Committee on Animal Research and were in compliance with the ARVO statement for the Use of Animals in Ophthalmic and Vision research.

Mice were anesthetized using 125 mg/kg 2,2,2-tribromoethanol (avertin, Sigma-Aldrich, St. Louis, MO) intraperitoneally that was supplemented during experiments to maintain deep anesthesia. Core temperature was monitored using a rectal probe and maintained at $37 \pm 1^\circ\text{C}$ with a heating pad. For all maneuvers, mice were immobilized with the cornea under study oriented to face upward in a custom-built stereotaxic device with a rotating jaw clamp. Following experiments, mice were killed by avertin overdose and cervical dislocation, and whole eyes were enucleated using forceps.

Models of Corneal Re-epithelialization

In vivo and organ culture models of mouse corneal re-epithelialization utilized the same wounding procedure. After anesthesia and topical proparacaine (0.5%; Akorn, Buffalo Grove, IL), the cornea was blotted dry with a surgical sponge (Medtronic, Chicago, IL). A 2.3-mm diameter region of central corneal epithelium was demarcated with a surgical trephine (Roboz, Gaithersburg, MD) under observation with a stereo epifluorescence microscope (SMZ1500, 1x objective, 2.8x zoom, Nikon, Tokyo, Japan) and full-thickness corneal epithelium was mechanically removed without damage to the basement membrane using a number 69 Beaver blade (Becton-Dickinson, Franklin Lakes, NJ) and standard scraping procedures.²¹ Corneas were allowed to resurface for up

to 48 hr, with epithelial defect size monitored with fluorescein staining (0.1% in PBS) just after scraping and 12, 18, and 24 hr later. Fluorescence was imaged using a cooled CCD camera (CoolSnap HQ, Photometrics, Tuscon, AZ) and 2-dimensional projections of relative wound area were quantified using ImageJ software (National Institutes of Health, Bethesda, MD).

For studies of healing kinetics in vivo, tobramycin ointment (0.3%; Alcon, Fort Worth, TX) was applied to wounded eyes following scraping. Mice were then returned to their cages and allowed to awaken. Each subsequent wound area measurement was performed under light anesthesia followed by recovery. For organ culture studies, eyes were scraped, excised, and incubated as described.^{22,23} After rinsing in PBS, each enucleated eye was placed in a well of a 24-well culture plate and immersed fully in 1 mL Dulbecco's Modified Eagle Medium (DMEM) with 25 mM glucose (Gibco, Rockville, MD), and supplemented with 2% fetal bovine serum (FBS), penicillin G (100 U/mL), and streptomycin (100 µg/mL). Eyes were kept in a tissue culture incubator (37 °C, 5% CO₂) for up to 30 hr. The left eyes served as controls, while right eyes were incubated in some studies in culture medium supplemented with 10 mg/mL of 5-fluorouracil (5-FU) or paclitaxel (Sigma-Aldrich), prepared at 2,000x stocks in DMSO.

AQP3 Immunodetection

Eyes were fixed for histology by immersion in 10% neutral buffered formalin (Accustain; Sigma-Aldrich) for 24 hr. The fixed tissue was processed with xylenes and graded ethanols and embedded in paraffin, and 5 µm sections were cut through the central cornea and optic nerve (Histoserv Inc., Germantown, MD). Sections were

deparaffinized in Citrisolv (Fisher Scientific, Pittsburgh, PA), rehydrated in a series of graded ethanols, and then either stained with hematoxylin and eosin (H & E) or processed for immunohistochemistry. Slides were treated for epitope retrieval in citrate buffer (10 mM sodium citrate, 0.05% Tween 20) for 30 min at 95 °C and while cooling, and then sections were hydrogen peroxide-quenched (3% H₂O₂). After blocking with goat serum, sections were incubated with a rabbit anti-AQP3 polyclonal antibody (1:500, Chemicon, Temecula, CA) and washed in PBS. Bound antibody was detected using the Rabbit Vectastain ABC kit (Vector Laboratories, Burlingame, CA) and developed using the substrate 3,3-diaminobenzidine. Photographs were taken on an upright DM4000B microscope (Leica, Solms, Germany) equipped with a cooled CCD camera (Spot, Diagnostic Instruments, Sterling Heights, MI).

For immunoblot analysis, corneal epithelia of anesthetized mice were scraped using sterile Beaver blades and pooled (2–4 eyes/sample) in extraction buffer containing 250 mM sucrose, 10 mM EDTA, and 1% protease inhibitor mix (Sigma-Aldrich). Cells were mechanically disrupted using an insulin syringe, and samples were loaded on a 4–12% SDS polyacrylamide gel (3 µg/lane). Protein was transferred to a PDVF membrane and incubated with rabbit anti-AQP3 antibody (1:1000) followed by anti-rabbit IgG horseradish peroxidase-linked antibody (1:10,000, Amersham Biosciences, Piscataway, NJ), and visualized using enhanced chemiluminescence (Amersham Biosciences).

Transmission Electron Microscopy

Freshly enucleated globes were immersed in 1.2% paraformaldehyde and 0.8% glutaraldehyde in 0.1 M Sorensen buffer (pH 9.2) for 90 min. Corneas were dissected from globes, postfixed in 1% osmium tetroxide in sodium Veronal buffer for 1 hr, dehydrated in graded ethanols, and embedded in araldite epoxy resin. Ultrathin sections (70–100 nm) were stained with aqueous saturated uranyl acetate and Reynold's lead citrate and screened at 2,000–30,000x magnification using a 1200 EX JEOL electron microscope operating at 80 kV. Also, 1 μm thick sections were cut and stained with Trumpp's toluidene blue for orientation under the light microscope. Ultrastructure was compared by an observer blinded to genotype information.

In Vivo Water and Glycerol Permeability Assays

Osmotic water permeability was measured using a calcein-quenching method.¹³ Briefly, epithelial cells of anesthetized mice were loaded with calcein by exposure of the cornea for 30 min to 25 μL isosmolar PBS containing 10 μM calcein-AM (Molecular Probes, Eugene, OR). A custom-built 33- μL microchamber with <50 ms solution exchange time was then positioned over the cornea for continuous measurement of cell calcein fluorescence under suction perfusion with solutions of specified osmolarities. The time course of fluorescence in response to solution osmolarity changes, $F(t)$, was fitted to a single exponential time constant, τ : $F(t) = A + Be^{-t/\tau}$, where A and B are related to system sensitivity and background signal.

For measurements of glycerol permeability in vivo, the corneal epithelium of anesthetized mice was exposed to 15 μ L isosmolar PBS containing 1 mM glycerol (Fluka, Buchs, Switzerland) and 30 μ Ci/mL [14 C]glycerol (specific activity 146 mCi/mmol; Amersham Biosciences) for 0–20 min. After anesthetic overdose the ocular surface was washed with the same solution at 4 °C (lacking radioactive glycerol), blotted with a surgical sponge, and scraped within the limbus to collect full-thickness corneal epithelium. Cell-associated 14 C radioactivity was measured by scintillation counting (one eye per sample). Assay of total scraped protein per eye indicated <10% differences from eye to eye.

Assays of Corneal Epithelial Glycerol and Glycogen Content

Cellular glycerol and glycogen contents were measured using coupled enzymatic assays. After anesthesia and topical proparacaine, the ocular surface was blotted with a surgical sponge and the corneal epithelium was scraped. Material from 2–4 eyes was dissolved in 30 μ L of cold PBS (for glycerol) or 50 μ L hot 5 N NaOH (for glycogen). Cellular glycerol was assayed by a glycerol kinase absorbance assay (Free Glycerol Reagent, Sigma-Aldrich) and normalized to tissue protein content. Glycogen was extracted in hot base, precipitated in ice-cold absolute ethanol, and hydrolyzed in 0.6 N HCl based on methods established for rabbit corneal epithelium.^{24,25} Liberated glucose was measured using a glucose oxidase absorbance assay (Wako Chemicals, Neuss, Germany) and expressed relative to protein measured in the supernatant collected during ethanol precipitation. Protein concentration was measured using a DC protein assay kit (Bio-Rad, Hercules, CA).

Primary Culture of Mouse Corneal Epithelial Cells

Primary cultures of corneal epithelia cells from wild-type and AQP3 knock-out mice were grown on either tissue culture plastic or on plastic coated with fibronectin (5 $\mu\text{g}/\text{mL}$, Roche Diagnostics, Indianapolis, IN) in supplementary hormonal epithelial medium (SHEM) according to the method of Kawakita et al.²⁶ SHEM consisted of equivolume HEPES-buffered DMEM and F12 media, containing 10 ng/mL mouse-derived EGF, 5 $\mu\text{g}/\text{mL}$ insulin, 5 $\mu\text{g}/\text{mL}$ transferrin, 5 ng/mL sodium selenite, 0.5 $\mu\text{g}/\text{mL}$ hydrocortisone, 10^{-10} M cholera toxin A subunit (all from Sigma-Aldrich), 5% FBS, 50 $\mu\text{g}/\text{mL}$ gentamicin, and 1.25 $\mu\text{g}/\text{mL}$ amphotericin B. Enucleated eyes of 4–8-week-old mice were washed in SHEM and then enzymatically digested for 18 hr at 4°C in SHEM containing 15 mg/mL dispase II (Roche Diagnostics) and 100 mM D-sorbitol. Each eye was then held under suction at its posterior pole by a Pasteur pipette, and the corneal-limbal epithelial cell sheet was removed intact by gentle shaking in SHEM. Sheets were broken up into single-cell suspensions in Hanks' Balanced Salt Solution containing 0.05% trypsin and 0.53 mM EDTA (Gibco) by pipetting for 8–10 min at room temperature. Cells from eyes of each genotype were pooled, centrifuged (5 min at 800g), resuspended in SHEM, counted with a hemocytometer, and seeded in 12-well plates at a density of 6×10^4 cells/cm² (for proliferation studies) or 1×10^5 cells/cm² (for migration studies). Medium was replaced after 24 hr to remove unattached, suprabasal cells.

Attached basal cells were grown for up to 5 days. To detect the corneal epithelial-specific marker, cytokeratin 12 (K12), cells were fixed with 4% paraformaldehyde, blocked with 1% BSA for 30 min, incubated with a rabbit anti-mouse K12 polyclonal

primary antibody (1:50, Santa Cruz Biotechnology, Santa Cruz, CA) for 2 hr, and washed with PBS. Antibody binding was detected using a Cy3-conjugated anti-rabbit secondary antibody (1:200, Sigma-Aldrich). Epithelial cell morphology was observed by phase contrast light microscopy. Samples for AQP3 immunoblotting were collected by cell scraping.

Cell Proliferation Assays

For in vivo studies, 5-bromo-2'-deoxyuridine (BrdU, 12 mg/mL, Sigma-Aldrich) was injected intraperitoneally (100 mg/kg) 2 hr prior to euthanasia, after which eyes were processed as described above. For organ culture studies, BrdU was added to culture wells (100 µg/mL final concentration) 2 hr prior to fixation and staining. For BrdU immunohistochemistry, tissue sections were processed as described above with the following differences: In place of citrate buffer epitope retrieval, sections were treated with 2 N HCl for 1 hr at 37 °C and then with 0.1 M sodium borate solution (pH 9) twice for 15 min at room temperature. Sections were blocked with rabbit serum and incubated with a rat anti-BrdU monoclonal primary antibody (1:40, Abcam, Cambridge, MA). Bound antibody was detected using the Rat Vectastain ABC kit. BrdU positive cells were counted from limbus to limbus in a central corneal section for each eye.

Cell proliferation was measured in primary cultures of mouse corneal epithelium at 5 days after seeding onto uncoated plastic by addition of [methyl-³H]thymidine (2 µCi/mL, specific activity 86 Ci/mmol; Amersham Biosciences) to cultures for 6 hr. Cells were washed three times with PBS and three times in 1 mL cold 10% trichloroacetic acid, and then solubilized by addition of 750 µL/well of 0.5 N NaOH for 30 min at room

temperature. The solution was then neutralized by addition of 75 μ L of 5 N HCl to each well. ^3H radioactivity incorporated in 250 μ L sample aliquots was measured by scintillation counting. Total DNA in 20 μ L of each sample was assayed by Hoechst 33258 fluorescence (Sigma-Aldrich) in 2 M NaCl, 50 mM Na_2HPO_4 , and 2 mM EDTA (pH 7.4) after an 8-hr incubation at room temperature.

Cell Migration Assay

A scratch wound closure assay^{7,27,28} was used to compare migration in primary cultures of wild-type and AQP3-deficient mouse corneal epithelia plated onto uncoated or fibronectin-coated (5 μ g/mL, Roche Diagnostic) wells of 12-well plates. Five days after seeding, when cultures formed confluent monolayers, cells were synchronized by replacing media with SHEM containing low serum (1% FBS) and lacking EGF for 10 hr. Monolayers were wounded by two perpendicular linear scratches across each well using a 10- μ L pipette tip to produce 300- μ m-wide strips. After washing away unattached cells, media was switched to SHEM containing EGF and 5% FBS. Wounds were photographed immediately by phase contrast imaging at 10x magnification, and at 18 hr after wounding at 4 marked regions per well near the crossing point. Wound healing for each culture was reported as the average linear speed of the wound edges over 18 hr.

Statistics

Data are expressed as mean \pm SE. Significance between experimental groups was determined by a two-tailed Student's *t*-test assuming a 95% confidence interval.

Results

Corneal Epithelial AQP3 Expression

Immunohistochemistry showed AQP3 expression in corneal epithelium of wild-type mice, with no specific staining found in AQP3-null mice (Fig. 1A, top). AQP3 was most abundant in plasma membranes of basal epithelial cells. Interestingly, AQP5-null corneas had remarkably greater AQP3 staining than wild-type corneas, which extended throughout cell layers of the stratified epithelium (Fig. 1A, top, right). AQP5-deficient corneal epithelium was also consistently thicker than wild-type epithelium, with grossly swollen basal cells. The increased AQP3 protein expression in corneas from AQP5-null mice was confirmed by immunoblot analysis, where specific bands corresponding to glycosylated and non-glycosylated AQP3 monomers were detected in freshly scraped corneal epithelia of wild-type but not knock-out mice. Total AQP3 protein was 4.6 ± 1.2 -fold greater in AQP5 knock-out mice compared to wild-type mice (3 samples per genotype, Fig. 1A, bottom).

The effects of AQP3 and AQP5 deletion on corneal epithelial ultrastructure were assessed by transmission electron microscopy. As shown in Figure 1B (top), full-thickness central corneal epithelia from wild-type and AQP3 knock-out mice had the same total thickness (27.0 ± 0.6 vs. $26.7 \pm 0.9 \mu\text{m}$, $\pm\text{SE}$, 4 eyes per genotype), basal cell height (10.3 ± 0.3 vs. $10.2 \pm 0.1 \mu\text{m}$), number of cell layers (6–7), and basal, wing, and superficial cell morphology. AQP5-null epithelia were thicker ($40.8 \pm 0.4 \mu\text{m}$) and had taller basal cells ($13.4 \pm 0.2 \mu\text{m}$), yet the same number of cell layers. At higher

magnification, comparable densities of desmosomal (Fig. 1B, bottom) and hemidesmosomal (not shown) extracellular communications were seen in basal cell layers of the three genotypes. However, substantial pools of intercellular fluid were seen between AQP5-deficient epithelial cells (Fig. 1B, bottom, insets). These findings suggest grossly normal corneal epithelial cell morphology and attachments in AQP3-null corneas, and edematous AQP5-null corneal epithelia

AQP3 Deficiency Impairs Epithelial Water and Glycerol Transport

Having confirmed expression of AQP3 protein in mouse corneal epithelium, water and glycerol permeabilities were measured in intact corneal epithelia of living mice to demonstrate functionally significant AQP3 expression in wild-type mice. Osmotic water permeability of corneal epithelial cells was measured by a calcein fluorescence method in which cytoplasmic calcein fluorescence provided an instantaneous readout of cell volume.¹³ The reversible kinetics of cell swelling is shown in Figure 2A (top) in response to serial perfusion of 470, 310 and 470 mOsm solutions. Osmotically induced cell volume changes were slowed by 2.4 ± 0.3 -fold in AQP3-null mice (Fig. 2A, bottom).

A [¹⁴C]glycerol uptake assay was developed to quantify AQP3-dependent corneal epithelial glycerol permeability in vivo. After anesthesia and immobilization, small aliquots of PBS containing [¹⁴C]glycerol were placed on proptosed eyes for specified times. Full-thickness corneal epithelium was harvested by scraping for measurement of cell-associated [¹⁴C]glycerol radioactivity. [¹⁴C]glycerol uptake was linear for at least 30 min in wild-type mice (Fig. 2B, top). [¹⁴C]glycerol uptake measured at 12 min was remarkably reduced in AQP3-null mice (Fig. 2B, bottom). However, despite the reduced

glycerol permeability, steady-state corneal epithelial glycerol content was not significantly affected by AQP3 deletion (Fig. 2C, top). There was a small but significant reduction in glycogen content (Fig. 2C, bottom).

AQP3 Deficiency Slows Re-epithelialization In Vivo

To determine the roles of aquaporins in corneal surface re-epithelialization, we utilized an established in vivo model of corneal epithelial wound healing in which healing was quantified based on fluorescein pooling on the bare stroma, indicating the advancement of marginal basal epithelia at the wound edge. The 2.3-mm diameter wound, chosen to avoid damage to the limbus, remained relatively constant for up to 10 hr following wounding (the latent phase), and then decreased in size from 10–24 hr (the migration phase). Re-epithelialization was quantified from the defect area during the time of rapid healing at 12, 18, and 24 hr after scraping (Fig. 3A). At the 12- and 18-hr time-points, a significant delay in resurfacing was found in AQP3-deficient corneas compared to wild-type corneas (Fig. 3B; 12 hr: 10 ± 4 vs. $28 \pm 3\%$ area healed; 18 hr: 36 ± 4 vs. $51 \pm 5\%$ healed). Interestingly, accelerated healing was found in AQP5 knock-out mice at 18 and 24 hr, which may be related to increased corneal AQP3 expression in these mice. AQP3 expression remained approximately constant in wild-type mice during the healing process, as demonstrated by immunoblot analysis and immunohistochemistry at 24 or 48 hr following corneal scraping (data not shown).

Starting at approximately 24 hr and lasting for several days, the healing response is dominated by cell proliferation and the re-establishment of a multilayered epithelium (the proliferation phase). The re-stratification process was assessed by histology of

central corneal sections from eyes fixed at various times after wounding (representative sections shown in Fig. 3C). In all three genotypes, large wounds with well-demarcated leading edges were visible at 12 hr. At 24 and 36 hr, AQP3-deficient corneas showed delayed monolayer surfacing and cell stratification/differentiation compared to wild-type corneas. AQP5-deficient corneas showed accelerated healing by both criteria. Periodic Acid-Schiff staining of adjacent sections during healing demonstrated comparable glycogen store depletion in basal cells of each genotype (not shown). Figure 3D (top) shows delayed recovery of epithelial thickness in AQP3-null corneas at 24, 36, and 48 hr. In contrast, restoration of full epithelial thickness was observed by 48 hr after wounding in wild-type mice (Fig. 3D, bottom). AQP5-null epithelia were confirmed to be thicker than wild-type corneas at baseline, with full restoration of corneal thickness by 48 hr after wounding (Fig. 3D, bottom). The central regions of AQP3-null corneas had 0–2 cell layers at 24 hr following wounding, compared to 3–4 layers in wild-type and AQP5-null corneas. At 36 and 48 hr, AQP3-null corneas were 3–4 cell layers thick, less than the 6–7 layers (full-thickness) found for wild-type and AQP5-null corneas, suggesting impaired proliferation in AQP3 deficiency. Transmission electron microscopy of the advancing wound edge after 20 hr of healing showed extensive filopodial and lamellipodial projections in the migrating epithelia (micrograph from wild-type cornea shown in Fig. 3E), enabling fast movement along intact basement membranes.

Defective Migration of AQP3-null Epithelial Cells in an Organ Culture Wound Healing Assay

Delayed re-epithelialization in AQP3-deficient corneas might arise from impairment in cell migration, proliferation, or both. To distinguish between these processes, an organ culture wound-healing model was used that has been shown to largely represent cell migration.^{22,23} In situ wounds were made as in the in vivo model, and then eyes were enucleated and cultured in serum-containing medium for up to 30 hr (Fig. 4A, inset). In preliminary experiments, no healing occurred when eyes were incubated in serum-free medium. To characterize the model, globes from wild-type mice were cultured in medium containing either 5-FU (10 $\mu\text{g}/\text{mL}$), paclitaxel (10 $\mu\text{g}/\text{mL}$), or DMSO vehicle (Fig. 4A). 5-FU impairs cell proliferation but not migration in cornea and other tissues, while paclitaxel inhibits both processes.^{29,30,31,32} In this model, epithelial resurfacing occurred in the control group at a slightly slower rate than in vivo. Paclitaxel, but not 5-FU, significantly slowed corneal resurfacing at 18, 24, and 30 hr, supporting the utility of organ culture for in vitro assessment of corneal cell migration.

There was a marked delay in re-epithelialization of AQP3-null vs. wild-type corneas (without 5-FU or paclitaxel; Fig. 4B), in agreement with the in vivo data. To confirm the absence of significant corneal epithelial cell proliferation in this in vitro assay, BrdU staining was done on corneas at 24 hr (4 corneas per genotype). Less than one BrdU positive cell on average was found in an entire section of cornea from wild-type or AQP3 knock-out mice (data not shown). Additionally, whereas the full-thickness, multilayered morphology observed in uninjured epithelia (Fig. 4B, inset, a) was restored

following 24 hr of healing in vivo (Fig. 4B, inset, b), organ-cultured eyes were always covered by only 1–2 layers of epithelial cells at 24 hr, including at and near the unwounded limbus (Fig. 4B, inset, c). This observation supports the conclusion that basal cell proliferative capacity is arrested under these organ culture conditions. These experiments thus indicate impaired corneal epithelial cell centripetal migration in AQP3 deficiency.

Defective Proliferation of AQP3-null Epithelia After Wounding In Vivo

The potential contribution of AQP3 function to corneal epithelial cell proliferation in vivo was studied by BrdU incorporation. Experiments were done in non-wounded mice, and at different times after wounding. Figure 5A shows representative images of mid-peripheral cornea (well outside of the advancing wound margin) stained for BrdU. No significant difference in BrdU staining was observed between the genotypes in the absence of wounding, with a greatly reduced number of BrdU-positive cells in AQP3-null and wild-type peripheral corneal epithelium at 12 hr after wounding (data not shown). As summarized in Figure 5B, at 24 hr AQP3-null corneas showed greatly diminished basal cell proliferation compared to wild-type corneas. AQP5-null corneas showed elevated proliferation at 24 hr, which persisted at 48 hr. A similar conclusion was reached when central, mid-peripheral, and peripheral areas of the corneal epithelium were counted separately (not shown).

LIBRARY
LIBRARY
LIBRARY
LIBRARY
LIBRARY

Defective Proliferation and Migration of AQP3-null Epithelial Cells in Primary Culture

The role of AQP3 in corneal epithelial cell proliferation was further examined using a recently developed mouse primary cell culture model.²⁶ Intact corneal-limbal epithelial sheets from wild-type and AQP3 knock-out mouse eyes were isolated by dispase II digestion, and non-passaged cells were cultured on plastic in SHEM medium. Substrate attachment of wild-type and AQP3-deficient cells was comparable, as measured by cell counting at 24 hr after seeding both from trypsinized cultures using a hemocytometer ($7.7 \pm 0.3 \times 10^4$ wild-type vs. $7.7 \pm 1.4 \times 10^4$ AQP3-null cells per well, \pm SE, 3 wells per genotype) and from imaging randomly selected 10x fields in undisturbed cultures (92 ± 3 wild-type vs. 89 ± 5 AQP3-null cells/field, \pm SE, 9 wells per genotype).

Approximately 30% of plated cells adhered to tissue culture plastic, as was reported previously.²⁶ Cells from both genotypes grew similarly as monolayers of mostly large basal epithelial cells (Fig. 6A, top), which began to stratify at areas of confluence, as appreciated by altering the microscope focus. Consistent with the earlier report, larger (basal) cells showed cytoplasmic immunostaining for the corneal epithelial-specific marker, K12 (Fig. 6A, middle, left). Immunoblot analysis showed AQP3 expression in cell cultures from wild-type but not AQP3-null corneas (Fig. 6B, middle, right).

Cell proliferation was measured after 5 days of culture, when cells were 50–70% confluent. Under maximal stimulation in the presence of serum and growth factors, AQP3-null cell cultures incorporated 3.8 ± 0.7 times less [³H]thymidine than cultures

from wild-type corneas (Fig. 6A, bottom). Cultures from wild-type corneas were found by Hoescht fluorescence to contain ~2 times more DNA (per well) than AQP3-null cultures, and qualitatively approached confluence 20–30% faster in all six separate sets of primary cell cultures prepared for these studies. These results support defective corneal epithelial cell proliferation in AQP3 deficiency, which likely accounts for the delayed restoration of full-thickness cornea in vivo over days following scraping.

Cell migration in confluent primary cultures of mouse corneal epithelia was measured using a standard wound scratch assay. Cultures grown on fibronectin-coated wells showed accelerated wound closure rates compared to cultures grown on uncoated plastic, in agreement with previous studies.^{28,33} In vitro wound healing was thus quantified in fibronectin cultures after a relatively short, 18 hr healing period to avoid confounding effects of cell proliferation on healing. Fig. 6B shows delayed wound closure in AQP3-deficient corneal epithelia at 18 hr following creation of linear wounds (4.0 ± 0.2 mm/hr for wild-type cells vs. 2.8 ± 0.1 for AQP3-null cells, \pm SE, 4 wells per genotype), supporting the conclusion from in vivo and organ culture experiments that AQP3 deletion impairs corneal epithelial cell migration following wounding.

Discussion

This study demonstrates AQP3-facilitated water and glycerol transport in mouse corneal epithelium and provides evidence for distinct roles of AQP3 in corneal epithelial cell migration and proliferation during re-epithelialization. Migration and proliferation are fundamental to normal corneal epithelial cell turnover (taking place over weeks) and

become greatly accelerated during wound healing. The expression of AQP3 in basal cells of the corneal epithelium suggested a role in one or both of these processes. Defective corneal resurfacing over the first 24 hr after wounding implicated a role for AQP3 in cell migration, which was proved using an organ culture model of wound healing in which cell proliferation was confirmed to be essentially absent by BrdU staining, epithelial morphology, and 5-FU insensitivity, and using an vitro wound closure assay comparing corneal epithelial cultures from wild-type and AQP3-null mice.

A separate defect in cell proliferation during re-epithelialization was discovered in AQP3-null corneal epithelium, providing evidence for a previously unrecognized role for an aquaporin in cell proliferation. Defective corneal epithelial cell proliferation was shown by a reduced number of BrdU-positive cells at 24 hr after wounding, and substantial slowing of re-stratification. Wild-type corneal epithelia achieved their normal thicknesses and cell numbers by 48 hr, while AQP3-deficient epithelia were delayed by both measures. AQP3-deficient corneal epithelia cells thus manifest impaired cell movement and DNA synthesis more slowly than wild-type cells following wounding. This conclusion is supported by the slowed cell proliferation measured in AQP3-null primary cultures of corneal epithelial cells.

Our findings in AQP5 knock-out mice also have potential relevance to human corneal disease. Kenney et al. reported AQP3 expression primarily in basal epithelial cells of normal human corneas,³⁴ similar to our findings in wild-type mice. AQP3 localization expands to include both basal and superficial epithelial cells in chronic edematous corneal diseases. These changes are similar to those in AQP5 knock-out

corneas, where AQP3 upregulation is also associated with stromal and epithelial edema. Despite the hyperproliferative response in wounded AQP5-deficient corneas, their increased epithelial thickness appears to arise from fluid accumulation and cell swelling rather than from increased cellularity. In contrast to the swollen and edematous AQP5-null corneal epithelia, AQP3-null epithelia appeared normal at the light and electron microscope levels.

The AQP3-dependent effects on cell migration and proliferation could each, in principle, be explained by deficiencies in water and/or glycerol transport, or by a mechanism independent of transporting functions. The migration phase of re-epithelialization involves lamellipodial and filopodial extension by marginal cells at the wound leading edge.¹⁷ Such protrusions and the rate of cell migration are reduced in a variety of aquaporin-deficient cells,^{7,27,35} suggesting a role for local water transport at the leading edge of migrating cells. Corneal epithelial cell migration also requires mobilization of energy stores, particularly glycogen.³⁶ Defective glycerol transport in AQP3 deficiency might impair glycogen synthesis or utilization by direct or indirect effects on glycolysis.⁹ However, basal epithelial glycerol content was similar in wild-type and AQP3-null mice, and although glycogen stores were slightly diminished in AQP3-null mice, Periodic Acid-Schiff staining of corneal sections during healing showed no evidence of differential basal cell glycogen-utilization kinetics compared to wild-type mice.

The involvement of AQP3 in cell proliferation may be related to its glycerol-transporting function. AQP3-mediated glycerol transport was found previously to be

important for lipid biosynthesis in skin,⁸ as glycerol is the backbone of phosphoglyceride, a major phospholipid in plasma membranes. The role of glycerol in corneal metabolism remains unexplored. Glycerol is a common ingredient in eye drop formulations, though primarily because its humectant properties promote ocular surface hydration.³⁷

Alternatively, the effect of AQP3 on cell proliferation might not involve glycerol transport, but instead AQP3 protein-protein interactions or modulation of membrane physical properties.

In conclusion, the involvement of AQPs in cell migration appears to represent a general phenomenon whose exact mechanism remains to be elucidated, but is likely dependent on water movement. The involvement of aquaglyceroporins, such as AQP3, in cell proliferation may also be a general phenomenon, which may be related to AQP3-dependent glycerol transport or to some non-transporting role of AQP3.

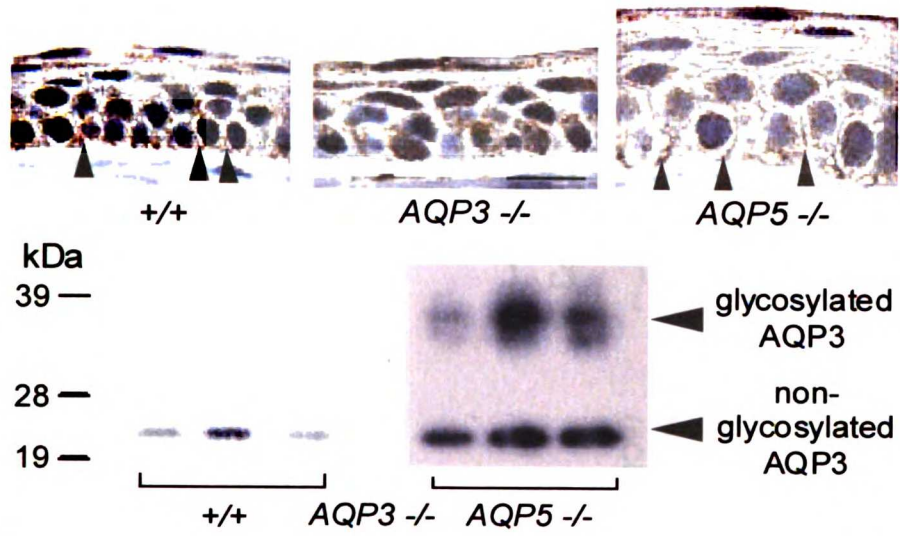
References

1. Ma T, Yang B, Gillespie A, Carlson EJ, Epstein CJ, Verkman AS. Severely impaired urinary concentration ability in transgenic mice lacking aquaporin-1 water channels. *J Biol Chem*. 1998;273:4296–4299.
2. Ma T, Song Y, Yang B, et al. Nephrogenic diabetes insipidus in mice lacking aquaporin-3 water channels. *Proc Natl Acad Sci USA*. 2000;97:4386–4391.
3. Ma T, Song Y, Gillespie A, Carlson EJ, Epstein CJ, Verkman AS. Defective secretion of saliva in transgenic mice lacking aquaporin-5 water channels. *J Biol Chem*. 1999;274:20071–20074.
4. Song Y, Verkman AS. Aquaporin-5 dependent fluid secretion in airway submucosal glands. *J Biol Chem*. 2001;276:41288–41292.
5. Zhang D, Vetrivel L, Verkman AS. Aquaporin deletion in mice reduced intraocular pressure and aqueous fluid production. *J Gen Physiol*. 2002;119:561–569.
6. Oshio K, Watanabe H, Song Y, Verkman AS, Manley GT. Reduced cerebrospinal fluid production and intracranial pressure in mice lacking choroids plexus water channel Aquaporin-1. *FASEB J*. 2005;19:76–78.
7. Saadoun S, Papadopoulos MC, Hara-Chikuma M, Verkman AS. Impairment of angiogenesis and cell migration by targeted aquaporin-1 gene disruption. *Nature*. 2005;434:786–792.
8. Hara M, Verkman AS. Glycerol replacement corrects defective skin hydration, elasticity, and barrier function in aquaporin-3-deficient mice. *Proc Natl Acad Sci USA*. 2003;100:7360–7365.
9. Hara-Chikuma M, Sohara E, Rai T, et al. Progressive adipocyte hypertrophy in aquaporin-7-deficient mice: adipocyte glycerol permeability as a novel regulator of fat accumulation. *J Biol Chem*. 2005;28:15493–15496.
10. Hara M, Ma T, Verkman AS. Selectively reduced glycerol in skin of aquaporin-3-deficient mice may account for impaired skin hydration, elasticity, and barrier recovery. *J Biol Chem*. 2002;277:46616–46621.
11. Patil RV, Saito I, Yang X, Wax MB. Expression of aquaporins in the rat ocular tissue. *Exp Eye Res*. 1997;64:203–209.
12. Hamann S, Zeuthen T, La Cour M, et al. Aquaporins in complex tissues: distribution of aquaporins 1-5 in human and rat eye. *Am J Physiol*. 1998;274:C1332–C1345.

13. Levin MH, Verkman AS. Aquaporin-dependent water permeation at the mouse ocular surface: in vivo microfluorimetric measurements in cornea and conjunctiva. *Invest Ophthalmol Vis Sci.* 2004;45:4423–4432.
14. Thoft RA, Friend J. The X, Y, Z hypothesis of corneal epithelial maintenance. *Invest Ophthalmol Vis Sci.* 1983;24:1442–1443.
15. Buck RC. Measurement of centripetal migration of normal corneal epithelial cells in the mouse. *Invest Ophthalmol Vis Sci.* 1985;26:1296–1299.
16. Nagasaki T, Zhao J. Centripetal movement of corneal epithelial cells in the normal adult mouse. *Invest Ophthalmol Vis Sci.* 2003;44:558–566.
17. Buck RC. Cell migration in repair of mouse corneal epithelium. *Invest Ophthalmol Vis Sci.* 1979;18: 767–784.
18. Lu L, Reinach PS, Kao WW. Corneal epithelial wound healing. *Exp Biol Med (Maywood).* 2001;226:653–664.
19. Macaluso DC, Feldman ST. Pathogenesis of sterile corneal erosions and ulcerations. In: Krachmer JH, Mannis MJ, Holland EJ, ed. *Cornea: Fundamentals of cornea and external disease.* St Louis, MO: Mosby-Year Book, Inc; 1997;199–212.
20. Ramamurthi S, Rahman MQ, Dutton GN, Ramaesh K. Pathogenesis, clinical features and management of recurrent corneal erosions. *Eye.* 2005; In press.
21. Kao WW, Liu C, Converse RL, et al. Keratin 12-deficient mice have fragile corneal epithelia. *Invest Ophthalmol Vis Sci.* 1996;37:2573–2584.
22. Saika S, Okada Y, Miyamoto T, et al. Role of p38 MAP kinase in regulation of cell migration and proliferation in healing corneal epithelium. *Invest Ophthalmol Vis Sci.* 2004;45:100–109.
23. Yeh L, Chen W, Li W, et al. Soluble lumican glycoprotein purified from human amniotic membrane promotes corneal epithelial wound healing. *Invest Ophthalmol Vis Sci.* 2005;46:479–486.
24. Thoft RA, Friend J. Biochemical transformation of regenerating ocular surface epithelium. *Invest Ophthalmol Vis Sci.* 1977;16:14–20.
25. Jumblatt MM, Neufeld AH. Characterization of cyclic AMP-mediated wound closure of the rabbit corneal epithelium. *Curr Eye Res.* 1981;1:189–195.

26. Kawakita T, Espana EM, He H, Yeh L, Liu C, Tseng SCG. Calcium-induced abnormal epidermal-like differentiation in cultures of mouse corneal-limbal epithelial cells. *Invest Ophthalmol Vis Sci.* 2004;45:3507–3512.
27. Hara-Chikuma M, Verkman AS. Aquaporin-1 facilitates epithelial cell migration in kidney proximal tubule. *J Am Soc Nephrol.* 2006;17:39–45.
28. Xu, KP, Riggs A, Ding Y, Yu FS. Role of ErbB2 in corneal epithelial wound healing. *Invest Ophthalmol Vis Sci.* 2004;45:4277–4283.
29. Jumblatt MM, Neufeld AH. A tissue culture assay of corneal epithelial wound closure. *Invest Ophthalmol Vis Sci.* 1986;27:8–13.
30. Capone A, Lance SE, Friend J, Thoft RA. In vivo effects of 5-FU on ocular surface epithelium following corneal wounding. *Invest Ophthalmol Vis Sci.* 1987;28:1661–1667.
31. Panjwani N, Zhao Z, Ahmad S, Yang Z, Jungalwala F, Baum J. Neolactoglycosphingolipids, potential mediators of corneal epithelial cell migration. *J Biol Chem.* 1995;270:14015–14023.
32. Wiskirchen J, Schober W, Schart N, et al. The effects of paclitaxel on the three phases of restenosis: smooth muscle cell proliferation, migration, and matrix formation: an in vitro study. *Invest Radiol.* 2004;39: 565–571.
33. Lee HK, Lee JH, Kim M, Kariya Y, Miyazaki K, Kim EK. Insulin-like growth factor-1 induces migration and expression of laminin-5 in cultured human corneal epithelial cells. *Invest Ophthalmol Vis Sci.* 2006;47:873–882.
34. Kenney MC, Atilano SR, Zorapapel N, Hogue B, Gaster RN, Ljubimov AV. Altered expression of aquaporins in bullous keratopathy and Fuchs' dystrophy corneas. *J Histochem Cytochem.* 2004;14:621–626.
35. Saadoun S, Papadopoulos MC, Watanabe H, Yan D, Manley GT, Verkman AS. Involvement of Aquaporin-4 in astroglial cell migration and glial scar formation. *J Cell Sci.* 2005;118:5691–5698.
36. Kuwabara T, Perkins DG, Cogan DG. Sliding of the epithelium in experimental corneal wounds. *Invest Ophthalmol.* 1976;15:4–14.
37. Solomon A, Merin S. The effect of a new tear substitute containing glycerol and hyaluronate on keratoconjunctivitis sicca. *J Ocul Pharmacol.* 1998;14:497–504.

A



B

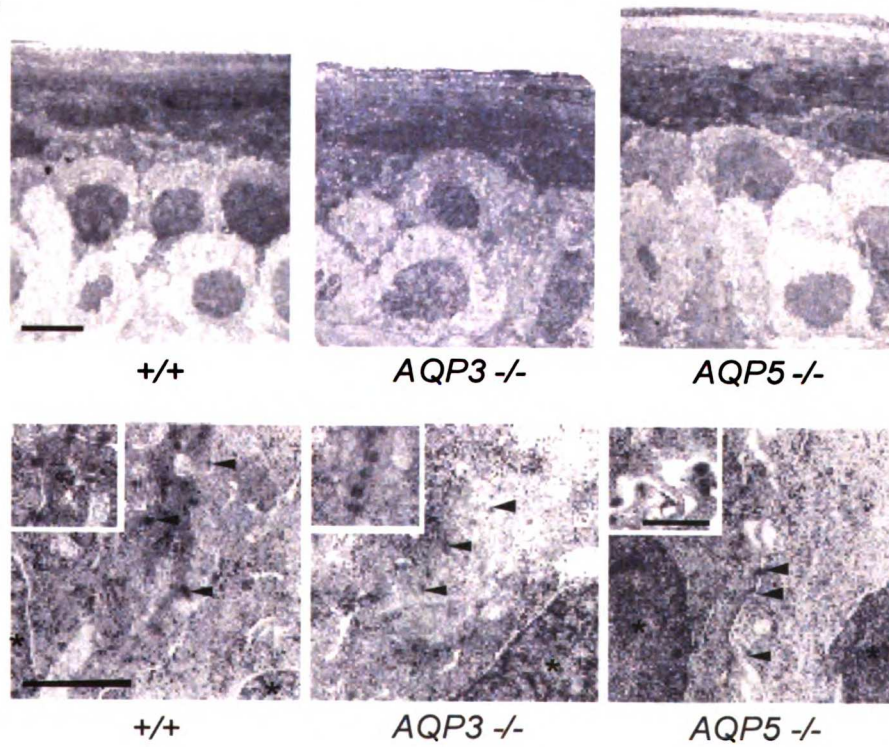


Figure 1

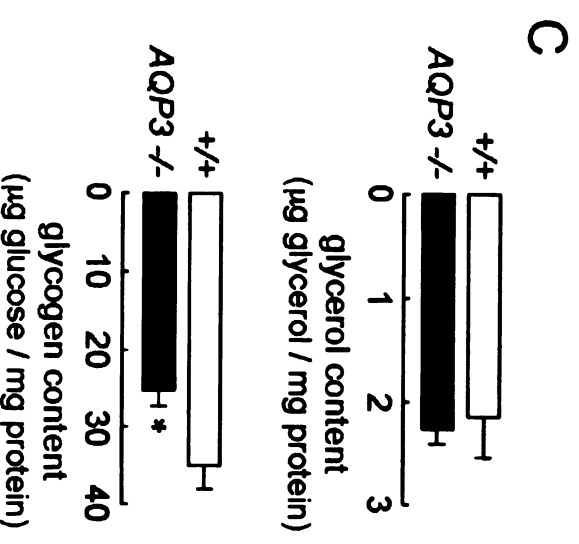
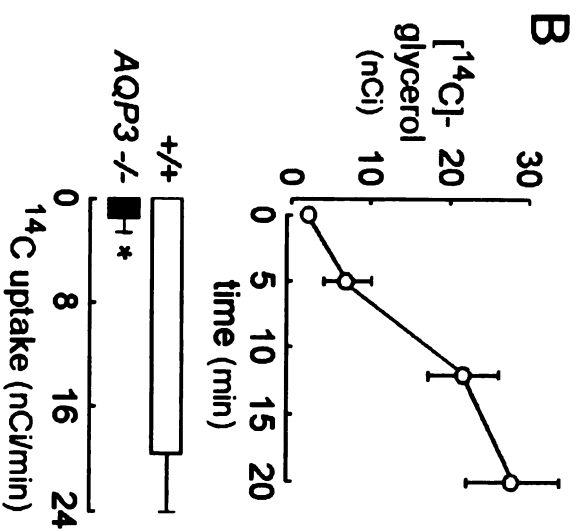
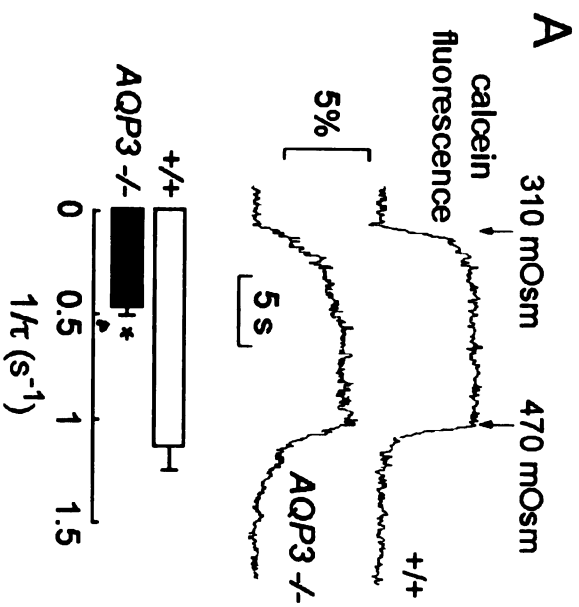


Figure 2

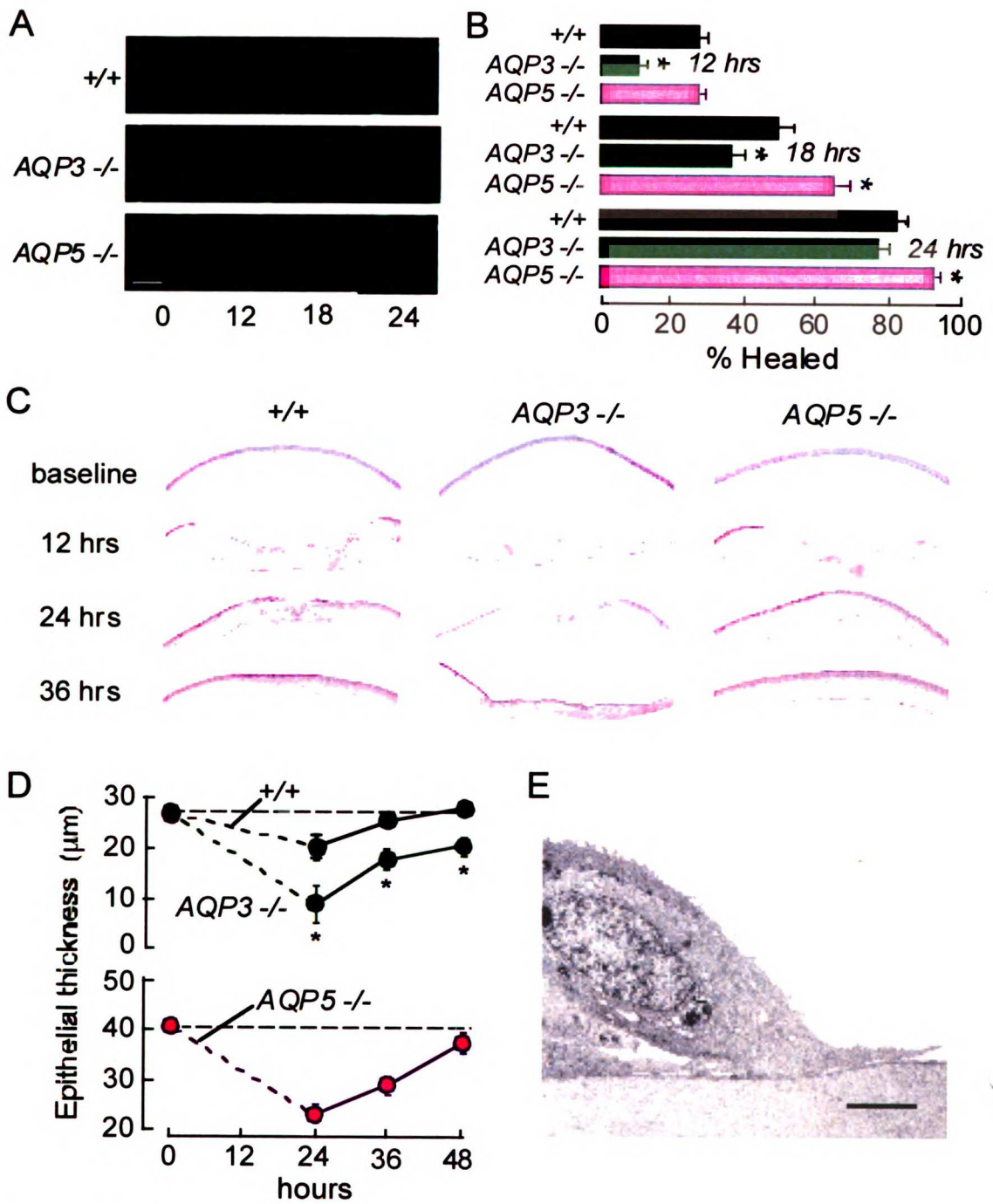
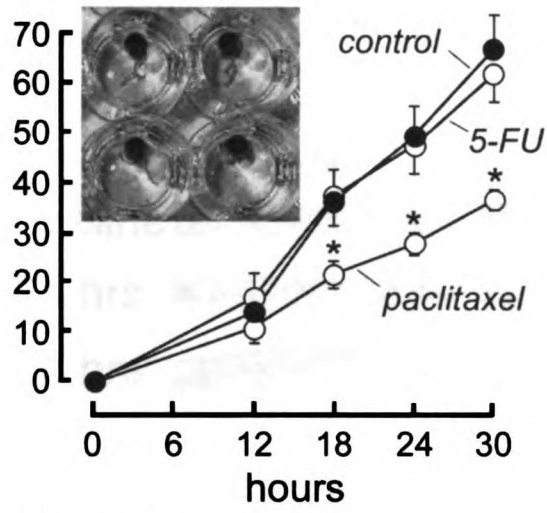


Figure 3

A % Healed



B % Healed

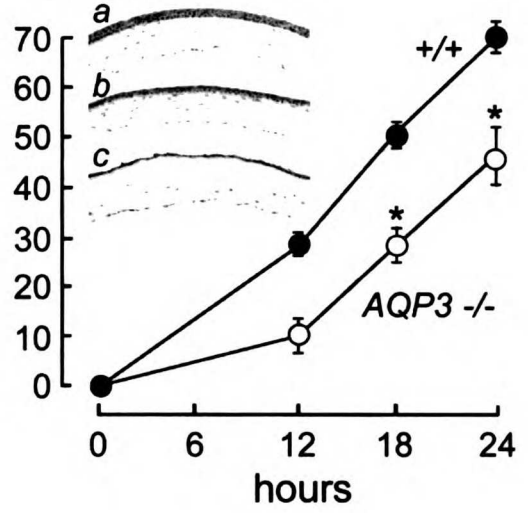


Figure 4

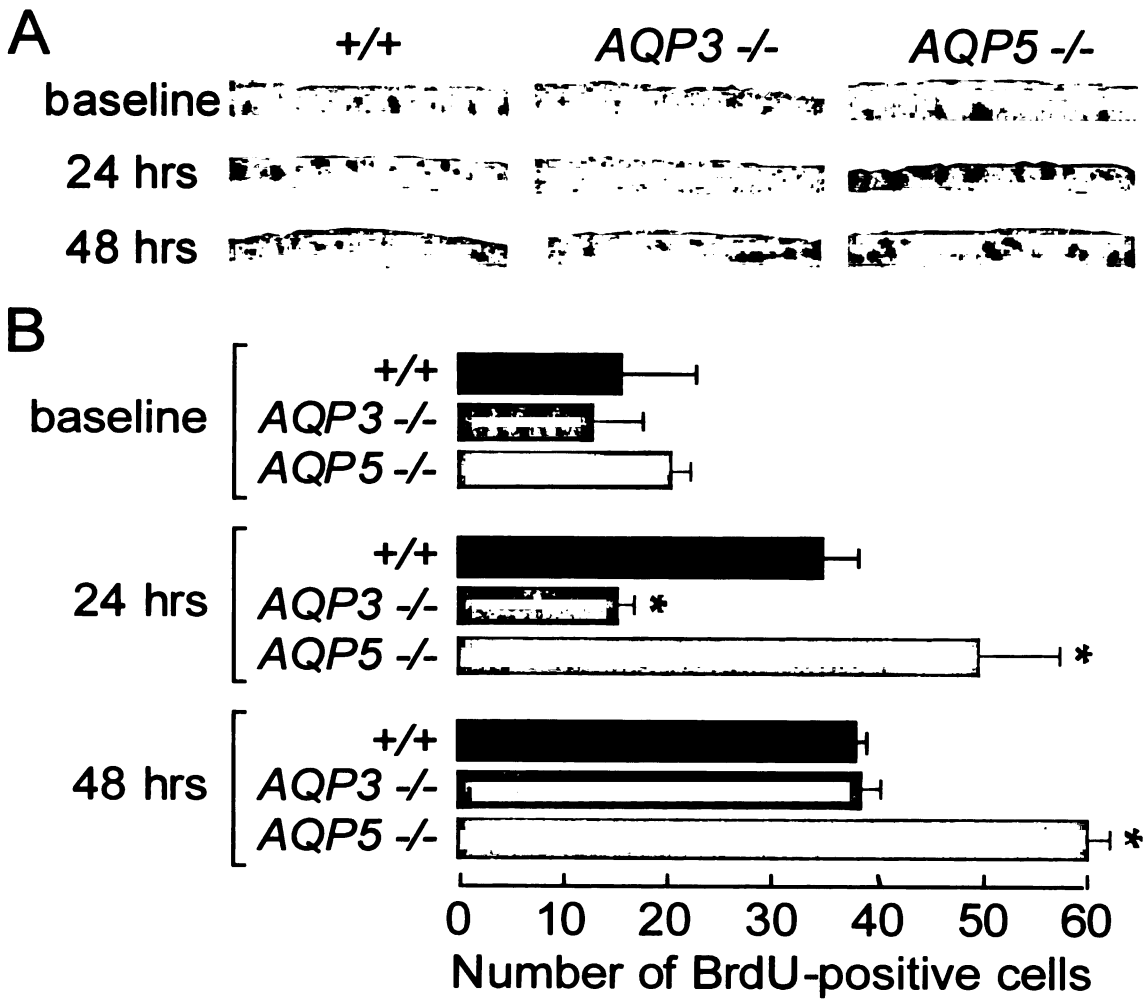


Figure 5

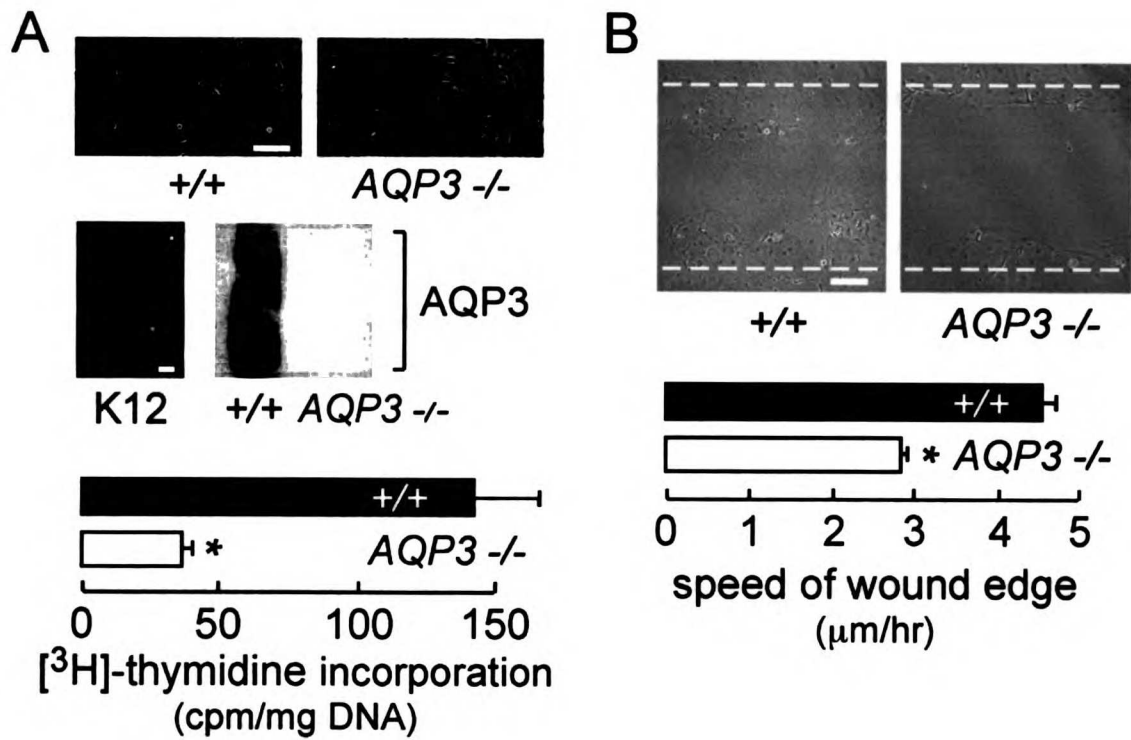


Figure 6

Figure Legends

FIGURE 1. Corneal epithelial AQP3 expression and morphology. **(A)** AQP3 protein expression in mouse corneal epithelia. *Top:* immunohistochemistry of sections through central cornea with AQP3 plasma membrane staining indicated (*arrowheads*). Scale bar = 20 μm . *Bottom:* immunoblot of corneal epithelia from mice of indicated genotypes. **(B)** Transmission electron microscopy representative of four corneas from four mice of each genotype. *Top:* full-thickness central corneal epithelium showing 6–7 cell layers. Scale bar = 5 μm . *Bottom:* basal cells with adjacent cell nuclei indicated by stars and desmosomes marked by arrowheads. Scale bar = 1 μm . *Insets:* magnified regions of intercellular desmosomal attachments. Scale bar = 0.5 μm .

FIGURE 2. Water and glycerol permeabilities of corneal epithelium. **(A)** Osmotic water permeability of corneal epithelial cells in mice *in vivo*, where the ocular surface was exposed to osmotic gradients. *Top:* representative time course of cellular calcein fluorescence, reflecting changes in cell volume, in response to changes of perfusate osmolality between 310 and 470 mOsm. *Bottom:* summary of averaged reciprocal single exponential time constants ($1/\tau$) fitted to kinetics of calcein fluorescence ($\pm\text{SE}$, 4 mice per genotype, with data from each mouse representing averaged data for 6–10 curves. $*P < 0.05$). **(B)** [^{14}C]glycerol uptake in corneal epithelium *in vivo*. *Top:* time course of [^{14}C]glycerol accumulation in wild-type full-thickness corneal epithelium ($\pm\text{SE}$, 4–6 eyes at each time point). *Bottom:* [^{14}C]glycerol uptake following 12 min exposure to [^{14}C]glycerol-containing buffer ($\pm\text{SE}$, 6 wild-type and 4 AQP3-null eyes, $*P < 0.01$). **(C)**

Corneal epithelial glycerol (*top*) and glycogen (*bottom*) content (\pm SE, 4 samples per genotype pooled from 2–3 eyes each, $*P < 0.05$).

FIGURE 3. Aquaporin-dependent corneal re-epithelialization in vivo following wounding. (A) An epithelial defect (diameter 2.3 mm) created at the center of corneas (*left column*) was monitored (*right columns*). Scale bar = 1 mm. (B) Imaging of corneal resurfacing after wounding. Percent remaining epithelial defects determined by fluorescein staining at 12, 18, and 24 hr after wounding (\pm SE, 8–14 eyes per genotype at each time point; $*P < 0.01$, comparing to wild-type). (C) Histology showing unwounded corneas (*top row*) and wounded corneas after 12, 24, and 36 hr of healing (*bottom rows*). (D) Averaged central corneal epithelial thicknesses before and at indicated times after wounding (\pm SE, 4 corneas from each genotype analyzed in two central sections separated by 50 μ m, $*P < 0.01$). (E) Transmission electron micrograph of the leading edge of migrating epithelial cell in wild-type mouse cornea after 20 hr of resurfacing. Representative of two wild-type and two AQP3-null corneas. Scale bar = 2 μ m.

FIGURE 4. Corneal epithelial cell migration during wound healing in organ culture. (A) Eyes were enucleated after corneal scraping and cultured (*inset*) in DMEM containing 2% FBS without or with 10 μ g/mL 5-FU or paclitaxel. Average percentages of resurfaced wound quantified by fluorescein staining (\pm SE, 6–7 eyes per group, $*P < 0.05$). (B) Averaged healing (\pm SE, 8 eyes per group, $*P < 0.05$). *Inset*: H & E-stained sections from uninjured wild-type cornea (a) and after 24 hr of healing in vivo (b) vs. organ culture (c).

FIGURE 5. AQP3-dependent corneal epithelial cell proliferation during re-epithelialization. (A) Representative sections of mid-peripheral cornea showing BrdU-immunoreactive

cells (dark brown nuclei) before (*top row*) and at 24 hr (*middle row*) or 48 hr (*bottom row*) after corneal scraping. **(B)** Histogram of BrdU-positive cells distributed from limbus to limbus in uninjured corneal epithelia and during healing (\pm SE, 4 corneas per genotype at each time point, $*P < 0.01$).

FIGURE 6. AQP3 deficiency impairs cell proliferation and migration in primary cultures of corneal epithelial cells. **(A)** Primary cultures of mouse corneal epithelial cells. *Top:* phase contrast light microscopy of confluent areas of wild-type and AQP3-null cells at 7 days following seeding. Scale bar = 30 μ m. *Middle, left:* K12 immunofluorescence staining of 5-day wild-type culture. Scale bar = 10 μ m. *Middle, right:* AQP3 immunoblot of 5-day wild-type and AQP3-null cultures. *Bottom:* averaged [methyl- 3 H]thymidine incorporation normalized to DNA content following 6 hr of incubation in [methyl- 3 H]thymidine containing medium (\pm SE, 4 wild-type and 5 AQP3-null 5-day cultures in 12-well plates, $*P < 0.01$). Representative of two sets of experiments. **(B)** In vitro wound closure model to study corneal epithelial cell migration. *Top:* Light micrographs of wounded cell monolayers grown on fibronectin-coated wells, showing delayed wound closure at 18 hr in AQP3-deficient corneal epithelia. *Dashed lines* indicate the wound margin immediately after scraping. Scale bar = 50 μ m. *Bottom:* Speed of wound edge in wild-type and AQP3-null cells (\pm SE, 4 cultures per genotype, $*P < 0.01$).

CHAPTER 4.

CFTR-Regulated Chloride Transport at the Ocular Surface in Living Mice Measured by Potential Differences

Abstract

PURPOSE. To define the role of the cystic fibrosis transmembrane conductance regulator (CFTR) in Cl^- secretion at the mouse ocular surface in vivo.

METHODS. Open-circuit potential differences (PDs) across the fluid-bathed ocular surface were measured in anesthetized wild-type and cystic fibrosis (CF) mice in response to Cl^- ion substitution and transport agonists and inhibitors.

RESULTS. Basal ocular surface PD was -23 ± 1 mV (SE; 20 wild-type mice), depolarizing to -16 ± 2 mV after amiloride, then hyperpolarizing to -34 ± 3 mV after low Cl^- . CFTR activation by forskolin or a selective activator caused further sustained hyperpolarization to -50 to -60 mV. UTP produced a comparable but transient hyperpolarization. The CFTR inhibitors CFTR_{inh}-172 and GlyH-101 largely reversed agonist- but not low Cl^- -induced hyperpolarizations. PD in CF mice hyperpolarized by 2.1 mV after low Cl^- and was insensitive to CFTR activators or inhibitors.

CONCLUSIONS. CFTR provides a major pathway for mouse ocular surface Cl^- secretion, suggesting the application of CFTR activators as therapy for dry eye. Amiloride-sensitive

Na⁺ transporters facilitate Na⁺ absorption. PD measurements provide a robust and reproducible means of assessing ocular surface ion transporting mechanisms.

The ocular surface, lined by corneal and conjunctival epithelia, plays an important role in regulating tear film volume and composition. Prior studies indicate that these "tight epithelia" are able to secrete chloride and absorb sodium (reviewed in Refs. ^{1,2}). Apical chloride secretion across ocular surface epithelia provides a primary driving force for near-isosmolar fluid transport across cornea and conjunctiva into the tear film. Measurements of basal and agonist-induced chloride-driven fluid secretion in several species suggest corneal and conjunctival involvement in basal tear production as well as their possible role in tear film dysfunction.^{3,4,5} Dry eye syndrome, or keratoconjunctivitis sicca (KCS), represents a diverse group of conditions that manifest as inadequate ocular surface lubrication. Dysfunction of various ocular adnexa can alter tear lipid, aqueous, or mucin components, resulting in dry eye symptoms in 15% to 60% of the population. In the United States, pathologic KCS is diagnosed in 7% of women aged 55 and older.⁶

The cystic fibrosis transmembrane conductance regulator (CFTR) is a cAMP-dependent chloride channel expressed in many mammalian tissues performing fluid transport, including epithelia of the airway, intestine, and pancreas (reviewed in Refs. ^{7,8}). CFTR is a voltage-independent anion channel and a regulator of other ion channels. CFTR activation requires nucleoside triphosphates and cAMP for phosphorylation by protein kinase A on a cytoplasmic-facing regulatory domain. In humans, CFTR mutations that alter its cellular processing, expression, and/or intrinsic transport function cause cystic fibrosis (CF), the most common lethal hereditary disease. In the eye, CFTR is

present in corneal endothelium and retinal pigment epithelium, where it has been proposed to facilitate corneal deturgescence⁹ and to regulate subretinal extracellular volume and chemical composition,^{10,11} respectively. CFTR has also been localized to apical superficial cell membranes of the stratified conjunctival epithelium,^{12,13} suggesting a role for CFTR in tear film homeostasis under normal conditions and as a target for therapy of KCS. Patients with CF exhibit subtle hints of ocular surface derangement, such as decreased tear production and increased corneal fluorescein staining.¹⁴ Characteristics of dry eye, including corneal and conjunctival squamous metaplasia, persist in patients with CF, even after correcting the potentially confounding Vitamin A deficiency that arises from intestinal malabsorption.^{15,16}

Short-circuit current measurements on rabbit cornea and conjunctiva^{17,18} and patch-clamp studies on cultured corneal epithelial cells¹⁹ demonstrated a cAMP-dependent outward apical chloride current, possibly due to activation of CFTR. Calcium and phospholipase C signaling stimulate transient chloride secretion across conjunctiva through an as yet unidentified channel.²⁰ INS365, a long-acting UTP agonist that stimulates calcium-sensitive chloride–fluid secretion,^{21,22} is currently in phase III clinical trials for treatment of dry eye. Our laboratory has identified potent CFTR-selective activators by high-throughput screening,^{23,24} with the potential for use in dry eye syndrome if CFTR is found to provide a major route for ocular surface chloride secretion. A potential advantage of agonists of CFTR versus calcium-activated chloride channels is the sustained versus transient activation kinetics.

The purpose of this study was to identify the major transport pathways for Cl^- at the ocular surface, focusing on the potential role of CFTR. Experiments were performed on mice based on the availability of transgenic mice lacking functional CFTR and on our prior work establishing optical methods to characterize aquaporin-dependent water transporting mechanisms at the mouse ocular surface.²⁵ In addition to comparative measurements in CF mice, potent CFTR inhibitors^{26,27} and an activator²⁴ identified by our laboratory were used to define the role of CFTR in ocular surface Cl^- transport. To study conductive Cl^- transport in vivo, we introduce a novel, minimally invasive potential difference (PD) measurement approach, which was motivated by the successful application of open-circuit PD measurements to study ion transport mechanisms in nasal and rectal epithelia.^{28,29,30} We found large, robust, and reproducible PDs at the mouse ocular surface that were sensitive to ion substitution and pharmacologic maneuvers, providing direct evidence for a major role of CFTR in ocular surface Cl^- secretion.

Methods

Mice

Wild-type mice and CF mice (homozygous G551D-CFTR mutant mice³¹) in a CD1 genetic background were bred at the University of California, San Francisco Animal Facility. G551D heterozygous mice were bred to generate homozygous CF mice. Wild-type mice were fed a standard diet, and CF mice were fed Peptamen (Nestle Nutrition, Vevey, Switzerland). Mice weighing 25 to 30 g were studied at age 8 to 12 weeks. Protocols were in compliance with the ARVO Statement for the Use of Animals in

Ophthalmic and Vision Research and were approved by the University of California at San Francisco Committee on Animal Research.

Mouse Preparation for PD Measurements

Mice were anesthetized with 2,2,2-tribromoethanol (avertin, 125 mg/kg intraperitoneal; Sigma-Aldrich, St. Louis, MO), with additional avertin injected during experiments to maintain anesthesia. Mice were immobilized with a custom-built stereotaxic device equipped with a rotating jaw clamp to orient the eye under study to face upward. Corneas were kept hydrated with PBS supplemented with NaCl to 320 mOsM to match mouse serum osmolarity. A heating pad and rectal temperature probe were used to maintain body temperature at $37 \pm 1^\circ\text{C}$. The cornea and bulbar conjunctiva were exposed by gently retracting the loose facial skin by hand (Fig. 1A , inset). A probe catheter fashioned from PE-90 polyethylene tubing beveled at a 45° angle was positioned ~ 1 mm above the ocular surface using a micropositioner and was not adjusted during experiments. Solutions were perfused through plastic tubing (0.16 cm inner diameter) using a multireservoir gravity pinch valve system (ALA Scientific), with the flow rate set at 6 mL/min using a variable-flow peristaltic pump (medium flow model, Fisher). A ~ 50 - μL fluid reservoir was maintained around the probe tip on the ocular surface throughout the experiment by surface tension, with a suction cannula positioned ~ 3 mm from the orbit to drain excess fluid. This setup permitted rapid solution changes (dye-exchange experiments indicated a solution exchange time of < 3 seconds) with minimal electrical noise.

Measurement of Ocular Surface PD

PD at the ocular surface was measured using a protocol adapted from nasal PD studies,²⁸ with the experimental apparatus depicted in Figure 1A . Ocular surface PD was measured continuously with the ocular surface perfused serially with up to eight different solutions. PD was insensitive to exact catheter probe orientation and was unaffected by switching between identical solutions. The probe was connected through a 1-M KCl agar bridge to an Ag/AgCl electrode and high-impedance digital voltmeter (IsoMilivolt Meter; World Precision Instruments, Sarasota, FL). Voltmeter input and system electrical resistances were 10^{12} and $1.1 \times 10^6 \Omega$, respectively. PD was recorded at 5 Hz with a 14-bit analog-to-digital converter. The reference electrode consisted of a second Ag/AgCl electrode with 1-M KCl agar bridge and was connected to a winged 21-gauge needle filled with 320 mOsM saline (PBS + NaCl). The needle was inserted in the subcutaneous tissue at the back of the neck, though PD was insensitive to reference electrode placement (<1 mV difference with subcutaneous placement in neck versus abdomen). Cl^- replacement produced a small positive junction potential (generally ~ 1 mV) that was measured daily and used to correct PDs measured with low Cl^- perfusates.

Compounds and Solutions

All perfusion solutions were isosmolar to mouse serum (320 ± 5 mOsM) as measured using a freezing point-depression osmometer (Precision Systems, Natick, MA). The compositions of each solution are provided in Table 1. Solution 1 (control solution) consisted of phosphate buffered-saline supplemented with 15 mOsM NaCl. In Solution 2 (low- Cl^- solution; 4.7 mM Cl^-), most Cl^- was replaced by gluconate. In some

experiments, NaCl was replaced isosmotically with 25 mM NaHCO₃ (solution 3). Unless noted otherwise, all chemicals were purchased from Sigma-Aldrich and prepared as 1000x stock solutions in dimethyl sulfoxide (DMSO). All perfusion solutions contained 10 μM indomethacin (see the Results section). In most experiments, amiloride (100 μM) was present in all solutions after baseline measurement. Other activators and inhibitors used in the perfusates included forskolin (2 or 10 μM); UTP (10 μM, freshly dissolved in PBS); DIDS (4, 4'-diisothiocyanatostilbene-2,2'-disulfonic acid; 200 μM); CFTR_{inh}-172 (3-[(3-trifluoromethyl)phenyl]-5-(3-carboxyphenyl)methylene]-2-thioxo-4-thiazolidinone; 10 μM)²⁶; GlyH-101 (*N*-(2-naphthalenyl)-[(3,5-dibromo-2,4-dihydroxyphenyl)methylene]glycine hydrazide; 20 μM)²⁷; and CFTR_{scr}-04 (2-(ethylimino)-3-ethyl-5-(1,3-benzodioxol-5-methylene)-4-thiazolidinone; 10 μM).²⁴

Experimental Protocols

Ocular surface PDs were measured continuously in response to topical application of isosmolar saline followed by isosmolar solutions containing various agonists and/or inhibitors that often imposed transepithelial ionic gradients. An idealized curve for a typical protocol is illustrated in Figure 1B. After a baseline PD was recorded (using solution 1), the perfusate was switched to an amiloride-containing solution to depolarize ocular surface PD if there were functional amiloride-sensitive Na⁺ channels. Amiloride was present in subsequent solutions to minimize the influence of Na⁺ channel function on interpretation of PDs in terms of Cl⁻ channel function. Perfusate Cl⁻ was then largely replaced by the relatively impermeant anion gluconate (solution 2) to give a sustained hyperpolarization related to cAMP-independent Cl⁻ secretion. Addition of a Cl⁻ channel

agonist (forskolin, CFTR_{act}-04, or UTP) produces a further hyperpolarization that can be subsequently reversed by a Cl⁻ channel inhibitor (CFTR_{inh}-172, GlyH-101, or DIDS). In some experiments, 25 mM HCO₃⁻ was present (solution 3) at various stages in the protocol to examine alternative mechanisms of anion transport.

Data Analysis

Data are expressed as the mean ± SE of absolute PDs or PD differences (Δ PD), with statistical comparisons between groups made using the one-tailed Student's *t*-test.

Results

Ocular surface PD was measured by modification of methods used in nasal PD studies. As diagrammed in Figure 1A, the ocular surface was perfused at constant flow (6 mL/min) with solutions that could be switched without interruption of flow. The baseline PD of approximately -23 mV in wild-type mice perfused with physiological saline generally remained constant over many minutes (0–2 mV fluctuation around a stable mean value). The high-resistance epithelial surface, comprising cornea and conjunctiva in parallel, was responsible for generating and maintaining the large PD. As expected, PD was reduced to near-zero after a low-resistance ion pathway was created by scraping the cornea or conjunctiva with a cotton swab. In some experiments, the ocular surface was perfused with the original chloride-containing solution at the end of the chloride transport protocol shown in Figure 1B, with PD returning to within 4 mV of baseline value.

Although minimal drift of PD in these control experiments implies the maintenance of epithelial barrier function, return to baseline was not routinely assessed, because the

various maneuvers performed in the study are expected to alter intracellular ionic activities over time, thus changing electrochemical driving forces. Moreover, some of the activators/inhibitors used may not be fully or rapidly reversible.

In preliminary experiments, the hyperpolarization due to Cl^- substitution was somewhat variable and was often larger than the effects of subsequently added agonists, which was attributed to variable basal cAMP stimulation related to stress- or trauma-induced prostaglandin production. As has been done in many tissue electrophysiology studies, indomethacin was present in all solutions to block prostaglandin production. We found large and reproducible effects of cAMP agonists in the presence of indomethacin with reduced initial low Cl^- -induced hyperpolarization.

Ocular Surface Cl^- Transport

The first series of experiments was designed to identify CFTR Cl^- channel function using the cAMP agonist forskolin and two classes of high-affinity CFTR inhibitors. Thiazolidinone (CFTR_{inh}-172) and glycine hydrazide (GlyH-101) CFTR inhibitors have low micromolar or better inhibitory potencies, and their application in vivo has been demonstrated in mouse models of secretory diarrhea and nasal epithelial CFTR Cl^- secretion.^{26,27,28,32} Representative ocular surface PD recordings in Figure 2A show a small amiloride-induced depolarization. The amiloride effect at 10 μM was $\approx 90\%$ of maximum response at 100 μM (not shown). Exchange to a low Cl^- perfusate resulted in a hyperpolarization, and subsequent activation of CFTR (and possibly other cAMP-dependent ion transporters) by forskolin produced a further hyperpolarization. CFTR_{inh}-172 or GlyH-101 added after forskolin produced a depolarization. Figure 2B summarizes

absolute PDs for a series of experiments as in Figure 2A. The forskolin-induced hyperpolarization was reversed by CFTR_{inh}-172 and to a lesser extent by GlyH-101. Higher concentrations of GlyH-101 were not used to avoid nonspecific inhibition of calcium-activated chloride channels. The forskolin-induced hyperpolarization in the presence of low Cl⁻ and its reversal by CFTR inhibitors provide evidence for functional CFTR Cl⁻ channels at the ocular surface.

UTP is a Cl⁻ channel agonist that stimulates ocular surface Cl⁻ secretion by a calcium-dependent process.³³ UTP in the low-Cl⁻ perfusate consistently produced a large, negative spike in PD, followed by a slower, transient hyperpolarization (Fig. 3A). Addition of the disulfonic stilbene inhibitor DIDS, but not CFTR_{inh}-172 (not shown), reversed the UTP-dependent hyperpolarization when added at any time during the transient hyperpolarization. A substantial forskolin response occurred after the transient UTP-induced hyperpolarization.

To determine the contribution of HCO₃⁻ transport to PDs, a small set of studies was performed in which 25 mM HCO₃⁻ was added to the perfusate. PD did not change when HCO₃⁻ was added to the physiological Cl⁻-containing solution, but depolarized reversibly by 1.5 ± 0.2 mV (SE) when HCO₃⁻ was added to the low-Cl⁻ perfusate after forskolin (six eyes studied); CFTR_{inh}-172 did not prevent the small HCO₃⁻-induced depolarization.

To investigate whether the low Cl⁻-induced hyperpolarization in the absence of agonists involves DIDS- or CFTR_{inh}-172-sensitive Cl⁻ channels, inhibitors were added without prior addition of the agonist. In some experiments, as shown in Figure 3B, DIDS

and CFTR_{inh}-172 partially reversed the low-Cl⁻-induced hyperpolarization. Significant variability was noted from mouse to mouse, though the combined depolarizations from DIDS and CFTR_{inh}-172 were always <30% of the low-Cl⁻-induced hyperpolarization.

Two additional strategies were applied to investigate the involvement of CFTR in ocular surface Cl⁻ secretion: use of a CFTR-selective agonist that activates CFTR without elevating cAMP (CFTR_{acr}-04) and measurements on transgenic mutant (CF) mice lacking functional CFTR. Figure 4A (left) shows a representative PD measurement as in Figure 2A, except that CFTR_{acr}-04 was added before forskolin. CFTR_{acr}-04 produced a prompt hyperpolarization that was increased relatively little by forskolin, and was reversed by CFTR_{inh}-172. Agonist-induced hyperpolarization was absent when CFTR_{inh}-172 was added with CFTR_{acr}-04 (not shown), and in some cases a small depolarization was noted, resembling the depolarization that occurred when CFTR_{inh}-172 was added after low Cl⁻ in the absence of agonists. Figure 4A (right) shows a study on CF mice. Although substantial amiloride-sensitive depolarization occurred, there was little effect of low Cl⁻ or CFTR agonists or inhibitors. Baseline ocular surface PD was similar in wild-type and CF mice, but the depolarization due to amiloride was significantly greater in CF mice. Absolute PDs are summarized in Figure 4B (left), and a paired analysis of PD changes after specific maneuvers (Δ PD) is given in Figure 4B (right). The CFTR agonist and CF mouse studies provide direct evidence for the involvement of CFTR in ocular surface Cl⁻ transport.

Discussion

In this study, we sought to clarify the involvement of CFTR in transepithelial chloride conductance at the mouse ocular surface. An ocular surface open-circuit potential difference approach was introduced, which is based on the generation of PDs across tight epithelia from asymmetries in apical and basal membrane ion conductances. Maurice^{34,35} and Klyce³⁶ measured electrical potentials between the body and tear film in rabbit of -15 to -30 mV (tears negative to blood). This original observation of the ability of the ocular surface to generate a PD was expanded on in the present study to characterize electrogenic Cl^- transport processes in living mice by perfusion of the ocular surface with solutions that created ionic gradients and contained transport activators or inhibitors. In contrast to short-circuit current and single-cell microelectrode approaches, which require tissue and cell isolations in vitro, the ocular surface PD approach is technically simple and permits minimally invasive in vivo measurements under physiological open-circuit conditions. Also, ocular PDs produce robust voltage changes that are readily interpreted in terms of specific ion transport processes. HCO_3^- transport contributed little to ocular surface PDs compared with Cl^- , demonstrating the relative importance of chloride channels in ocular surface anion flux.

Several lines of evidence implicate the functional involvement of CFTR in ocular surface Cl^- secretion, including activation of Cl^- secretion by CFTR agonists and reversal of agonist effects by CFTR inhibitors. The incomplete reversal by GlyH-101 may be related to its external pore-blocking mechanism in which reduced extracellular Cl^- concentration and plasma membrane depolarization are predicted to reduce its potency.²⁷

While agonists were shown to stimulate CFTR conductance, experiments where Cl^- channel inhibitors were added under low Cl^- but in the absence of agonists indicate that CFTR does not mediate most cAMP-independent Cl^- secretion at the ocular surface. Because DIDS is a relatively nonspecific Cl^- channel inhibitor, the partial DIDS effect in these experiments cannot be interpreted to implicate the activity of specific Cl^- channels.

The absence of CFTR agonist and inhibitor effects in CF mice provides additional evidence for CFTR involvement in ocular surface Cl^- transport. One interesting observation was the near-zero hyperpolarization in CF mice after low Cl^- in the absence of CFTR agonists. This observation seems at variance with the conclusion based on CFTR inhibitor studies that only a small fraction of the low- Cl^- -induced hyperpolarization involves CFTR-mediated transport. However, similar results were found in nasal PD measurements in CF mice,^{28,29} where it has been proposed that the low- Cl^- response results from Cl^- transport by a CFTR-regulated Cl^- channel, though not CFTR itself. An alternative possibility is that the non-CFTR Cl^- channel responsible for the low- Cl^- response is downregulated in CF mice.

Previous RT-PCR and immunocytochemical studies have detected CFTR in corneal and conjunctival epithelial cell cultures and tissue mounts from rabbit.^{12,13,19} However, functional studies on in vitro preparations relied exclusively on nonspecific channel activators (e.g., genistein) and inhibitors (e.g., glibenclamide), and cAMP-elevating agents (IBMX [3-isobutyl-1-methylxanthine] and forskolin). In our in vivo studies, we treat the ocular surface as a single functional unit as in the intact eye, so that ocular surface PDs represent the aggregate of corneal and conjunctival properties.

Another reason that we performed measurements on the minimally perturbed whole ocular surface is that mechanical isolation of the two tissues in vivo disrupted epithelial cell integrity. A machined plastic chamber, beveled to create a seal at the limbus and permit selective perfusion and measurement of cornea or conjunctiva, results in a slow, progressive reduction in PD toward zero. Such contact also imposed a stress that may affect cellular transport processes. Further studies are needed to quantify the relative contributions of cornea versus conjunctiva to the ion channel-dependent PD responses recorded in the study and to determine whether increasing CFTR-dependent fluid transport across each tissue could supplement tear formation in states of aqueous deficiency.

Although CF is not generally associated with overt dry eye symptoms, the results of the current study suggest that CFTR provides an important pathway for agonist-stimulated fluid secretion across the ocular surface. Several factors may account for the mild ocular phenotype in CF. Basal CFTR activity may be very low under normal conditions, so that ocular surface hydration does not depend on CFTR function. Also, upregulation of alternative secretory pathways either in tear-producing glands, or within the cornea or conjunctiva, may compensate for impaired CFTR Cl^- channel function. Indeed, calcium-activated Cl^- channels have been found in some models to compensate for CFTR dysfunction.³⁷

Our results suggest the possibility of using CFTR activators for treatment of dry eye syndrome. Topical application of IBMX, a phosphodiesterase inhibitor/CFTR activator, has been found to reduce the osmolarity of collected tears in humans and

rabbits with KCS.^{38,39} In our study, CFTR activation produced sustained, large increases in ocular surface Cl⁻ secretion, with quantitatively much greater time-integrated hyperpolarization than UTP, an activator of calcium-sensitive Cl⁻ channels. Currently, topical cyclosporin A, which suppresses downstream inflammatory cascades that ultimately compromise epithelial barrier function, is the only drug approved for treatment of dry eye, with UTP analogues currently under development.^{21,22}

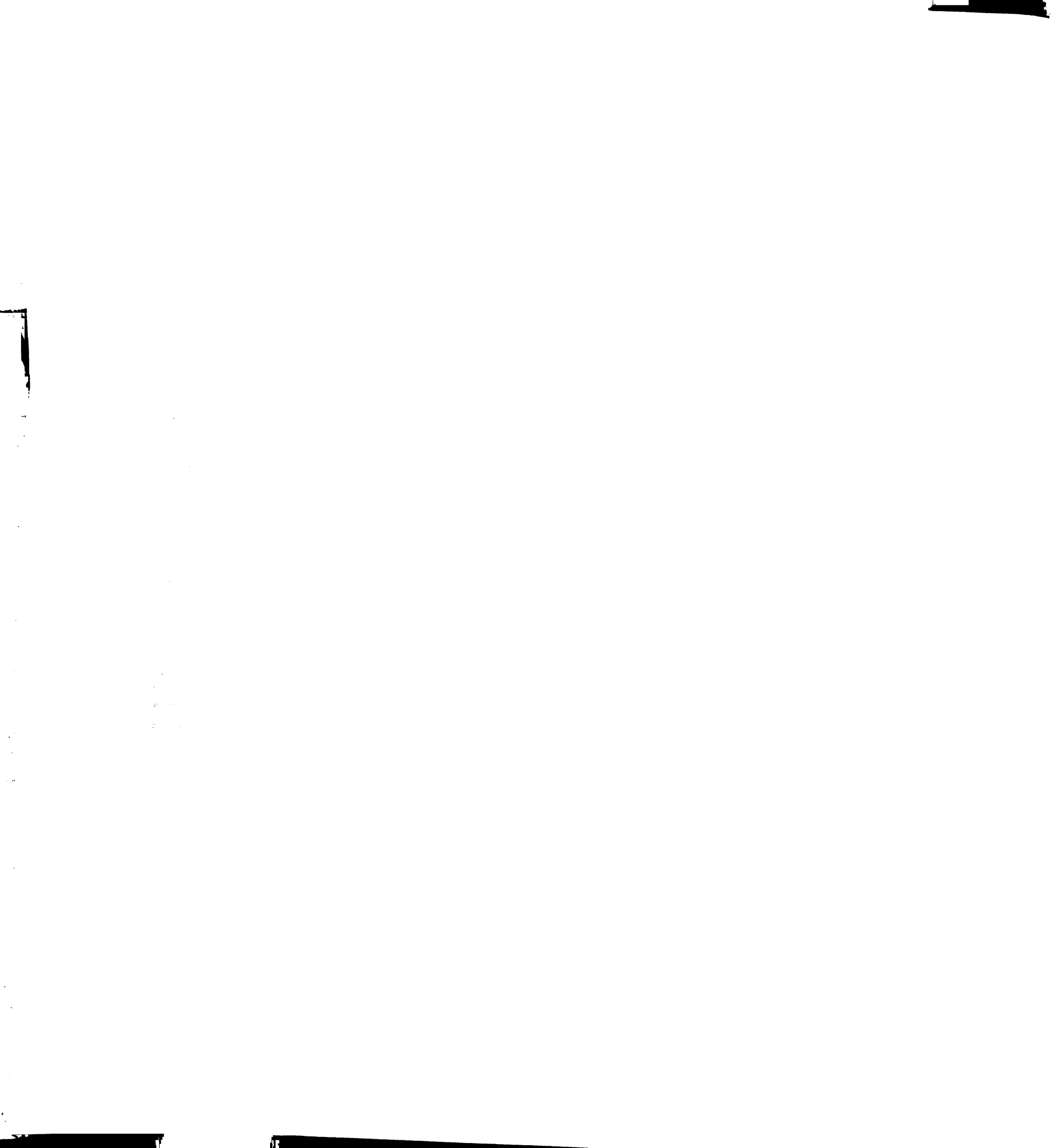
Although this study was focused primarily on mechanisms of Cl⁻ secretion, ocular surface PD measurements in response to amiloride indicated the involvement of amiloride-sensitive Na⁺ channels, such as ENaC, in ocular surface Na⁺ absorption. Inhibitors of Na⁺ absorption may provide another therapy for dry eye syndrome. The evidence here for the involvement of amiloride-sensitive Na⁺ channels in mice contrasts with short-circuit experiments in rabbit tissue.^{17,40} However, functional evidence for ENaC was reported in bovine cornea by Midelfart,^{41,42} and ENaC protein has been found by immunocytochemistry in rat and human cornea.⁴³ The roles of individual ocular surface transporters are probably species specific; for example, cAMP activates basolateral K⁺ channels in frog corneal epithelium but inhibits them in rabbit.^{44,45} The amiloride-induced depolarization was greater in CF than wild-type mice, as has been reported in nasal PD measurements.²⁸ The greater depolarization in nasal PDs in CF mice has been interpreted as increased ENaC activity in CF resulting from direct or indirect CFTR-ENaC interaction, though it remains controversial whether altered electrochemical driving forces for Na⁺ absorption in CF can account fully for the greater depolarization in CF.^{46,47}

In summary, measurements of ocular surface PD in mice indicated the involvement of CFTR in ocular surface Cl^- secretion. Based on evidence for Na^+ absorption by corneal and conjunctival epithelia^{1,2,17} and the amiloride effects described herein, ocular surface PDs should also be useful in studying mechanisms of electrogenic Na^+ transport at the ocular surface. The substantial and sustained activation of CFTR-mediated Cl^- secretion by CFTR agonists supports the evaluation of CFTR-selective activators as potential treatment for dry eye syndromes.

References

1. Candia OA. Electrolyte and fluid transport across corneal, conjunctival, and lens epithelia. *Exp Eye Res.* 2004;78:527–535.
2. Dartt DA. Regulation of mucin and fluid secretion by conjunctival epithelial cells. *Prog Retin Eye Res.* 2002;21:555–576.
3. Candia OA, Zamudio AD. Chloride-activated water permeability in the frog corneal epithelium. *J Membr Biol.* 1995;143:259–266.
4. Yang H, Reinach PS, Koniarek JP, Wang Z, Iserovich P, Fischbarg J. Fluid transport by cultured corneal epithelial cell layers. *Br J Ophthalmol.* 2000;84:199–204.
5. Murakami T, Fujihara T, Nakamura M, Nakata K. P2Y(2) receptor stimulation increases tear fluid secretion in rabbits. *Curr Eye Res.* 2000;21:782–787.
6. Dogru M, Tsubota K. New insights into the diagnosis and treatment of dry eye. *Ocul Surface.* 2004;2:59–75.
7. Pilewsky JM, Frizzell RA. Role of CFTR in airway disease. *Physiol Rev.* 1999;79:S215–S255.
8. Sheppard DM, Welsh MJ. Structure and function of the CFTR chloride channel. *Physiol Rev.* 1999;79:S23–S45.
9. Sun CS, Bonanno JA. Expression, localization, and functional evaluation of CFTR in bovine corneal endothelial cells. *Am J Physiol.* 2002;282:C673–C683.
10. Reigada D, Mitchell CH. Release of ATP from retinal pigment epithelial cells involves both CFTR and vesicular transport. *Am J Physiol.* 2005;288:C132–C140.
11. Blaug S, Quinn R, Quong J, Jalickee S, Miller SS. Retinal pigment epithelial function: a role for CFTR?. *Doc Ophthalmol.* 2004;106:43–50.
12. Turner HC, Bernstein A, Candia OA. Presence of CFTR in the conjunctival epithelium. *Curr Eye Res.* 2002;24:182–187.
13. Shiue MH, Gukasyan HJ, Kim K-J, Loo DD, Lee VHL. Characterization of cyclic AMP-regulated chloride conductance in the pigmented rabbit conjunctival epithelial cells. *Can J Physiol Pharmacol.* 2002;80:533–540.

14. Sheppard JD, Orenstein DM, Chao C, Butala S, Kowalski RP. The ocular surface in cystic fibrosis. *Ophthalmology*. 1989;96:1624–1630.
15. Ansari EA, Sahni K, Etherington C, et al. Ocular signs and symptoms and vitamin A status in patients with cystic fibrosis treated with daily vitamin A supplements. *Br J Ophthalmol*. 1999;83:688–691.
16. Morkeberg JC, Edmund C, Prause JU, Lanng S, Koch C, Michaelsen KF. Ocular findings in cystic fibrosis patients receiving vitamin A supplementation. *Graefes Arch Clin Exp Ophthalmol*. 1995;233:709–713.
17. Shi XP, Candia OA. Active sodium and chloride transport across the isolated rabbit conjunctiva. *Curr Eye Res*. 1995;37:927–935.
18. Klyce SD, Neufeld AH, Zadunaisky JA. The activation of chloride transport by epinephrine and DB cyclic-AMP in the cornea of the rabbit. *Invest Ophthalmol*. 1973;12:127–139.
19. Al-Nakkash L, Reinach PS. Activation of a CFTR-mediated chloride current in a rabbit corneal epithelial cell line. *Invest Ophthalmol Vis Sci*. 2001;42:2364–2370.
20. Shiue MH, Kim K-J, Lee VHL. Modulation of chloride secretion across the pigmented rabbit conjunctiva. *Exp Eye Res*. 1998;66:275–282.
21. Murakami T, Fujihara T, Horibe Y, Nakamura M. Diquafosol elicits increases in net Cl^- transport through P2Y2 receptor stimulation in rabbit conjunctiva. *Ophthalmic Res*. 2004;36:89–93.
22. Li Y, Kuang K, Yerxa B, Wen Q, Rosskothén H, Fischbarg J. Rabbit conjunctival epithelium transports fluid and P2Y2(2) receptor agonists stimulate Cl^- and fluid secretion. *Am J Physiol*. 2001;281:C595–C602.
23. Galiotta LJ, Springsteel MF, Eda M, et al. Novel CFTR chloride channel activators identified by screening of combinatorial libraries based on flavone and benzoquinolizinium lead compounds. *J Biol Chem*. 2001;276:19723–19728.
24. Ma T, Vetrievel L, Yang H, et al. High-affinity activators of cystic fibrosis transmembrane conductance regulator (CFTR) chloride conductance identified by high-throughput screening. *J Biol Chem*. 2002;277:37235–37241.
25. Levin MH, Verkman AS. Aquaporin-dependent water permeation at the mouse ocular surface: in vivo microfluorometric measurements in cornea and conjunctiva. *Invest Ophthalmol Vis Sci*. 2004;45:4423–4432.



26. Ma T, Thiagarajah JR, Yang H, et al. Thiazolidinone CFTR inhibitor identified by high-throughput screening blocks cholera toxin-induced intestinal fluid secretion. *J Clin Invest.* 2002;110:1651–1658.
27. Muanprasat C, Sonawane ND, Salinas DB, Taddei A, Galietta LJ, Verkman AS. Discovery of glycine hydrazide pore-occluding CFTR inhibitors: mechanism, structure-activity analysis and in vivo efficacy. *J Gen Physiol.* 2004;124:125–137.
28. Salinas DB, Pedemonte N, Muanprasat C, Finkbeiner WF, Nielson DW, Verkman AS. CFTR involvement in nasal potential differences in mice and pigs studied using a thiazolidinone CFTR inhibitor. *Am J Physiol.* 2004;287:L963–L943.
29. Brady KG, Kelley TJ, Drumm ML. Examining basal chloride transport using the nasal potential difference response in a murine model. *Am J Physiol.* 2001;281:L1173–L1179.
30. Rozmahel R, Gyomerey K, Plyte S, et al. Incomplete rescue of cystic fibrosis transmembrane conductance regulator deficient mice by the human CFTR cDNA. *Hum Mol Genet.* 1997;6:1153–1162.
31. Delaney SJ, Alton EW, Smith SN, et al. Cystic fibrosis mice carrying the missense mutation G551D replicate human genotype-phenotype correlations. *EMBO J.* 1996;15:955–963.
32. Thiagarajah JR, Broadbent T, Hsieh E, Verkman AS. Prevention of toxin-induced intestinal ion and fluid secretion by a small-molecule CFTR inhibitor. *Gastroenterology.* 2004;126:511–519.
33. Kimura K, Nishimura T, Satoh Y. Effects of ATP and its analogues on $[Ca^{2+}]_i$ dynamics in the rabbit corneal epithelium. *Arch Histol Cytol.* 1999;62:129–138.
34. Maurice DM. Epithelial potential of the cornea. *Exp Eye Res.* 1967;6:138–140.
35. Maurice DM. Electrical potential and ion transport across the conjunctiva. *Exp Eye Res.* 1973;15:527–532.
36. Klyce SD. Electrical profiles in the corneal epithelium. *J Physiol.* 1972;226:407–429.
37. Tarran R, Loewen ME, Paradiso AM, et al. Regulation of murine airway surface liquid volume by CFTR and Ca^{2+} -activated Cl^- conductances. *J Gen Physiol.* 2002;120:407–418.
38. Gilbard JP, Rossi SR, Heyda KG, Dartt DA. Stimulation of tear secretion and treatment of dry-eye disease with 3-isobutyl-1-methylxanthine. *Arch Ophthalmol.* 1991;109:672–676.

39. Gilbard JP. Treatment of keratoconjunctivitis sicca in rabbits with 3-isobutyl-1-methylxanthine. *Arch Ophthalmol*. 1994;112:1614–1616.
40. Marshall WS, Klyce SD. Cellular and paracellular pathway resistance in the "tight" Cl-secreting epithelium of rabbit cornea. *J Membr Biol*. 1983;73:275–282.
41. Midelfart A. The effects of amiloride, ouabain, and osmolality on sodium transport across bovine cornea. *Pflügers Arch*. 1987;408:243–248.
42. Midelfart A. The effect of amiloride on Na, K, and water in bovine corneal epithelium. *Exp Eye Res*. 1987;45:751–762.
43. Mirshahi M, Nicolas C, Mirshahi S, Golestaneh N, d'Hermies F, Agarwal MK. Immunochemical analysis of the sodium channel in rodent and human eye. *Exp Eye Res*. 1999;69:21–32.
44. Wolosin JM, Candia OA. Cl⁻ secretagogues increase basolateral K⁺ conductance of frog corneal epithelium. *Am J Physiol*. 1987;253:C555–C560.
45. Candia OA, Zamudio AC. Cl secretagogues reduce basolateral K⁺ permeability in the rabbit corneal epithelium. *J Membr Biol*. 2002;190:197–205.
46. Horisberger JD. ENaC-CFTR interactions: the role of electrical coupling of ion fluxes explored in an epithelial cell model. *Pflügers Arch*. 2003;445:522–528.
47. Schreiber R, Hopf A, Mall M, Greger R, Kunzelmann K. The first-nucleotide binding domain of the cystic-fibrosis transmembrane conductance regulator is important for inhibition of the epithelial Na⁺ channel. *Proc Natl Acad Sci USA*. 1999;96:5310–5315.

Table 1

Composition of Perfusate Solutions (mM)

Solution	Name	Cl⁻	gluconate	HCO₃⁻
1	Control	160.0	0	0
2	Low Cl ⁻	4.7	155	0
3	Bicarbonate	135.0	0	25

All solutions contained (in mM): 170 Na⁺, 4.2 K⁺, 9.5 phosphate, 1 Ca²⁺, 0.5 Mg²⁺ (pH 7.40).

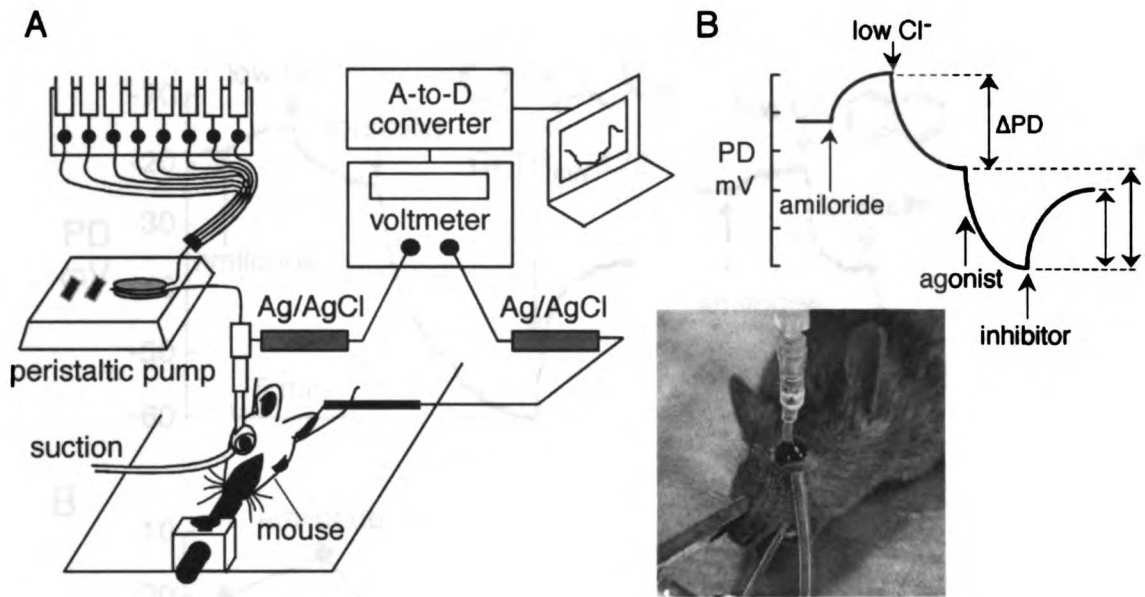


Figure 1

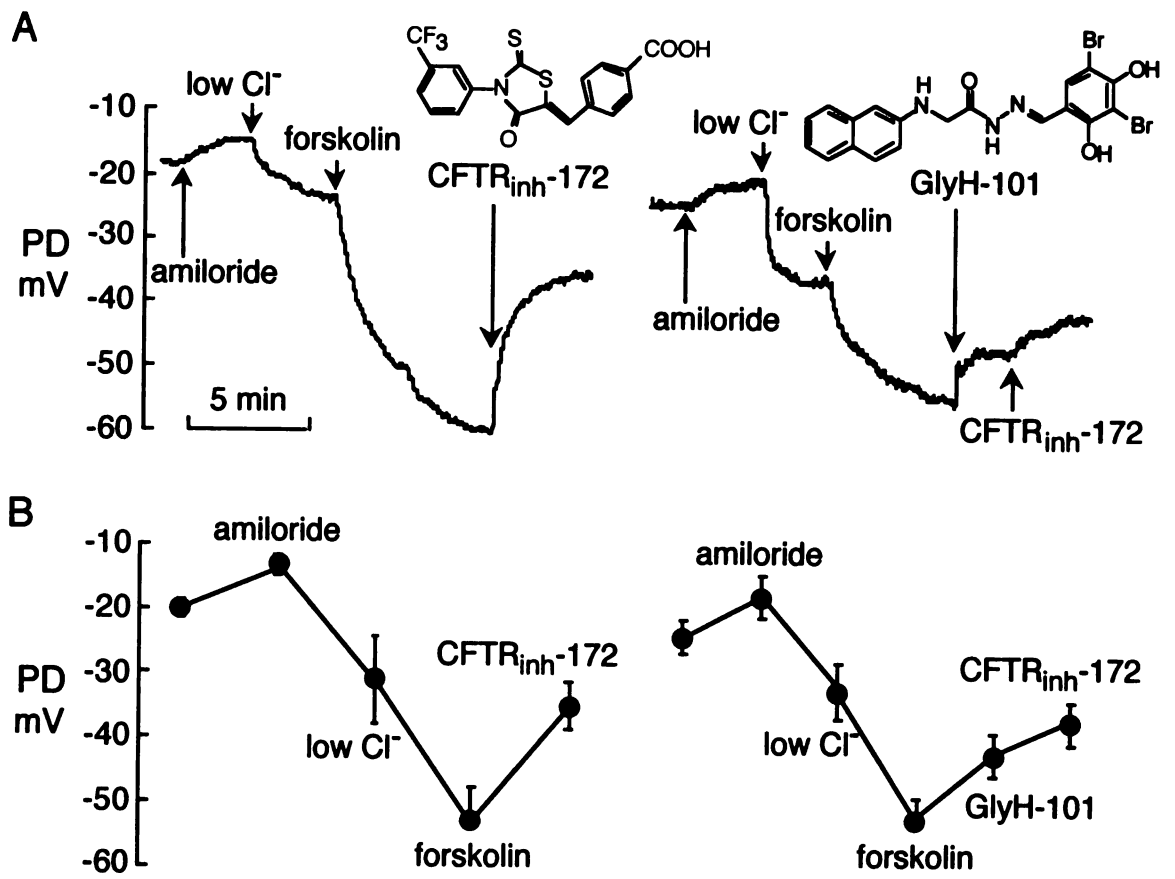


Figure 2

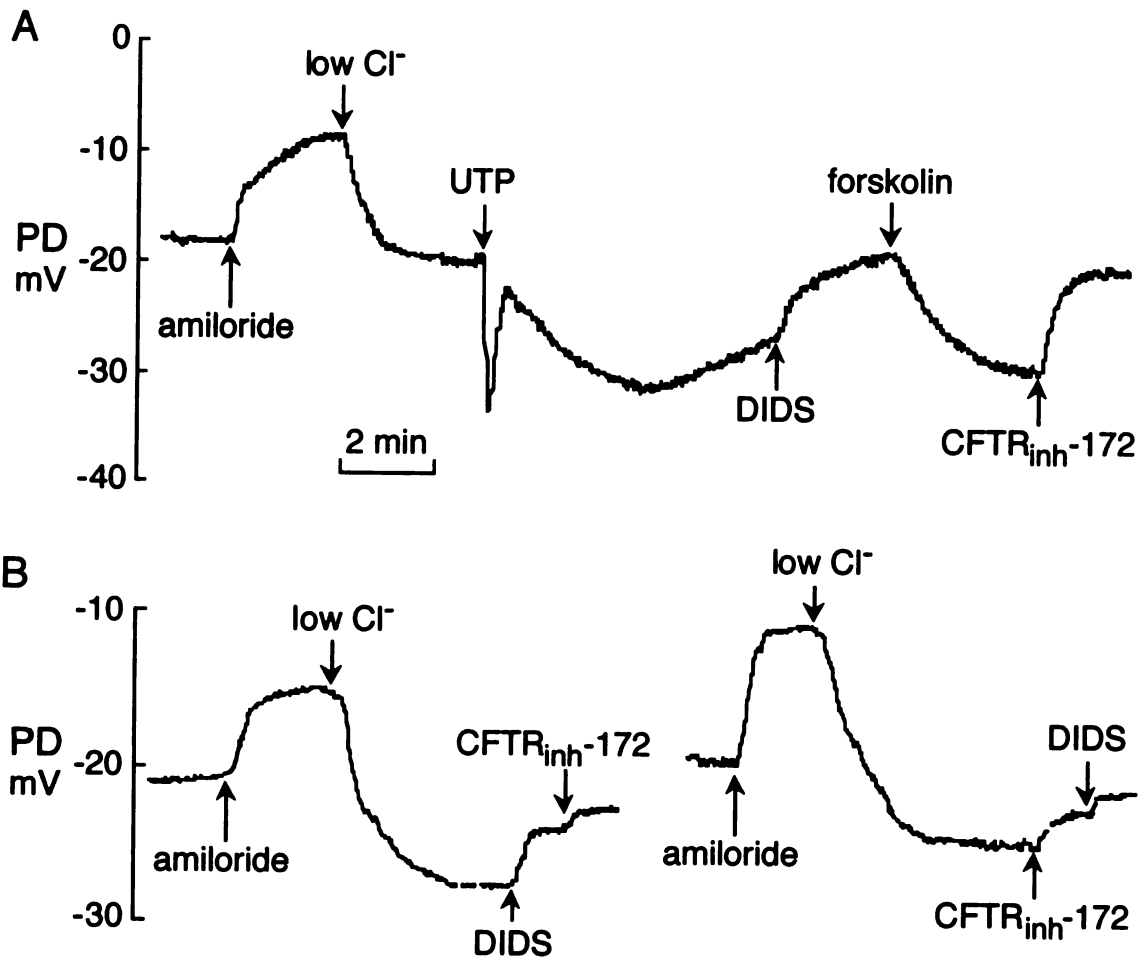
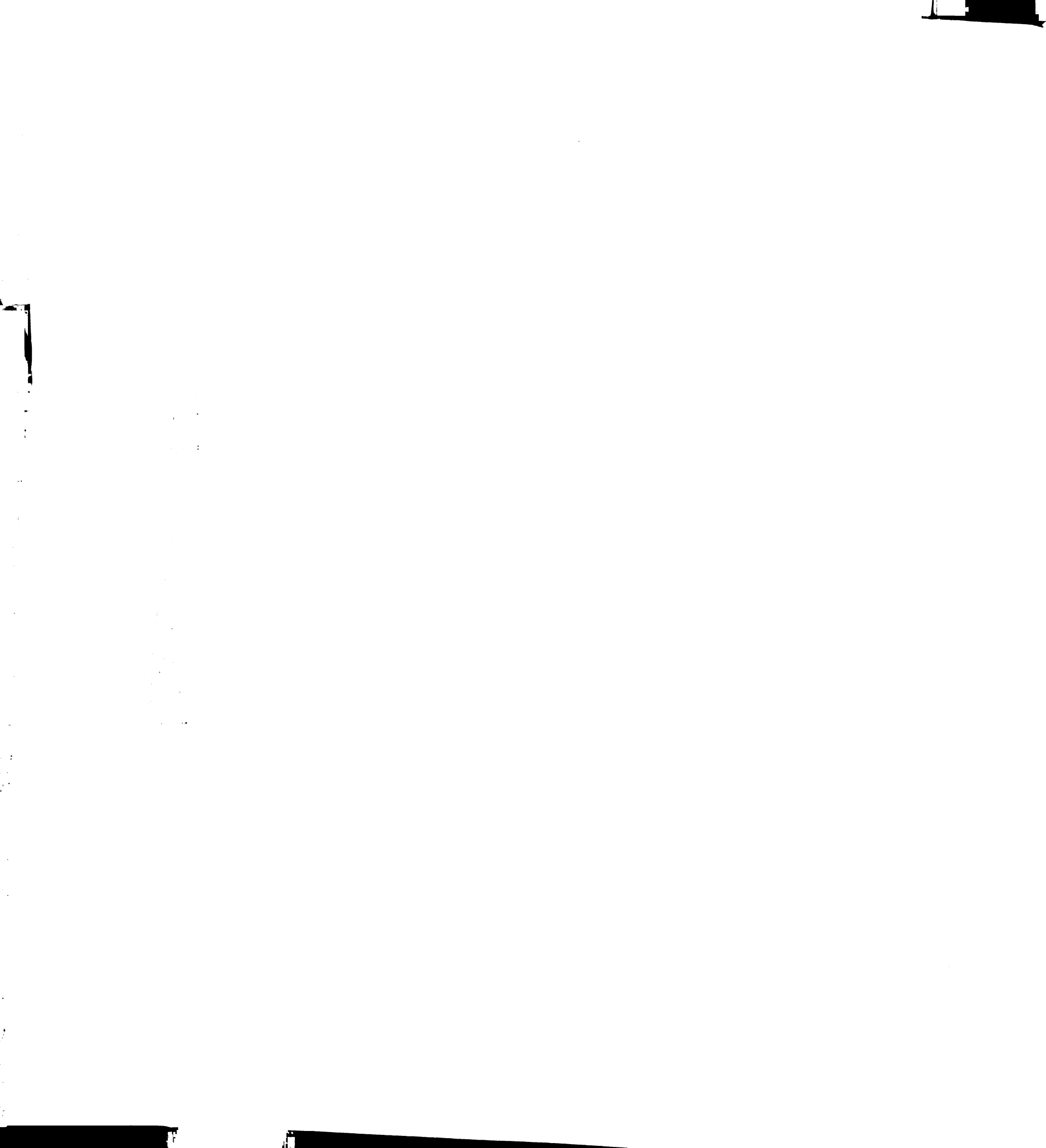


Figure 3



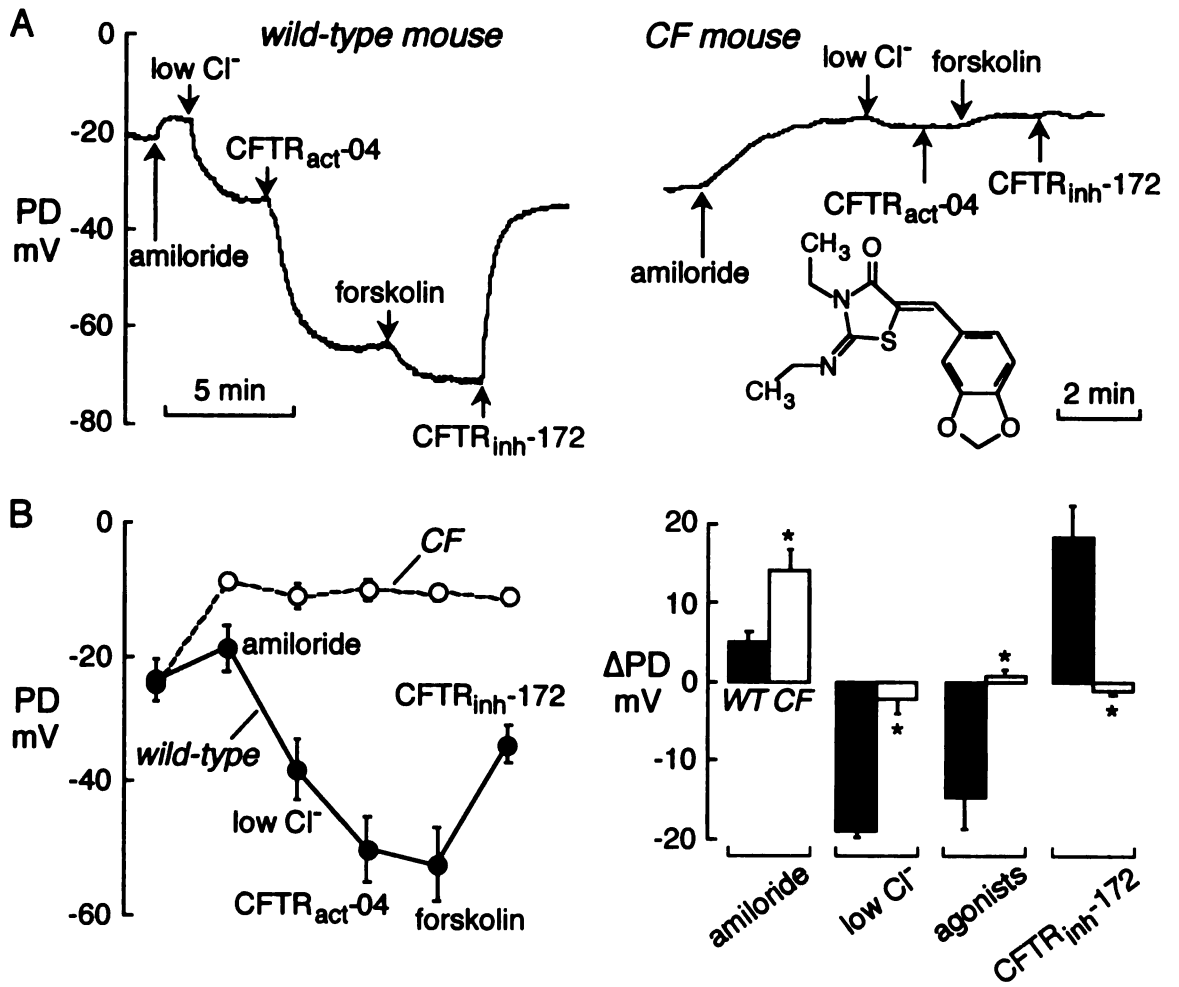


Figure 4

Figure Legends

FIGURE 1. Schematic of ocular surface perfusion and PD recording methods. (A)

Anesthetized mouse immobilized in a stereotaxic platform with PE-90 tubing (attached to perfusion and electrical recording systems) immersed in solution contacting the ocular surface. *Inset:* Photograph of perfused ocular surface. (B) Ocular surface PD recordings showing PD changes after sequential solution exchanges. Typical protocol for studying Cl^- transport, with perfusates containing amiloride, low Cl^- , agonists, and inhibitors. PD changes (ΔPD) shown as used for statistical comparisons.

FIGURE 2. CFTR inhibitors reverse cAMP-dependent ocular surface Cl^- conductance. (A)

Representative PD recordings showing responses to amiloride, low Cl^- , forskolin, and CFTR_{inh}-172 (*left*) or GlyH-101 before CFTR_{inh}-172 (*right*). Solutions used: 1 alone, 1+amiloride, 2+amiloride, 2+amiloride+forskolin, and 2+amiloride+forskolin+CFTR inhibitor. Inhibitor chemical structures are shown. Concentrations: amiloride, 100 μM ; forskolin, 10 μM ; CFTR_{inh}-172, 10 μM ; GlyH-101, 20 μM . (B) PDs (mean \pm SE, $n = 8$ [left] and $n = 4$ [right] mice) measured from experiments as in (A).

FIGURE 3. Purinergic-stimulated and agonist-independent ocular surface Cl^- conductance.

(A) PD recording showing responses to amiloride, low- Cl^- , UTP (10 μM), DIDS (200 μM), forskolin, and CFTR_{inh}-172 (10 μM). Representative of eight experiments.

Solutions used: 1 alone, 1+amiloride, 2+amiloride, 2+amiloride+UTP,

2+amiloride+UTP+DIDS, 2+amiloride+UTP+DIDS+forskolin, and

2+amiloride+UTP+DIDS+forskolin+CFTR_{inh}-172. (B) PD recordings showing effects of

DIDS and CFTR_{inh}-172 (added in different orders) in the absence of agonists.

Representative of eight experiments. Solutions used: 1 alone, 1+amiloride, 2+amiloride, 2+amiloride+DIDS or CFTR_{inh}-172, and 2+amiloride+DIDS+CFTR_{inh}-172.

FIGURE 4. Reduced ocular surface Cl⁻ conductance in CF mice. (A) PD recordings in wild-type (*left*) and CF (*right*) mice in response to amiloride, low-Cl⁻, CFTR_{acr}-04 (10 μM), forskolin (2 μM), and CFTR_{inh}-172 (10 μM). *Inset:* CFTR_{acr}-04 structure. Solutions used: 1 alone, 1+amiloride, 2+amiloride, 2+amiloride+CFTR_{acr}-04, 2+amiloride+CFTR_{acr}-04+forskolin, 2+amiloride+CFTR_{acr}-04+forskolin+CFTR_{inh}-172. (B, *left*) PD (mean ± SE) measured after indicated maneuvers from experiments as in (A). (•) Wild-type mice (*n* = 7); (●) CF mice (*n* = 3). *Right:* Paired analysis of ΔPD for wild-type and CF mice for indicated maneuvers. **P* < 0.01 comparing wild-type versus CF mice.

CHAPTER 5.

Potential Difference Measurements of Ocular Surface

Na⁺ Absorption Analyzed

Using an Electrokinetic Model

Abstract

PURPOSE. Corneal and conjunctival epithelia are capable of transcellular Na⁺ absorption and Cl⁻ secretion, which drives water movement across these tissues. A recent study demonstrated with a new open-circuit potential difference (PD) technique that Cl⁻ moves across the ocular surface in mice through Ca²⁺- and cAMP-sensitive Cl⁻ channels, the latter pathway being the cystic fibrosis (CF) transmembrane conductance regulator (CFTR). The purpose of the present study was to identify transporting mechanisms involved in Na⁺ absorption and to develop a mathematical model of ocular surface ion transport to quantify the relative magnitudes of and electrochemical coupling among transporting processes.

METHODS. PDs across the fluid-bathed ocular surface were measured in anesthetized wild-type and CF mice in response to Na⁺, Cl⁻, and K⁺ ion substitution and transporter agonists, inhibitors, and substrates. An electrokinetic model of the ocular surface epithelium was developed to simulate PD measurements, which involved computation of membrane potentials and cell [Na⁺], [K⁺], [Cl⁻] and volume from transporter activities and extracellular ion concentrations.

11
12
13
14
15
16
17
18
19
20
21
22
23
24
25
26
27
28
29
30
31
32
33
34
35
36
37
38
39
40
41
42
43
44
45
46
47
48
49
50
51
52
53
54
55
56
57
58
59
60
61
62
63
64
65
66
67
68
69
70
71
72
73
74
75
76
77
78
79
80
81
82
83
84
85
86
87
88
89
90
91
92
93
94
95
96
97
98
99
100

RESULTS. Na^+ replacement produced a 6 ± 2 -mV depolarization that was blocked by amiloride (K_i 0.8 μM) and benzamil (K_i 0.2 μM). The Na^+ -dependent depolarization by amiloride was significantly greater in CF mice (19 ± 3 mV). In wild-type mice, D-, but not L-glucose produced a phloridzin-sensitive, 4.1-mV hyperpolarization in the presence of Na^+ and amiloride, with a K_m for D-glucose of 2.5 mM. Glycine and L-arginine also produced Na^+ -dependent hyperpolarizations. The epithelial transport model accurately reproduced experimental PD measurements.

CONCLUSIONS. PD measurements coupled with model computations defined quantitatively the roles of Na^+ and Cl^- transport processes in ocular surface ion and fluid secretion, and indicated that CFTR-dependent changes in apparent epithelial Na^+ channel (ENaC) activity could be accounted for by electrochemical coupling, without requiring ENaC-CFTR interactions. The data and modeling also predicted significant enhancement of ocular surface fluid secretion by ENaC inhibitors and CFTR activators as possible therapies for dry eye syndromes.

The ocular surface, lined by corneal and conjunctival epithelia, can actively absorb Na^+ from and secrete Cl^- into the tear film (reviewed by Dartt¹ and Candia²). The relative magnitudes of net Na^+ absorption and Cl^- secretion largely dictate the direction and magnitude of fluid movement across the ocular surface. A quantitative, mechanistic understanding of ocular surface ion transport is important in understanding the pathophysiology of dry eye conditions, or keratoconjunctivitis sicca (KCS), and in identifying targets for development of therapies to treat KCS. At present, INS365, a uridine triphosphate (UTP) agonist that stimulates chloride-fluid secretion through as yet

unidentified channels, is in phase III clinical trials for treatment of KCS.³ The purpose of this study was to establish, through experimental electrical potential measurements and mathematical modeling, a quantitative description of ion transport at the ocular surface.

We recently introduced an open-circuit potential difference (PD) method to study ion transport at the ocular surface *in vivo*.⁴ In this method, electrical potentials generated at the superfused ocular surface (with respect to the body) are measured by a high-impedance voltmeter in response to ion substitution, agonist-inhibitor addition, or other maneuvers. Surface PDs arise from polarized ion conductances in apical and basolateral membranes across tight epithelia and so can provide, in principle, quantitative information about electrogenic transporting systems. The corneal and conjunctival surfaces are superfused as a single compartment in this method to mimic native tear film physiology, allowing assessment of the relative contributions of individual transporters to tear film homeostasis. In our initial study, CFTR was identified as a major route for Cl⁻ secretion across the ocular surface into the tear film, and CFTR activators were proposed as a possible therapy for dry eye conditions.

In the current study, we extend the initial experimental analysis of ocular surface Cl⁻ transport to include Na⁺-transporting mechanisms and, by mathematical modeling, to assess the contributions of individual ion transporting pathways to net solute and fluid movement across the ocular surface. Prior experimental data with regard to Na⁺ channels include short-circuit current experiments on *in vitro* albino rabbit cornea and conjunctiva, where amiloride-sensitive Na⁺ conductance could not be demonstrated.^{5,6} However, short-circuit measurements on excised bovine cornea,⁷ and more recently on primary cultures of

rabbit corneal epithelium,⁸ have provided functional evidence for amiloride-sensitive channels. Of potential relevance to human ocular disorders, the epithelial Na⁺ channel (ENaC) subunit proteins have been localized to the apical membrane of human corneal epithelium.⁹

In this study, ocular surface PDs were used to identify and characterize Na⁺ channel and Na⁺-coupled glucose- and amino acid-transporting pathways at ocular surface epithelia in living mice. A model of ocular surface epithelial ion transport was developed to compare quantitatively the rates of Na⁺ absorption versus Cl⁻ secretion and to analyze mechanisms of proposed coupling between CFTR and ENaC.^{10,11} Modeling computations were applied to test the hypotheses that ENaC provides a quantitatively significant mechanism for ocular surface fluid transport that may be exploited for therapy of KCS and that enhanced Na⁺ absorption in CF mice can be accounted for by CFTR-ENaC electrochemical coupling. The mathematical model describing ocular surface epithelial transport is an extension of prior models developed by our laboratory and others for non-ocular epithelial ion transport.^{12,13,14} Figure 1 diagrams the transporting systems and pathways included in the model. The model allowed the computation of epithelial cell membrane potentials and currents, transepithelial water flow, and cellular [Na⁺], [K⁺], [Cl⁻] and volume in response to experimental maneuvers such as transporter activation-inhibition and ion substitution. Although such an epithelial transport model contains multiple parameters, constraints imposed by experimental observations allowed little freedom in selecting model parameters. The model was able to reproduce experimental findings closely and to provide quantitative information and insights not otherwise possible.

Methods

Mice

Wild-type and CF mice (homozygous $\Delta F508$ mutant mice)¹⁵ on a CD1 genetic background were bred and cared for at the University of California, San Francisco, Animal Facility. Wild-type mice were fed a standard diet, and CF mice were fed a nutritional supplement (Peptamen; Nestlé, Vevey, Switzerland). Mice aged 8 to 12 weeks weighing 25 to 30 g were used. Protocols were approved by the University of California, San Francisco, Committee on Animal Research and were in compliance with the ARVO Statement for the Use of Animals in Ophthalmic and Vision Research.

Mice were anesthetized with 125 mg/kg 2,2,2-tribromoethanol (Avertin; Sigma-Aldrich, St. Louis, MO) intraperitoneally, with supplementation during experiments to maintain deep anesthesia. Mice were immobilized, with the eye under study oriented to face upward in a custom-built stereotaxic device equipped with a rotating jaw clamp. Corneas were kept hydrated with isosmolar saline (PBS with NaCl added to give 320 mOsM) before measurements began. Core temperature was monitored with a rectal probe and maintained at $37 \pm 1^\circ\text{C}$ with a heating pad.

Measurement of Ocular Surface PD

PD was measured continuously, with the ocular surface perfused serially with different solutions, as described in detail previously.⁴ Briefly, solutions were perfused at 6 mL/min through plastic tubing using a multireservoir gravity pinch-valve system (ALA

Scientific, Westbury, NY) and a variable-flow peristaltic pump (medium flow model; Fisher Scientific, Fair Lawn, NJ). An ~50- μ L fluid reservoir was maintained at the ocular surface by surface tension, with the probe catheter (PE-90 polyethylene tubing) fixed ~1 mm from the eye surface by a micropositioner and a suction cannula positioned ~3 mm from the orbit. Solution exchange time was generally less than 3 seconds. The measuring and reference electrodes consisted of Ag/AgCl with 1-M KCl agar bridges. The measuring electrode was located near the catheter probe and connected to a high-impedance digital voltmeter (IsoMillivolt Meter; World Precision Instruments, Sarasota, FL), having input and system electrical resistances of 10^{12} and $1.1 \times 10^6 \Omega$, respectively. The reference electrode was connected via a continuous liquid (320 mOsM saline) column to a winged, 21-gauge needle inserted in the subcutaneous tissue at the back of the neck. PDs were recorded at 5 Hz with a 14-bit analog-to-digital converter.

Solutions and Compounds

All perfusion solutions were isosmolar to mouse serum (320 ± 5 mOsM) as measured by freezing point-depression osmometry (Precision Systems, Natick, MA). Solution compositions are listed in Table 1. Solution 1 (control solution) was PBS supplemented with 30 mOsM NaCl. Solution 2 (Na^+ -free solution) was made by replacing NaCl with choline chloride and Na_2HPO_4 with 8 mM phosphoric acid, titrating to pH 7.4 with choline base and then adding choline chloride to achieve 320 mOsM. In some experiments, NaCl was replaced isosmotically with 30 mM D-glucose, L-glucose, or D-mannitol (solution 3). In solution 4, choline chloride (from solution 3) was replaced isosmotically with 30 mM D-glucose or D-mannitol. Solutions 1 and 3 or 2 and 4 were

mixed to give solutions of intermediate organic solute concentrations. In solution 5 (low Cl^- solution; 4.7 mM Cl^-), most Cl^- was replaced by gluconate. Solution 6 (high- K^+ solution; 174.2 mM K^+) differed from solution 1 in that NaCl and Na_2HPO_4 were replaced by equimolar amounts of KCl and K_2HPO_4 . Whereas Cl^- replacement produced a small junction potential (generally $\sim +1$ mV) that was measured daily and used to correct PDs measured with low- Cl^- perfusates, Na^+ -free and high- K^+ solutions did not produce junction potentials.

Compounds were purchased from Sigma-Aldrich unless indicated otherwise. Inhibitors, activators, and substrates used in the perfusates included amiloride or benzamil (0.1–100 μM), phloridzin (100 μM), forskolin (10 μM), and L-arginine or glycine (0.1–10 mM, freshly dissolved in perfusate). CFTR_{inh}-172 (3-[(3-trifluoromethyl)phenyl]-5-(3-carboxyphenyl) methylene]-2-thioxo-4-thiazolidinone; 10 μM) was synthesized as described.¹⁶ In protocols in which solution 5 (low- Cl^- solution) was used, all solutions contained 10 μM indomethacin to suppress CFTR activation by mechanical or other stimulation under control (unstimulated) conditions, as discussed previously.⁴ Inhibitors-activators were prepared as 1000x stock solutions in dimethyl sulfoxide (DMSO), unless otherwise indicated.

PD Protocols and Data Analysis

Na^+ transport was studied by measuring PDs during continuous perfusion of the ocular surface with a series of solutions that imposed Na^+ gradients and contained transporter substrates and/or inhibitors. Cl^- channel function was assessed with protocols described previously.⁴ Data are expressed as the mean \pm SE of absolute PDs or changes in

PD (Δ PD), and statistical comparisons between groups were made with the two-tailed Student's *t*-test.

Model Formulation

Overview

The model treats the ocular surface as an infinite, homogeneous monolayer of cells containing transcellular and paracellular solute transport pathways (Fig. 1). Programming was done using Visual Fortran (Compaq; Hewlett Packard, Palo Alto, CA). Intracellular solute activities, cell membrane potentials, and cell height (reflecting volume) were allowed to vary in time. Mucosal and serosal compartments consisted of infinite well-stirred solute pools with compositions that could be altered at specified time(s). Transporting systems for Na^+ , K^+ , and Cl^- were included in the model.

In ocular surface epithelia, the basolateral ouabain-sensitive $3\text{Na}^+/2\text{K}^+$ ATPase (transporter 7) establishes the electrochemical potential that drives electroneutral (bumetanide-inhibitable) $\text{Na}^+/\text{K}^+/2\text{Cl}^-$ symport (transporter 6). Na^+ can also enter cells through an amiloride-sensitive Na^+ channel (transporter 1), and organic solute-coupled cotransporters (transporter 2). Distinct glucose- and amino-acid transporters, assumed to be coupled 1:1 to Na^+ based on data from rabbit conjunctiva^{17,18} are represented in the model as a single " Na^+ -org" transporter. A neutral exit pathway for organic solutes is included that represents cellular efflux and/or utilization (transporter 9). Cl^- secretion occurs at the apical membrane through transporter 4, now known to be the cAMP-regulated Cl^- channel CFTR, as well as a Ca^{2+} -activated Cl^- channel (transporter 5). Apical and basolateral K^+ conductances are included as possible exit pathways for K^+

(transporters 3 and 8). Paracellular pathways for all charged species (transporters 10–14) are also included. Although cellular pH regulation may be important in cornea and conjunctiva, bicarbonate and proton transport pathways are not considered significant determinants of ocular surface fluid transport, as seen by the small, ~2-mV bicarbonate effect on ocular PD.⁴ As such, bicarbonate transport and Na⁺/H⁺ exchange pathways are not included in this model.

Parameters

Definitions and units of symbols are listed in Table 2. Transporter permeability coefficients were determined from open-circuit ion flux and membrane potential data (see Tables A1 and A2 in the Chapter 4 Appendix) deduced from measured ocular PDs and literature values, as explained in the Chapter 4 Appendix. Solute activities were related to absolute concentrations and osmotic activities according to intracellular and extracellular activity and osmotic coefficients, as listed in Table A3.

Solute flux (J_i^X) through each membrane and paracellular transport pathway was defined as a function of solute concentrations on each side of the membrane and, if electrogenic, a membrane potential. Electrodiffusive flux of solute X through the i th transport pathway was assumed to be nonsaturable and nonallosteric, unless otherwise noted, as given by the Goldman-Hodgkin-Katz equation:

$$J_i^X = P_i \cdot z_i \cdot U_z (X_1 - X_2 \cdot e^{-z_i \cdot U_i}) / (1 - e^{-z_i \cdot U_i}) \quad , \quad (1)$$

where P_i is the permeability coefficient (in centimeters per second), z_i is the ionic charge, and X_1 and X_2 are the activities of transported solute (in millimolar) in compartments to the left and right of the diffusive barrier, respectively. U_z , the dimensionless membrane potential, is related to the appropriate potential difference (ψ_z) in Table 2. Equations for flux through each transport pathway (J_i^X), and the resultant net apical, basolateral, and paracellular currents (I_a , I_b , and I_p) are provided in the Chapter 4 Appendix, Equation A1–A17).

Numerical Solution

Cell membrane potentials at time $(t + \Delta t)$ were calculated iteratively with the Newton-Raphson method based on electroneutral conditions. The open-circuit model requires equal opposing transcellular and paracellular currents ($I_a = I_b = -I_p$). An option was included to model transport under short-circuit conditions, where $I_a = I_b$ and $U_a = U_b$. U_a and U_b were computed iteratively by user-supplied initial guess. Assuming instantaneous osmotic equilibration and constant cell surface area, cell height $h(t + \Delta t)$ (in micrometers) was computed as

$$h(t + \Delta t) = h(t) + \Delta t \cdot \sum^{a-b} \phi_x \cdot J_i^X / \Psi_s \quad (2)$$

$\sum^{a-b} \phi_x J_i^X$ generically represents the net osmotic flux (in milliosmolar per square centimeter per second) into the cell and is related to individual transporter fluxes in equation A18. Ψ_s is mouse serum osmolarity (in milliOsmols per cubic centimeter).

1. The first part of the document discusses the importance of maintaining accurate records of all transactions and activities. It emphasizes that proper record-keeping is essential for ensuring transparency and accountability in financial reporting.

2. The second part of the document outlines the various methods and techniques used to collect and analyze data. It highlights the need for consistent and reliable data collection processes to support effective decision-making.

3. The third part of the document focuses on the analysis and interpretation of the collected data. It discusses the various statistical and analytical tools used to identify trends, patterns, and insights from the data.

4. The fourth part of the document addresses the challenges and limitations of data analysis. It acknowledges that while data analysis provides valuable insights, it is not without its own set of challenges and limitations.

5. The fifth part of the document concludes by summarizing the key findings and recommendations. It emphasizes the importance of ongoing monitoring and evaluation to ensure that the data analysis process remains effective and relevant over time.

Intracellular solute activities were computed from fluxes and the updated cell height from equation 2 according to

$$X(t + \Delta t) = [X(t) \cdot h(t) + \Delta t \cdot \sum a_x \cdot J_i^X] / h(t + \Delta t) \quad (3)$$

$\sum a_x J_i^X$ is defined as the net rate of entry of active solute X (in 10^4 meq/cm² per second) into the cellular compartment through the various transporters. Refer to equations A19–A22 for the specific expressions used in computing $Na^+(t + \Delta t)$, $K^+(t + \Delta t)$, $Cl^-(t + \Delta t)$, and $org(t + \Delta t)$. The model also offers the option to impose brief current or voltage spikes (one each minute) to compute total tissue resistance. The observed change in voltage or current can be used to monitor transepithelial electrical resistance (TEER, in kilo-ohms per square centimeter) under open- or short-circuit conditions, respectively ($TEER = \Delta \psi / \Delta I_a$). Though the exact mechanism of transepithelial fluid movement remains controversial, it is agreed that it results in near-isosmolar water flux driven by solute transport. As such, net transepithelial water secretion or absorption (microliters per square centimeter per hr) was computed assuming isosmolar fluid flow across the apical membrane and paracellular tight-junctional barrier by

$$J_v(t + \Delta t) = \sum^{a+p} \phi_x \cdot J_i^X / \Psi_s \quad (4)$$

where $\sum^{a+p} \phi_x J_i^X$ is the net osmotic flux (in milliOsmols per square centimeter per second) into the apical compartment from individual transport pathway fluxes (equation A23), and Ψ_s is serum osmolarity (in Osmols per liter).

Vertical text on the left margin, possibly a page number or page header, mostly illegible due to blurring and low resolution.

Faint vertical text located in the left margin, possibly a page number or page header, mostly illegible due to blurring and low resolution.

Results

Amiloride-Sensitive Na⁺ Transport

Na⁺ channel function was studied by using ion replacement and transporter substrates and inhibitors. Baseline PD was first established (using solution 1) before replacement of perfusate Na⁺ by the relatively impermeant cation choline (solution 2). This exchange produced a 5- to 10-mV depolarization that was reversed by reintroduction of Na⁺ (solution 1). Representative PD recordings in Figure 2A show the reversible changes in PD on Na⁺ substitution, depolarization by amiloride (100 μM) in the presence of a Na⁺-containing perfusate (left), and blocking of the Na⁺-induced hyperpolarization by amiloride (right). Dose-inhibition studies were performed for amiloride and its analogue, benzamil. A representative dose–response curve for amiloride is shown in Figure 2B (left). K_i was 0.82 μM for amiloride and 0.22 μM for benzamil (right). These data indicate the involvement of amiloride- and benzamil-sensitive Na⁺ channel(s) in ocular surface Na⁺ absorption, which is probably ENaC.

To determine the contribution of the other major cation K⁺ to apical electrogenic transport, experiments were performed using a high-K⁺ solution (solution 6). Amiloride was first added to solution 1 to minimize the influence of Na⁺ channel function on interpretation of PDs in terms of K⁺ channel function. Switching to solution 6 produced a very small 1- to 2-mV reversible hyperpolarization (data not shown, $n = 5$ separate experiments). Model computations supported the conclusion that apical K⁺ conductance is much lower than apical Na⁺ or Cl⁻ conductance.

Ion Transport in CF Mice

Ocular surface Cl^- transport was assayed as described previously.⁴ Figure 3A shows PD data from wild-type versus CF mice in which baseline PDs (of similar values) were first recorded with solution 1. Switching to an amiloride-containing solution depolarized ocular surface PDs, with CF mice showing a significantly greater response (15–20 mV in CF vs. 5–10 mV in wild-type mice). Replacing most Cl^- by the relatively impermeant anion gluconate (solution 5) gave a sustained hyperpolarization in wild-type but not CF mice, which is related to cAMP- but not CFTR-independent Cl^- secretion. The CFTR agonist forskolin produced a further hyperpolarization in wild-type mice that was reversed by CFTR_{inh}-172.

The protocol used in Figure 2A was applied to investigate amiloride-sensitive Na^+ conductance in CF mice. Representative PD recordings in Figure 3B (left) show reversible depolarizations in wild-type and CF mice in response to Na^+ substitution. Depolarizations of similar magnitude were produced by amiloride (100 μM) in the presence of Na^+ -containing perfusate. The CF mice consistently showed greater responses than wild-type mice to both Na^+ replacement and amiloride addition. As summarized in Figure 3B (right), Na^+ replacement and amiloride administration produced ΔPDs of 20 ± 3 and 19 ± 2 mV, (SE, $n = 6$) in CF mice, respectively. The same maneuvers produced 6 ± 2 - and 7 ± 1 -mV depolarizations in wild-type mice ($n = 6$). These results indicate the presence of an amiloride-sensitive Na^+ channel at the ocular surface, with apparent increased activity in CF mice.

Modeling Ocular Surface Na⁺ and Cl⁻ Transport

The PD measurements suggest that active Na⁺ and Cl⁻ transport processes dictate net fluid movement across corneal-conjunctival epithelia, and comparative experiments performed on wild-type versus CF mice suggest a complex interaction among these pathways. As such, we developed a model to gain better qualitative understanding and to define quantitatively the key determinants of active ocular surface fluid secretion.

According to the model in Figure 1 with parameters for the ocular surface of wild-type mice selected as described in the Chapter 4 Appendix, Figure 4A shows the time course of the major cellular variables in mice after "inhibition" (by amiloride) of transporter 1 (ENaC conductance). Before inhibition, all parameters were stable to within 0.01% for a 60-minute simulation (not shown). The top graph shows the time-dependent apical, basolateral, and transepithelial potentials (ψ_a , ψ_b , and PD). Conductances were chosen to give a baseline PD of -23 mV and a ratio of active Na⁺ to Cl⁻ flux of 1:1, which produced a 5.5-mV amiloride-induced PD depolarization. The second graph shows total transepithelial current before and after amiloride. The steady-state current of 8.0 $\mu\text{A}/\text{cm}^2$ was reduced by 22% by ENaC inhibition. The current spikes produced by the periodic brief voltage spikes gave a baseline TEER of 5.3 $\text{k}\Omega/\text{cm}^2$, which increased to 6.8 $\text{k}\Omega/\text{cm}^2$ after amiloride addition. The bottom two panels in Figure 4A show the influence of apical Na⁺ conductance on the three major intracellular ions and cell height. There was a small decrease in cell height consequent to reduced cellular Na⁺. Secondly enhanced transport of K⁺ into the cell produced a small 0.4% final increase in cell height. In

general, each cell parameter reached a new steady state within minutes after inhibition of transporter 1.

Figure 4B shows the time-dependent PD response in open-circuit conditions after a series of maneuvers commonly used to elucidate transport mechanisms. As seen in the top graph, simulated Na^+ replacement by choline yielded a depolarization similar to the experimental findings in Figures 2A and 3B. The immediate and sustained hyperpolarization of 9.5 mV predicted on replacing most apical Cl^- with gluconate (solution 1 switched to solution 5) also replicated experimental trends. The bottom two panels predict the time course of PD reduction toward zero after basolateral inhibition of the lone source of cellular Cl^- , the $\text{Na}^+/\text{K}^+/\text{2Cl}^-$ symporter (transporter 6), and the transepithelial current generator, the $3\text{Na}^+/\text{2K}^+$ ATPase (transporter 7). Because the electroneutral $\text{Na}^+/\text{K}^+/\text{2Cl}^-$ symporter lacks a membrane-potential dependence, no immediate change in PD was present on its inhibition.

The main findings from ocular PD experiments were modeled. In Figure 5A, the protocol for studying chloride transport was simulated, with initial ENaC inhibition, followed serially by switching to a low- Cl^- solution, addition of a CFTR activator, and then addition of a CFTR inhibitor. This simulation resembled experimental PD data (as in Fig. 3A, top) with one exception. Simulated instantaneous Cl^- channel activation yielded a significant transient hyperpolarization followed by more modest sustained hyperpolarization. Such PD behavior is not seen experimentally in response to either forskolin or direct CFTR activators, but is observed after addition of UTP.⁴ Of note, incorporating rectification into the basolateral K^+ channel (transporter 8) conductance (as

described by Horsberger¹¹) did not alter this general behavior. To mimic the finite solution exchange time and the noninstantaneous time course of CFTR activation after addition of the agonist, an additional simulation was performed in which apical chloride conductance was increased to the same extent, but over 4 minutes (not shown). The slower channel activation blunted much of the transient hyperpolarization, but did not change steady state PD.

Direct CFTR activators and the general cAMP agonist forskolin have been found to elicit nearly identical diffusion potentials under low-Cl⁻ conditions.⁴ To test whether isolated CFTR activation can be predicted to enhance apical Cl⁻ secretion in a manner similar to forskolin, simulations were performed in which basolateral K⁺ (transporter 8) conductance was activated to various degrees along with CFTR. Indeed, only a small augmentation of CFTR-activator-induced hyperpolarization could be achieved by concurrent stimulation of basolateral K⁺ conductance (-35.4-mV PD after threefold CFTR and K⁺ channel activation vs. -34.4 mV for CFTR activation alone, not shown). These findings have implications regarding strategies of pharmacological modulation of fluid secretion (see the Discussion section).

The simulation in Figure 5B focused on the difference in amiloride effect in wild-type versus CF mice (as seen in Figs. 3A, 3B) and the possibility of CFTR-ENaC interactions. Model parameters for wild-type and CF mice were chosen to yield identical baseline PDs of -23 mV, as reported previously⁴ and depicted in Figure 3B. Apical Cl⁻ permeability in CF mice was chosen to be 20% of that in wild-type mice, to recapitulate the observed amiloride effect in CF mice whereas Na⁺ conductance was fixed to that in

wild-type mice. As seen in Figure 5B, PD depolarized by 14.5 mV upon ENaC inhibition in CF mice, similar to that measured in Figure 3B. Switching the apical compartment to a low-Cl⁻ solution (solution 5) correctly predicted a small diffusion potential of 2.1 mV in CF mice, compared with the 8.7-mV hyperpolarization in wild-type mice. Simulations were also performed in which ENaC permeability was increased twofold (using parameters from CF or wild-type mice), examining effects of ENaC inhibition and low-Cl⁻ substitution. ENaC inhibition yielded depolarizations of 19 and 10 mV with CF and wild-type parameters, respectively, and hyperpolarizations of 4.1 and 8.8 mV for low Cl⁻. In both cases, ENaC hyperactivity produced substantial low-Cl⁻ effects, which was inconsistent with experimental findings. Of importance, the model reproduced the major ocular surface electrophysiological properties in wild-type and CF mice only in the absence of CFTR-dependent ENaC conductance (see the Discussion section).

By assuming isosmolar fluid secretion, implying fixed coupling between transepithelial solute and water transport, we also modeled the ability of transporter modulators to increase transepithelial water secretion. Computations were performed under physiological conditions (in the absence of transepithelial ionic gradients) to simulate compound action on fluid secretion into the native tear film. Figure 5C shows that both ENaC inhibition and CFTR activation increased net fluid secretion by inhibiting Na⁺ absorption and enhancing Cl⁻ secretion, respectively, and that the effects were additive.

Organic Solute-Coupled Na⁺ Transport

In addition to amiloride-sensitive Na⁺ channels, electrogenic Na⁺ transport across the ocular surface, and thus fluid secretion, may also involve Na⁺-glucose and Na⁺-amino acid cotransport. Figure 6A (left) shows that isosmolar addition of D-glucose but not of D-mannitol produced a small hyperpolarization that was reversed by the Na⁺-glucose cotransporter inhibitor phloridzin. L-Glucose (5 mM) produced no significant change in PD (data not shown, $n = 4$ eyes). Under physiological conditions of high apical Na⁺ concentration, extracellular D-glucose saturability (K_m) was 2.5 mM as measured from PDs at increasing concentrations of D-glucose (Fig. 6A, middle and right). Hill analysis gave a D-glucose-Na⁺ coupling ratio of 0.89, consistent with 1:1 Na⁺-glucose cotransport. The PD data in Figure 6A were modeled to determine the turnover rates of transporters 2 and 9 (see Chapter 4 Appendix for explanation of parameter selection). Modeling of the experimentally measured ~4-mV hyperpolarization under conditions of saturated cotransport and tonic ENaC inhibition (Fig. 6B) indicated a J_2 (SGLT-1) turnover equal to ~75% of the J_1 (ENaC) basal activity (0.11 vs. 0.15 $\mu\text{eq}/\text{cm}^2$ per hr). Because SGLT-1 likely transports two solutes per turnover, this implies similar osmolar absorptive capacities of amiloride-insensitive and amiloride-sensitive pathways. The basic and neutral amino acids L-arginine and glycine also produced small, reversible hyperpolarizations in the presence of Na⁺ (Fig. 6C). Amino acid transport was saturated only at relatively high concentration (several mM) for both amino acids studied. L-Arginine and glycine, added at 10 mM, yielded hyperpolarizations of 1.5 ± 0.9 mV ($n = 4$, SE) and 2.1 ± 0.4 mV ($n = 5$), respectively. PD analysis also revealed competitive substrate binding, where addition of L-arginine to glycine-containing solution

reproducibly caused a depolarization (Fig. 6C, right). The Na^+ dependence of these electrogenic pathways of glucose and amino acid absorption was confirmed. Figure 6D (left) shows hyperpolarizations produced by 5 mM D-glucose and 1 mM L-arginine (but not mannitol) in the presence of Na^+ and amiloride. The hyperpolarizations were abolished after Na^+ replacement by choline. Averaged results are summarized in Figure 6D (right). Together, these results provide evidence for at least three distinct electrogenic Na^+ pathways at the ocular surface: amiloride-sensitive Na^+ channels, Na^+ -glucose cotransport, and Na^+ -amino acid cotransport.

Discussion

The goals of this study were to identify experimentally and to quantify by modeling the major Na^+ -transporting pathways at the ocular surface and to use experimental and modeling results to examine the roles of epithelial transporters in driving fluid secretion and putative CFTR-ENaC interactions. This approach provides a framework to define electrochemical coupling relevant to a variety of epithelial disorders, and for ocular surface epithelium, this approach allowed us to predict computationally the efficacy of therapies for states of tear deficiency. The PD measurement method is technically simple and permits minimally invasive in vivo measurements under physiological open-circuit conditions. The high-resistance epithelial surface, comprising cornea and conjunctiva in parallel, is responsible for generating and maintaining a large PD. The dependence of ocular PDs on specific Na^+ and Cl^- transport processes, combined with transport agonist-inhibitor and ion substitution maneuvers, allows for rapid qualitative assessment of solute transport in vivo. In this study, we extended the PD

measurement concept by developing a mathematical model to rigorously relate measured PDs to transporter permeabilities and transporting mechanisms.

A major role for amiloride-sensitive apical Na^+ absorption was found, which, according to the model, was equal in magnitude to total net Cl^- secretion. The inhibitory half-concentrations of amiloride (K_i , 0.82 mM) and benzamil (K_i , 0.22 mM) measured are in close agreement with those reported recently in primary cultures of pigmented rabbit corneal epithelial cells⁸ and are consistent with the greater potency of benzamil than amiloride for ENaC. Comparable depolarizations were observed for Na^+ replacement and amiloride application in both wild-type and CF mice, suggesting that amiloride-sensitive Na^+ conductance provides the primary route for apical membrane Na^+ transport under the experimental conditions (solution 1, which lacks D-glucose and amino acids). Modeling of fluid secretion in the absence of an ionic gradient predicted that Na^+ channel inhibition or CFTR Cl^- channel activation would increase fluid secretion into the tear film and that both together would provide an even greater benefit than either strategy alone.

In contrast to the large measured apical Na^+ conductance, a weak dependence of ocular surface PD on perfusate K^+ concentration was found in the presence of amiloride, indicating a relatively small apical surface K^+ conductance. Similar results were reported for human nasal epithelia.¹⁹ At steady state, basolateral K^+ channels enhance the electrochemical driving force for fluid secretion. However, modeling of PDs in this study predicted that increased basolateral K^+ conductance would augment apical Cl^- secretion little, suggesting that CFTR-specific activators would be as effective as general cAMP

agonists (which activate CFTR and some basolateral K^+ channels) in increasing apical chloride-driven fluid secretion.

Ocular surface PD measurements also provided direct evidence for transepithelial glucose- and amino acid-coupled Na^+ absorption. The kinetics of substrate activation for the Na^+ -glucose cotransporter (SGLT-1) varies widely among species.²⁰ Whereas tear Na^+ concentration (>100 mM) is thought to provide a saturating concentration for Na^+ ($K_m \sim 60$ mM), the affinity of SGLT-1 for glucose must be determined experimentally for a given system. The K_m of 2.5 mM for glucose measured in this study is lower than that of 16.7 mM measured in rabbit conjunctiva.¹⁸ The relatively low concentration of glucose in the normal human tear film (~ 200 μ M) is unlikely to cause significant fluid absorption.²⁰ However, elevated tear glucose may contribute to the ocular surface disease noted in hyperglycemic diabetes (~ 1 mM) by producing net absorption in the steady state.^{21,22} This prediction is supported by data in rabbits obtained by Shiue et al.,²³ who found a $\sim 75\%$ reduction in transconjunctival fluid secretion upon apical addition of saturating glucose.

Na^+ -dependent neutral–basic amino acid cotransport has also been characterized in rabbit conjunctiva, where both high (micromolar K_m)- and low (millimolar K_m)-affinity processes have been described for L-arginine.¹⁷ We measured qualitatively significant absorption at superphysiologic (in millimolar) amino acid concentrations, compared with the low-micromolar values reported by Puck et al.²⁴ in native tear film. Thus, although Na^+ -coupled amino acid cotransport may not be relevant to steady-state tear fluid balance,

our results support the strategy of delivering ocular therapeutics, either as amino acid analogues or conjugates, through cotransporters.²⁵

Although both corneal and conjunctiva epithelia are complex multilayered tissues, the ocular surface epithelial cell is modeled in the current study as a single cell layer with a parallel shunt, as was done previously to study passive solute fluxes across corneal epithelium.²⁶ Measurements in rabbit corneal epithelium have documented intimate electrical connection among superficial and wing cell layers, in support of this assumption.²⁷ Moreover, the apical superficial cell membrane largely dictates the electrical properties of stratified ocular surface epithelia because of its highly resistive tight junctions.^{27,28} The magnitudes of flux chosen in this simulation yielded a TEER of $5.3 \text{ k}\Omega/\text{cm}^2$, between the range of 12 to $17 \text{ k}\Omega/\text{cm}^2$ measured under short-circuit conditions in rabbit cornea^{5,29} and that of 1 to $2 \text{ k}\Omega/\text{cm}^2$ reported in rabbit conjunctiva.^{6,17,25} A potential weakness of the current model is the simplistic consideration of paracellular conductances in the context of a complicated multilayered epithelium, where possible unstirred layers could affect intercellular solute movement. In polarized epithelia that can both absorb and secrete ions to comparable extents, such as those lining the ocular surface, relative paracellular ion conductances largely determine the degree of basal fluid absorption and secretion.²⁹ However, the treatment of paracellular conductance would only affect estimates of basal fluid secretion and not predictions regarding the utility of membrane-transport modulators. Relative impermeant-to-permeant paracellular ion permeabilities of 0.7 were selected for anions and cations, to reproduce the minimal effect of Na^+ replacement by choline or K^+ in the presence of

1. The first part of the document discusses the importance of maintaining accurate records of all transactions and activities. It emphasizes that this is crucial for ensuring transparency and accountability in the organization's operations.

2. The second part of the document outlines the various methods and tools used to collect and analyze data. It highlights the need for consistent data collection practices and the use of advanced analytical techniques to derive meaningful insights from the data.

3. The third part of the document focuses on the role of technology in data management and analysis. It discusses how modern software solutions can streamline data collection, storage, and analysis processes, thereby improving efficiency and accuracy.

4. The fourth part of the document addresses the challenges associated with data management, such as data quality, security, and privacy. It provides strategies to mitigate these risks and ensure that the organization's data remains reliable and secure.

5. The fifth part of the document concludes by summarizing the key findings and recommendations. It stresses the importance of a data-driven approach in decision-making and the need for continuous monitoring and improvement of data management practices.

amiloride. Of note, these parameters are also in accord with the measurements of Amasheh et al.³⁰

As has been found in nasal PD measurements in CF versus wild-type mice^{31,32} and CF versus non-CF human subjects,¹⁹ amiloride produced a much greater depolarization at the ocular surface in CF versus wild-type mice (seen in Fig. 3). We also found an enhanced depolarization in CF mice after Na⁺ replacement. There is ongoing controversy regarding the mechanism responsible for these apparent CFTR-ENaC interactions. Whereas some studies have suggested direct inhibition of ENaC function by CFTR,^{10,33} recent modeling and careful experimentation suggest that electrochemical coupling accounts for the apparent hyperabsorption of Na⁺ across CF epithelia.^{11,34} We investigated purported CFTR-ENaC interactions by modeling the system with parameters for CF mice chosen to test whether enhanced Na⁺ absorption across CF epithelia can be explained by electrochemical coupling between parallel-functioning transporters. PDs from the CF mouse ocular surface were accurately simulated with fivefold reduced apical Cl⁻ conductance, yet identical Na⁺ conductance, compared with wild-type mice, indicating that direct regulation of ENaC by CFTR by a mechanism other than electrochemical coupling is not necessary to explain the experimental results. Although CF epithelia are predicted to have 20% of normal function, both experiments and modeling suggest that most of the unstimulated (cAMP- and Ca²⁺-independent) Cl⁻ flux passes through CFTR-dependent channels, though not through CFTR itself. We showed previously that the low-Cl⁻ hyperpolarization in wild-type mice was reversed only to a small extent by a CFTR inhibitor.⁴ Our model also demonstrated that reduced apical Cl⁻ conductance and unaltered Na⁺ absorptive capacity were both necessary to abolish most

1. The first part of the document discusses the importance of maintaining accurate records of all transactions and activities. It emphasizes that proper record-keeping is essential for ensuring transparency and accountability in financial reporting.

2. The second part of the document outlines the various methods and techniques used to collect and analyze data. It highlights the need for consistent and reliable data sources to support the findings and conclusions of the study.

3. The third part of the document presents the results of the research, including a detailed analysis of the data collected. It discusses the trends and patterns observed, as well as the implications of the findings for the field of study.

4. The fourth part of the document provides a comprehensive discussion of the research findings, including a comparison of the results with existing literature and theoretical frameworks. It also addresses the limitations of the study and suggests areas for future research.

5. The final part of the document concludes the study by summarizing the key findings and their significance. It emphasizes the importance of the research in advancing the understanding of the topic and provides recommendations for further exploration.

of the low Cl^- effect in CF mice (2.1-mV hyperpolarization predicted in CF as found experimentally).

In conclusion, our results define quantitatively the principal Na^+ -transporting pathways at the ocular surface and the electrochemical coupling between Na^+ and Cl^- transport in wild-type and CF ocular surface epithelia. The model predicted significant enhancement of serosal-to-mucosal fluid transport by Na^+ channel inhibitors and Cl^- channel activators. Direct measurement of fluid secretion across the intact ocular surface and studies in animal models of dry eye syndrome are needed to guide and validate the modeling of fluid secretion.

1. The first part of the document is a list of names and titles, including "The Hon. Mr. Justice" and "The Hon. Mr. Justice".

2. The second part of the document is a list of names and titles, including "The Hon. Mr. Justice" and "The Hon. Mr. Justice".

3. The third part of the document is a list of names and titles, including "The Hon. Mr. Justice" and "The Hon. Mr. Justice".

4. The fourth part of the document is a list of names and titles, including "The Hon. Mr. Justice" and "The Hon. Mr. Justice".

5. The fifth part of the document is a list of names and titles, including "The Hon. Mr. Justice" and "The Hon. Mr. Justice".

6. The sixth part of the document is a list of names and titles, including "The Hon. Mr. Justice" and "The Hon. Mr. Justice".

7. The seventh part of the document is a list of names and titles, including "The Hon. Mr. Justice" and "The Hon. Mr. Justice".

8. The eighth part of the document is a list of names and titles, including "The Hon. Mr. Justice" and "The Hon. Mr. Justice".

9. The ninth part of the document is a list of names and titles, including "The Hon. Mr. Justice" and "The Hon. Mr. Justice".

10. The tenth part of the document is a list of names and titles, including "The Hon. Mr. Justice" and "The Hon. Mr. Justice".

Appendix

Model Flux Equations

For electrogenic fluxes, individual transport pathways were governed by simple electrodiffusion unless otherwise specified, with fluxes defined by the Goldman-Hodgkin-Katz equation (equation 1 in the main text). Neutral transport pathways lacked a potential dependence. Each equation is provided below, along with any necessary explanation.

$$J_1 = P_1 U_a [Na_a^+ - Na^+(t)e^{-U_a}] / (1 - e^{-U_a}) \quad (A1)$$

$$J_2 = P_2 U_a \frac{Na_a^+ org_a - Na^+(t) org(t) e^{-U_a}}{(\frac{Na_a^+}{K_2^{Na}} + 1)(\frac{org_a}{K_2^{org}} + 1)(1 - e^{-U_a})} \quad (A2)$$

Transporter 2, when modeled as the Na⁺-glucose cotransporter, was assigned extracellular saturability values for both Na⁺ (K_2^{Na}) and glucose (K_2^{org}). K_2^{Na} was assumed to be 60 mM based on data of Horibe et al.¹⁸ in rabbit conjunctiva. K_2^{org} was determined experimentally to be 2.5 mM at the mouse ocular surface by dose-response experiments under conditions of saturating apical Na⁺.

$$J_3 = P_3 U_a [K_a^+ - K^+(t)e^{-U_a}] / (1 - e^{-U_a}) \quad (A3)$$

$$J_4 = -P_4 U_a [Cl_a^- - Cl^-(t)e^{U_a}] / (1 - e^{U_a}) \quad (A4)$$

$$J_5 = -P_5 U_a [Cl_a^- - Cl^-(t)e^{U_a}] / (1 - e^{U_a}) \quad (A5)$$

$$J_6 = P_6 \frac{Na^+(t)K^+(t)Cl^-(t)^2 - Na_b^+K_b^-(Cl_b^-)^2}{\left[1 + \frac{Na_b^+}{K_6^{Na}}\right] \left[1 + \frac{K_b^+}{K_6^K}\right] \left[1 + \frac{Cl_b^-}{K_6^{Cl}}\right]^2} \quad (A6)$$

$$J_7 = P_7 \left[\frac{Na^+(t)}{Na^+(t) + K_7^{Na}} \right]^3 \left[\frac{K^+(t)}{K_b^+ + K_7^K} \right]^2 (a \cdot U_b + b) \quad (A7)$$

Flux equations for transporters 6 and 7 (the $Na^+/K^+/2Cl^-$ symporter and $3Na^+/2K^+$ ATPase) were identical with those used in the model of tracheal epithelia by Hartmann and Verkman.¹⁴ Saturability (in millimolar) was assigned accordingly ($K_6^{Na} = 3.8$; $K_6^K = 7.5$; $K_6^{Cl} = 26$; $K_7^{Na} = 11.8$; $K_7^K = 1.4$), as were the constants in equation A7 that define the weak basolateral membrane potential dependence of $3Na^+/2K^+$ ATPase ($a=0.006$; $b=1 - a \cdot U_b$).

$$J_8 = P_8 U_b [K^+(t) - K_b^+ e^{-U_b}] / (1 - e^{-U_b}) \quad (A8)$$

$$J_9 = P_9 (org(t) - org_b) \quad (A9)$$

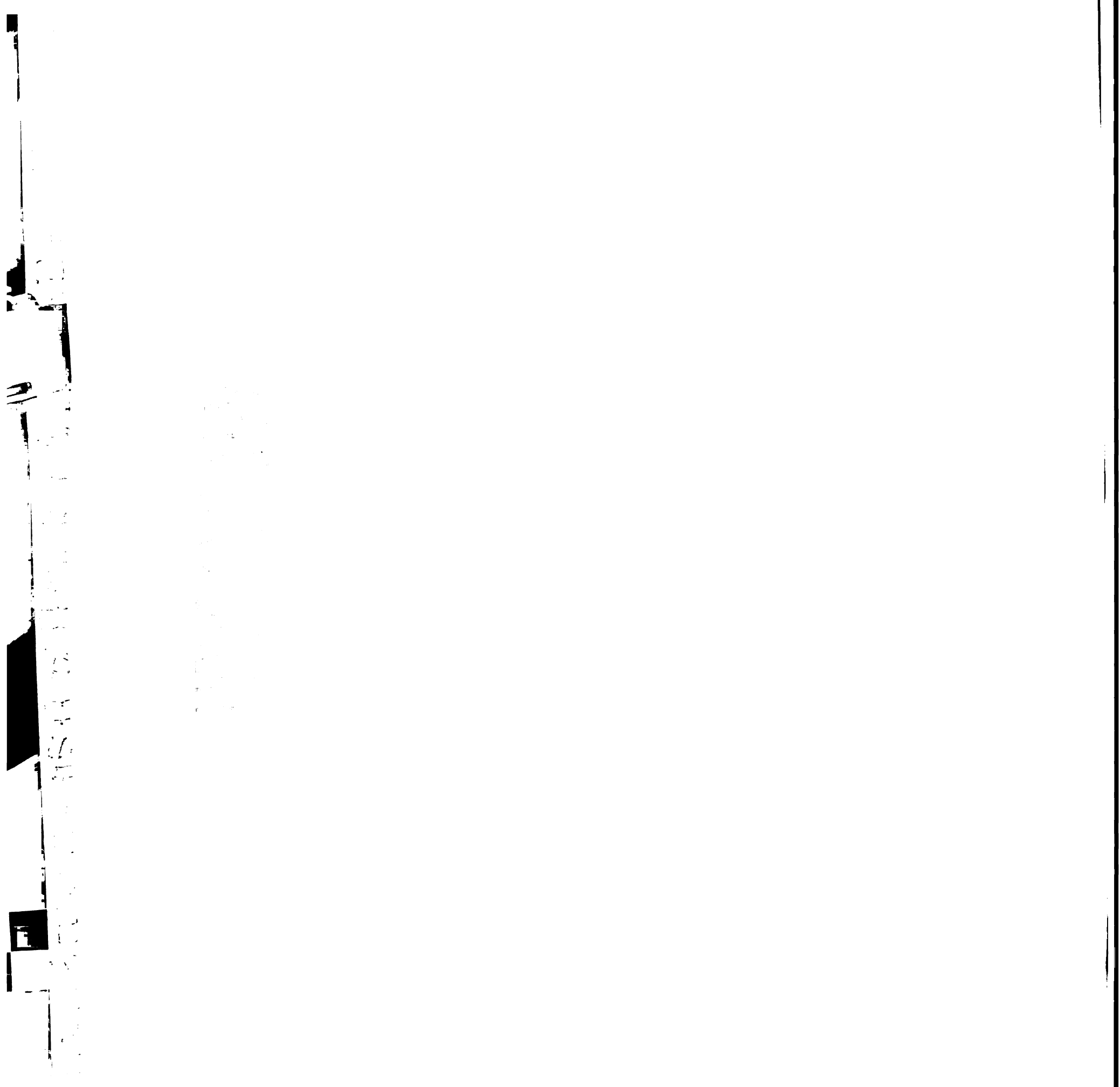
$$J_{10} = P_{10} U_p [Na_a^+ - Na_b^+ e^{-U_p}] / (1 - e^{-U_p}) \quad (A10)$$

$$J_{11} = P_{11} U_p [K_a^+ - K_b^+ e^{-U_p}] / (1 - e^{-U_p}) \quad (A11)$$

$$J_{12} = -P_{12} U_p [Cl_a^- - Cl_b^- e^{U_p}] / (1 - e^{U_p}) \quad (A12)$$

$$J_{13} = P_{13} U_p [chol_a^+ - chol_b^+ e^{-U_p}] / (1 - e^{-U_p}) \quad (A13)$$

$$J_{14} = -P_{14} U_p [gluc_a^- - gluc_b^- e^{U_p}] / (1 - e^{U_p}) \quad (A14)$$



Model Parameter Selection

Transporter permeability coefficients were calculated from the flux equations using estimated ion activities, membrane potentials, and net transcellular Na^+ and Cl^- fluxes under open-circuit conditions (see Table A1 for a summary of parameters for simulations in wild-type mice). Apical ion activities were chosen from the composition of solution 1. Basolateral ion activities were assigned based on serum concentrations from CD1 wild-type mice (measured by the University of California, San Francisco, Moffitt Hospital Clinical Laboratory; $n = 5$). Cellular ion activities and apical and basolateral membrane potentials were estimated from intracellular microelectrode measurements made in frog and rabbit corneal epithelial in vitro systems.^{35,36} Baseline cellular Cl^- activity was set at 33 mM, 1.9-fold greater than predicted for passive distribution across the apical membrane.³⁵ Values of -50 and -73 mV were chosen for ψ_a and ψ_b , respectively, to yield the experimentally measured steady state transepithelial potential ($\psi_a - \psi_b = -23$ mV).

All transcellular permeability coefficients (with the exceptions of P_2 and P_9) were determined from estimated steady state net active Na^+ and Cl^- fluxes. The ratio of active Na^+ absorption to Cl^- secretion (1:1 in wild-type mice and 5:1 in CF mice) was deduced experimentally from the magnitude of the amiloride effect, as described in the Results and Discussion sections. Because no levels of ion fluxes across mouse ocular surface epithelia have been determined, the absolute magnitudes of active Na^+ and Cl^- flux for wild-type mice were chosen as intermediate values between those for cornea and

conjunctiva, which were reported from rabbit and frog under both open- and short-circuit conditions.^{6,8,17,18,29}

We had some freedom in selecting the relative apical and basolateral K^+ fluxes (J_3 and J_8 , respectively). However, modeling of the very weak experimentally determined dependence of PD on apical K^+ confirmed that most of the K^+ flux occurred through transporter 8 ($J_3:J_8 = -1:224$ in wild-type mice). Paracellular permeability values were selected based on the small effect of Na^+ replacement on PD (see Fig. 2A). Equal and opposing transcellular and paracellular Na^+ fluxes were assumed.²⁹ A combination of higher assumed baseline absolute transcellular Na^+ and Cl^- and relative paracellular Na^+ flux values would increase the predicted baseline ocular surface fluid secretion rate. Based on constraints imposed by our own experimental observations and in accordance with flux measurements through tight junctions,³⁰ Na^+ and K^+ permeabilities (P_{10} and P_{11}) were assumed to be equal, with relative selectivity for choline⁺ versus Na^+ and K^+ as $P_{13}:P_{10}:P_{11} = 0.7:1:1$, and for gluconate versus chloride as $P_{14}:P_{12} = 0.7:1$ (Table A2).

Simulations involving Na^+ -organic cotransport (Fig. 6B) focused on Na^+ -coupled glucose permeation. P_2 was chosen to produce in simulations the 4- to 5-mV hyperpolarization measured experimentally in the presence of amiloride. P_9 was then selected to give equal apical and basolateral membrane glucose fluxes in the steady state ($J_2 = J_9$). Parameters for these simulations were selected based on the intracellular Na^+ activity (12.1 mM) and ψ_a (-59.9 mV) achieved after amiloride addition and on the apical Na^+ and Cl^- contents of solution 3.

1. The first part of the document discusses the importance of maintaining accurate records of all transactions and activities. It emphasizes the need for transparency and accountability in financial reporting.

2. The second part of the document outlines the various methods used to collect and analyze data. It includes a detailed description of the sampling process and the statistical techniques employed to ensure the reliability of the results.

3. The third part of the document presents the findings of the study. It highlights the key trends and patterns observed in the data, along with the implications of these findings for the industry and stakeholders.

4. The final part of the document provides a conclusion and offers recommendations for future research and practice. It suggests ways to improve data collection and analysis methods, as well as ways to enhance the transparency and accountability of financial reporting.

Iterative Procedure

Computations in this study were performed under open-circuit conditions. Fluxes through each transport conduit were computed using the guesses for ψ_a and ψ_b over time intervals of $\Delta t = 1$ second. Computations using a smaller step size ($\Delta t = 0.1$ second) gave similar results, confirming the adequacy of the 1-second step size. Total currents across each major barrier were then calculated at the end of each time interval:

$$I_a = 96500 \cdot (J_1 + J_2 + J_3 - J_4 - J_5) \quad (\text{A15})$$

$$I_b = 96500 \cdot (J_7 + J_8) \quad (\text{A16})$$

$$I_p = 96500 \cdot (J_{10} + J_{11} - J_{12} + J_{13} - J_{14}) \quad (\text{A17})$$

where 96,500 represents Faraday's constant, which converts flux into current. The threshold for acceptable relative deviation from open-circuit electroneutrality was set at 0.01%. If boundary conditions were not met, both ψ_a and ψ_b were modified by 1 mV and the two-dimensional Newton-Raphson method was used to update guesses for both ψ_a and ψ_b for the next iteration.

Once electroneutrality was established ($I_a = I_b = -I_p$), changes in cell volume (expressed as height, assuming a constant surface area) were computed based on net isosmolar water fluxes. The equation for computing net osmotically active solute flux into the cellular compartment is

$$\sum^{a-b} \phi_X J_i^X = \phi_{Na} J_1 + (\phi_{Na} + \phi_{org}) J_2 + \phi_K J_3 + \phi_{Cl} J_4 + \phi_{Cl} J_5 - (\phi_{Na} + \phi_K + 2\phi_{Cl}) J_6 - (3\phi_{Na} - 2\phi_K) J_7 - \phi_K J_8 - \phi_{org} J_9 \quad (\text{A18})$$

1. The first step is to identify the problem. This involves understanding the current situation and the goal that needs to be achieved. It is important to gather all relevant information and to define the problem clearly.

2. The second step is to generate possible solutions. This involves brainstorming ideas and considering different approaches to solve the problem. It is important to think creatively and to consider all possible options.

3. The third step is to evaluate the solutions. This involves comparing the different options and determining which one is the most feasible and effective. It is important to consider the costs, benefits, and risks of each solution.

4. The fourth step is to implement the chosen solution. This involves putting the plan into action and monitoring progress. It is important to communicate the plan to all relevant parties and to ensure that everyone is working towards the same goal.

5. The final step is to evaluate the results. This involves assessing the effectiveness of the solution and determining whether the goal has been achieved. It is important to gather feedback from all relevant parties and to use this information to improve future decision-making.

Steady state cell height was assumed to be 5 μm , similar to the height of the superficial ocular surface cell layer. The exact choice of cell height was important only for pre-steady-state kinetics after perturbation. Employing the updated cell height as well as solute fluxes, new intracellular solute activities at time $(t + \Delta t)$ were computed:

$$Na^+(t + \Delta t) = [Na^+(t) \cdot h(t) + \Delta t \cdot a_{Na} \cdot 10^4 \cdot (J_1 + J_2 - J_6 - 3J_7)] / h(t + \Delta t) \quad (\text{A19})$$

$$K^+(t + \Delta t) = [K^+(t) \cdot h(t) + \Delta t \cdot a_K \cdot 10^4 \cdot (J_3 + 2J_7 - J_6 - J_8)] / h(t + \Delta t) \quad (\text{A20})$$

$$Cl^-(t + \Delta t) = [Cl^-(t) \cdot h(t) + \Delta t \cdot a_{Cl} \cdot 10^4 \cdot (J_4 + J_5 - 2J_6)] / h(t + \Delta t) \quad (\text{A21})$$

$$org(t + \Delta t) = [org(t) \cdot h(t) + \Delta t \cdot a_{org} \cdot 10^4 \cdot (J_2 - J_9)] / h(t + \Delta t) \quad (\text{A22})$$

Net isosmolar water movement across the apical cell membrane and intercellular space into the apical compartment was calculated (equation 4 in the Methods section; Table A3) using the summed osmotically active solute movement:

$$\sum^{a+p} \phi_X J_i^X = -[\phi_{Na,e} J_1 + (\phi_{Na,e} + \phi_{org,e}) J_2 + \phi_{K,e} J_3 + \phi_{Cl,e} J_4 + \phi_{Cl,e} J_5 + \phi_{Na,e} J_{10} + \phi_{K,e} J_{11} + \phi_{Cl,e} J_{12} + \phi_{cho,e} J_{13} + \phi_{gluc,e} J_{14}] \quad (\text{A23})$$

References

1. Dartt DA. Regulation of mucin and fluid secretion by conjunctival epithelial cells. *Prog Retin Eye Res.* 2002;21:555–576.
2. Candia OA. Electrolyte and fluid transport across corneal, conjunctival, and lens epithelia. *Exp Eye Res.* 2004;78:527–535.
3. Li Y, Kuang K, Yerxa B, Wen Q, Rosskothan H, Fischbarg J. Rabbit conjunctival epithelium transports fluid and P2Y₂(2) receptor agonists stimulate Cl⁻ and fluid secretion. *Am J Physiol.* 2001;281:C595–C602.
4. Levin MH, Verkman AS. CFTR-regulated chloride transport at the ocular surface in living mice measured by potential differences. *Invest Ophthalmol Vis Sci.* 2005;46:1428–1434.
5. Marshall WS, Klyce SD. Cellular and paracellular pathway resistance in the "tight" Cl-secreting epithelium of rabbit cornea. *J Membr Biol.* 1983;73:275–282.
6. Shi XP, Candia OA. Active sodium and chloride transport across the isolated rabbit conjunctiva. *Curr Eye Res.* 1995;37:927–935.
7. Midelfart A. The effects of amiloride, ouabain, and osmolality on sodium transport across bovine cornea. *Pflügers Arch.* 1987;408:243–248.
8. Chang-Lin JE, Kim KJ, Lee VH. Characterization of active ion transport across primary rabbit corneal epithelial cell layers (RCrECL) cultured at an air-interface. *Exp Eye Res.* 2005;60:827–836.
9. Mirshahi M, Nicolas C, Mirshahi S, Golestaneh N, d'Hermies F, Agarwal MK. Immunochemical analysis of the sodium channel in rodent and human eye. *Exp Eye Res.* 1999;69:21–32.
10. Schreiber R, Hopf A, Mall M, Greger R, Kunzelmann K. The first-nucleotide binding domain of the cystic-fibrosis transmembrane conductance regulator is important for inhibition of the epithelial Na⁺ channel. *Proc Natl Acad Sci USA.* 1999;96:5310–5315.
11. Horisberger JD. ENaC-CFTR interactions: the role of electrical coupling of ion fluxes explored in an epithelial cell model. *Pflügers Arch.* 2003;445:522–528.
12. Latta R, Clausen C, Moore LC. General method for the derivation and numerical solution of epithelial transport models. *J Membr Biol.* 1984;82:67–82.

1. The first part of the document is a list of names and titles, including "The Hon. Mr. Justice G. D. C. O'Connell, Chief Justice of the High Court of Justice, Ireland, and President of the Royal College of Physicians, London." This list continues with several other names and titles, including "The Hon. Mr. Justice G. D. C. O'Connell, Chief Justice of the High Court of Justice, Ireland, and President of the Royal College of Physicians, London." The list ends with "The Hon. Mr. Justice G. D. C. O'Connell, Chief Justice of the High Court of Justice, Ireland, and President of the Royal College of Physicians, London."

13. Verkman AS, Alpern RJ. Kinetic transport model for cellular regulation of pH and solute concentration in the renal proximal tubule. *Biophys J*. 1987;51:533–546.
14. Hartmann T, Verkman AS. Model of ion transport regulation in chloride-secreting airway epithelial cells. *Biophys J*. 1990;58:391–401.
15. Colledge WH, Abella BS, Southern KW, et al. Generation and characterization of a delta F508 cystic fibrosis mouse model. *Nat Genet*. 1995;10:445–452.
16. Ma T, Thiagarajah JR, Yang H, et al. Thiazolidinone CFTR inhibitor identified by high-throughput screening blocks cholera toxin-induced intestinal fluid secretion. *J Clin Invest*. 2002;110:1651–1658.
17. Hosoya K, Horibe Y, Kim KJ, Lee VH. Na⁺-dependent L-arginine transport in the pigmented rabbit conjunctiva. *Exp Eye Res*. 1997;65:547–553.
18. Horibe Y, Hosoya K, Kim KJ, Lee VH. Kinetic evidence for Na⁺-glucose co-transport in the pigmented rabbit conjunctiva. *Curr Eye Res*. 1997;16:1050–1105.
19. Knowles M, Gatzky J, Boucher R. Relative ion permeability of normal and cystic fibrosis nasal epithelium. *J Clin Invest*. 1983;71:1410–1417.
20. Hirayama BA, Lostao MP, Panayotova-Heiermann M, Loo DD, Turk E, Wright EM. Kinetic and specificity differences between rat, human, and rabbit Na⁺-glucose cotransporters (SGLT-1). *Am J Physiol*. 1996;270:G919–G926.
21. Sen DK, Sarin GS. Tear glucose levels in normal people and in diabetic patients. *Br J Ophthalmol*. 1980;64:693–695.
22. Ozdemir M, Buyukbese MA, Cetinkaya A, Ozdemir G. Risk factors for ocular surface disorders in patients with diabetes mellitus. *Diabetes Res Clin Pract*. 2003;59:195–199.
23. Shiue MH, Kulkarni AA, Gukasyan HJ, Swisher JB, Kim KJ, Lee VH. Pharmacological modulation of fluid secretion in the pigmented rabbit conjunctiva. *Life Sci*. 2000;67:PL105–PL111.
24. Puck A, Liappis N, Hildenbrand G. Ion exchange column chromatographic investigation of free amino acids in tears of healthy adults. *Ophthalmic Res*. 1984;16:284–288.
25. Hosoya KI, Horibe Y, Kim KJ, Lee VH. Carrier-mediated transport of NG-nitro-L-arginine, a nitric oxide synthase inhibitor, in the pigmented rabbit conjunctiva. *J Pharmacol Exp Ther*. 1998;285:223–227.

26. Friedman MH. Mathematical modeling of transport in structured tissues: corneal epithelium. *Am J Physiol.* 1978;234:F215–F224.
27. Klyce SD, Wong RK. Site and mode of adrenaline action on chloride transport across the rabbit corneal epithelium. *J Physiol.* 1977;226:777–799.
28. Klyce SD. Electrical profiles in the corneal epithelium. *J Physiol.* 1972;226:407–429.
29. Klyce SD. Transport of Na, Cl, and water by the rabbit corneal epithelium at resting potential. *Am J Physiol.* 1975;228:1446–1452.
30. Amasheh S, Meiri N, Sitter AH, et al. Claudin-2 expression induces cation-selective channels in tight junctions of epithelial cells. *J Cell Sci.* 2002;115:4969–4976.
31. Grubb BR, Vick RN, Boucher RC. Hyperabsorption of Na⁺ and raised Ca(2+)-mediated Cl⁻ secretion in nasal epithelia of CF mice. *Am J Physiol.* 1994;266:C1478–C1483.
32. Salinas DB, Pedemonte N, Muanprasat C, Finkbeiner WF, Nielson DW, Verkman AS. CFTR involvement in nasal potential differences in mice and pigs studied using a thiazolidinone CFTR inhibitor. *Am J Physiol.* 2004;287:L336–L347.
33. Mall M, Grubb BR, Harkema JR, O'Neal WK, Boucher RC. Increased airway epithelial Na⁺ absorption produces cystic fibrosis-like lung disease in mice. *Nat Med.* 2004;10:487–493.
34. Nagel G, Barbry P, Chabot H, Brochiero E, Hartung K, Grygorczyk R. CFTR fails to inhibit the epithelial sodium channel ENaC, when expressed in *Xenopus laevis* oocytes. *J Physiol.* 2005;564:671–682.
35. Festen CM, Slegers JF, Van Os CH. Intracellular activities of chloride, potassium and sodium in rabbit corneal epithelium. *Biochim Biophys Acta.* 1983;732:394–404.
36. Reuss L, Reinach P, Weinman SA, Grady TP. Intracellular ion activities and Cl-transport mechanisms in bullfrog corneal epithelium. *Am J Physiol.* 1983;244:C336–C347.

Table 1

Composition of Perfusate Solutions

Solution	Name	Na ⁺	Cl ⁻	K ⁺	Gluconate ⁻	Choline ⁺	Organic
1	Control	170		160	4.2	0	0
2	Na ⁺ -free	0		160	4.2	0	170
3	Organic	154		144	4.2	0	30
4	Organic (-Na ⁺)	0		144	4.2	0	154
5	Low Cl ⁻	170		4.7	4.2	155	0
6	High K ⁺	0		160	174.2	0	0

All solutions contained (in mM): 9.5 phosphate, 1 Ca²⁺, 0.5 Mg²⁺ (pH 7.40).
'Organic' signifies D-glucose, L-glucose, or D-mannitol

Table 2

Model Symbols and Definitions

$X(t)$	Activity of solute X in cytoplasm (mM)
X_a	Activity of solute X in apical bathing solution (mM)
X_b	Activity of solute X in basolateral bathing solution (mM)
a_x	Cellular activity coefficient of solute X
ϕ_x	Cellular osmotic coefficient of solute X
a_x^e	Extracellular activity coefficient of solute X
ϕ_x^e	Extracellular osmotic coefficient of solute X
Ψ_s	Serum osmolarity (units vary and are specified for each equation)
$h(t)$	Cell height (μm)
J_i	Turnover rate of i th transporter (Fig. 1). Solute flux for X is the product of J_i and the number of X transported per turnover event (J_i^x , $\mu\text{eq}\cdot\text{cm}^2$ per second), defined as positive from left-to-right
I_a	Apical-to-cell membrane current ($\mu\text{A}/\text{cm}^2$)
I_b	Cell-to-basolateral membrane current ($\mu\text{A}/\text{cm}^2$)
I_p	Apical-to-basolateral paracellular current ($\mu\text{A}/\text{cm}^2$)
P_i	Permeability coefficient for i th transporter (units provided in Table AII)
K_i^x	Apparent binding constant for solute X to transporter i (mM), used for saturable transporters as described in the Chapter 4 Appendix.
ψ_a	Apical membrane potential (cell with respect to apical solution); (mV)
ψ_b	Basolateral membrane potential (cell with respect to basolateral solution); (mV)
ψ_t	Transepithelial potential (PD; $\psi_b - \psi_a$); (mV)
U_z	Dimensionless potential ($U_z = \psi_z F/RT$, where $F = 23$ cal/mV per mole, $R = 1.9872$ cal/K per mole, and $T = 310$ K)

Table A1

Baseline, Steady State Cell Parameters for Wild-Type Mouse Open-Circuit PDs

Solute activities (mM)	Apical	Cell	Basolateral	
Na ⁺	119	20	112	
Cl ⁻	112	33	84	
K ⁺	3.3	75	3.2	
Organic*	30	20	10	
Net active ion fluxes ($\mu\text{eq}/\text{cm}^2$ per hr)			J_{Na^+}	J_{Cl^-}
			0.15	-0.15
Membrane potentials (mV)	ψ_a		ψ_b	ψ_p
	-50		-73	-23

* Organic (D-glucose) was absent from most apical perfusates but was included at 30 mM when calculating P_2 and P_9 .

Table A2.

Transporter Permeabilities and Baseline, Steady-State Fluxes

Transporter	P_i	units	J_i ($\mu\text{eq}/\text{cm}^2$ per hr)
Apical membrane			
1 Na^+ conductance	1.63×10^{-7}	cm/s	0.15
2 Na^+ /org symporter	1.43×10^{-7}	$\text{cm}/\text{s}/\text{mM}^2$	0.11
3 K^+ conductance	1.52×10^{-8}	cm/s	-0.001
4/5 Cl^- conductance	1.21×10^{-6}	cm/s	-0.15
Basolateral membrane			
6 $\text{Na}^+/\text{K}^+/\text{2Cl}^-$ symporter	1.81×10^{-8}	$\text{cm}/\text{s}/\text{mM}^4$	0.075
7 $3\text{Na}^+/\text{2K}^+$ ATPase	1.73×10^{-4}	$\mu\text{mol}/\text{cm}^2 \cdot \text{s}$	0.075
8 K^+ conductance	1.24×10^{-5}	cm/s	0.224
9 Org conductance	3.06×10^{-6}	cm/s	0.11
Paracellular			
10 Na^+ conductance	4.54×10^{-7}	cm/s	-0.15
11 K^+ conductance	4.54×10^{-7}	cm/s	-0.00439
12 Cl^- conductance	3.53×10^{-7}	cm/s	0.145
13 Choline ⁺ conductance	3.18×10^{-7}	cm/s	-
14 Gluconate ⁻ conductance	2.47×10^{-7}	cm/s	-

Transporter numbers correspond to those depicted in Figure 1.

Table A3

Activity and Osmotic Coefficients

Solute	a_x	ϕ_x	a_x^e	ϕ_x^e
Na ⁺ , K ⁺ , Cl ⁻	0.75	0.7	0.75	0.92
Org	1	1	1	1

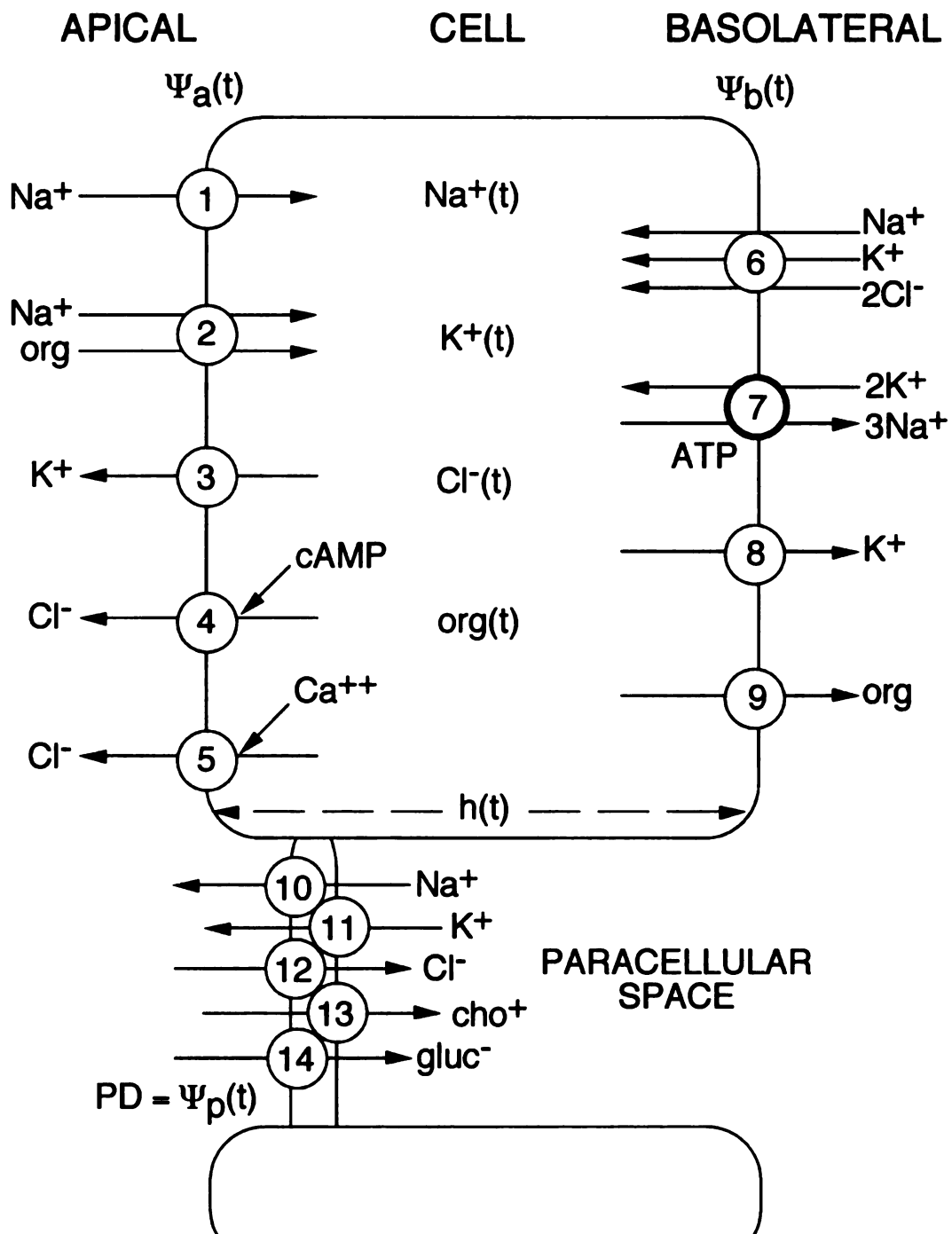


Figure 1

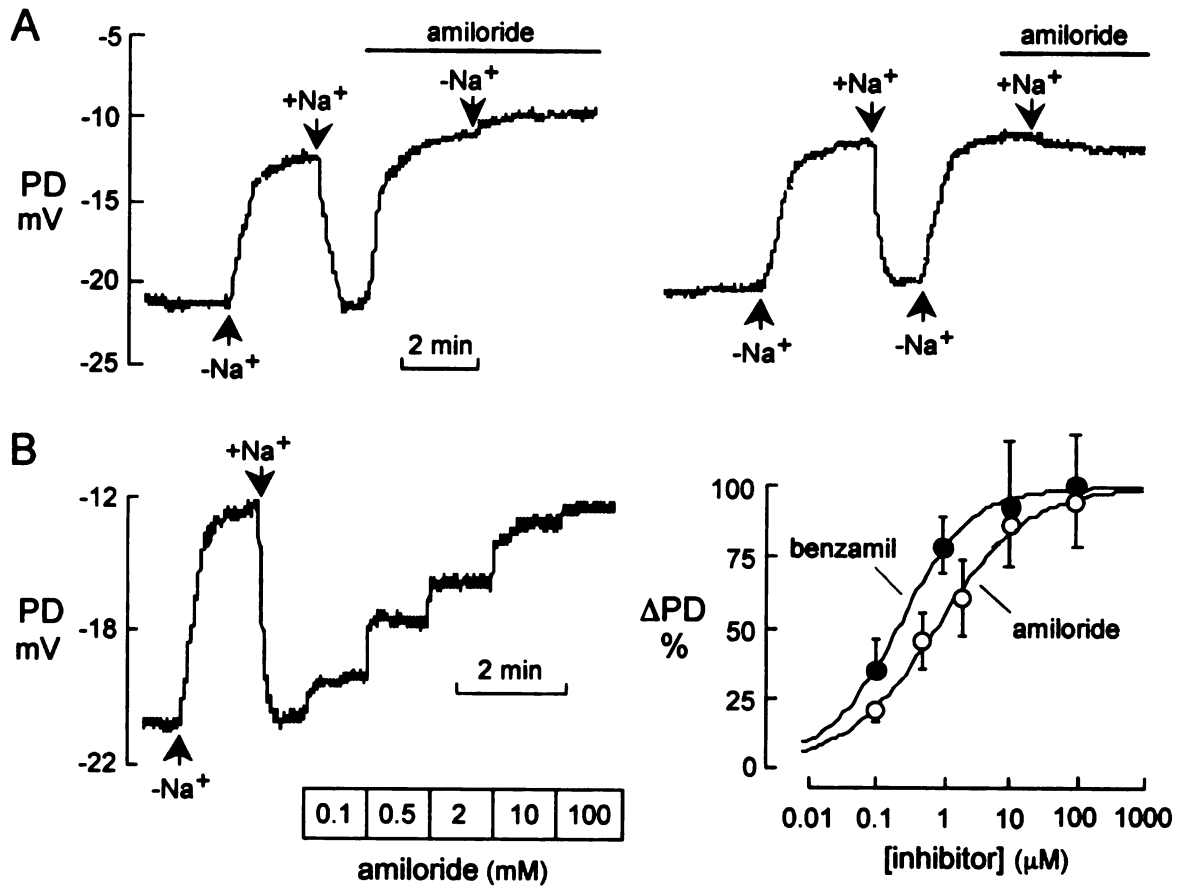


Figure 2

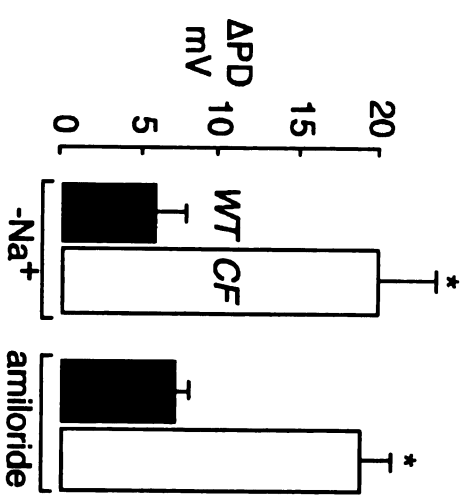
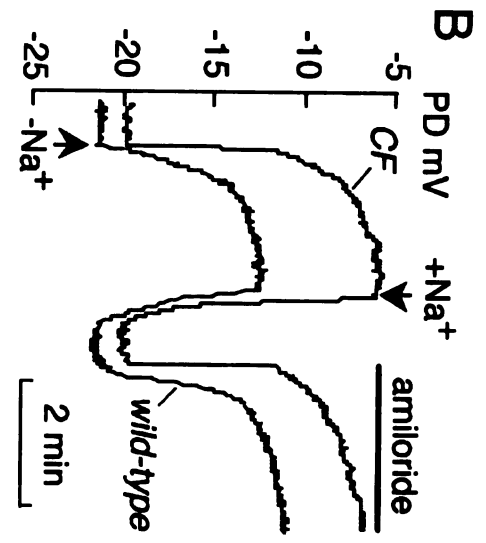
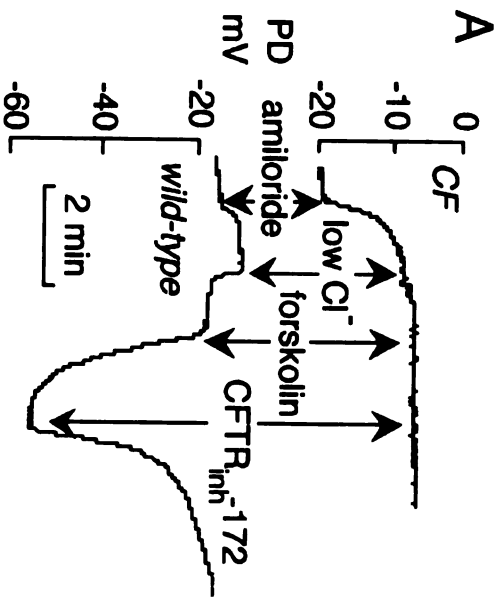


Figure 3

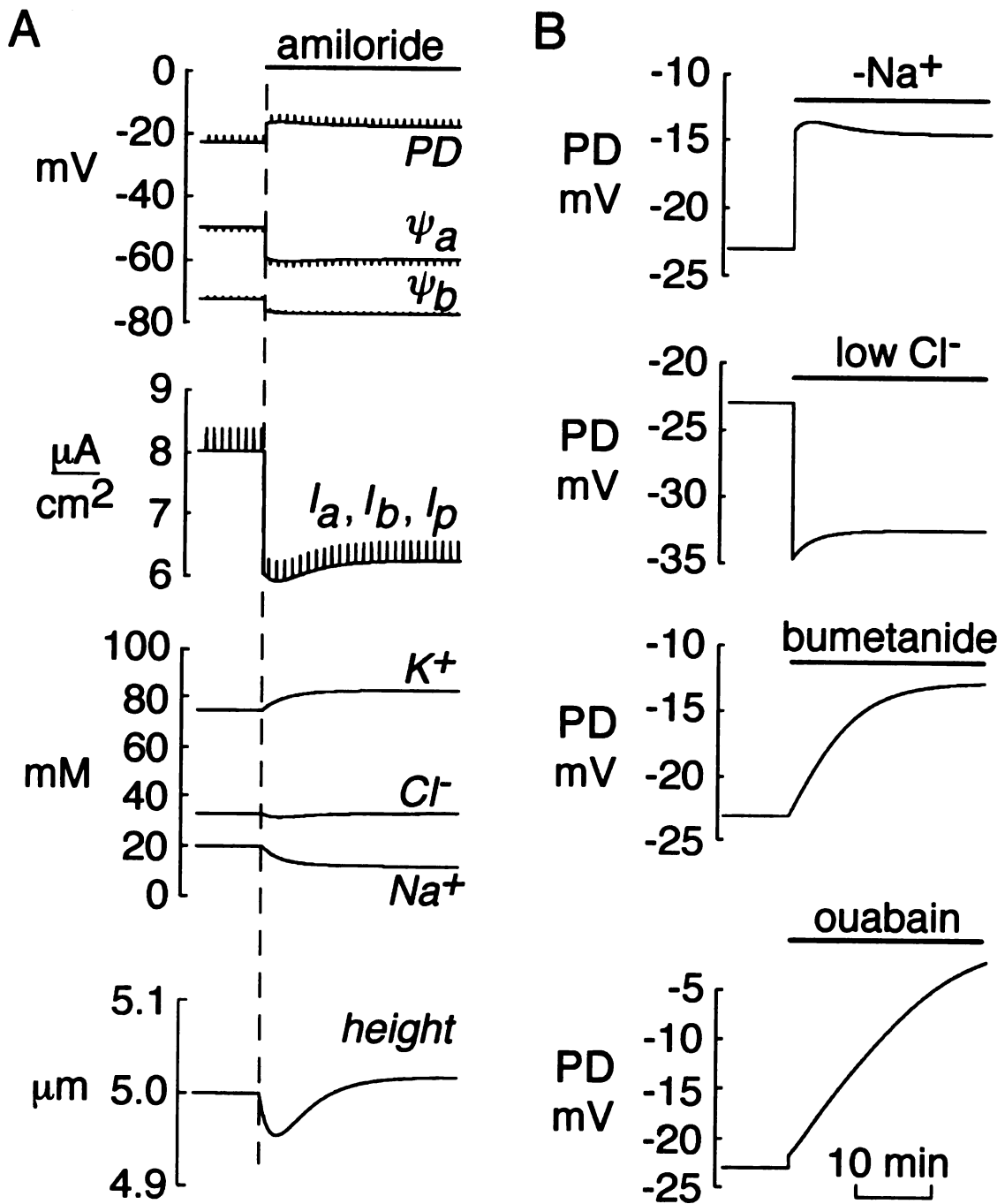


Figure 4

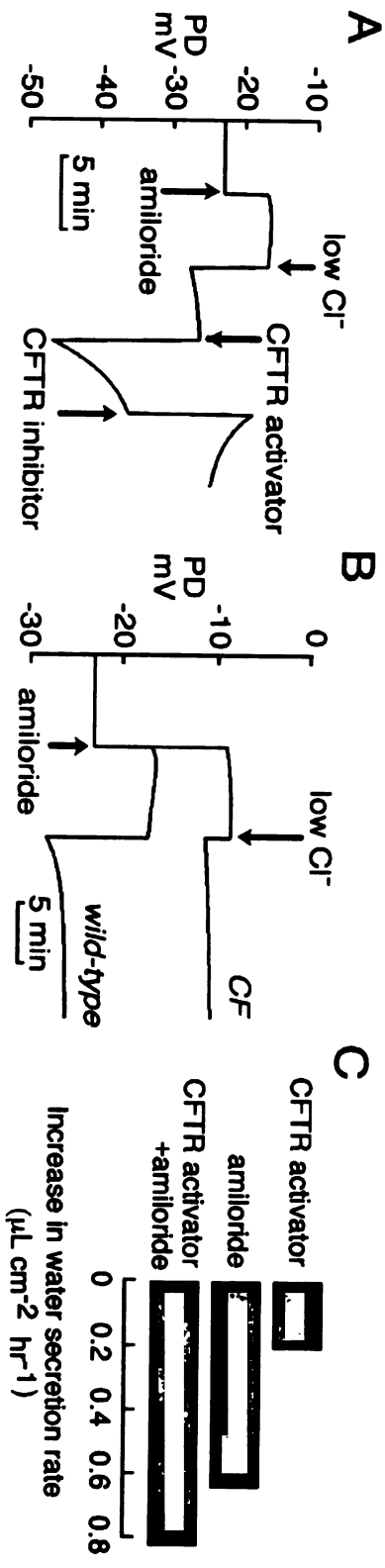


Figure 5

1. The first part of the document is a list of names and titles, including the names of the authors and the titles of their works. This list is organized in a structured manner, likely serving as a table of contents or a reference list for the document.

2. The second part of the document contains a series of numbered entries, each corresponding to a specific item or topic. These entries are arranged in a list format, providing a clear and organized overview of the content.

3. The third part of the document consists of a detailed description or explanation of the items listed in the previous sections. This section provides the necessary context and information for understanding the significance of the items.

4. The fourth part of the document is a concluding section, which may include a summary of the findings, a final statement, or a reference to further research. This section serves to wrap up the document and provide a clear end point for the reader.

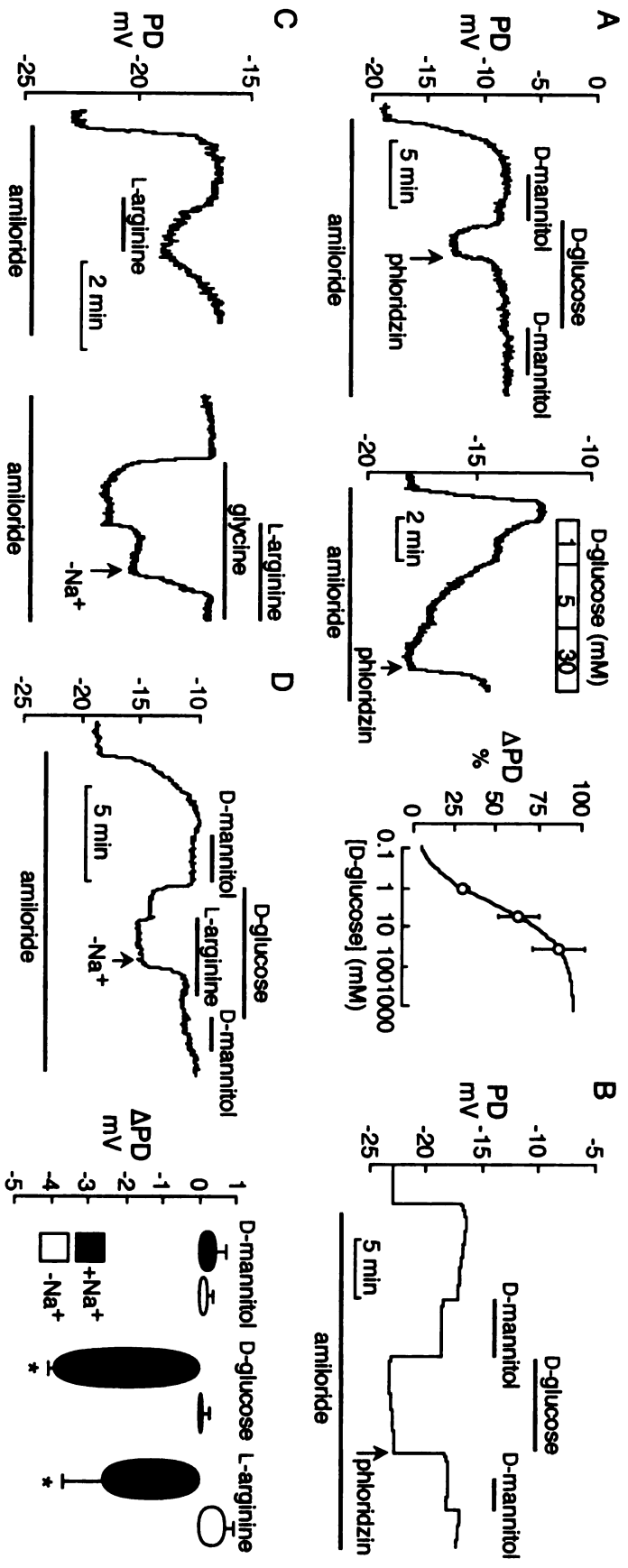


Figure 6

1. The first part of the document discusses the importance of maintaining accurate records of all transactions and activities. It emphasizes that this is crucial for ensuring transparency and accountability in the organization's operations.

2. The second part of the document outlines the various methods and tools used to collect and analyze data. It highlights the need for consistent data collection procedures and the use of advanced analytical techniques to derive meaningful insights from the data.

3. The third part of the document focuses on the role of technology in data management and analysis. It discusses how modern software solutions can streamline data collection, storage, and analysis, thereby improving efficiency and accuracy.

4. The fourth part of the document addresses the challenges associated with data management, such as data quality, security, and privacy. It provides strategies to mitigate these risks and ensure that the data remains reliable and secure.

5. The fifth part of the document discusses the importance of data governance and the role of a data governance committee. It outlines the key principles of data governance and the responsibilities of the committee members.

6. The sixth part of the document provides a detailed overview of the data governance framework, including the policies, procedures, and standards that govern the use of data within the organization.

7. The seventh part of the document discusses the role of data in decision-making and the importance of data-driven insights. It highlights how data can be used to identify trends, opportunities, and risks, and to inform strategic decisions.

8. The eighth part of the document discusses the importance of data literacy and the need for training and education. It outlines the key skills and knowledge required for data literacy and provides recommendations for developing a data-literate workforce.

9. The ninth part of the document discusses the role of data in innovation and the importance of fostering a data-driven culture. It highlights how data can be used to drive innovation and create new products and services.

10. The tenth part of the document provides a summary of the key findings and recommendations of the report. It emphasizes the need for a comprehensive data governance framework and the importance of ongoing monitoring and improvement.

Figure Legends

FIGURE 1. Ocular surface epithelial cell ion transport. Transport pathways are numbered and time-dependent intracellular solute activities, cell height, and membrane potentials are shown. Solute fluxes are defined as positive in the *left* (apical) to *right* (basolateral) direction. *Arrowheads*: direction of solute movement under open-circuit conditions. See Table A2 for specific transporter parameters under baseline, steady state conditions.

FIGURE 2. Amiloride-sensitive Na^+ transport at the ocular surface. (A) PD recordings showing effects of switching between sodium-containing ($+\text{Na}^+$) and sodium-free ($-\text{Na}^+$, sodium replaced by choline) solutions. *Horizontal line*: presence of amiloride, added to either the $+\text{Na}^+$ (*left*) or $-\text{Na}^+$ (*right*) solutions. Representative of six experiments.

Solutions used were *left*: 1 alone, 2 alone, 1 alone, 1+amiloride, and 2+amiloride; *right*: 1 alone, 2 alone, 1 alone, 2 alone, and 2+amiloride. (B) Dose-dependent inhibition of sodium absorption by amiloride and benzamil. *Left*: Representative time course of PD inhibition, first by Na^+ replacement, and then by adding amiloride to the perfusate at increasing concentrations. Solutions used: 1 alone, 2 alone, 1 alone, and 1+amiloride. *Right*: dose response of benzamil and amiloride for depolarizing PD, determined from experiments as shown on the *left* (mean \pm SE, $n = 5$ for benzamil; $n = 6$ for amiloride).

FIGURE 3. Ion transport at the ocular surface in CF mice. (A) PD recordings in CF (*top*) and wild-type (*bottom*) mice in response to amiloride, low Cl^- , forskolin ($10 \mu\text{M}$), and $\text{CFTR}_{\text{inh}}-172$ ($10 \mu\text{M}$). Solutions used: 1 alone, 1+amiloride, 5+amiloride, 5+amiloride+forskolin, and 5+amiloride+forskolin+ $\text{CFTR}_{\text{inh}}-172$. (B) Elevated

1. The first part of the document discusses the importance of maintaining accurate records of all transactions and activities. It emphasizes that this is crucial for ensuring transparency and accountability in the organization's operations.

2. The second part of the document outlines the various methods and tools used to collect and analyze data. It highlights the need for consistent data collection procedures and the use of advanced analytical techniques to derive meaningful insights from the data.

3. The third part of the document focuses on the role of technology in data management and analysis. It discusses how modern software solutions can streamline data collection, storage, and processing, thereby improving efficiency and accuracy.

4. The fourth part of the document addresses the challenges associated with data management, such as data quality, security, and privacy. It provides strategies to mitigate these risks and ensure that the data remains reliable and secure throughout its lifecycle.

5. The fifth part of the document concludes by summarizing the key findings and recommendations. It stresses the importance of ongoing monitoring and evaluation to ensure that the data management processes remain effective and aligned with the organization's goals.

amiloride-sensitive Na^+ absorption in CF mice. *Left*: PD tracings in wild-type versus CF mice (curves overlaid) in response to Na^+ replacement and amiloride. Solutions used: 1 alone, 2 alone, 1 alone, and 1+amiloride. *Right*: Summary of ΔPD for wild-type and CF mice for indicated maneuvers (SE, $n = 6$ eyes per genotype). $*P < 0.01$ comparing wild-type versus CF mice.

FIGURE 4. Ocular surface epithelial ion transport model. For each maneuver, individual transporter conductances or apical compartment solute compositions were changed instantaneously. See the Chapter 4 Appendix for model parameters. **(A)** Influence of amiloride on time-dependent model parameters in open-circuit conditions. Transporter 1 (apical Na^+) conductance was fully inhibited (at *dashed line*). Changes in (from *top* to *bottom*) membrane potentials, currents, intracellular ion activities, and cell height are shown. Brief voltage spikes were applied every minute (*top tracings*) by an imposed current spike (*second trace from top*) with a magnitude that was a fixed proportion of the instantaneous current. **(B)** Effects of different maneuvers on open-circuit PD. From top to bottom, apical Na^+ replaced with choline, apical Cl^- replaced by gluconate, basolateral $\text{Na}^+/\text{K}^+/\text{2Cl}^-$ symporter inhibited, and basolateral $3\text{Na}^+/\text{2K}^+$ ATPase inhibited.

FIGURE 5. Modeling PD protocols and fluid secretion. **(A)** Simulation of protocol for studying chloride transport (as in the experiment in Fig. 3A). CFTR activation was produced by a threefold increase in apical Cl^- permeability. **(B)** Simulation of protocol for studying sodium transport. Comparison of wild-type versus CF mouse ocular PDs in response to amiloride and then low Cl^- . Solutions simulated: 1 alone, 1+amiloride, and 5+amiloride. CF mouse apical Cl^- permeability was 20% of that in wild-type mouse,

whereas apical Na^+ permeability was not changed in the CF mouse parameter set. (C) Incremental steady state water secretion (above baseline), modeled in response to addition to solution 1 of amiloride, a CFTR activator (increasing apical Cl^- conductance threefold), or both together.

FIGURE 6. Solute-coupled Na^+ absorption. (A, *left*) PD response to additions of D-mannitol (30 mOsm, replacing NaCl) and D-glucose (30 mOsm, replacing D-mannitol), followed by the Na^+ -glucose cotransporter inhibitor phloridzin (100 μM), all in solutions containing amiloride (100 μM). Solutions used: 1 alone, 1+amiloride, 3(D-mannitol)+amiloride, 3(D-glucose)+amiloride, 3(D-glucose)+amiloride+phloridzin, 3(D-mannitol)+amiloride+phloridzin, and 1+amiloride+phloridzin. *Middle:* Concentration-dependent effect of D-glucose on PD in the presence of amiloride (100 μM). Solutions used: 1 alone, 1+amiloride, and a series of mixtures of 1 and 3(D-glucose)+amiloride. *Right:* Corresponding concentration–response curve (mean \pm SE, $n = 5$). (B) Simulated PD tracing of maneuvers identical with those performed experimentally and depicted in (A, *left*). (C) PD responses to amino acids, in the presence of amiloride. *Left:* L-arginine (1 mM) was added to and then removed from solution 1. Representative of six experiments. Solutions used: 1 alone, 1+amiloride, 1+amiloride+L-arginine, and 1+amiloride. *Right:* addition to solution 1 of glycine (5 mM) followed by L-arginine (5 mM) before Na^+ replacement by choline. Representative of four experiments. Solutions used: 1+amiloride, 1+amiloride+glycine, 1+amiloride+glycine+L-arginine, and 2+amiloride+glycine+L-arginine. (D, *left*) Representative PD response to serial isosmolar additions of 30 mM D-mannitol, 30 mM D-glucose, and 1 mM L-arginine in the presence of amiloride. Solutions used: 1 alone, 1+amiloride, 3(D-mannitol)+amiloride, 3(D-

1. The first part of the document discusses the importance of maintaining accurate records of all transactions and activities related to the business. It emphasizes the need for transparency and accountability, particularly in the context of financial reporting and tax compliance. The text highlights how thorough record-keeping can help identify areas for improvement and ensure that all legal obligations are met.

2. The second part of the document focuses on the role of technology in modern business operations. It explores various digital tools and platforms that can streamline processes, improve communication, and enhance data security. The author notes that while technology offers significant benefits, it also introduces new challenges, such as data privacy and cybersecurity risks, which must be carefully managed.

3. The third part of the document addresses the importance of human resources and organizational culture. It discusses the need for a diverse and skilled workforce, as well as the role of leadership in fostering a positive and productive work environment. The text suggests that investing in employee development and training can lead to long-term success and innovation within the organization.

4. The final part of the document provides a summary of the key points discussed and offers some practical advice for business owners and managers. It encourages a proactive approach to business management, emphasizing the importance of staying up-to-date on industry trends and regulations. The author concludes by expressing confidence in the future of the business and the potential for continued growth and success.

glucose)+amiloride, 3(D-glucose)+amiloride+L-arginine, 4(D-glucose)+amiloride+L-arginine, 4(D-glucose)+amiloride, 4(D-mannitol)+amiloride, and 2+amiloride. *Right:* Paired analysis of Δ PD measured in +Na⁺ or -Na⁺ solutions. SE, $n = 3-5$ mice; * $P < 0.01$, comparing PD responses to zero.

1. The first part of the document discusses the importance of maintaining accurate records of all transactions and activities. It emphasizes that this is crucial for ensuring transparency and accountability in the organization's operations.

2. The second part of the document outlines the various methods and tools used to collect and analyze data. It highlights the need for consistent data collection procedures and the use of advanced analytical techniques to derive meaningful insights from the data.

3. The third part of the document focuses on the role of technology in data management and analysis. It discusses how modern software solutions can streamline data collection, storage, and analysis, thereby improving efficiency and accuracy.

4. The fourth part of the document addresses the challenges associated with data management, such as data quality, security, and privacy. It provides strategies to mitigate these risks and ensure that the data remains reliable and secure.

5. The fifth part of the document concludes by summarizing the key findings and recommendations. It stresses the importance of ongoing monitoring and evaluation to ensure that the data management processes remain effective and up-to-date.

CHAPTER 6.

Non-Invasive Measurements of Mouse Tear Film Ionic Composition

Abstract

PURPOSE. The cornea and conjunctiva are semi-permeable barriers at the ocular surface involved in regulation of tear film composition and volume.

METHODS. To measure absolute tear $[\text{Na}^+]$, $[\text{Cl}^-]$, and pH, ratioable and cell impermeant small-molecule fluorescent indicators were dissolved in the intact murine tear film for quantitative dual wavelength ratio imaging microscopy.

RESULTS. For CD1 wild-type mice, tear $[\text{Na}^+]$ was 123 ± 5 mM, $[\text{Cl}^-]$ was 127 ± 4 mM, and pH was 7.63 ± 0.06 (SE, n=9–12 mice per ion).

CONCLUSIONS. $[\text{Na}^+]$, $[\text{Cl}^-]$, and pH were measured in the tear film of wild-type mice at baseline. This technical advance will allow us to test the hypotheses that tear fluid salinity increases in experimental dry eye, and that these alterations normalize along with other functional and histopathological tear film properties in successfully treated dry eye.

Tear film osmolarity is elevated in both evaporative (caused by excessive tear evaporation rates) and tear-deficient (caused by inadequate tear aqueous secretion) dry

eye and has long been an objective, quantitative index of KCS severity.¹ Sodium, in particular, is thought to correlate to ocular surface inflammatory changes that characterize keratoconjunctivitis sicca (KCS).² All previous studies assessing tear film ion content have assayed microsamples, an approach that introduces potential artifacts. For example, samples must be collected from the tear meniscus, which likely has a lower osmolarity than the rest of the tear film. For example, samples must be collected from the tear meniscus, which likely has a lower osmolarity than the rest of the tear film. This would result in an underestimate of the degree of hyperosmolarity experienced in KCS.³ In situ fluorescence measurements of tear film pH have been previously reported.^{4,5,6} Fluorescence techniques were previously developed to measure $[\text{Na}^+]$, $[\text{Cl}^-]$, and pH in microscopic quantities of airway surface liquid (ASL) in vivo.⁷ Here, this methodology is adapted to the murine tear film, where it should be useful in both characterizing tear film ionic elevations that are present in KCS and evaluating improvement of ocular surface health during therapy.

Methods

Mice

Wild-type CD1 mice (ages 6–10 weeks, 22–30 g) were anesthetized intraperitoneally with ketamine (40 mg/kg) and xylazine (20 mg/kg). Core body temperature was maintained at 38°C with a heating pad and monitored using a rectal thermometer. The mouse head was rotated and fixed using a custom-built stereotaxic device, with the central corneal surface positioned perpendicular to the optical axis for

imaging. Protocols were approved by the University of California at San Francisco Committee on Animal Research and are in compliance with the ARVO Statement for the Use of Animals in Ophthalmic and Vision Research.

Fluorescence Probes

Tear film pH measurements were performed using the dual-excitation wavelength pH indicator BCECF (2',7'-bis-[carboxyethyl]-5-carboxyfluorescein) conjugated to a dextran (10 kDa, Molecular Probes). pH is measured from green images (520 nm emission) taken at two excitation wavelengths (440 and 490 nm).

Tear $[Cl^-]$ was measured from red (TMR) and green (BAC) images of BAC-TMR-dextran-stained tear film. The ratioable Cl^- sensitive fluorescent indicator BAC-TMR-dextran synthesized as described previously,⁸ in which the Cl^- -sensitive, green fluorescent chromophore BAC (10,10'-bis[3-carboxypropyl]-9,9'-biacridinium) was conjugated covalently to dextran (40 kDa) together with the Cl^- -insensitive, red fluorescent chromophore TMR (tetramethylrhodamine, Molecular Probes). BAC fluorescence is quenched by Cl^- by a collisional mechanism.

Tear $[Na^+]$ was measured from red (Corona RedTM) and green (BODIPY-fl) images taken of tears stained with fluorescent Na^+ -sensing beads. A ratioable Na^+ -sensitive fluorescent indicator prepared by incubation of carboxyl-modified latex beads (200-nm diameter, Polymer Laboratories Inc., Amherst, Massachusetts, USA) with the Na^+ -insensitive, green fluorescent chromophore BODIPY-fl-EDA (Molecular Probes) and the Na^+ -sensitive, red fluorescent chromophore Corona RedTM (Molecular Probes).

Indicator beads for $[\text{Na}^+]$ were prepared according to Jayaraman et al.,⁹ with slight modification. BODIPY-fl-EDA was dissolved in ethanol and added at a final concentration of 100 μM to a 1% (vol/vol) suspension of beads in suspended in 4 mL water. After shaking for 2 hr at room temperature, “sodium red” (Molecular Probes Inc.) was added to 10 μM . The beads were shaken for 1 more hr, centrifuged at 14,000 g for 30 minutes, dispersed by brief sonication, and washed three times with water. The chromophores remained quantitatively immobilized on the beads for approximately 2 weeks storage in water at 4°C in the dark, with aggregation prevented by brief sonication prior to each use.

Tear Film Labeling

After anesthesia was initiated, the tear film was maintained throughout an experiment by 31–35°C humidified air streaming through a 2 cm opening 2 cm away from the corneal surface and periodic mechanical blinking.⁹ To label tears for measurement of pH, ~2 mg of BCECF-dextran was dispersed in 1 mL of low-boiling perfluorocarbon (compound FC-72, boiling point 56°C; 3M company, St. Paul, Minnesota, USA) using brief-probe sonication. Two minutes before measurements, 50–100 μL of perfluorocarbon was pipetted onto the ocular surface and the lids were briefly closed to disperse and dissolve the dye homogeneously throughout the tear film. To instill Cl^- indicator into tears, solid BAC-TMR-dextran was inserted into the outer canthus with a needle tip and dissolved with repeated mechanical blinking. The Na^+ indicator was added to tears by direct pipetting of 0.25 μL of beads into the outer canthus

followed by several forced blinks. For all three ion measurements, dye was redistributed with blinking between most measurements.

Fluorescence Microscopy

Ratio imaging was done using a set-up initially described by Song et al.¹⁰ A Nikon SMZ1500 stereo epifluorescence microscope was equipped with a mercury arc lamp, 1.6x objective lens (numerical aperture 0.21, working distance 24 mm), cooled CCD camera (Photometrics), and custom filter sets (Chroma, Rockingham, VT) for BAC, tetramethylrhodamine, Corona Red™, BODIPY-fl, and BCECF. For ratio image analysis, images (1,000-ms acquisitions for pH and 1,500-ms acquisitions for Cl⁻ and Na⁺) were obtained from pairs of filter sets that were manually switched with <1 s lag. Tear fluorescence ratios were computed over randomly selected regions after subtraction of background determined from three regions of the ocular surface imaged before adding fluorescent indicator. [Na⁺], [Cl⁻], or pH were determined from fluorescence ratios using calibrations as described below. Photobleaching, insignificant for the Na⁺ and pH indicators, was minimized for the Cl⁻ indicator by limiting BAC excitation to periods of image acquisition.

Calibration Protocols.

In vitro calibrations were performed to obtain absolute ion concentrations from the in vivo fluorescence ratio measurements. Ratiometric imaging of [Na⁺], [Cl⁻], or pH was performed on 10 μL drops of buffer standards of varied composition containing fluorescent dyes. The base buffer, designed to approximate native tear ion composition,

consisted of 120 mM NaCl, 30 mM KCl, 20 mM HEPES, 0.7 mM MgCl₂, and 0.7 mM CaCl₂ (pH 7.4). For Na⁺ calibrations, a Na⁺-free buffer (choline chloride replacing NaCl) was mixed with the base buffer at varied proportion. For Cl⁻ calibrations, a Cl⁻-free buffer (sodium gluconate replacing NaCl) was mixed similarly with the base buffer. The base buffer was titrated with nitric acid or potassium hydroxide for pH calibrations.

Results

In Vitro Calibrations

For Na⁺ measurements, bead red-to-green fluorescence ratio (R/G) increased linearly with [Na⁺] from 0 to >200 mM and was not affected by pH. For Cl⁻ measurements, indicator red-to-green fluorescence ratio (R/G) decreased linearly with [Cl⁻] from 0 to >200 mM Cl⁻ and was not affected by pH. For pH measurements, BCECF-dextran fluorescence measured at 490 and 440 nm excitation wavelengths (F_{490}/F_{440}) was pH sensitive with a pKa ~7.0. Calibration curves to later determine absolute tear [Na⁺], [Cl⁻], and pH in situ are shown in Figure 1 (A–C).

In Vivo Controls

Control experiments were performed included adding variable amounts of indicator to the same eye between measurements or taping the eyelids shut until seconds before dye instillation and measurement to mitigate against evaporative changes. Buffered solutions with known ion contents were also added to acutely alter ion

concentrations or pH. The expected changes were observed with a gradual return to the original steady state over several minutes.

In Vivo [Na⁺], [Cl⁻], and pH

A preliminary study using untreated wild-type mice validated these protocols and provided the first in situ measurements of tear fluid composition (Fig. 1, A–C). Tear fluid [Na⁺] was 123 ± 5 mM, [Cl⁻] was 127 ± 4 mM, and pH was 7.63 ± 0.06 (\pm SE, n=9–12 mice).

Discussion

Chemical indicators (fluorescent ratioable sensors) for measurement of $[\text{Na}^+]$, $[\text{Cl}^-]$, and most recently, $[\text{K}^+]$, have been developed by our lab for in vivo measurements in microscopic fluid compartments. Measurements of $[\text{Na}^+]$ and $[\text{Cl}^-]$, as well as pH, involve introduction of ratioable fluorescent dyes and in vivo fluorescence microscopy. Additionally tear fluid $[\text{K}^+]$ will soon be measured to complete the analysis of in situ ionic composition, given the recent development of the first long-wavelength K^+ selective fluorescent sensor (TAC-Red), based on a triazacryptand-chromophore covalent conjugate.¹¹ For measurement of tear fluid composition of anesthetized mice, the eye is maintained in a heated, humidified air atmosphere and fluorescent indicator dye is distributed throughout the tear film with periodic mechanical blinking.

We propose that this approach will facilitate a more accurate correlation of dry eye severity with altered ionic content. This prediction will soon be tested using a well-characterized experimental mouse model of KCS (systemic scopolamine + dry air current) which reproduces features of the human disorder, including decreased tear production, clearance, and barrier function, conjunctival squamous metaplasia, and decreased conjunctival goblet cell density.¹² In this model, changes in tear ion composition are predicted to precede the progression of functional and histopathological changes of KCS. Such a time-course would be consistent with the measurements of Gilbard et al.¹³ made on collected tear microvolumes from a surgical rabbit model. If tear ionic composition is indeed altered in this dry eye model, effective topical treatment

(with a CFTR activator and/or ENaC inhibitor, for example)¹⁴ would be expected to normalize electrolyte disturbances.

References

1. Gilbard JP, Farris RL, Santamaria J. Osmolarity of tear microvolumes in keratoconjunctivitis sicca. *Arch Ophthalmol*. 1978;96:677–681.
2. Stewart P, Chen Z, Farley W, Olmos L, Pflugfelder SC. Effect of experimental dry eye on tear sodium concentration in the mouse. *Eye Contact Lens*. 2005;31:175–178.
3. Yamada M, Mochizuki H, Kawai M, Yoshino M, Mashima Y. Fluorophotometric measurement of pH of human tears in vivo. *Curr Eye Res*. 1997;16:482–486.
4. Yamada M, Kawai M, Mochizuki H, Hata Y, Mashima Y. Fluorophotometric measurement of the buffering action of human tears in vivo. *Curr Eye Res*. 1998;17:1005–1009.
5. Chen FS, Maurice DM. The pH in the precorneal tear film and under a contact lens measured with a fluorescent probe. *Exp Eye Res*. 1990;50:251–259.
6. Bron AJ, Tiffany JM. The contribution of meibomian disease to dry eye. *The Ocular Surface*. 2004;2:149–164.
7. Sonawane ND, Thiagarajah JR, Verkman AS. Chloride concentration in endosomes measured using a ratioable fluorescent Cl⁻ indicator: evidence for chloride accumulation during acidification. *J Biol Chem*. 2002;277:5506–5513.
8. Jayaraman S, Song Y, Vetrivel L, Shankar L, Verkman AS. Noninvasive in vivo fluorescence measurement of airway-surface liquid depth, salt concentration, and pH. *J Clin Invest*. 2001;107:317–324.
9. Zhao J, Nagasaki T, Maurice DM. Role of tears in keratocyte loss after epithelial removal in mouse cornea. *Invest Ophthalmol Vis Sci*. 2001;42:1743–1749.
10. Song Y, Thiagarajah J, Verkman AS. Sodium and chloride concentrations, pH, and depth of airway surface liquid in distal airways. *J Gen Physiol*. 2003;122:511–519.
11. Padmawar P, Yao X, Bloch O, Manley GT, Verkman AS. K⁺ waves in brain cortex visualized using a long-wavelength K⁺-sensing fluorescent indicator. *Nat Methods*. 2005;2:825–827.
12. Dursun D, Wang M, Monroy D, Li D, Lokeshwar BL, Stern ME, Pflugfelder SC. A mouse model for keratoconjunctivitis sicca. *Invest Ophthalmol Vis Sci*. 2002;43:632–638.

13. Gilbard JP, Rossi SR, Gray KL. A new rabbit model for keratoconjunctivitis sicca. *Invest Ophthalmol Vis Sci.* 1987;28:225–228.
14. Levin MH, Kim JK, Hu J, Verkman AS. Potential difference measurements of ocular surface Na⁺ absorption analyzed using an electrokinetic model. *Invest Ophthalmol Vis Sci.* 2006;47:306–316.

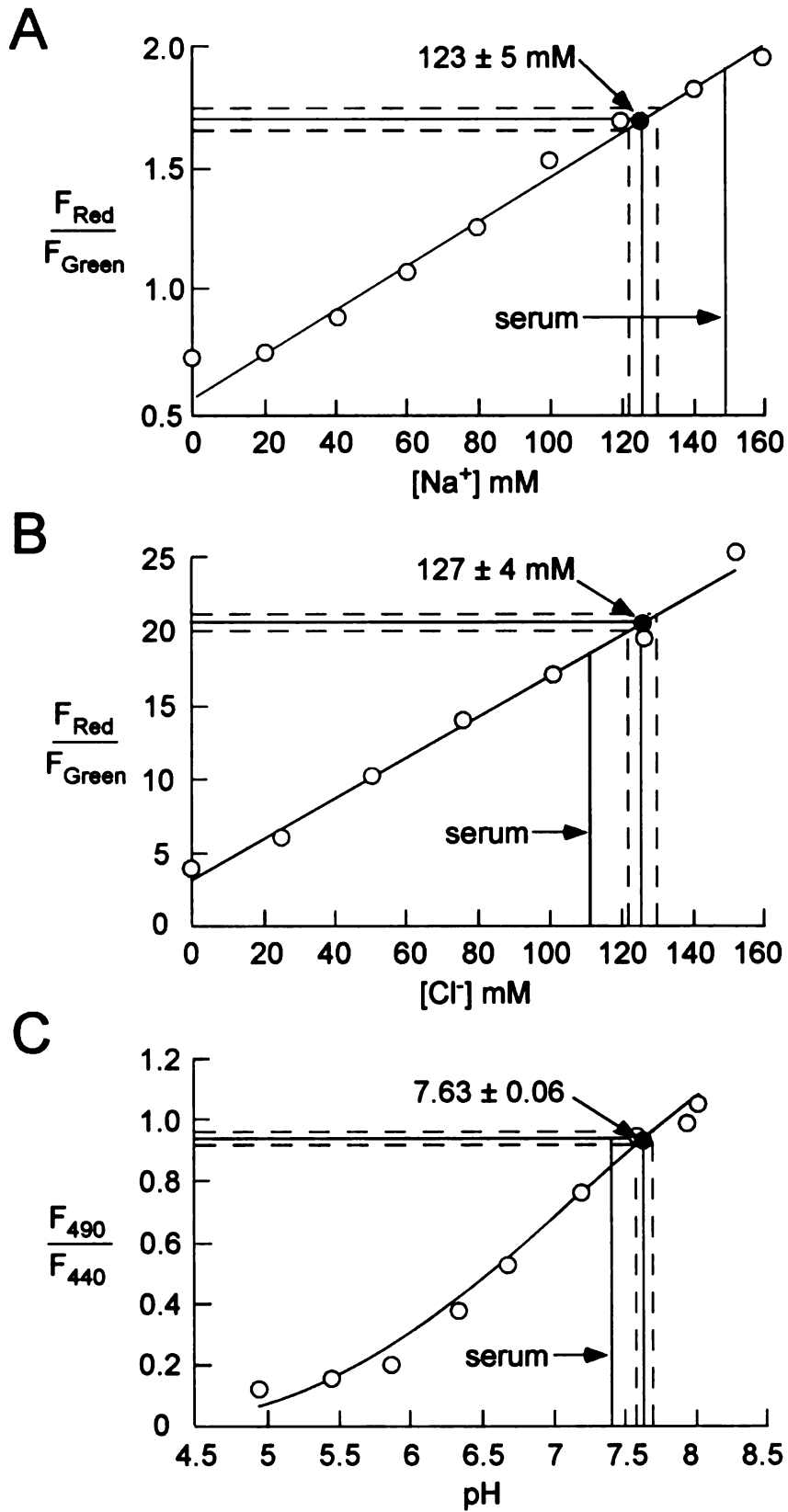


Figure 1

Figure Legend

FIGURE 1. Biophysical measurements of tear film ionic content. **(A)** Na^+ calibration in standard solutions and in situ concentration in tear fluid. Measurements done using NaRed beads as described in text (\pm SE, n=9 eyes, >3 regions measured per eye). **(B)** Cl^- calibration and in situ concentration measured using BAC-tetramethylrhodamine dextran (\pm SE, n=12 eyes). **(C)** pH measured using BCECF-dextran (\pm SE, n=11 eyes).

CHAPTER 7.

Hypertonic Saline Therapy in Cystic Fibrosis: Evidence Against the Proposed Mechanism Involving Aquaporins

Abstract

PURPOSE: Recent data indicate clinical benefit of nebulized hypertonic saline in cystic fibrosis lung disease, with a proposed mechanism involving sustained increase in airway surface liquid (ASL) volume. To account for the paradoxical observation that amiloride suppressed the beneficial effect of hypertonic saline, Donaldson et al. (*N. Engl. J. Med.* 354:241–250, 2006) concluded that amiloride-inhibitable aquaporin (AQP) water channels in airway epithelia modulate ASL volume.

METHODS: Here, we characterize water permeability and amiloride effects in well-differentiated, primary cultures of human airway epithelial cells, stably transfected Fisher Rat Thyroid (FRT) epithelial cells expressing individual airway/lung AQPs, and perfused mouse lung.

RESULTS: We found high transepithelial water permeability (P_f , $54 \pm 5 \mu\text{m/s}$) in airway epithelial cells that was weakly temperature-dependent and inhibited by > 90% by reduced pH in the basal membrane-facing solution. RT-PCR and immunofluorescence suggested the involvement of AQPs 3, 4, and 5 in the high airway water permeability.

CONCLUSION: Experiments using several sensitive measurement methods indicated that amiloride does not inhibit water permeability in non-CF or CF airway epithelia, AQP-transfected FRT cells, or intact lung. Our data provide evidence against the mechanism proposed by Donaldson et al. to account for effects of amiloride and hypertonic saline in CF lung disease, indicating the need to identify alternate mechanisms.

Cystic fibrosis (CF) is a relatively common hereditary disease in Caucasians caused by mutations in the CF transmembrane conductance regulator (CFTR) chloride channel. Morbidity and mortality in CF result primarily from chronic airway infection, which results in progressive deterioration of lung function.

Two recent clinical studies have demonstrated short- and long-term benefits of nebulized hypertonic saline in improving lung function in CF.^{1,2} Prior clinical studies also support the efficacy of various inhaled hyperosmolar agents in CF.^{3,4,5,6} The recent study by Donaldson et al.¹ concluded that hypertonic saline produces sustained elevation in airway surface liquid (ASL) volume, which improves mucociliary clearance in the airways. However, a paradoxical effect was found when amiloride was administered together with hypertonic saline. Rather than improving lung function because of its inhibitory effect on ENaC and consequent prevention of ASL absorption, amiloride negated the beneficial effect of hypertonic saline. To account for these findings, Donaldson et al. postulated the involvement of airway AQPs in establishing ASL volume (Fig. 1), and reported strong amiloride inhibition of osmotic water permeability in airway epithelial cells. In their model, ENaC hyperactivity dehydrates the ASL in CF airways (left panel), and hypertonic saline restores ASL volume (middle panel). If amiloride acts

only on ENaC, then amiloride is predicted to increase ASL volume (right, top panel). To account for the clinical data, they hypothesize that amiloride inhibits airway AQPs, which prevents water from entering the airways (right, bottom panel).

The proposed involvement of AQPs in ASL regulation is surprising, as is the inhibition of AQP water permeability by amiloride. Osmotically induced water transport across airways was shown to be high and likely AQP-dependent in microperfused small airways,⁷ and later in cultured human tracheal epithelial cells⁸ and in spheroids composed of airway epithelial cell monolayers.⁹ Despite this, reduction of airway epithelial water permeability by deletion of the various lung/airway aquaporins (AQPs 1, 3, 4 and 5) in transgenic mice did not affect ASL volume or ionic composition.¹⁰ Inhibition of AQP water permeability by amiloride is surprising because amiloride has no aquaretic effect at concentrations that inhibit ENaC in the renal distal tubule.

Here, we tested the hypothesis of Donaldson et al.¹ by characterizing water permeability and amiloride effects in human bronchial epithelial cell cultures, stably transfected epithelial cells expressing airway/lung AQPs, and intact lung, using a variety of biophysical methods to quantify water transport. Water permeabilities of airway cells and intact lung surface were found to be high and AQP-dependent, though amiloride did not inhibit water permeability, nor did it inhibit water permeability of the individual AQPs. These findings have important implications for understanding the benefit of hypertonic saline in CF, and for the future development of related strategies for therapy of CF lung disease.

Methods

Cell Culture

Surface bronchial epithelial cells were obtained from non-CF human lung specimens that were not suitable for lung transplantation. CF bronchial epithelial cells were obtained from patients at the time of transplantation. Cells were dissociated by enzymatic digestion, as described.¹¹ Isolated cells were suspended in a 1:1 mixture of Dulbecco's modified Eagle's medium (DMEM) and Ham's F12 medium containing 5% fetal calf serum (FCS, Hyclone; Logan, UT), gentamicin (50 mg/mL), penicillin (100 U/mL), streptomycin (1 mg/mL), and fungizone (2.5 mg/mL), and seeded as passage 0 (P0) cultures at a density of 10^6 cells/cm² onto 12-mm Transwell polycarbonate inserts (0.4 μ m pore size; Costar, Corning, NY) overlaid with a thin coat (15 μ g/cm²) of human placental collagen (HPC, Sigma-Aldrich, St. Louis, MO). The next day, cells were rinsed with PBS and medium was replaced with ALI medium¹² containing gentamicin, penicillin, and streptomycin at the concentrations given above. Medium was changed daily. When the cell sheets became confluent and actively absorbed mucosal fluid, as indicated by loss of apical fluid in the central portion of the insert (generally 3–5 days), the mucosal surface was rinsed with PBS, and media was added only to the basal side of the insert.

For some experiments bronchial epithelial cells (non-CF and CF) were obtained after expansion in HPC-coated tissue culture flasks. After 80–90% confluence, cells were released using 0.05% trypsin and 0.2% EDTA in 0.9% NaCl at 37 °C. The trypsin was

neutralized with DMEM/Ham's F12 medium containing 20% FCS, and propagated cells were resuspended in plating medium and seeded onto cell culture inserts as described above, but designated as passage 1 (P1) cultures. By day 15 after seeding, both P0 and P1 cultures formed tight layers with transepithelial resistance of 1–2 $\text{k}\Omega\cdot\text{cm}^2$, at which time they were used for experiments. Cultures were confirmed to express cAMP-activated CFTR by measurement of short-circuit current, as reported.¹³ Protocols were approved by the University of California, San Francisco Committee on Human Research.

Fisher rat thyroid epithelial (FRT) cells stably transfected with either control plasmid (encoding yellow fluorescent protein, YFP) or with plasmids encoding AQP1, AQP3, or AQP4¹⁴ were grown in F12-Coombs medium (Sigma-Aldrich) supplemented with 10% fetal bovine serum (Hyclone), penicillin G (100 U/mL), streptomycin (100 $\mu\text{g}/\text{mL}$), and appropriate antibiotic selection markers. For dye-dilution experiments, FRT cells were plated onto uncoated Transwell inserts and used for flux measurements at resistances of 2–5 $\text{k}\Omega\cdot\text{cm}^2$.

Transepithelial Water Permeability

Osmotic water permeabilities across HBE and FRT cell layers were determined using a dye dilution method, as depicted in Figure 2A. The dilution of a cell-impermeant, photostable, inert dye (Texas RedTM-dextran, 10 kDa, Molecular Probes, Eugene, OR) was used as a measure of transcellular osmotic water flux. The basal surface of cells on the porous filter was bathed in 1 mL of isosmolar PBS. The apical surface was bathed in 200 μL of hyperosmolar PBS (PBS + 300 mM D-mannitol) containing 0.25 mg/mL Texas Red-dextran. In some experiments, 500 μM amiloride (Sigma-Aldrich), dissolved

freshly from powder, was added to the apical buffer, as done by Donaldson et al.¹, or to both the apical and basal-bathing buffers. Cultures were placed in a 5% CO₂ tissue culture incubator (at 27 or 37°C), and 5 μL samples of dye-containing apical fluid was collected at specified times. Samples were diluted in 2 mL of PBS and fluorescence was measured by cuvette fluorimetry (Fluoro Max-3, Horiba, Tokyo, Japan). In some experiments, the osmotic gradient was reversed by addition of mannitol to the basal rather than the dye-containing apical solution. In other experiments, the pH of either the basal or apical solutions was adjusted to 5.0 using buffers containing 137.6 mM NaCl, 5 mM KCl, 2 mM CaCl₂, 1 mM MgCl₂, 6 mM D-glucose, and 10 mM HEPES (for pH 7.4) or MES (for pH 5.0).

For computation of transepithelial osmotic water permeability coefficients (P_f , in cm/s), the time course of fluorescence in response to solution osmolarity changes, $F(t)$, was fitted to a single-exponential time constant: $F(t)/F_0 = B + A e^{-t/\tau}$, where F_0 is initial fluorescence, A is amplitude and τ is the exponential time constant. Because of dye binding to cells and/or the support, data used for exponential regression was collected at 5 min and later after establishing the osmotic gradient. Water flux was computed as the rate of dye dilution by: $dV(t)/dt = V_0 A/\tau$, which follows from the relation: $F(t)/F_0 = V_0 / (V_0 + V(t))$. V_0 is the initial volume of dye-containing apical buffer (0.2 cm³) and $V(t)$ is apical solution volume at time t . From these equations, P_f was computed as: $dV(t)/dt = P_f S v_w (\Phi_1 - \Phi_2)$, where S is the tissue surface area assuming a smooth surface (1.13 cm²), v_w is the partial molar volume of water (18 cm³/mol), and $(\Phi_1 - \Phi_2)$ is the transepithelial osmotic gradient (3×10^{-4} mol/cm³).

Plasma Membrane Water Permeability

Plasma membrane osmotic water permeability was measured using a calcein-quenching method (shown in Fig. 3A) that has been applied previously to in vitro and in vivo cell systems.^{15,16} Cells were loaded with calcein by incubation with PBS containing 10 μ M calcein-AM (Molecular Probes) for 30 min at 37 °C. HBE cultures grown on collagen-coated supports were studied by cutting the flat supports from the plastic inserts and mounting them in a custom-built perfusion chamber, with support bottoms pressed against a cover slip and apical cell surfaces exposed to perfusate. FRT cells grown on glass cover slips were inserted in a similar perfusion chamber but with cells facing upwards. Solutions were exchanged between PBS (290 mOsm) and hyperosmolar PBS (590 mOsm, PBS with added D-mannitol) using a gravity pinch valve system (ALA Scientific Instruments, Westbury, NY). Perfusates contained either DMSO vehicle (0.1%) or amiloride (500 μ M) added from a 1000x DMSO stock solution. Fluorescence was excited using an X-cite 120 mercury lamp (EXFO Life Sciences, Ontario, Canada) and focused through an inverted epifluorescence microscope through a long-working-distance 25x air objective (numerical aperture 0.35, Leitz, Germany). Excitation and emission light was filtered using a custom cube (Chroma, Rockingham, VT), and fluorescence was collected using a 14-dynode photomultiplier, amplified, digitized and recorded using custom software (written in LabView, National Instruments, Austin, TX).

To compute plasma membrane P_f , relative fluorescence, $F(t)/F_o$, was fitted to a single exponential function (as above) for FRT cell studies, or a biexponential function, $F(t)/F_o = A e^{-t/\tau_1} + B e^{-t/\tau_2} + C$, for HBE studies. Plasma membrane P_f was computed as

described above, where surface area, S , was taken as apical surface area of the cell monolayer, assuming a flat, smooth surface. The time-varying cell layer height, $h(t)$, was related to normalized amplitudes according to the predicted 50% final decrease from initial height (h_0) under hypertonic conditions. For FRT and HBE cells, h_0 was taken as 5 and 20 μm , respectively. P_f was then computed from: $dh(0)/dt = P_f v_w (\Phi_1 - \Phi_2)$.

Airspace-Capillary Water Permeability in Intact Lung

Wild-type and AQP5-deficient mice in a CD1 genetic background (age 8–14 weeks)¹⁷ were sacrificed using an overdose of 2,2,2-tribromoethanol (avertin, Sigma-Aldrich) intraperitoneally. Protocols were approved by the University of California, San Francisco Committee on Animal Research. The trachea was transected and cannulated, the pulmonary artery was cannulated, and the heart and lungs were moved en bloc to a perfusion chamber as described.¹⁸ After ensuring that no air leaks were present, 0.5 mL of FITC-dextran solution (10 kDa, 0.5 mg/mL in PBS; Sigma-Aldrich), with or without freshly dissolved amiloride (500 μM), was instilled into the tracheal catheter. The pulmonary artery was perfused at constant pressure (~ 60 cm H_2O) with PBS, with or without 500 μM amiloride, for at least 5 min before measurements. The pleural surface was washed continuously with PBS, and perfusate and wash effluent were continuously withdrawn from the chamber by suction (perfusate flow 5 mL/min). The time course of fluorescence intensity from a 3–5 mm spot on the lung pleural surface, in a similar location for all samples, was continuously monitored while perfusate fluid was exchanged between isosmolar and hyperosmolar PBS (PBS + 300 mM D-mannitol),

using the microscope set-up, detection system, and gravity pinch valve system described above.

Histology and Immunocytochemistry

Paraffin sections of P0 HBE cell culture inserts and fixed human trachea were prepared. For paraffin sections, inserts were fixed for at least 30 min in buffered formalin (10%) and stored in 0.1 M phosphate buffer (pH 7.4). Standard tissue dehydration and paraffin infiltration was performed in a Tissue-Tek VIP processor (Sakura Finetek, Torrance, CA). Sections were cut at 4 μ m on a rotary microtome and stained with hematoxylin and eosin. Specimens were viewed and photographed on an Olympus light microscope (Olympus America, Inc., Melville, NY) equipped with a digital imaging system (QImaging, Burnaby, Canada). Immunostaining was done by standard procedures using polyclonal antibodies for AQP3, AQP4 and AQP5 (Chemicon, Temecula, CA) incubated for 2 hr and Cy3-conjugated goat anti-mouse IgG (1:200; Sigma-Aldrich) incubated for 30 min.

RT-PCR

Total RNA from HBE cells scraped freshly from P0 culture inserts was isolated by homogenization in TRIzol reagent (Invitrogen, Carlsbad, CA), and mRNA was extracted using the Oligotex mRNA midi kit (Qiagen, Valencia, CA). cDNA was reverse transcribed from mRNA with oligo(dT) (SuperScript II preamplification kit, Invitrogen). Primers were designed to amplify 300-350 base pair fragments of cDNAs encoding human β -actin (sense, 5'-GCATGGAGTCCTGTGGCATCC-3'; antisense, 5'-

CATTGCGGTGGACGATGGAC-3'), AQP1 (sense, 5'-GCCATCGGCCTCTCTGTAGCC-3'; antisense 5'-CTATTGGGCTTCATCTGCAC-3'), AQP2 (sense, 5'-ACCTCCTTGGGATCCATTACA-3'; antisense, 5'-TCAGGCCTTGGTACCCCGTGG-3'), AQP3 (sense, 5'-CTGGTGGTCCTGGTCATTGGC-3'; antisense, 5'-CTGCTCCTTGTGCTTCACATG-3'), AQP4 (sense, 5'-GGACCTGCAGTTATCATGGGA-3'; antisense, 5'-CAATACCTCTCCAGATTGTGC-3'), AQP5 (sense, 5'-CTGTCCATTGGCCTGTCTGTC-3', antisense, 5'-GCGGGTGGTCAGCTCCATGGT-3'), AQP6 (sense, 5'-CTGGGCCACCTCATTGGGATC-3'; antisense, 5'-TCACACACTCTCCATCTCCAC-3), AQP7 (sense, 5'-CAGGTCTTCAGCAATGGGGAG-3'; antisense, 5'-CTCTAGGGCCATGGATTCATG-3'), AQP8 (sense, 5'-GTGGCAGAGATCATCCTGACG-3'; antisense, 5'-TTCAGGATGAGGCGGGTCTTC-3'), and AQP9 (sense, 5'-GACTCCAGAACTTGGGAGCC-3'; antisense, 5'-TTGTCCTCAGATTGTTCTGCC-3'). RT-PCR (for stained agarose gels) was performed with the Taq DNA polymerase kit (Invitrogen) and PCR products were electrophoresed on a 1.2 % agarose gel.

Fluorescence-based real-time RT-PCR was done to compare relative AQP3, AQP4, and AQP5 mRNA expression in non-CF vs. CF cells using the LightCycler™ and with LightCycler FastStart DNA Master^{PLUS} SYBR Green I kit (Roche Diagnostics Corp., Indianapolis, IN) according to the manufacturer's instructions. Surface epithelial cells were dissociated from human bronchi, quick-frozen, and stored at -80 °C until thawed for RNA isolation. PCR primers were as described above. Results were reported as a normalized, calibrated ratio with all samples normalized to β-actin. Concentration

ratios for each CF and non-CF sample were calibrated to calibrator samples (pooled cDNA from non-CF subjects), with the results reported as a normalized ratio with the calibrator sample as the denominator: relative mRNA level = ratio of sample (target / reference) / ratio of calibrator (target / reference).

Results

Amiloride-Independent Transepithelial Water Permeability in HBE Cultures

Water transport in airway surface epithelium was studied using well-differentiated human bronchial epithelial (HBE) cell cultures. Transepithelial osmotic water permeability was measured using a dye dilution method that assays water flux across tight epithelia cultured on porous filters (Fig. 2A). The fluorescence of an apical solution volume marker provided a quantitative readout of osmotically driven water transport across the cell layer. An induced osmotic gradient caused transepithelial water movement, from which osmotic water permeability (P_f) was deduced. The P0 non-CF cultures were first characterized. Figure 2B (top) shows fluorescence dilution at 37 °C, in which a 300 mM gradient of D-mannitol induced osmotic water flux into the apical, dye-containing solution. Data in the absence vs. the presence of amiloride (500 μ M) are compared. Figure 2C summarizes transepithelial P_f values. There was no significant difference in P_f upon exposure of P0 HBE cultures to high-dose amiloride (control vs. amiloride: 54 ± 5 vs. 52 ± 7 μ m/s).

When the direction of the osmotic gradient was reversed by addition of mannitol to the basal-bathing solution, the fluorescent volume marker became concentrated over

time (Fig. 2B, middle). The deduced transepithelial P_f ($46 \pm 15 \mu\text{m/s}$) did not differ significantly from that in control studies (mannitol in apical solution), indicating symmetrical water transport. To investigate the involvement of AQPs in HBE water permeability, experiments were done at reduced temperature (27°C), and with reduced pH in the apical or basal-bathing solutions (Fig. 2C, bottom). P_f at 27°C ($47 \pm 9 \mu\text{m/s}$) was similar to that at 37°C , indicating a low Arrhenius activation energy as expected for AQP-facilitated water transport. Reducing apical solution pH to 5 did not change P_f significantly, whereas a basolateral solution pH of 5 decreased P_f by $> 90\%$, providing functional evidence for the involvement of basolateral membrane AQP3 in water permeability; the water permeability of AQP3 is inhibited at low pH, whereas that of other AQPs is not.¹⁹

Non-CF and CF P1 cell cultured were also studied to mimic the culture conditions employed by Donaldson et al.¹ As summarized in Figure 2D, P1 cultures had $\sim 50\%$ lower water permeability than P0 cultures, but without significant differences comparing non-CF vs. CF cultures, or control cultures vs. cultures exposed apically to $500 \mu\text{M}$ amiloride. Finally, as an additional attempt to look for amiloride-sensitive water transport, water permeability was measured in P0 cultures in the presence of both apically and basolaterally added amiloride ($500 \mu\text{M}$). As seen from the raw fluorescence data in Figure 3E, osmotic water flux was not inhibited by high-dose amiloride, indicating lack of amiloride inhibition of apical or basolateral AQPs.

Amiloride-Independent Plasma Membrane Water Permeability in HBE Cultures

Plasma membrane water permeability in P0 HBE cultures was determined using a calcein-quenching method, which is based on rapid changes in cytoplasmic calcein fluorescence in response to changes in concentration of cytoplasmic anionic proteins and hence to changes in cell volume (Fig. 3A, Ref. ¹⁵). Supports with calcein-loaded HBE cells were mounted in a perfusion chamber for continuous measurement of cytoplasmic calcein fluorescence. Switching between isosmolar and hyperosmolar perfusates produced reversible changes in fluorescence with biexponential kinetics (Fig. 3B), probably reflecting the heterogeneous distribution of AQPs and the complicated geometry of bronchial epithelia. P_f was quantified from initial kinetics of fluorescence change in response to osmotic gradients as described under Methods. As summarized in Figure 3C, plasma membrane P_f was not significantly affected by inclusion of 500 μ M amiloride in the perfusates.

Aquaporin Expression in HBE Cultures

AQP expression was characterized in P0 HBE cells. Hematoxylin and eosin-stained transverse paraffin sections confirmed the differentiation of 2-week old cultures into a \sim 20 μ m thick pseudostratified epithelium with numerous cilia (Fig 4A). Cultures were scraped for RT-PCR analysis, which detected mRNA for several AQPs (Fig 4B). Transcripts of AQP3, AQP4, and AQP5 were found in highest abundance, consistent with previous studies (see Discussion). Lesser, but non-zero expression of AQP1, AQP6, and AQP7 mRNA was detected. Quantitative real-time RT-PCR was done to compare expression of the principal AQPs in P0 HBE cultures from non-CF vs. CF airways. As

summarized in Figure 4C, no significant differences were found in AQP transcript expression in non-CF vs. CF cells. Immunofluorescence done on paraffin sections of HBE cultures and intact human bronchus demonstrated AQP3 and AQP4 protein expression on basolateral membranes, while AQP5 protein expression was not detected. Positive control staining of kidney for AQP3 and AQP4 is shown, and of salivary gland for AQP5.

Amiloride-Independent Water Permeabilities in AQP-Expressing FRT Cells

We next investigated possible effects of amiloride on the major lung AQPs, including AQP1 (expressed in microvascular endothelia), using AQP-transfected epithelial cells and intact mouse lung. Transepithelial and plasma membrane water permeabilities were measured in FRT cells expressing either YFP (control), AQP1, AQP3 or AQP4. Transepithelial water permeability of FRT cell lines grown on Transwell supports was measured after cultures formed electrically tight monolayers. Water permeabilities of AQP-expressing FRT cells were greater than that in control cells, and not sensitive to amiloride (Fig. 5A, top). Figure 5A (bottom) summarizes transepithelial P_f values. Plasma membrane water permeability was measured on the FRT cells, with calcein fluorescence curves fitted to single-exponential functions (representative traces for FRT-AQP3 and FRT-AQP4 cells shown in Fig 5B, top). In agreement with measurements of transepithelial water permeability, plasma membrane P_f was increased with AQP expression, and not sensitive to amiloride (Fig. 5B, bottom).

Amiloride-Insensitive Airspace-Capillary Water Permeability in Perfused Mouse Lung

Last, the effect of amiloride was investigated in intact, perfused mouse lung using a pleural surface method to measure airspace-capillary osmotic water permeability.¹⁸ The airspace compartment was filled with isotonic fluid containing FITC-dextran as a volume marker. The kinetics of pleural surface FITC-dextran fluorescence was measured in response to changes in osmolality of the pulmonary artery perfusate. There was rapid osmotic equilibration across the airspace-capillary barrier, which was not affected by inclusion of 500 μM amiloride in the airway instillate and pulmonary artery perfusate (Fig. 6A, top). In agreement with previous results,²⁰ osmotic equilibration was ~ 10 -fold slowed in lungs of AQP5-deficient mice (Fig. 6A, bottom), indicating the involvement of AQP5 in airspace-capillary osmotic water transport. The rates of osmotic water equilibration in lungs from wild-type mice (with and without amiloride) are summarized in Figure 6B.

Discussion

The primary purpose of this study was to investigate a proposed AQP-dependent mechanism to account for the clinical effects of nebulized hypertonic saline (HS) and amiloride on lung function in CF. The validity of the proposed mechanism of clinical benefit involving amiloride-sensitive airway AQPs has important implications regarding the use of HS vs. non-salt hyperosmolar agents in CF therapy, as well as in the proposed use of amiloride-type ENaC inhibitors in preventing ASL dehydration.

HS is being used increasingly as a chronic therapy in CF, particularly following the recent publication of two clinical trials in the *New England Journal of Medicine* demonstrating clinical benefit.^{1,2} The larger of the two studies reported that 4 mL of 7% HS nebulized twice daily for 48 weeks decreased exacerbation rate by 56% in CF subjects.² Exacerbations were defined by the need for intravenous antibiotics, or using a symptom score involving increased sputum production, lethargy, dyspnea and fever. In previous smaller studies of CF subjects, a single nebulized dose of 6–7% HS increased mucociliary clearance at 60 and 90 min, as measured by radionucleotide imaging.^{3,5} Increased mucociliary clearance was dose-dependent up to 12% HS in 10 adults treated with a single dose and tested at 90 min.⁴ In a 2-week study in 52 CF subjects, 10 mL of 6% HS improved lung function as measured by a 12% increase in forced expiratory volume in one second (FEV1).⁶ HS has also been shown to increase mucociliary clearance in healthy subjects and in subjects with asthma or chronic obstructive lung disease.^{21,22} Various non-salt hyperosmolar agents have been posited to improve mucus clearance in CF and other chronic inflammatory lung diseases. The best-studied non-salt hyperosmolar agent is mannitol. In 12 CF subjects, single-dose administration of 300 mg mannitol as a dry powder improved bronchial mucus clearance at 60 min, though there was a small decline in FEV1 immediately after inhalation that was unresponsive to bronchodilator premedication.⁵ The same dose of mannitol improved mucus clearance two-fold in healthy, asthmatic, and bronchiectatic subjects.^{21,23} A 12-day trial of 400 mg mannitol daily in 9 non-CF bronchiectatic subjects gave no change in FEV1, but improved various sputum characteristics such as surface tension and spinnability.²⁴ Another inhaled hyperosmolar agent, xylitol, reduced ASL salt concentration in CF and

non-CF airway epithelia in vitro.²⁵ Pretreatment of human airway explants for 1 hour with 60–80 mg/mL xylitol reduced binding of a *Burkholderia cepacia* isolate.²⁶

As part of the present study we characterized AQP expression and function in water transport across human bronchial epithelial cells. As discussed in the Introduction, a central prediction of the mechanism proposed by Donaldson et al. is the inhibition of AQP water permeability by amiloride. To support their mechanism, the authors measured transepithelial flux across HBE cultures in response to an apically directed mannitol gradient as we have done here (Fig. 2A), with two differences. First, in their study, the concentration of Texas Red-dextran was measured in the basolateral (rather than apical) solution. Second, in their study fluorescence was measured by confocal microscopy, without any buffer sampling. They detected membrane transport rates as changes in cell height over time, with cytoplasmic calcein fluorescence imaged using reconstructed x-z confocal stacks. From both approaches, they reported a >70% reduction in osmotic water transport by 100–400 μ M amiloride in non-CF and CF HBE cultures. Amiloride also prevented the transient increase in ASL volume upon acute addition of perfluorocarbon-dispersed NaCl to the mucosal surface of epithelial cultures. HgCl_2 , a toxic and non-specific inhibitor of AQPs, dramatically inhibited this ASL volume response, though this finding appears at odds with their prior report of a much milder (~30 %) reduction of transepithelial and membrane water permeability by apically added HgCl_2 .⁸ Based on these data, the authors proposed that inhibition of airways AQPs by amiloride accounted for clinical effect, and supported the hypothesis of ASL dehydration in CF.

Here, using essentially the same airway epithelial cell culture model used Donaldson et al., we found no effect of amiloride on transepithelial or plasma membrane osmotic water permeability. Our fluorescence-based methods are capable of detecting small water permeability differences of under 10%. Also, we found no effect of amiloride on the water permeability of individual airway/lung AQPs in transfected epithelial cells, or in AQP5-dependent airspace-capillary water permeability in intact perfused mouse lung. We conclude that amiloride does not inhibit osmotically-driven water transport in the airways or lung, indicating the need to identify other mechanism(s) to explain the paradoxical clinical observations reported by Donaldson et al. The discrepancy between our findings and those of Donaldson et al. may be related to differences in measurement techniques, as discussed above. The techniques of Donaldson et al. were first employed by Matsui et al.⁷ in characterizing HBE water permeabilities. This earlier study reported in both non-CF and CF P1 cultures a plasma membrane P_f (~90 $\mu\text{m/s}$) ~2-fold less than transepithelial P_f (~160 $\mu\text{m/s}$), which is a physical impossibility for a tight epithelium since the apical and basolateral membranes are barriers in series. Here, our results for P0 cultures are very different: a higher membrane P_f (~200 $\mu\text{m/s}$), which is ~4-fold greater than transepithelial P_f (~50 $\mu\text{m/s}$). For non-CF and CF P1 cultures, we found a lower transepithelial P_f (~25 $\mu\text{m/s}$). Our results are consistent with the predicted lower transepithelial permeability of a multi-layered cell culture.

Without confirmed inhibition of AQP function, it remains difficult to understand the reported deleterious clinical effect of amiloride. Several small studies, including that by Donaldson et al.,¹ have shown that amiloride does not reverse the HS-mediated acute increase in mucociliary clearance. For example, in 16 healthy subjects, a single dose of

inhaled amiloride plus 7% HS did not increase or decrease mucociliary clearance compared to 7% HS alone.²⁷ There is some evidence to suggest that inhaled amiloride alone, not paired with HS, may have a beneficial effect on mucociliary clearance in healthy and CF subjects.^{27,28} However, it is reported that amiloride should not remain in lung tissue long enough to have significant long-term effect on lung function.²⁹ Amiloride is known to inhibit Na^+/H^+ exchange, so it is possible that the apparently negative effects of amiloride in the presence of a large hyperosmotic load are related to action at other site(s) on airway epithelial cells, via alteration of cell pH regulation or ion balance.

Prior immunolocalization studies have reported the expression of AQP4 at the basolateral membrane surface in epithelial cells throughout large and small airways in mice, rats and humans (reviewed in Ref. ³⁰). AQP3 was found to have a more limited expression pattern in basolateral membranes in basal cells of large and central airways and nasopharynx. Several studies have shown the expression of AQP1 in microvascular endothelia through the airways/lung, but not in epithelial cells.^{31,32} AQP5 is expressed strongly type I alveolar epithelial cells in humans and rodents, and likely in some airway epithelial cells in human large airways.^{32,33} In well-differentiated primary cultures of human airway epithelial cells and in fixed human bronchi, we found here expression of AQP3 and AQP4 in the basolateral membranes of airway epithelia, but did not detect AQP5 protein expression. However, the lack of AQP5 immunostaining probably reflects a lack of antibody specificity rather than the absence of functional protein, given the demonstrated presence of AQP5 in nasal and bronchial epithelial cells in previous studies.³³

Prior functional studies have suggested the involvement of AQPs in airway water permeability. Our initial measurements in microperfused small airways from guinea pig showed high transepithelial water permeability ($P_f \sim 50 \mu\text{m/s}$) that was weakly temperature-sensitive and was mercury-insensitive, suggesting the involvement of AQP4.⁷ Recent data from spheroid explants of human nasal polyps provided evidence for AQP5 function in airway epithelia. In these large, spherical airway cell monolayers, with ciliated apical membrane facing outward, Pederson et al.⁹ reported high membrane P_f ($\sim 150 \mu\text{m/s}$) that was sensitive to brief exposure to low-concentration mercury. Here, our high P_f values for HBE cultures and the weak temperature-dependence of permeability suggest AQP-mediated water movement (Fig. 2). Additionally, the reduced transepithelial osmotic water permeability under low pH in the basal (but not apical) membrane-facing solution provides indirect evidence for function of AQP3 (the only pH-regulated airway AQP regulated) in HBE basolateral membranes.¹⁹ CF cultures had similar water permeability to non-CF cultures, consistent with our RT-PCR data (Fig. 3C) and with previous reports.^{8,9}

On theoretical grounds the functioning of airway AQPs is not expected to be a significant determinant of ASL volume, composition or other properties. Because the lipid bilayer in plasma membranes has substantial water permeability, the presence of AQPs generally increases plasma membrane water permeability by only 5–10 fold, which is important for rapid fluid movement such as in kidney or salivary gland, but not for the many orders of magnitude slower fluid movement in the lung (reviewed in Ref.³⁴). Indeed, despite 10-fold slowed osmotic water permeability in mouse lung by deletion of AQP1 and AQP5, isosmolar fluid absorption was unaffected.^{20,35} Also, we reported

previously that deletion of each of the airway/lung aquaporins (AQP1, AQP3, AQP4 and AQP5), individually and in combinations, did not affect ASL volume or ionic composition, and had only minimal effect of airway hydration at maximal respiratory rates.¹⁰

The discussion above indicates the difficulty in ascribing aquaporin function, and increased ASL volume in general, to account for the effects of nebulized HS. Another potential problem with the hypothesis of increased ASL volume is that the excess fluid added to the intact airways/lung is likely to dissipate over minutes or tens of minutes, rather than produce a sustained increase in ASL volume over hours between hypertonic saline treatments. Because of the large surface-to-volume ratio of the alveoli and airways and their high water permeability, added hypertonic fluid becomes nearly isotonic within one minute due to osmotic water efflux into the airspaces. We showed rapid osmotic equilibration initially in sheep lung,³⁶ and later in other mammals,¹⁸ including mouse as seen in Figure 6. Because of rapid isosmolar fluid absorption in mammalian lung, including human lung (reviewed in Ref. ³⁷), the ~40 mL of isosmolar fluid produced by nebulizing 5 mL of 7 % HS is likely to be absorbed in < 15–30 min. However, the exact clearance rate of HS would depend on its distribution in small vs. large airways following nebulization. Rapid isosmolar fluid absorption has also been shown in the CF lung despite absent CFTR, because basal, cAMP-independent lung fluid absorption does not involve CFTR.³⁸ Thus, it is difficult to reconcile the clinical benefit of HS with the expected transient increase in ASL volume; however, the exact location of excess fluid, in terms of airways vs. alveoli and periciliary vs. mucus fluid, is not known. The

increased ASL volume mechanism would also predict better outcome of inhaling non-absorbed solutes such as mannitol or xylitol, which from clinical studies is not the case.⁵

Alternative mechanisms have been proposed to account for the apparent clinical benefit of inhaled hyperosmolar agents. One mechanism involves the direct effects of NaCl and mannitol on mucus rheology.⁵ HS has been proposed to reduce mucin entanglement by shielding fixed negative charges on the mucin backbone; mannitol has been proposed to compete with oligopolysaccharides on mucin macromolecules, thereby disrupting hydrogen bonds and reducing entanglements.^{39,40,41} A proposed mechanism for benefit of mannitol is based on the hypothesis that a relatively salty ASL in CF decreases innate immune defenses such as lysozyme, lactoferrin, and beta-defensins. If correct, a nonionic osmotic agent such as mannitol might be of benefit by reducing ASL salt concentration.^{5,25,42} Another proposed mechanism is the induction of cough in subjects inhaling hyperosmolar agents, which are quite irritating to the airways, although some studies concluded that changes in the mucociliary clearance are unlikely to be attributed to increased cough.^{3,4,22} Another proposed mechanism involves the direct or indirect action of hyperosmotic agents on mucus-secreting cells or sensory nerves in stimulating mucus secretion, whereby increased mucus secretion and ciliary action are proposed to 'flush out' sticky, bacteria-laden secretions.⁵ We would add to this list the possibility of transient osmotic flow-induced convection of mucus into the airways as a major factor in the clinical benefit of HS. A critical re-examination of the mechanism(s) by which HS improves lung function in cystic fibrosis might lead to a better, mechanism-based approach for inhaled osmolar therapy.

References

1. Donaldson SH, Bennett WD, Zeman KL, Knowles MR, Tarran R, Boucher RC. Mucus clearance and lung function in cystic fibrosis with hypertonic saline. *N Engl J Med.* 2006;354: 241–250.
2. Elkins MR, Robinson M, Rose BR, et al. A controlled trial of long-term inhaled hypertonic saline in patients with cystic fibrosis. *N Engl J Med.* 2006;354:229–240.
3. Robinson M, Regnis JA, Bailey DL, King M, Bautovich GJ, Bye PT. Effect of hypertonic saline, amiloride, and cough on mucociliary clearance in patients with cystic fibrosis. *Am J Respir Crit Care. Med.* 1996;153:1503–1509.
4. Robinson M, Hemming AL, Regnis JA, et al. Effect of increasing doses of hypertonic saline on mucociliary clearance in patients with cystic fibrosis. *Thorax.* 1997;52:900-903.
5. Robinson M, Daviskas E, Eberl S, et al. The effect of inhaled mannitol on bronchial mucus clearance in cystic fibrosis patients: a pilot study. *Eur Respir J.* 1999;14:678–685.
6. Eng PA, Morton J, Douglass JA, Riedler J, Wilson J, Robertson CF. Short-term efficacy of ultrasonically nebulized hypertonic saline in cystic fibrosis. *Pediatr Pulmonol.* 1996;21:77–83.
7. Folkesson H, Matthay M, Frigeri A, Verkman AS. High transepithelial water permeability in microperfused distal airways: evidence for channel-mediated water transport. *J Clin Invest.* 1996;97:664–671.
8. Matsui H, Davis CW, Tarran R, Boucher RC. Osmotic water permeabilities of cultured, well-differentiated normal and cystic fibrosis airway epithelia. *J Clin Invest.* 2000;105:1419–1427.
9. Pedersen PS, Procida K, Larsen PL, Holstein-Rathlou NH, Frederiksen O. Water permeability in human airway epithelium. *Pflügers Arch.* 2005;451:464–473.
10. Song Y, Jayaraman S, Yang B, Matthay MA, Verkman AS. Role of aquaporin water channels in airway fluid transport, humidification and surface liquid hydration. *J Gen Physiol.* 2001;117;573–582.
11. Yamaya M, Finkbeiner WE, Chun SY, Widdicombe JH. Differentiated structure and function of cultures from human tracheal epithelium. *Am J Physiol.* 1992;262:L713–L724.

12. Fulcher ML, Gabriel S, Burns, KA, Yankaskas JR, Randell SH. Well-differentiated human airway epithelial cell cultures. *Methods Mol Med*. 2005;107:183–206.
13. Pedemonte N, Lukacs GL, Du K, et al. Small-molecule correctors of defective DeltaF508-CFTR cellular processing identified by high-throughput screening. *J Clin Invest*. 2005;115 :2564–2571.
14. Saadoun S, Papadopoulos MC, Hara-Chikuma M, Verkman AS. Impairment of angiogenesis and cell migration by targeted aquaporin-1 gene disruption. *Nature*. 2005;434:786–792.
15. Solenov E, Watanabe H, Manley GT, Verkman AS. Sevenfold-reduced osmotic water permeability in primary astrocyte cultures from AQP-4-deficient mice, measured by a fluorescence quenching method. *Am J Physiol*. 2004;286:C426–C4232.
16. Levin MH, Verkman AS. Aquaporin-dependent water permeation at the mouse ocular surface: in vivo microfluorimetric measurements in cornea and conjunctiva. *Invest Ophthalmol Vis Sci*. 2004;45:4423–4432.
17. Ma T, Song Y, Gillespie A, Carlson EJ, Epstein CJ, Verkman AS. Defective secretion of saliva in transgenic mice lacking aquaporin-5 water channel. *J Biol Chem*. 1999;274:20071–20074.
18. Carter EP, Matthay MA, Farinas J, Verkman AS. Transalveolar osmotic and diffusional water permeability in intact mouse lung measured by a novel surface fluorescence method. *J Gen Physiol*. 1996;108:133–142.
19. Zeuthen T, Klairke DA. Transport of water and glycerol in aquaporin 3 is gated by H(+). *J Biol Chem*. 1999;274:21631–21636.
20. Ma T, Fukuda N, Song Y, Matthay MA, Verkman, A.S. Lung fluid transport in aquaporin-5 knock-out mice. *J Clin Invest*. 2000;105:93–100.
21. Daviskas E, Anderson SD, Gonda I, et al. Inhalation of hypertonic saline aerosol enhances mucociliary clearance in asthmatic and healthy subjects. *Eur Respir J*. 1996;9:725–732.
22. Pavia D, Thomson ML, Clarke SW. Enhanced clearance of secretions from the human lung after the administration of hypertonic saline aerosol. *Am Rev Respir Dis*. 1978;117:199–203.
23. Daviskas E, Anderson SD, Brannan JD, Chan HK, Eberl S, Bautovich G. Inhalation of dry powder mannitol increases mucociliary clearance. *Eur Respir J*. 1997;10:2449–2454.

24. Daviskas E, Anderson SD, Gomes K, et al. Inhaled mannitol for the treatment of mucociliary dysfunction in patients with bronchiectasis: Effect on lung function, health status, and sputum. *Respirology*. 2005;10:46–56.
25. Zabner J, Seiler MP, Launspach JL, et al. The osmolyte xylitol reduces the salt concentration of airway surface liquid and may enhance bacterial killing. *Proc Natl Acad Sci USA*. 2000;97:11614–11619.
26. Saijan U, Moreira J, Liu M, et al. The novel model to study bacterial adherence to the transplanted airway: Inhibition of *Burkholderia cepacia* adherence to human airway by dextran and xylitol. *J Heart Lung Transpl*. 2004;23:1382–1391.
27. Sood N, Bennett WD, Zeman K, Brown J, Foy C, Boucher RC. Increasing Concentration of inhaled saline with or without amiloride. *Am J Respir Crit Care Med*. 2003;167:158–163.
28. App EM, King M, Helfesrieder R, Kohler D, Mattys H. Acute and long-term amiloride inhalation in cystic fibrosis lung disease. A rational approach to cystic fibrosis therapy. *Am Rev Respir Dis*. 1990;141:605–612.
29. Hirsch AJ, Sabater JR, Zamurs A, et al. Evaluation of second generation amiloride analogs as therapy for cystic fibrosis lung disease. *J Pharmacol Exp Ther*. 2004;311:929–938.
30. Borok Z, Verkman AS. Lung edema clearance: 20 years of progress: Invited review: Role of aquaporin water channels in fluid transport in lung and airways. *J Appl Physiol*. 2002;93:2199–2206.
31. Hasegawa H, Lian SC, Finkbeiner WE, Verkman AS. Extrarenal tissue distribution of CHIP28 water channels by in situ hybridization and antibody staining. *Am J Physiol*. 1994;266:C893–C903.
32. Nielsen S, King LS, Christensen BM, Agre P. Aquaporins in complex tissues. II. Subcellular distribution in respiratory and glandular tissues of rat. *Am J Physiol*. 1997;273:C1541–C1548.
33. Kreda SM, Gynn MC, Fenstermacher DA, Boucher RC, Gabriel SE. Expression and localization of epithelial aquaporins in the adult human lung. *Am J Respir Cell Mol Biol*. 2001;24:224–234.
34. Verkman AS. More than just water channels: unexpected cellular roles of aquaporins. *J Cell Sci*. 2005;118:3225–3232.
35. Bai C, Fukuda N, Song Y, Ma T, Matthay MA, Verkman AS. Lung fluid transport in aquaporin-1 and aquaporin-4 knock-out mice. *J Clin Invest*. 1999;103:555–561.

36. Folkesson HG, Matthay MA, Hasegawa H, Kheradmand F, Verkman AS. Transcellular water transport in lung alveolar epithelium through mercurial-sensitive water channels. *Proc Natl Acad Sci USA*. 1994;91:4970–4974.
37. Matthay MA, Folkesson H, Verkman AS. Salt and water transport across alveolar and distal airway epithelia in the adult lung. *Am J Physiol*. 1996;270:L487–L503.
38. Fang X, Fukuda N, Barbry P, Sartori C, Verkman AS, Matthay MA. Novel role for CFTR in fluid absorption from the distal airspaces of the lung. *J Gen Physiol*. 2002;119:199–207.
39. King M, Dasgupta B, Tomkiewicz RP, Brown NE. Rheology of cystic fibrosis sputum after in vitro treatment with hypertonic saline alone and in combination with recombinant human deoxyribonuclease I. *Am J Respir Crit Care Med*. 1997;156:173–177.
40. Wills PJ, Hall RL, Chan W, Cole PJ. Sodium chloride increases the ciliary transportability of cystic fibrosis and bronchiectasis sputum on the mucus-depleted bovine trachea. *J Clin Invest*. 1997;99:9–13.
41. Feng W, Garrett H, Speert DP, King M. Improved clearability of cystic fibrosis sputum with dextran treatment in vitro. *Am J Respir Crit Care Med*. 1998;157:710–714.
42. Durairaj L, Launspach J, Watt JL, et al. Safety assessment of inhaled xylitol in mice and healthy volunteers. *Respir Res*. 2004;5:13.

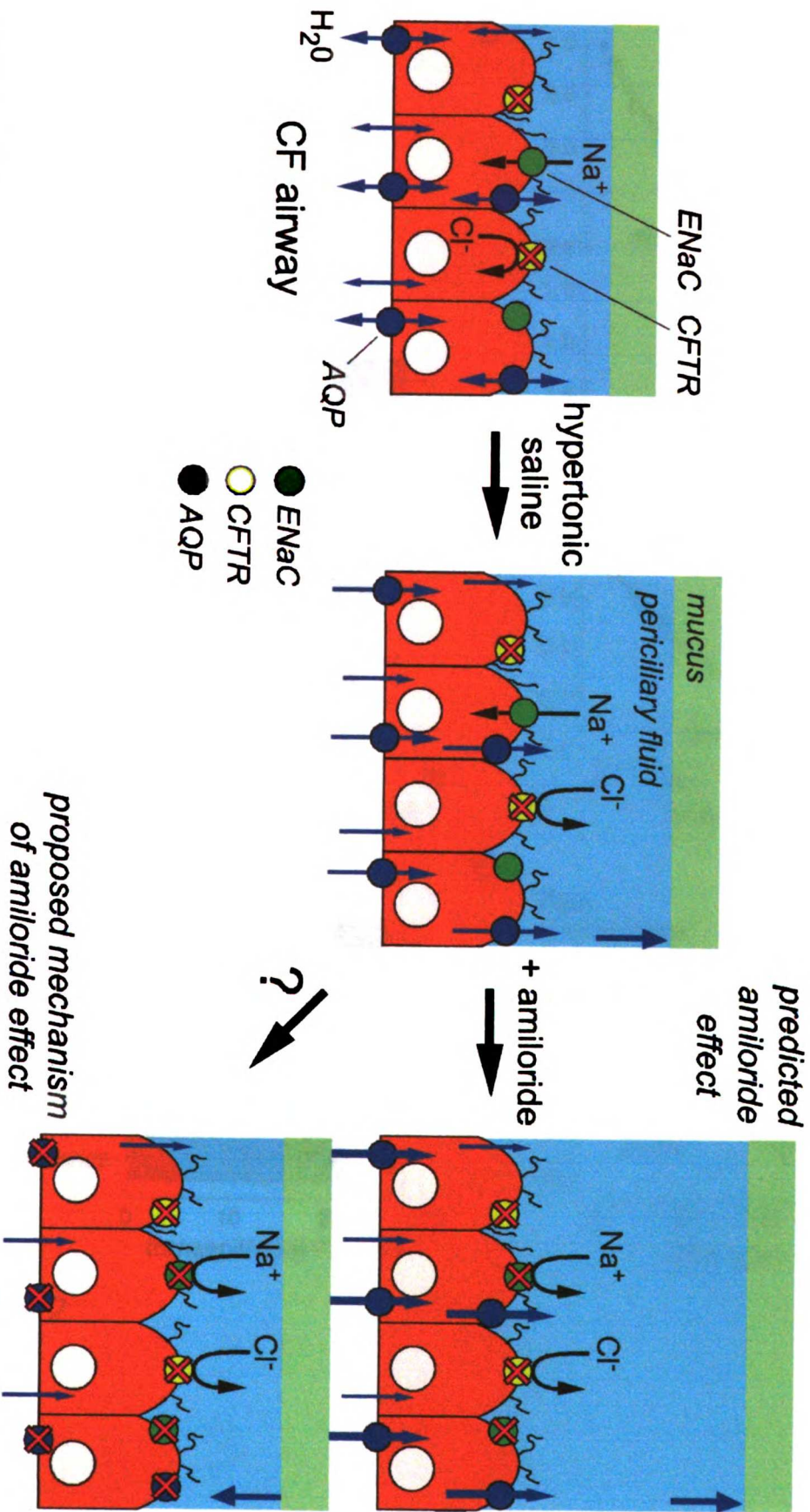


Figure 1

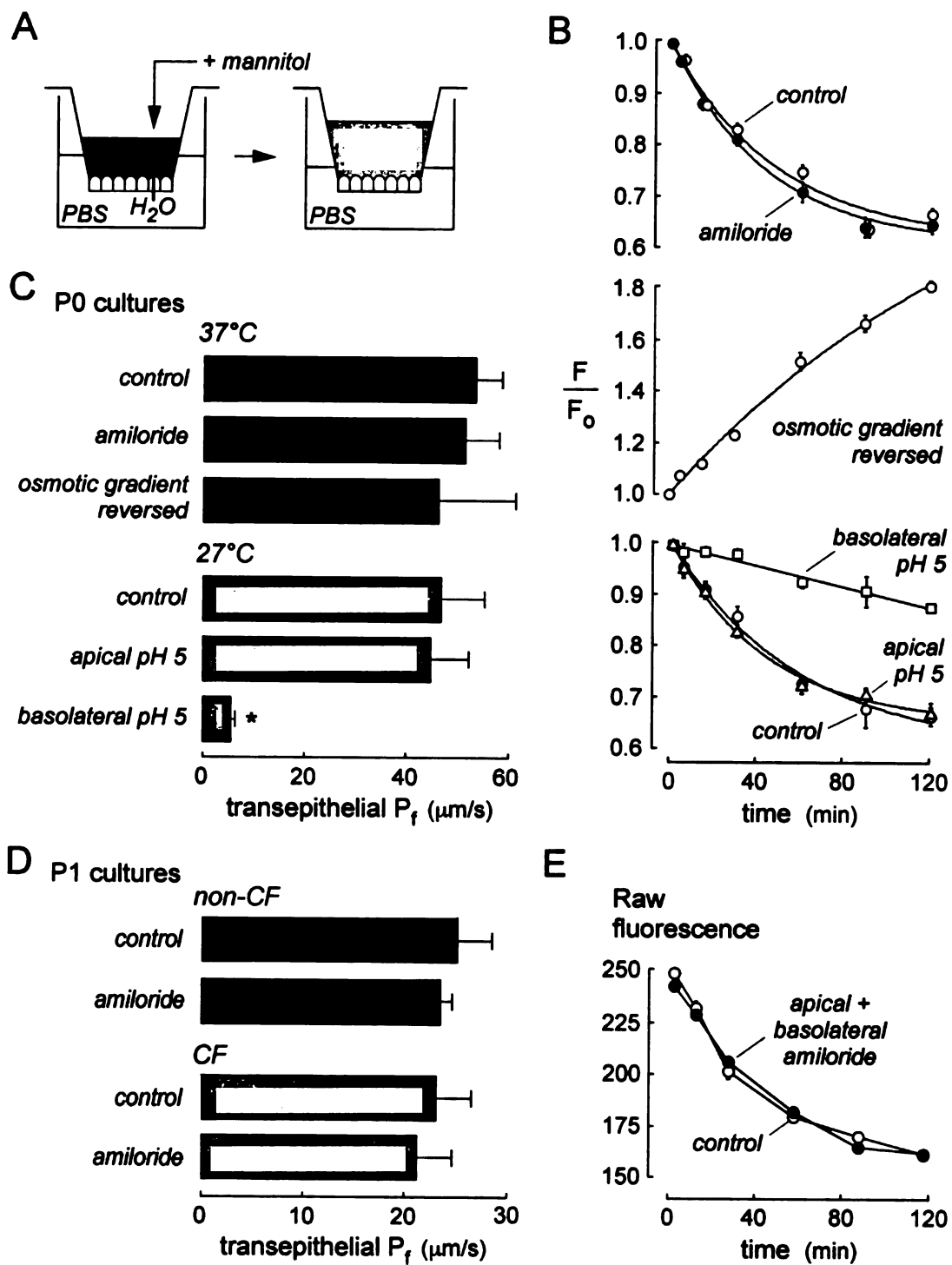


Figure 2

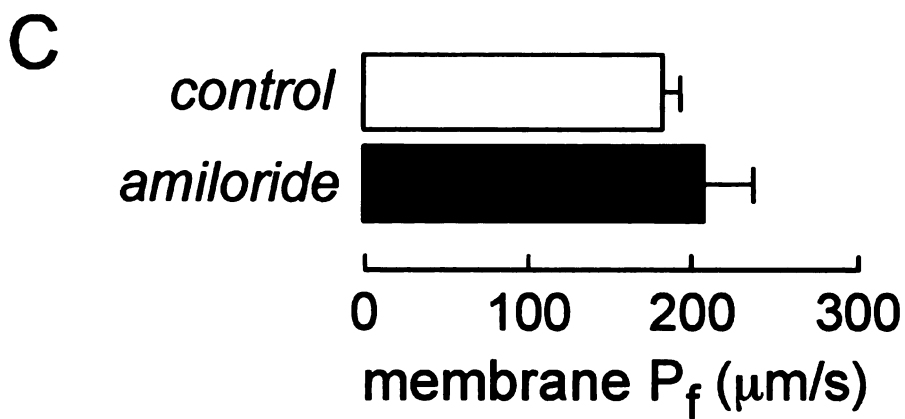
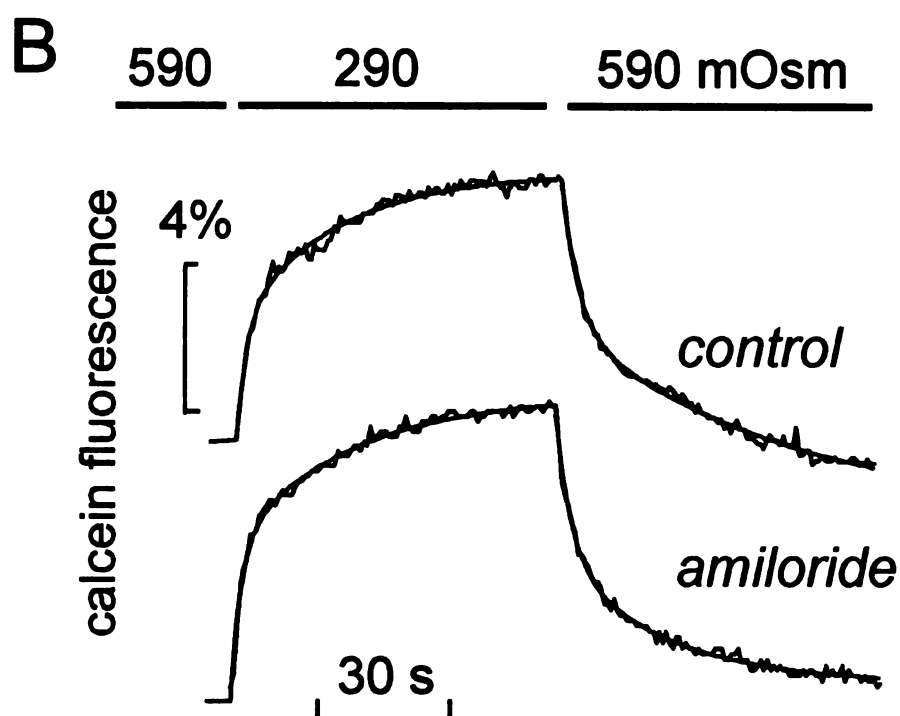
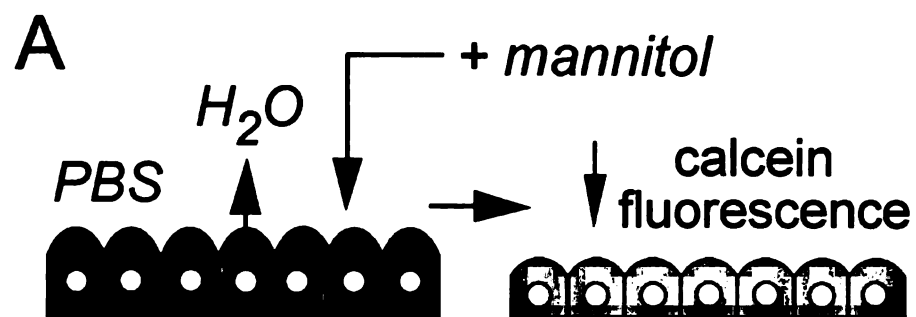


Figure 3

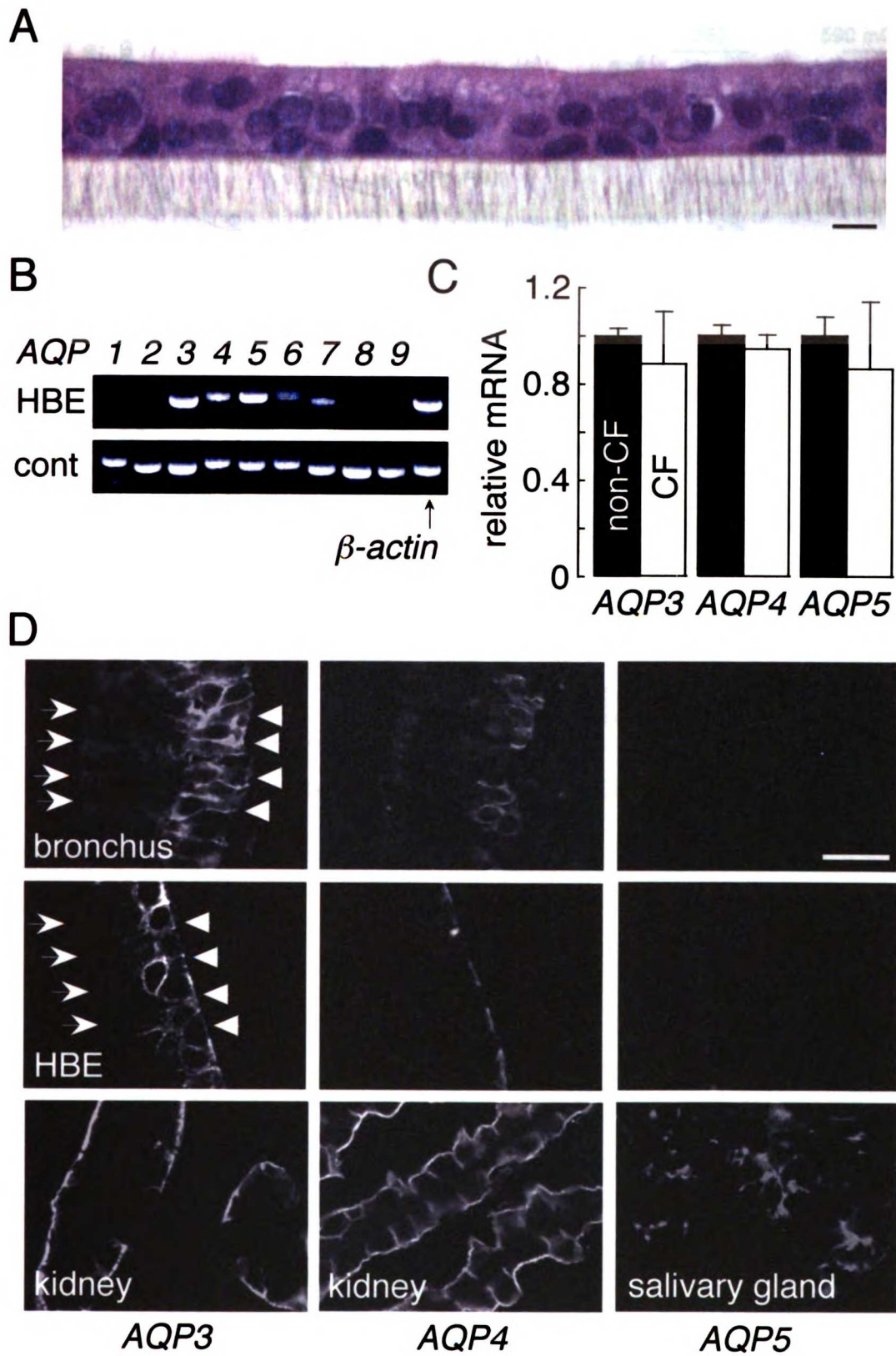


Figure 4

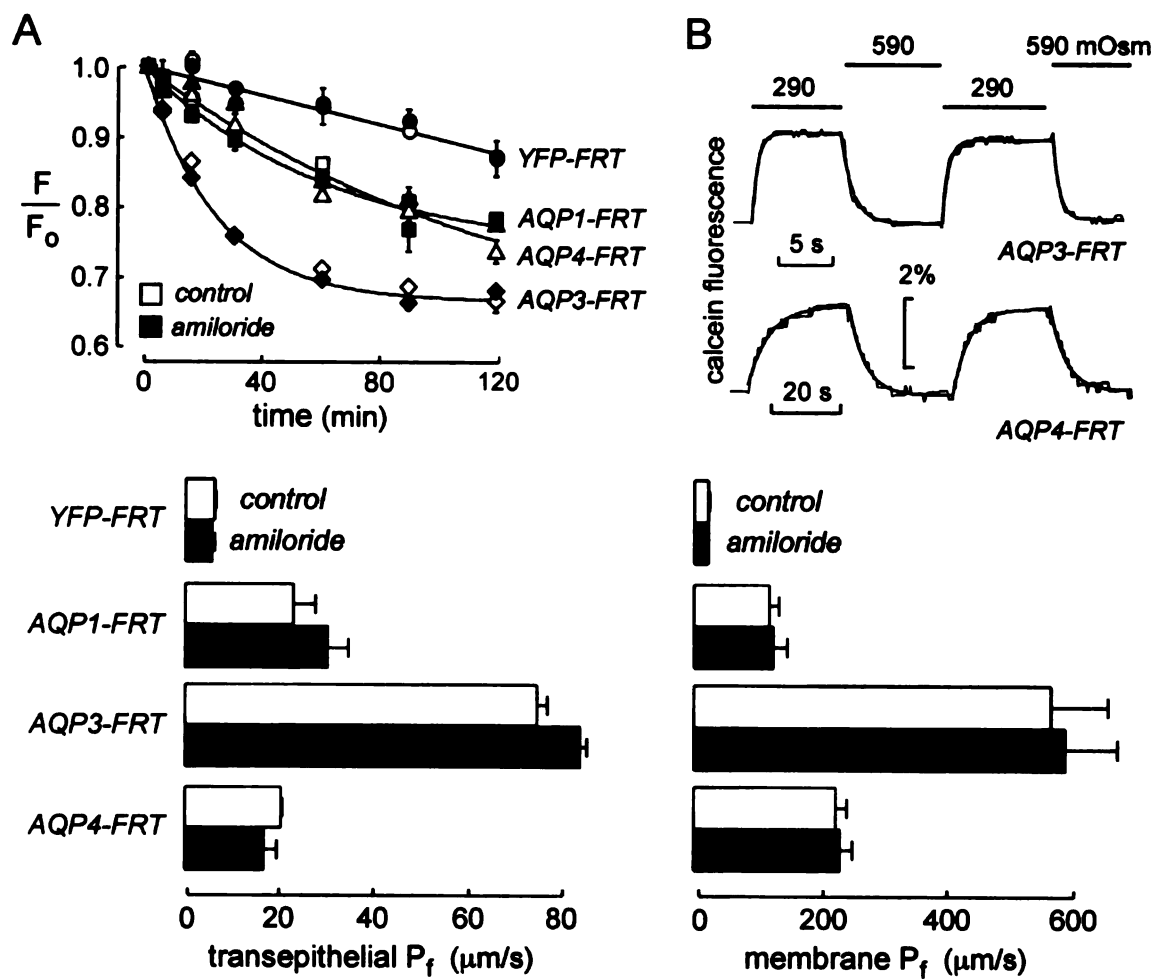


Figure 5

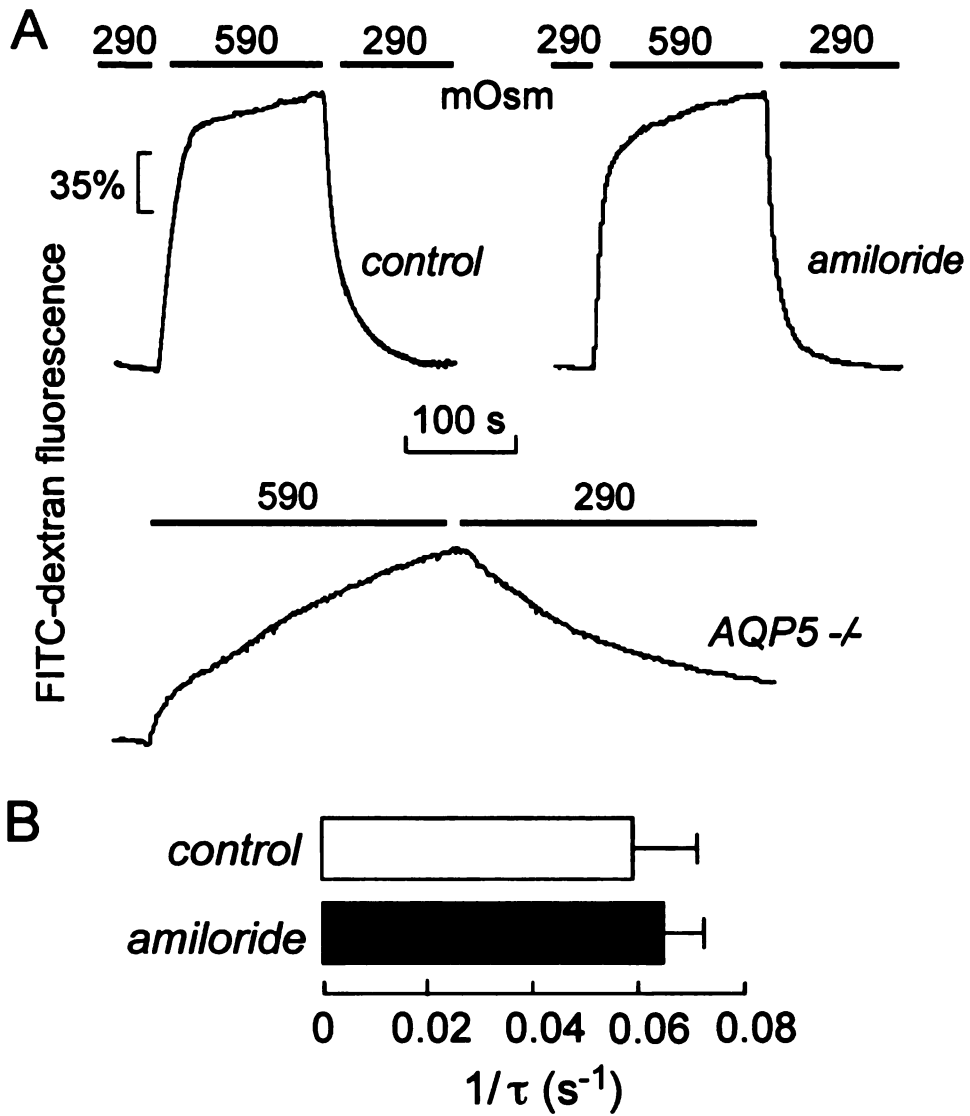


Figure 6

Figure Legends

FIGURE 1. Proposed mechanism of hypertonic saline and amiloride effects on airway surface liquid (ASL) in cystic fibrosis. In CF, periciliary fluid is depleted due to impaired Cl^- secretion through CFTR, and increased Na^+ absorption through ENaC (*left panel*). Hypertonic saline is proposed to increase ASL volume (*middle panel*) via AQP-mediated and/or transmembrane water movement (*blue arrows*). By inhibition of ENaC, amiloride is postulated to increase ASL volume by blocking Na^+ and fluid absorption (*right, top panel*). Amiloride inhibition of AQP water channels was proposed as a mechanism to account for the amiloride effect of negating the beneficial clinical effects of hypertonic saline (*right, bottom panel*). See text for explanations.

FIGURE 2. Transepithelial water permeability of human bronchial cell cultures. Water permeability across HBE cell layers measured by a dye dilution fluorescence method. (A) Schematic of osmotically induced transcellular water flux across porous Transwell membranes. Water movement from basal to apical solutions reduces the concentration of an inert volume marker in the apical solution. (B) Time course of osmotic water movement across P0 HBE cell cultures, with apical solution fluorescence normalized as F/F_0 , and single-exponential fits shown as solid lines (see Methods). *Top:* comparison of control cultures (*open circles*) with cultures exposed to 500 μM amiloride at their apical surface (*closed circles*). Measurements performed at 37 °C (7 cultures per group, \pm SE). *Middle:* time course of apical solution fluorescence upon inclusion of 300 mM D-mannitol in basal (rather than apical) surface-facing buffer (37°C, 4 cultures, \pm SE). *Bottom:* comparison of control cultures (*open circles*) with cultures exposed to low pH at

their apical (*open triangles*) or basolateral (*open squares*) surfaces (27 °C, 4 cultures, ± SE). (C) Summary of P_f for experiments in (B). * $P < 0.05$. (D) Summary of P_f for experiments done on P1 non-CF and CF HBE cells, in the absence and presence of 500 μM apical amiloride (37 °C, 4 cultures for each non-CF group and 5 cultures for each CF group, ± SE). (E) Time course of osmotic water movement across P0 HBE cells, comparing control cultures (*open circles*) with cultures exposed to 500 μM amiloride at both apical and basolateral surfaces (*closed circles*). Data expressed as absolute fluorescence in arbitrary units (4 cultures per group, ± SE).

FIGURE 3. Plasma membrane water permeability of human bronchial cell cultures. Water permeability measured by a calcein fluorescence quenching method. (A) Schematic of cell-volume-dependent calcein quenching, where apical plasma membrane exposure to hypertonic buffer induces cell shrinking, reducing cytoplasmic calcein fluorescence due to quenching by anionic cytoplasmic proteins. (B) Representative time-courses of calcein fluorescence in HBE cells in response to hyperosmolar challenge followed by return to isosmolar solution, in the absence (*top*) or presence (*bottom*) of 500 μM amiloride. Double-exponential fits used for P_f determination are overlaid (see Methods). (C) Summary of calculated P_f (3–6 curves averaged for individual cultures, 3 cultures per condition, ± SE). Differences not significant.

FIGURE 4. (A) Histology of well-differentiated HBE cells. Hematoxylin and eosin-stained section cut from non-CF culture embedded in paraffin. Scale bar = 20 μm. (B) AQP transcript expression in HBE cultures. *Top*: RT-PCR analysis of HBE cultures. *Bottom*: positive control taken from cDNA pooled from human brain, kidney, and lung. (C)

Quantitation of relative AQP3, AQP4, and AQP5 mRNA expression in P0 CF vs. non-CF HBE cells by fluorescence-based RT-PCR (see Methods; 2 CF and 3 non-CF subject isolates analyzed, \pm SE). (D) AQP3, AQP4 and AQP5 immunostaining of paraffin sections of human bronchus tissue (*top panes*), HBE culture (*middle panels*), and positive controls (mouse renal cortex, *bottom left*; renal medulla, *bottom middle*; salivary gland, *bottom right*). *Arrows* denote apical side and *arrowheads* denote basal side. Scale bar = 50 μ M.

FIGURE 5. Transepithelial and membrane water permeabilities in AQP-transfected FRT cell cultures. (A) Transepithelial osmotic water permeability of transfected FRT cells measured by dye-dilution. *Top*: averaged time courses of osmotic water movement in FRT cell cultures transfected with YFP (*circles*), AQP1 (*squares*), AQP3 (*diamonds*), and AQP4 (*triangles*), with apical solution fluorescence normalized as F/F_0 . Controls cultures (*open symbols*) were compared with cultures exposed to 500 μ M amiloride at their apical surface (*closed symbols*). Measurements performed at 37 °C (3 cultures per group, \pm SE). Single-exponential fits shown as solid lines. *Bottom*: summary of P_f values. Differences not significant. (B) Plasma membrane osmotic water permeabilities of YFP-, AQP-transfected FRT cells measured by calcein quenching. *Top*: representative time courses of calcein fluorescence in cultures of AQP3- (*top curve*) and AQP4- (*bottom curve*) transfected cells in response to hyperosmolar challenge and return to isosmolar solution, in the absence of amiloride. *Bottom*: summary of P_f (4–8 curves averaged from single cultures, 3 sets of cultures per condition, \pm SE). Differences not significant.

FIGURE 6. Airspace-capillary water permeability in perfused mouse lung. (A)

Representative traces of pleural surface FITC-dextran fluorescence from wild-type mouse lung without (*top, left*) and with (*top, right*) 500 μ M amiloride, and untreated lung of AQP5-null mouse (*bottom*). Pulmonary artery perfusate osmolality indicated. **(B)**

Summary of rates of capillary-airspace osmotic equilibration from experiments as in (A).

(4 mice per condition, \pm SE). Difference not significant.

CHAPTER 8.

Nanomolar Potency Small-Molecule Inhibitors of Urea Transporter UT-B Identified by High-Throughput Screening

Abstract

PURPOSE: Functional studies in knock-out mice indicate a critical role for urea transporters (UTs) in the urinary concentrating mechanism and in renal urea clearance. However, potent and specific urea transport blockers have not been available. Here, we used high-throughput screening to discover high-affinity small-molecule inhibitors of the UT-B urea transporter.

METHODS: A collection of 50,000 diverse, drug-like compounds was screened using a human erythrocyte lysis assay based on UT-B-facilitated acetamide transport. ~700 structurally similar analogs of 'hits' were also tested to establish structure-activity relationships and to identify potent inhibitors.

RESULTS: Primary screening yielded ~30 UT-B inhibitors belonging to the phenylsulfoxoxazole, benzenesulfonanilide, phthalazinamine and aminobenzimidazole chemical classes. Screening of analogs of 'hits' gave many active chemicals, the most potent of which inhibited UT-B urea transport with EC_{50} ~10 nM, with ~100% inhibition at higher concentrations. Phenylsulfoxoxozoles and phthalazinamines also blocked

rodent UT-B at higher concentrations ($EC_{50} \sim 200$ nM), and had good UT-B vs. UT-A specificity. The UT-B inhibitors did not reduce aquaporin-1-facilitated water transport. In AQP1-null erythrocytes, 'chemical UT-B knock-out' by UT-B inhibitors reduced by ~3-fold UT-B-mediated water transport, providing strong support for the hypothesis that UT-B contains an aqueous pore pathway.

CONCLUSIONS: UT-B inhibitors may represent a new class of diuretics, 'urearetics,' which are predicted to increase renal water and solute clearance in water-retaining states.

Urea is generated as the major end product of hepatic nitrogen metabolism and is excreted primarily by the kidney. Urea and NaCl are the major solutes in the hyperosmolar renal medulla. In the antidiuretic kidney urea is greatly concentrated with respect to plasma (up to 100 times in humans and 250 times in rodents) by countercurrent multiplication and exchange mechanisms.¹ Of central importance to these mechanisms is intrarenal urea recycling, which requires facilitated urea transport by molecular urea transporters (UTs). UTs are comprised of two major subfamilies encoded by different genes (UT-A and UT-B, reviewed in Refs. ^{2,3}). In kidney, a single UT-B isoform is expressed in vasa recta while several splice variant UT-A-type transporters are expressed in kidney tubule epithelia (reviewed in Ref. ⁴).

Phenotype analysis of mice separately lacking vasa recta UT-B or inner medullary collecting duct UT-A1/3 implicated UT involvement in the formation of concentrated urine and in renal urea clearance.^{5,6,7} The UT-B knock-out mice generated by our lab manifest a urea-selective urinary concentrating defect associated with urinary

hyposmolality and increased renal urea clearance.⁵ UT-B is also expressed outside of the kidney, most notably and in highest abundance in red blood cell (RBC) membranes. Loss-of-function human UT-B mutations result in greatly reduced RBC urea permeability and a mild urinary concentrating defect.^{8,9} The mouse and human phenotypes support the possible use of UT-B inhibitors as unique urea-clearance-enhancing diuretics, which we call ‘urearetics.’ However, studies in genetically modified mice are potentially confounded by changes in expression of other proteins such as membrane transporters. ‘Chemical knock-out’ by potent and specific small-molecule inhibitors would largely obviate these concerns.

The only available UT inhibitors include the non-specific membrane intercalating agent phloretin (acting at >0.5 mM), urea analogs such as thiourea, methylurea, and dimethylurea (acting at 50–100 mM),¹⁰ and chemically modified urea analogs (acting irreversibly at 30–100 μ M).¹¹ The goal of this study was to identify potent, small-molecule UT inhibitors. Since no structural information about UTs is available, nor are existing UT inhibitors useful for ‘lead-based’ discovery, our strategy to identify UT inhibitors was high-throughput screening of a drug-like small molecules with high chemical diversity.

Our high-throughput screening strategy, as diagrammed in Figure 1, was based on measurement of lysis of human RBCs after imposing a large, outwardly directed gradient of acetamide, a urea analog that is transported efficiently by UT-B. RBCs were chosen for the primary screening assay because of their: (a) availability in large quantities; (b) high urea permeability resulting from strong expression of only one UT, UT-B; and (c)

high aquaporin (AQP)-mediated water permeability (for a lysis-based assay). We used human RBCs for primary compound screening with the aim of discovering inhibitors that could be further developed as therapeutics. In the assay, imposing a large, outwardly directed gradient of acetamide causes cell swelling, which is limited by UT-B-facilitated acetamide efflux. Under appropriate conditions, UT-B inhibition slows acetamide efflux and increases cell lysis, which was assayed by near-infrared light scattering. Our cell-based lysis assay was validated and used to discover novel small-molecule UT-B inhibitors, which were then optimized by screening of chemical analogs, and further characterized.

Methods

Mouse and Human Blood Collection

Human venous blood obtained from a single donor (M.H.L.) was collected into Vacutainers coated with sodium heparin (Becton-Dickinson, Franklin Lakes, NJ), stored at 4 °C, and used within 48 hr of collection. All human procedures were approved by the University of California, San Francisco Committee on Human Research. Whole mouse blood was collected from 8–12 week-old (25–35 g) wild-type, AQP1-null,¹² or UT-B-null⁵ mice in a CD1 genetic background by orbital puncture following subcutaneous injection with sodium heparin (150 USP units). All animal protocols were approved by the University of California, San Francisco Committee on Animal Research.

Instrumentation and Compounds for High-Throughput Screening

Screening was carried out using a Beckman Coulter (Fullerton, CA) integrated system consisting of a 3-meter robotic arm, microplate carousel, liquid handling work station with parallel 96-well solution mixing and transfer (Biomek FX), plate sealer, and two fluorescence plate readers (FLUOstar Optima; BMG LABTECH GmbH; Durham, NC), each equipped with a 710 ± 5 nm absorption filter (Chroma, Rockingham, VT). Primary screening was done using a collection of 50,000 diverse, drug-like compounds (>90% with molecular size of 250–500 Da) from a commercial source (ChemDiv Inc., San Diego, CA). 96-well plates containing four compounds per well (each 2.5 mM) were prepared for screening and stored frozen in DMSO. Plates with one compound per well (at 10 mM in DMSO) were stored separately and used later to identify and characterize active compounds.

Screening Procedures

At the time of the assay, whole human blood was diluted to a hematocrit of 1% in hyperosmolar PBS containing 1.25 M acetamide and 5 mM glucose (1550 mOsm, measured using freezing point-depression osmometry; Precision Systems, Natick, MA). Identical assay results were obtained when washed/centrifuged RBCs were used instead of whole blood. RBC suspensions were maintained at room temperature for up to 2 hr by periodic pipette mixing. 99 μ L from a reservoir containing the RBC suspension was added to each well of a 96-well round-bottom microplate (FALCON, Becton Dickinson), to which test compounds were added (1 μ L, 25 μ M final compound concentration, 1% final DMSO concentration). After 6 min incubation, 20 μ L of the RBC suspension was

added rapidly to each well of a 96-well black-walled plate (Costar, Corning, NY) containing 180 μ L isosmolar buffer (PBS containing 1% DMSO) in each well. Vigorous mixing was achieved by repeated pipetting.

RBC lysis was quantified from a single time-point measurement of absorbance at 710-nm wavelength,^{13,14} made within 5 min after hypoosmolar shock. Absorbance values were stable for at least 1 hr. Each assay plate contained eight negative ‘no-lysis’ controls (isotonic buffer; PBS + 1.25 M acetamide with 1% DMSO) and eight positive ‘full-lysis’ controls (distilled H₂O with 1% DMSO) that were mixed with DMSO vehicle-treated blood. The statistical z' -factor, indicating ‘goodness of the assay,’¹⁵ was computed using data from test plates as defined by: $z' = 1 - 3[(SD_{pos} + SD_{neg}) / (A_{pos} - A_{neg})]$, where SD_i and A_i are the standard deviations and mean absorbance values for positive (*pos*) and negative (*neg*) controls. The percentage of RBC lysis in each test well of a given plate was calculated using control values from the same plate as: $\% \text{ lysis} = 100\% (A_{neg} - A_{test}) / (A_{neg} - A_{pos})$, where A_{test} is the absorbance value from a test well. During assay optimization, some test wells were incubated with the non-specific UT-B inhibitor phloretin (0.7 mM, dissolved at 100x in DMSO stock solution) as an additional positive control. Chemicals were purchased from Sigma-Aldrich (St. Louis, MO) unless otherwise noted.

Stopped-Flow Measurement of RBC Urea and Water Permeabilities

RBC urea and water permeabilities were assayed by stopped-flow light scattering using a Hi-Tech Sf-51 instrument (Wiltshire, UK). For measurement of urea permeability, dilutions of whole blood (human or mouse) in PBS (hematocrit ~0.5%)

were incubated with test compounds for 5 min and then subjected to a 250-mM inwardly directed gradient of urea. After an initial osmotic shrinking phase, the kinetics of increasing cell volume caused by urea influx was measured as the time-course of 90° scattered light intensity at 530 nm, with increasing cell volume resulting in reduced scattered light intensity. As a positive control, 0.7 mM phloretin was added to the RBC suspension prior to stopped-flow experiments. Measurements of water permeability were carried out similarly, with sucrose (cell-impermeant) used instead of urea to establish a 250-mM osmotic gradient. As a positive control, HgCl₂ (0.3 mM) was added to the RBC suspension prior to stopped-flow measurements. Osmotic water permeability coefficients (P_f) were computed from light scattering data as described.¹⁶

Inhibitor Optimization by Analysis of Structure-Activity Relationships (SARs)

Approximately 700 commercially available analogs (ChemDiv Inc. and Asinex; Moscow, Russia) of active compounds identified in the primary screen were tested against human and mouse UT-B using the RBC lysis assay. For some of the more active compounds dose-response experiments were done using human and/or mouse blood by the lysis assay. EC_{50} was calculated by non-linear regression to the equation: $\% \text{ lysis} = \% \text{ lysis}_{min} + (\% \text{ lysis}_{max} [inh]^H) / (EC_{50}^H + [inh]^H)$, where $[inh]$ is inhibitor concentration and H is the Hill coefficient.

Determination of EC_{50} for UT-B Inhibition from Stopped-Flow Measurements

EC_{50} for inhibition of RBC urea transport was determined independently by comparing stopped-flow light scattering curves to a model of cell shrinking-swelling. For

stopped-flow experiments, a 100-mM gradient of urea (for human RBCs) or *N*-methylurea (for mouse RBCs) was used to minimize competition effects (apparent urea and *N*-methylurea affinities at 23 °C are ~200 and 100 mM, respectively).¹⁰ *N*-methylurea, with >2-fold slower RBC permeability than urea, was used in mouse studies to better resolve overlapping water and urea transport kinetics. Dose-response data was also collected for human RBCs using a high concentration of 1 M urea to distinguish between competitive vs. non-competitive inhibitor binding.

The two coupled differential equations describing water efflux and solute influx in response to externally added urea or methylurea were numerically integrated using the forward Euler method ($\Delta t = 0.01$ s) to reproduce the biphasic changes in cell volume observed experimentally. Computations done using the smaller time step ($\Delta t = 0.001$ s) gave similar results, confirming the adequacy of the 0.01 s time step. Water flux, J_v (in cm^3/s), across erythrocyte membranes is: $J_v = -P_f S v_w [(I_e - I_c(i)) + (U_e - U_c(i))]$; solute flux, J_s (in mol/s), is: $P_s S (U_e - U_c(i))$. Permeability coefficients (P_f and P_s) are expressed in units of cm/s, cell surface area (S) in cm^2 , extracellular (e) and cellular (c) concentrations of impermeant (I) and urea/methylurea (U) solute in mol/cm^3 , and v_w is 18 mol/cm^3 . Initial conditions were: $I_e = I_c(0) = 2.9 \times 10^{-4} \text{ mol}/\text{cm}^3$, $U_e = 10^{-4} \text{ mol}/\text{cm}^3$, and $U_c(0) = 0$. For each time step, a new cell volume (normalized to the initial size; $V(i+1)/V(0)$) and a new cell permeant concentration ($U(i+1)$) were calculated from: $V(i+1)/V(0) = V(i)/V(0) - \Delta t P_f (S/V(0)) v_w [I_e (1 - V(i)/V(0)) + (U_e - U_c(i))]$ and $U_c(i+1) = U_c(i)/V(0) - \Delta t U_s (S/V(0)) v_w (U_e - U_c(i))$. Normalized cell volume was assumed to be inversely proportional to scattered light intensity. The product of P_f and the surface area-to-volume ratio ($S/V(0)$) was determined to be $3.4 \times 10^2 \text{ s}^{-1}$ and $8.5 \times 10^2 \text{ s}^{-1}$ for human

and mouse erythrocytes, respectively, from water permeability measurements. P_s was varied to reproduce experimental data, and EC_{50} was computed using non-linear regression (see above) of P_s vs. $[inh]$ data.

In some experiments, to determine the sidedness of inhibitor action, compounds were added only to the urea-containing solution (at concentrations 2 times higher than their EC_{50}) before mixing with RBCs in stopped-flow measurements. To assay for reversibility, compounds (at concentrations 4 times higher than their EC_{50}) were added to RBCs for 10 min and then washed by centrifugation prior to stopped-flow measurements.

Assay of UT-A1-Facilitated Urea Transport

MDCK cells stably transfected with rat UT-A1 (MDCK-UT-A1)¹⁷ were generously provided by Dr. Jeffrey Sands. Cells were grown in Dulbecco's Modified Eagle Medium (DMEM) with bicarbonate and supplemented with 10% fetal bovine serum (FBS), 25 mM HEPES buffer, penicillin G (100 U/mL), streptomycin (100 μ g/mL) and hygromycin (500 μ g/mL). For assay of urea flux, cells were grown on 12-mm collagen-coated Transwell inserts (0.4 μ m pore size; Costar) as described.^{17,18} Inserts were incubated in hygromycin-free medium for 1 hr in a 5% CO₂ tissue culture incubator (37°C), and then 2×10^5 cells/cm² were loaded onto each insert. Cells were used after culture for 4 days in hygromycin-free medium, at which time they formed tight monolayers (transepithelial resistance 500–600 Ω cm²).

UT-A1-facilitated urea flux in the basolateral-to-apical direction across unstimulated and forskolin-stimulated MDCK-UT-A1 cell layers was measured in

response to a 15-mM urea gradient. Experiments were carried out in 12-well plates in which PBS, containing either DMSO vehicle or forskolin, with or without UT-B inhibitor, added to both the apical-facing (0.2 mL) and basal-facing (1 mL) surfaces of cells on the porous filters. Cultures were incubated in the absence of urea for 30 min at 37°C. Then, the basal-facing solution was replaced with PBS (containing same components) with 15 mM urea. Five- μ L samples of apical fluid were collected at specified times during incubation at 37°C for assay of urea concentration using a commercial kit based on chromogenic urea complexation at 520-nm wavelength (Quantichrom™ Urea Assay Kit, BioAssay Systems, Hayward, CA). Forskolin (10 μ M), with or without UT-B transport inhibitors, was added from 1000x DMSO stock solutions (0.2% final DMSO content). Inhibition of UT-A1-mediated transport was defined as % inhibition = $100\% (A_{forsk} - A_{test}) / (A_{forsk} - A_{phlor})$. A_{forsk} , and A_{phlor} are averaged absorbance values (at 520 nm) for cultures treated with forskolin and forskolin + phloretin, respectively, and A_{test} are values from cultures treated with forskolin + test compound.

Results

Assay Development and Validation

An RBC lysis assay was optimized for identification of small-molecule UT-B inhibitors. As shown in Figure 1 and explained in the Introduction, UT-B inhibition was assayed by increased RBC lysis when urea- or acetamide-loaded RBCs were rapidly diluted into PBS. Conditions were optimized to give a robust assay with high sensitivity

and a low false-positive rate for high-throughput screening. Absorbance at 710 nm was measured as a read-out of RBC lysis to minimize interference by test compounds and hemoglobin. Urea and a panel of small urea-like solutes (formamide, *N*-methylurea, acetamide, proprianamide, butyramide and isobutyramide) were evaluated as the loading solute based on their transport kinetics and passage through UT-B. Acetamide was selected because its equilibration in RBCs was ~2-fold slower than water, which is optimal in an osmotic lysis assay, and because >95% of its transport in RBCs is UT-B-dependent (as determined by stopped-flow light scattering, data not shown).

The optimal acetamide loading concentration was determined to identify UT-B inhibitors in an automated, 96-well format. Figure 2A shows RBC lysis, determined by absorbance at 710 nm (O.D.₇₁₀), as a function of the acetamide concentration used to load RBCs prior to mixing with acetamide-free buffer. Greater lysis, seen as reduced O.D.₇₁₀, was found with increasing acetamide concentration, as expected. Fifty percent lysis was seen at ~1.6 M acetamide under control conditions (open circles) and at ~1.1 M when UT-B-facilitated acetamide transport was inhibited by phloretin (filled circles). To best distinguish between control vs. inhibited UT-B, we chose to use 1.25 M acetamide (dashed vertical line) for the assay. Other technical considerations that were addressed during assay optimization included maintenance of RBC viability and uniform suspension, mixing conditions (rates, volumes and pipette tip locations in wells) and incubation time/temperature. The goodness of the optimized assay was evaluated by screening a series of plates containing positive and negative controls (0 and 100% lysis), which gave a very good statistical *z*'-factor of 0.57 for the screen (Fig. 2B).

Identification and Optimization of Small-Molecule UT-B Inhibitors

A collection of 50,000 small, drug-like compounds with high chemical diversity was screened at 25 μM to identify UT-B inhibitors. Figure 2C shows the frequency histogram of O.D.₇₁₀ values for all test compounds in the primary screen. Most compounds showed no significant apparent UT-B inhibition based on little (<30%) RBC lysis. Approximately 100 compounds producing >75% lysis were selected for further evaluation.

After confirming active compounds using the 96-well plate RBC lysis assay, bona fide urea transport inhibition was confirmed by stopped-flow light scattering from the kinetics of urea influx (RBC swelling) in response to an inwardly directed urea gradient. Rapid mixing of an RBC suspension with a hyperosmolar solution containing excess 250 mM urea produced rapid cell shrinking due to osmotic water efflux, followed by cell swelling as urea (and water) influx occurred. Thirty-two compounds in four distinct chemical structural classes were identified that at 5 μM produced substantial inhibition (>95%) of UT-B-facilitated urea transport. Other compounds, with either much lower or no activity in the stopped-flow assay, probably had apparent UT-B inhibitory activity in the primary screen in part due to RBC toxicity and consequent increased lysis. Original stopped-flow urea transport data for one representative compound (at 5 μM) of each class is shown in Figure 2D (left). Tracings from control (no inhibitors) and phloretin-treated RBCs are provided for comparison. The new compounds at 5 μM inhibited UT-B-facilitated urea transport in human RBCs by >95%, which is as good as or better than that with 0.7 mM phloretin. Figure 2D (right) shows that none of the UT-B inhibitors, tested

at an even higher concentration of 25 μM , inhibited RBC osmotic water permeability as measured by cell shrinking in response to a sucrose gradient. Curves from negative control (no inhibitor) and positive control (HgCl_2 water transport inhibitor) are provided for comparison.

We next screened ~ 700 commercially available analogs of compounds from the four chemical classes in order to establish structure-activity relationships (SAR) and to potentially identify compounds with improved UT-B inhibitory potency. Analogs were screened at 25 μM . Concentration-inhibition data were obtained for those compounds producing $>75\%$ apparent UT-B inhibition by the RBC lysis assay. Figure 3A shows chemical structures of potent compounds from each of the phenylsulfoxyoxazole, benzenesulfonamide, phthalazinamine, and aminobenzimidazole classes. These structures are unrelated to phloretin or urea analog inhibitors. Figure 3B shows concentration-inhibition data with apparent EC_{50} values (in nM): urea_{inh}-101, 30; urea_{inh}-201, 300; urea_{inh}-302, 100; and urea_{inh}-404, 400. However, the apparent EC_{50} values in this acetamide-based RBC lysis assay are not true EC_{50} values because of non-linearity between acetamide permeability and percentage RBC lysis, and possible acetamide-inhibitor competition.

To determine EC_{50} values for urea transport inhibition directly, RBC urea transport was measured by stopped-flow light scattering using a non-saturating concentration of extracellular urea (to avoid possible competition effects). Figure 4A shows representative data for inhibition of RBC urea transport by urea_{inh}-101 and urea_{inh}-302. Urea permeability coefficients (P_s) were determined from light-scattering curves by

numerical integration of the flux equations for coupled RBC water/urea transport (see Methods). An example of computed concentration-inhibition data is plotted in Figure 4B. The deduced EC_{50} values from stopped-flow measurements were in general agreement with the EC_{50} values determined in the lysis assay. Of note, as expected, the computations indicated that 50% UT-B inhibition produces only a subtle (~2-fold slowing) change in the light-scattering curve, whereas the more obvious visual evidence for slowed kinetics is seen at >95% inhibition. Additionally, these computations indicated that many of the new inhibitors produced >99% UT-B inhibition.

To determine the sidedness of UT-B inhibitor action, RBCs were exposed externally to urea_{inh}-101 and urea_{inh}-302 at final concentrations of 0.05 and 0.2 μ M, respectively (~2 times their EC_{50}) just at the time of stopped-flow experiments (inhibitor inclusion only in urea-containing solution). Whereas urea_{inh}-101 did not inhibit urea transport under these conditions, suggesting an intracellular site of action, urea_{inh}-302 had a sizable effect. The inhibition of urea permeability by externally added urea_{inh}-302 was concentration-dependent at concentrations down to 0.05 μ M. To test reversibility of inhibition, RBCs were pre-incubated with urea_{inh}-101 or urea_{inh}-302 for 10 min (at 0.1 and 0.4 μ M, respectively), producing >95% transport inhibition. After washing, urea transport was identical to that in non-inhibitor-exposed RBCs, indicating fully reversible inhibition.

Structure-Activity Analysis of UT-B Inhibitors

UT-B inhibitory potencies for the most active compounds of each of the chemical classes are summarized in Tables 1–4. The conclusions from SAR analysis are

summarized in Figure 5. Class 1 compounds consisted primarily of phenylsulfoxyoxozoles, but also included several phenylsulfoxyimidazoles (urea_{inh}-130–132). In highly active compounds, unsubstituted thioglycoamide was present as R1 (urea_{inh}-101–119). Compounds with reduced activity often had amino groups such as mono/dialkylated amines (urea_{inh}-120–123), *n*-morpholino (urea_{inh}-124–125), and hexahydro-1-*H*-azepine-1-yl (urea_{inh}-126–128) as R1, whereas activity was lost with R1 as thioglycoamides or mono/dialkylated amides. The best compounds ($EC_{50} < 100$ nM) contained 2-thiophene or phenyl rings as R2, though 2-furan also gave submicromolar potency. Methyl or halo substitutions at the 4-position of the phenyl ring as R2 reduced activity, while compounds with 3/di/tri-substituted phenyl rings as R2 were inactive. For R3 substitutions, halo and methyl groups conferred substantial activity compared to unsubstituted analogs.

Most active benzenesulfonanilides of Class 2 contained either 2,5-dimethoxy groups (urea_{inh}-201–205) or a fused 1,4-dioxane ring at the 3,4 positions (urea_{inh}-207–216) of the aniline phenyl, with the former producing greater UT-B inhibition. Compounds with other mono/di-substitutions at R1/R2, including 3-methoxy, 4-amino, and 3,4-dimethoxy, were inactive. The benzenesulfonamide phenyl ring tolerated a range of mono-substitutions as R3, including bromo, fluoro, thiomethyl, methoxy, and acetyl (urea_{inh}-203–205, 209), but not methoxy or methyl functions. However, methoxy and methyl groups were tolerated as di-substitutions as R3/R5 (urea_{inh}-201, 208) and to a lesser extent as R3/R4 (urea_{inh}-212, 214).

SAR of Class 3 phthalazinamines indicated preferred mono-substitution at the 4 position of the 4-phenyl ring, especially with carboxamide or methoxy functions (urea_{inh}-301–308, 312). Other acceptable 4-phenyl mono-substitutions included 4-methyl, 4-hydroxy, 4-diethylcarboxamide, and 4-*n*-hydroethylcarboxamide (urea_{inh}-309–311, 314–317). Active phthalazinamines containing di-substitutions on this phenyl ring combined methyl at the 3-position, with a variety of unsubstituted and mono/di-alkylated sulfonyls at the 4-position (urea_{inh}-321–331). Alkylation of 1-amino resulted in complete loss of activity, whereas replacement by oxygen reduced activity partially (urea_{inh}-332, 333). Inhibitory activity was also lost when the 1-amino group was substituted by phenylmethyl rather than phenyl. Analogs were active when the *n*-phenyl-1-amino moiety was substituted at the 4-position, particularly with methyl and methoxy groups and mono/di-alkylated carboxamides (urea_{inh}-301–304); also well tolerated were hydroxy, sulfonyl, glycoamide and *n*-methyl-glycoamide substitutions (urea_{inh}-306, 307, 311, 312).

For the Class 4 aminobenzimidazoles, no substitutions were allowed at R1 except for methyl, which reduced activity (urea_{inh}-404 vs. 420). The 2-hydroxyphenylmethyl group was necessary for activity, with activity eliminated by replacement of hydroxy with methoxy or substituted sulfonyl amino groups. The loss of activity upon hydroxy-methylation could be due to disruption of hydrogen bond donor effects. Additional substitutions at the benzyl function, such as 5-bromo, 5-chloro, and 5-methyl, increased activity (urea_{inh}-401–406, 414–417), though compounds without 5-position substitutions were also active (urea_{inh}-407–413). In contrast, compounds with substituents at the 3-, 4- or 6-positions were generally inactive. Alkylation of the imidazole nitrogen (R3) was

favorable, especially with ethyl, *n*-propyl, isopropyl, and 2-propenyl groups (urea_{inh}-401–406, 409–411, 414–416). Several bulky alkyl chains carrying substituted amino functions were also active (urea_{inh}-407, 408).

UT-B Inhibitor Efficacy on Rodent UTs

In order to identify UT-B inhibitors for future application to mouse models, we screened the inhibitors of human UT-B for activity against mouse UT-B. Interestingly, whereas many highly active phenylsulfoxyoxozoles and phthalazinamines (Classes 1 and 3) against human UT-B were active against mouse UT-B by lysis assay, no benzenesulfonanilides or aminobenzimidazoles (Classes 2 or 4) were active even at 25 μM , which was surprising given the 85% sequence identity of human and mouse UT-B.⁵ Similar UT-B inhibitory potencies were measured in mouse and rat RBCs (data not shown), as expected from the closely related sequences of mouse vs. rat UT-B.

As done above with human RBCs, EC_{50} for the most potent compounds with activity in the mouse RBC lysis assay was determined by stopped-flow light scattering. Representative curves for two UT-B inhibitors (urea_{inh}-101 and urea_{inh}-302) are shown in Figure 6A. For these studies methylurea was used as the transported solute instead of urea because its transport is slower, allowing better estimation of EC_{50} values. Concentration-inhibition data indicated EC_{50} ~200 nM for mouse UT-B for the most potent Class 1 and 3 compounds. These compounds, when tested at 25 μM , did not affect urea transport in RBCs from UT-B-null mice (data not shown).

Because of significant sequence similarities between UT-B and UT-A urea transporter isoforms, we carried out concentration-inhibition studies for the active mouse UT-B inhibitors against UT-A. These studies were done using available MDCK cells expressing rat UT-A1. MDCK-UT-A1-expressing cells were grown on collagen-coated porous filters until they were electrically tight, at which point 15 mM urea was introduced into buffer bathing the basolateral cell surface. Figure 6B shows the kinetics of urea appearance in the apical solution. As reported previously, UT-A1-facilitated urea transport was strongly increased by the cAMP agonist forskolin, and inhibited by phloretin.¹⁷ Concentration-inhibition data were obtained at a 15-min time point, when urea accumulation in the apical bathing solution is approximately linear. Urea_{inh}-101 was more active ($EC_{50} \sim 1.2 \mu\text{M}$) against rat UT-A1 than urea_{inh}-302 ($EC_{50} \sim 15 \mu\text{M}$) (Figure 6C). For comparison, concentration-inhibition data are shown for mouse UT-B, indicating good selectivity of these compounds for UT-B over UT-A1. Neither urea_{inh}-201 nor urea_{inh}-404 significantly inhibited rat UT-A1 at 25 μM (not shown).

UT-B ‘Chemical Knock-out’ in RBCs Reveals UT-B-Facilitated Water Transport

Compounds urea_{inh}-101, and urea_{inh}-302, which have good inhibitory potencies against mouse UT-B, were used to test the hypothesis that UT-B contains a pore that conducts water in response to an osmotic gradient (see Discussion). Osmotic water permeability was measured by stopped-flow light scattering in RBCs from wild-type and AQP1-null mice as shown in Figure 7A. Water permeability coefficients are summarized in Figure 7B. The UT-B inhibitors phloretin, urea_{inh}-101 and urea_{inh}-302 had little effect on water transport in RBCs from wild-type mice, as expected since AQP1 provides the

principle route for water transport. Phloretin at 0.7 mM produced a small but significant reduction in P_f that is likely due to its non-specific effects on membrane fluidity. AQP1-null RBCs had >5-fold reduced P_f compared to wild-type RBCs. As seen in Figure 7B, urea_{inh}-101 and urea_{inh}-302 further inhibited water permeability in AQP1-null RBCs, providing strong evidence for UT-B-facilitated water transport.

Discussion

We report here the discovery of potent small-molecule inhibitors of the UT-B urea transporter. The primary goal of this study was to identify small molecules with strong activity against human UT-B to initiate development of a new type of clinically useful diuretic—a ‘urearetic.’ A secondary goal was to identify those compounds with activity against rodent UT-B to enable ‘chemical knock-out’ studies in animal tissues. We developed a lysis-based high-throughput screening assay that relied on opposing water and urea transport processes in RBCs. Our assay allowed a simple, static read-out of percentage RBC lysis, which provided an accurate surrogate of the complex and difficult-to-measure kinetics of RBC water/solute transport. The high ‘hit’ rate in the primary screen, and the ease in identification of analogs with submicromolar potency indicate the ‘druggability’ of urea transporters.

Diuretics are used widely to increase renal salt and water clearance in a variety of conditions associated with total body fluid overload, such as congestive heart failure and cirrhosis, as well in normovolemic states such as hypertension and syndrome of inappropriate secretion of antidiuretic hormone (SIADH). Most diuretics are inhibitors of

salt absorption by kidney tubules, such as furosemide block of $\text{Na}^+/\text{K}^+/\text{2Cl}^-$ co-transport in the thick ascending limb of Henle and thiazide block of Na^+/Cl^- co-transport in the distal tubule. Recently, a new type of diuretic, called an ‘aquaretic,’ has been introduced to increase renal water clearance in hyponatremia associated with fluid overload or SIADH (reviewed in Refs. ^{19,20}). Vasopressin-2 receptor (V2R) antagonist aquaretics have been approved for clinical use in some countries, though not yet in the United States, and aquaporin inhibitor aquaretics are under development. We propose here the concept of a ‘urearetic’ as a third type of diuretic, which targets renal urea clearance mechanisms. Since urea is of at least equal importance to NaCl in the renal countercurrent mechanism for urinary concentration,^{1,21} possible indications of urearetics would include increasing solute clearance in states of fluid overload, hypertension, and perhaps in prolonging dialysis-free survival in chronic renal insufficiency.

Many active phenylsulfoxyoxazole, benzenesulfonanilide, phthalazinamine, and aminobenzimidazole compounds were identified in the primary and analog screens, none of which have been reported previously to have significant biological activity based on a SciFinder search of basic radical structures from each compound class. The most potent compounds of each class had submicromolar potency for inhibition of human UT-B as measured by the RBC lysis assay (Fig. 3). The phenylsulfoxyoxazole class contained the most potent UT-B inhibitors, with several compounds identified in the primary screen having EC_{50} between 20 and 100 nM. The EC_{50} obtained by this indirect measure of acetamide transit were in general agreement with EC_{50} measured for the most potent compounds by direct stopped-flow measurement of urea permeability (Figs. 5A and B). Analysis of a series of chemical analogs of each class indicated the structural

requirements for UT-B inhibition, and provided many potent UT-B inhibitors for optimization of ADME (absorption, distribution, metabolism, excretion) properties for use as possible diuretics.

Membrane sidedness-of-action and reversibility and were studied for the most potent phenylsulfoxyoxozoles and phthalazinamines. External addition of the phthalazinamine inhibitor just at the time of stopped-flow experiments (at non-saturating concentration) produced strong UT-B inhibition, suggesting an external site of action for Class 3 compounds. It is unlikely that inhibition was produced by action at an intracellular site, which would require permeation of this relatively polar compound (CLogP 4.8) in less than 1 second. In contrast, the lack of inhibition of external added phenylsulfoxyoxozole suggests an intracellular site of action, though very slow binding to an external site, while unlikely, cannot be ruled out. Inhibition by both the phenylsulfoxyoxozoles and phthalazinamines was fully reversible upon washout.

One additional application of UT-B inhibitors is in the analysis of UT-B functions in animal tissues by 'UT-B chemical knock-out.' Here we used UT-B inhibitors and mouse erythrocytes to clarify the possibility of UT-B-facilitated water transport. Our lab first reported UT-B-facilitated osmotic water transport from measurements of urea permeability and reflection coefficient in UT-B-expressing *Xenopus* oocytes.²² A subsequent study confirmed our original data, but concluded that UT-B-facilitated water transport is only a phenomenon seen at supra-physiological UT-B expression levels, and thus likely to be insignificant in mammalian physiology.²³ A follow-up study from our lab comparing RBCs from AQP1-null and AQP1/UT-B double knockout mice provided

evidence for UT-B-facilitated osmotic water transport.²⁴ The ~3-fold reduced osmotic water permeability measured in AQP1-deficient erythrocytes upon specific chemical inhibition of UT-B (Figure 7) supports the conclusions by Yang et al. that UT-B provides an efficient, bona fide route for water transport.

After characterization of inhibitor pharmacokinetics and ADME properties, acute inactivation of renal medulla UT-B in animal models should reveal the role of UT-B in normal kidney physiology and as a possible drug target in states of fluid overload and azotemia. ‘Chemical knock-out’ of renal UT-B will be particularly useful because upregulation of UT-A and AQP expression has been found in UT-B knock-out mice,²⁵ which might influence their urinary concentrating ability and confound conclusions about the role of UT-B. Compared to UT-B knock-out mice, UT-A1/3-deficient mice have a more severe urinary concentrating defect, with ~65% reduced urine osmolarity.⁶ Given the important contribution of UT-A to urinary concentration in the medullary collecting duct, either a UT-A-selective inhibitor or a non-selective UT inhibitor would be most desirable for evaluation as a urearetic. The UT-A1 isoform evaluated here contains both UT-A2 and UT-A3 amino acid sequences.² As such, similar UT-A2 and UT-B sequences and predicted membrane topologies (62% identity in rat)²⁶ likely account for the measured cross-reactivity of UT-B inhibitors toward UT-A1. Nevertheless, the most potent of the ‘rodent-active’ inhibitors had a high degree of selectivity, with more than 10-times greater potency for rodent UT-B vs. UT-A1 (Figure 6C). Class 3 phthalazinamines had even greater specificity than Class 1 phenylsulfoxyoxozoles. UT-B inhibitors should enable selective chemical knock-out of UT-B in the renal medulla to define the role of UT-B in the urinary concentrating mechanism.

References

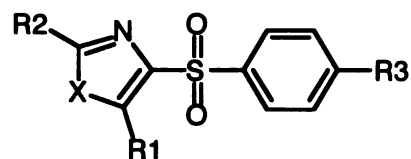
1. Bankir L, Trinh-Trang-Tan MM. In: Brenner, BM, ed. *The Kidney (6th Edition)*, Philadelphia, PA: WB Saunders Company; 2000;637–679.
2. Bagnasco SM. Gene structure of urea transporters. *Am J Physiol*. 2003;284:F3–F10.
3. Shayakul C, Hediger MA. The SCL14 gene family of urea transporters. *Pflügers Arch*. 2004;447:603–609.
4. Sands JM. Renal urea transporters. *Curr Opin Nephrol Hypertens*. 2004;13:525–532.
5. Yang B, Bankir L, Gillespie A, Epstein CJ, Verkman AS. Urea-selective concentrating defect in transgenic mice lacking urea transporter UT-B. *J Biol Chem*. 2002;277:10633–10637.
6. Fenton RA, Chou C, Stewart GS, Smith CP, Knepper MA. Urinary concentrating defect in mice with selective deletion of phloretin-sensitive urea transporters in the renal collecting duct. *Proc Natl Acad Sci USA*. 2004;101:7469–7474.
7. Fenton RA, Flynn A, Shodeinde A, Smith CP, Schnermann J, Knepper MA. Renal phenotype of UT-A urea transporter knockout mice. *J Am Soc Nephrol*. 2005;16, 1583–1592.
8. Sands JM, Gargus JJ, Fröhlich O, Gunn RB, Kokko JP. Urinary concentrating ability in patients with Jk(a–b–) blood type who lack carrier-mediated urea transport. *J Am Soc Nephrol*. 1992;2:1689–1696.
9. Lucien N, Sidoux-Water F, Olives B, et al. Characterization of the gene encoding the human Kidd blood group/urea transporter protein. Evidence for splice site mutations in Jknull individuals. *J Biol Chem*. 1998;273:12973–12980.
10. Mayrand RR, Levitt DF. Urea and ethylene glycol-facilitated transport systems in the human red cell membrane. Saturation, competition, and asymmetry. *J Gen Physiol*. 1983;81:221–237.
11. Martial S, Neau P, Degeilh F, Lamotte H, Rousseau B, Ripoché P. Urea derivatives as tools for studying the urea-facilitated transport system. *Pflügers Arch*. 1993;423:51–58.

12. Ma T, Yang B, Gillespie A, Carlson EJ, Epstein CJ, Verkman AS. Severely impaired urinary concentrating ability in transgenic mice lacking aquaporin-1 water channels. *J Biol Chem*. 1998;273:4296–4299.
13. Mazon P, Didelon J, Muller S, Stolz JF. A theoretical approach of the measurement of osmotic fragility of erythrocytes by optical transmission. *Photochem Photobiol* 2000;72:172–178.
14. Cohn JV, Alkhalil A, Wanger MA, Rajapandi, Desai SA. Extracellular lysines on the plasmodial surface anion channel involved in Na⁺ exclusion. *Mol Biochem Parasitol*. 2003;132:27–34.
15. Oldenburg, KR, Karivk I, Zhang JH, Chung TDY, Lin S. In: Seethala R, Fernandes PB, eds. Handbook of Drug Screening, New York, NY; Marcel Dekkar, Inc.; 2001;549–554.
16. van Hoek AN, Verkman AS. Functional reconstitutions of the isolated erythrocyte water channel CHIP28. *J Biol Chem*. 1992;267:18267–18269.
17. Fröhlich O, Klein JD, Smith PM, Sands JM, Gunn RB. Regulation of UT-A1-mediated transepithelial urea flux in MDCK cells. *Am J Physiol*. In press.
18. Fröhlich O, Klein JD, Smith PM, Sands JM, Gunn RB. Urea transport in MDCK cells that are stably transfected with UT-A1. *Am J Physiol*. 2004;286:C1264–C1270.
19. Goldsmith SR. Current treatments and novel pharmacologic treatments for hyponatremia in congestive heart failure. *Am J Cardiol*. 2005;95:14B–23B.
20. Miller M. Hyponatremia and arginine vasopressin dysregulation: mechanisms, clinical consequences, and management. *J Am Geriatr Soc*. 2006;54:345–353.
21. Masilamani S, Knepper MA, Burg MB. In: Brenner, BM, ed. *The Kidney (6th Edition)*, Philadelphia, PA: WB Saunders Company; 2000;595–635.
22. Yang B, Verkman AS. Urea transporter UT3 functions as an efficient water channel. Direct evidence for a common water/urea pathway. *J Biol Chem*. 1998;273:9369–9372.
23. Sidoux-Walter F, Lucien N, Olives B, et al. At physiological expression levels the Kidd blood group/urea transporter protein is not a water channel. *J Biol Chem*. 1999;274:30228–30235.
24. Yang B, Verkman AS. Analysis of double knockout mice lacking Aquaporin-1 and urea transporter UT-B. Evidence for UT-B-facilitated water transport in erythrocytes. *J Biol Chem*. 2002;277:36782–36786.

25. Klein JD, Sands JM, Qian L, Wang X, Yang B. Upregulation of urea transporter UT-A2 and water channels AQP2 and AQP3 in mice lacking urea transporter UT-B. *J Am Soc Nephrol.* 2004;15:1161–1167.
26. Tsukaguchi H, Shayakul C, Berger UV, Tokui T, Brown D, Hediger MA. Cloning and characterization of the urea transporter UT3. Localization in Rat and Testis. *J Clin Invest.* 1997;99:1506–1515.

Table 1

Structure-activity analysis of phenylsulfoxyoxolozes.

**Class 1:
Phenylsulfoxyoxolozes**

Active compounds					
Compound	X	-R1	-R2	-R3	EC ₅₀ (μ M)
urea _{inh} -101*	O	-S-CH ₂ -CO-NH ₂	-Ph	-Br	0.03
urea _{inh} -102*	O	-S-CH ₂ -CO-NH ₂	-Ph	-Cl	0.04
urea _{inh} -103*	O	-S-CH ₂ -CO-NH ₂	-Ph	-Me	0.1
urea _{inh} -104*	O	-S-CH ₂ -CO-NH ₂	-Ph	-H	1
urea _{inh} -105*	O	-S-CH ₂ -CO-NH ₂	-(4-F)-Ph	-Me	0.1
urea _{inh} -106	O	-S-CH ₂ -CO-NH ₂	-(4-F)-Ph	-Cl	0.2
urea _{inh} -107*	O	-S-CH ₂ -CO-NH ₂	-(4-F)-Ph	-F	6
urea _{inh} -108*	O	-S-CH ₂ -CO-NH ₂	-(4-F)-Ph	-H	15
urea _{inh} -109*	O	-S-CH ₂ -CO-NH ₂	-(4-Me)-Ph	-Br	0.2
urea _{inh} -110*	O	-S-CH ₂ -CO-NH ₂	-(4-Me)-Ph	-Me	1
urea _{inh} -111	O	-S-CH ₂ -CO-NH ₂	-(4-Me)-Ph	-Cl	1
urea _{inh} -112	O	-S-CH ₂ -CO-NH ₂	-(4-Me)-Ph	-H	15
urea _{inh} -113	O	-S-CH ₂ -CO-NH ₂	-2-thiophene	-Cl	0.02
urea _{inh} -114*	O	-S-CH ₂ -CO-NH ₂	-2-thiophene	-Me	0.5
urea _{inh} -115	O	-S-CH ₂ -CO-NH ₂	-2-thiophene	-F	0.6
urea _{inh} -116	O	-S-CH ₂ -CO-NH ₂	-2-thiophene	-H	1
urea _{inh} -117*	O	-S-CH ₂ -CO-NH ₂	-2-furan	-Cl	0.1
urea _{inh} -118*	O	-S-CH ₂ -CO-NH ₂	-2-furan	-Br	0.2
urea _{inh} -119*	O	-S-CH ₂ -CO-NH ₂	-2-furan	-Me	1
urea _{inh} -120	O	-NH-CH ₂ -Ph	-(2-F)-Ph	-Cl	1
urea _{inh} -121	O	-S-CH ₂ -CO-NH-CH ₂ -2-furan	-Ph	-Br	4
urea _{inh} -122	O	-S-CH ₂ -CO-NH-CH ₂ -2-furan	-Ph	-Cl	15
urea _{inh} -123	O	-N(CH ₃) ₂	-(2-Cl)-Ph	-H	5
urea _{inh} -124	O	- <i>n</i> -morpholino	-(2-F)-Ph	-H	7

urea _{inh} -125	O	- <i>n</i> -morpholino	-(2-Cl)-Ph	-Me	11
urea _{inh} -126	O	-hexahydro-1-H-azepine-1-yl	-(2-OMe)-Ph	-H	10
urea _{inh} -127	O	-hexahydro-1-H-azepine-1-yl	-(4-Me)-Ph	-H	10
urea _{inh} -128	O	-hexahydro-1-H-azepine-1-yl	-(4-F)-Ph	-H	10
urea _{inh} -129*	O	-SMe	-2-furan	-Cl	20
urea _{inh} -130*	N	-SMe	-(4-Me)-Ph	-H	2
urea _{inh} -131	N	-SH	-Ph	-Me	6
urea _{inh} -132	N	-S-CO-Ph	-Ph	-H	7

Inactive compounds

R1: SCH₂-CO-NR₂, SCH₂-CO-NHR (R is substituted Ph or bulky aliphatic)

R2: 3-, di-, or tri-substituted phenyls

* Denotes inhibitors identified in primary screening

Table 2

Structure-activity analysis of benzenesulfonanilides.

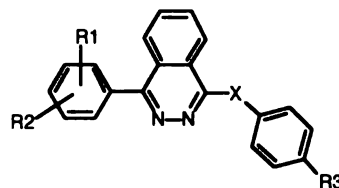
Class 2: Benzenesulfonanilides						
Active compounds						
Compound	-R1	-R2	-R3	-R4	-R5	EC ₅₀ (μM)
urea _{inh} -201*	2-OMe	5-OMe	OMe	H	OMe	0.3
urea _{inh} -202*	2-OMe	5-OMe	H	Br	H	0.4
urea _{inh} -203*	2-OMe	5-OMe	Br	H	H	0.7
urea _{inh} -204*	2-OMe	5-OMe	F	H	H	1
urea _{inh} -205*	2-OMe	5-OMe	SMe	H	H	1
urea _{inh} -206*	4-OMe	-H	<i>i</i> -Pr	OH	SO ₂ -[4-(OMe)-Ph]	1
urea _{inh} -207	3-O-C ₂ H ₄ -O-4		H	CO-NH ₂	H	2
urea _{inh} -208	3-O-C ₂ H ₄ -O-4		Me	H	H	4
urea _{inh} -209	3-O-C ₂ H ₄ -O-4		OMe	H	H	6
urea _{inh} -210	3-O-C ₂ H ₄ -O-4		CO-Me	H	H	6
urea _{inh} -211	3-O-C ₂ H ₄ -O-4		Br	H	H	8
urea _{inh} -212	3-O-C ₂ H ₄ -O-4		Me	Me	H	10
urea _{inh} -213	3-O-C ₂ H ₄ -O-4		3-C ₄ H ₄ -4		H	10
urea _{inh} -214	3-O-C ₂ H ₄ -O-4		OMe	OMe	H	15
urea _{inh} -215	3-O-C ₂ H ₄ -O-4		CF ₃	H	H	15
urea _{inh} -216	3-O-C ₂ H ₄ -O-4		H	NH-CO-Me	H	15
urea _{inh} -217	3-O-CO-N(Me)-4		CF ₃	H	H	4

Inactive compounds**R1, R2:** 3,4-di-OMe, 3-OMe, 4-amino**R3, R5:** di-(halo/carboxy)**R4:** acetyl, Ph-acetyl, Me, OMe, F, sulfonyl-aminos

* Denotes inhibitors identified in primary screening

Table 3

Structure-activity analysis of phthalazinamines.

**Class 3:
Phthalazinamines**

Active compounds						
Compound	X	-R1	-R2	-R3	EC ₅₀ (μ M)	
urea _{inh} -301	NH	4-CO-NH ₂	-H	OMe	0.1	
urea _{inh} -302	NH	4-CO-NH ₂	-H	Me	0.2	
urea _{inh} -303	NH	4-CO-NH ₂	-H	CO-N(Me) ₂	0.2	
urea _{inh} -304	NH	4-CO-NH ₂	-H	CO-NH-Me	0.6	
urea _{inh} -305	NH	4-CO-NH ₂	-H	pyran	0.7	
urea _{inh} -306	NH	4-CO-NH ₂	-H	OH	2	
urea _{inh} -307	NH	4-CO-NH ₂	-H	SO ₂ -NH ₂	3	
urea _{inh} -308	NH	4-CO-NH ₂	-H	CO-NH-Me	2	
urea _{inh} -309	NH	4-CO-N(Et) ₂	-H	OH	5	
urea _{inh} -310	NH	4-CO-N(Et) ₂	-H	CO-N(Me) ₂	3	
urea _{inh} -311	NH	4-CO-NH-C ₂ H ₄ -OH	-H	O-CH ₂ -CO-NH-Me	0.8	
urea _{inh} -312	NH	4-OMe	-H	O-CH ₂ -CO-NH ₂	1	
urea _{inh} -313	NH	4-OMe	-H	2-benzimidazole	10	
urea _{inh} -314	NH	4-Me	-H	O-CH ₂ -CO-NH ₂	2	
urea _{inh} -315	NH	4-Me	-H	O-CH ₂ -CO-NH-Me	2	
urea _{inh} -316*	NH	4-OH	-H	OMe	2	
urea _{inh} -317*	NH	4-OH	-H	NH-CO-Me	3	
urea _{inh} -318	NH	-H	-H	O-CH ₂ -CO-NH ₂	2	
urea _{inh} -319	NH	-H	-H	O-CH ₂ -CO-NH-Me	3	
urea _{inh} -320	NH	-H	-H	OMe	4	
urea _{inh} -321	NH	3-SO ₂ -N(Me) ₂	4-Me	CO-NH ₂	1	
urea _{inh} -322	NH	3-SO ₂ -N(Me) ₂	4-Me	O-CH ₂ -CO-NH ₂	2	
urea _{inh} -323	NH	3-SO ₂ -NH-C ₂ H ₄ -OH	4-Me	CO-OMe	2	
urea _{inh} -324	NH	3-SO ₂ -NH-C ₂ H ₄ -OH	4-Me	CO-NH ₂	5	
urea _{inh} -325	NH	3-SO ₂ -NH-Me	4-Me	O-CH ₂ -CO-NH ₂	2	

urea _{inh} -326	NH	3-SO ₂ -NH-Me	4-Me	O-CH ₂ -CO-NH-Me	2
urea _{inh} -327	NH	3-SO ₂ -NH-Me	4-Me	CO-NH-Me	2
urea _{inh} -328	NH	3-SO ₂ - <i>n</i> -morpholino	4-Me	OH	3
urea _{inh} -329	NH	3-SO ₂ -NH ₂	4-Me	CO-NH ₂	5
urea _{inh} -330	NH	3-SO ₂ -NH ₂	4-Me	O-CH ₂ -CO-NH-Me	10
urea _{inh} -331	NH	3-SO ₂ -NH-C(Me) ₂ (CH ₂ -OH)	4-Me	OH	9
urea _{inh} -332	O	4-OMe	-H	H	2
urea _{inh} -333	O	4-Me	-H	H	3

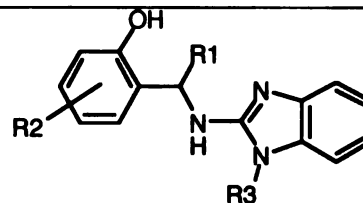
Inactive compounds

X: NR, where R is any aliphatic

* Denotes inhibitors identified in primary screening

Table 4

Structure-activity analysis of aminobenzimidazoles.

**Class 4:
Aminobenzimidazoles**

Active compounds				
Compound	-R1	-R2	-R3	EC ₅₀ (μM)
urea _{inh} -401	H	5-Cl	- <i>n</i> -Pr	0.3
urea _{inh} -402	H	5-Cl	-Et	0.4
urea _{inh} -403*	H	5-Cl	- <i>i</i> -Pr	5
urea _{inh} -404	H	5-Br	Et	0.4
urea _{inh} -405*	H	5-Br	- <i>i</i> -Pr	0.4
urea _{inh} -406*	H	5-Br	-CH ₂ -CH=CH ₂	1
urea _{inh} -407	H	-H	-C ₂ H ₄ -N(Et) ₂	0.8
urea _{inh} -408	H	-H	-C ₂ H ₄ - <i>n</i> -piperidine	0.9
urea _{inh} -409	H	-H	-Et	2
urea _{inh} -410	H	-H	- <i>n</i> -Pr	2
urea _{inh} -411	H	-H	- <i>i</i> -Pr	5
urea _{inh} -412	H	-H	-C ₂ H ₄ - <i>n</i> -morpholino	6
urea _{inh} -413	H	-H	-CH ₂ -CH=CH ₂	9
urea _{inh} -414	H	5-Me	- <i>n</i> -Pr	1
urea _{inh} -415	H	5-Me	- <i>i</i> -Pr	1
urea _{inh} -416	H	5-Me	-Et	1
urea _{inh} -417	H	5-Me	- <i>n</i> -Bu	2
urea _{inh} -418	H	5-OMe	- <i>n</i> -Pr	6
urea _{inh} -419	H	5-OMe	-CH ₂ -CH=CH ₂	25
urea _{inh} -420	H	5-OMe	- <i>i</i> -Pr	3
urea _{inh} -421	H	5-C ₄ H ₄ -6	-Et	3
urea _{inh} -422	H	3-OMe	-Et	11
urea _{inh} -423	Me	5-Cl	-Et	5

Inactive compounds

R1: Me reduces activity, bulkier aliphatics are inactive

R2: most 3-, 4-, 6-substitutions

* Denotes inhibitors identified in primary screening

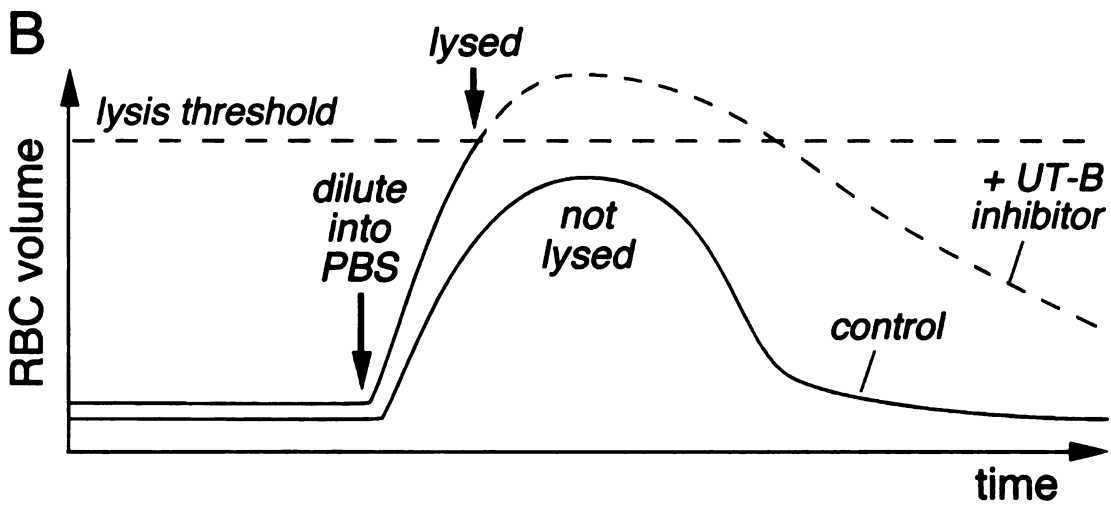
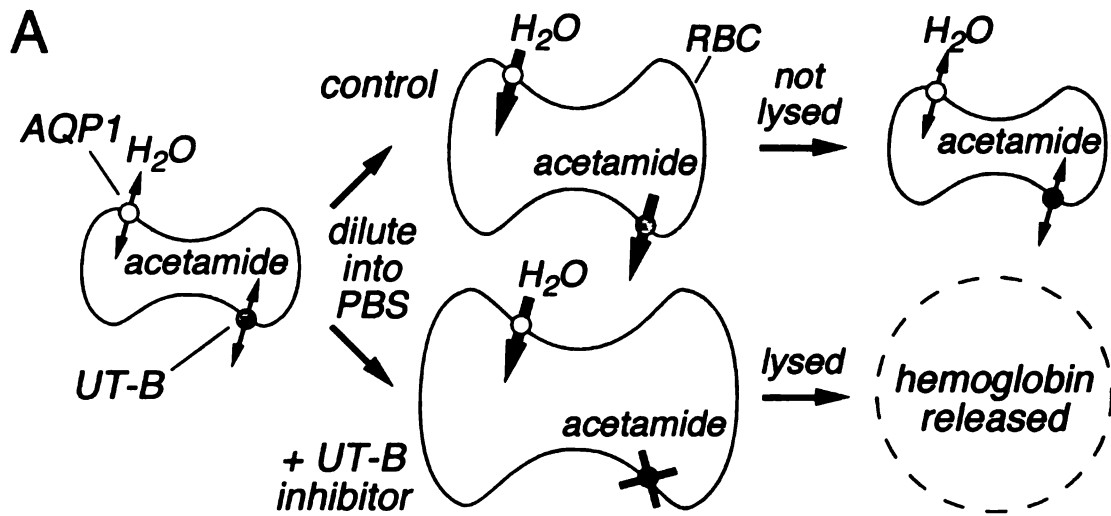


Figure 1

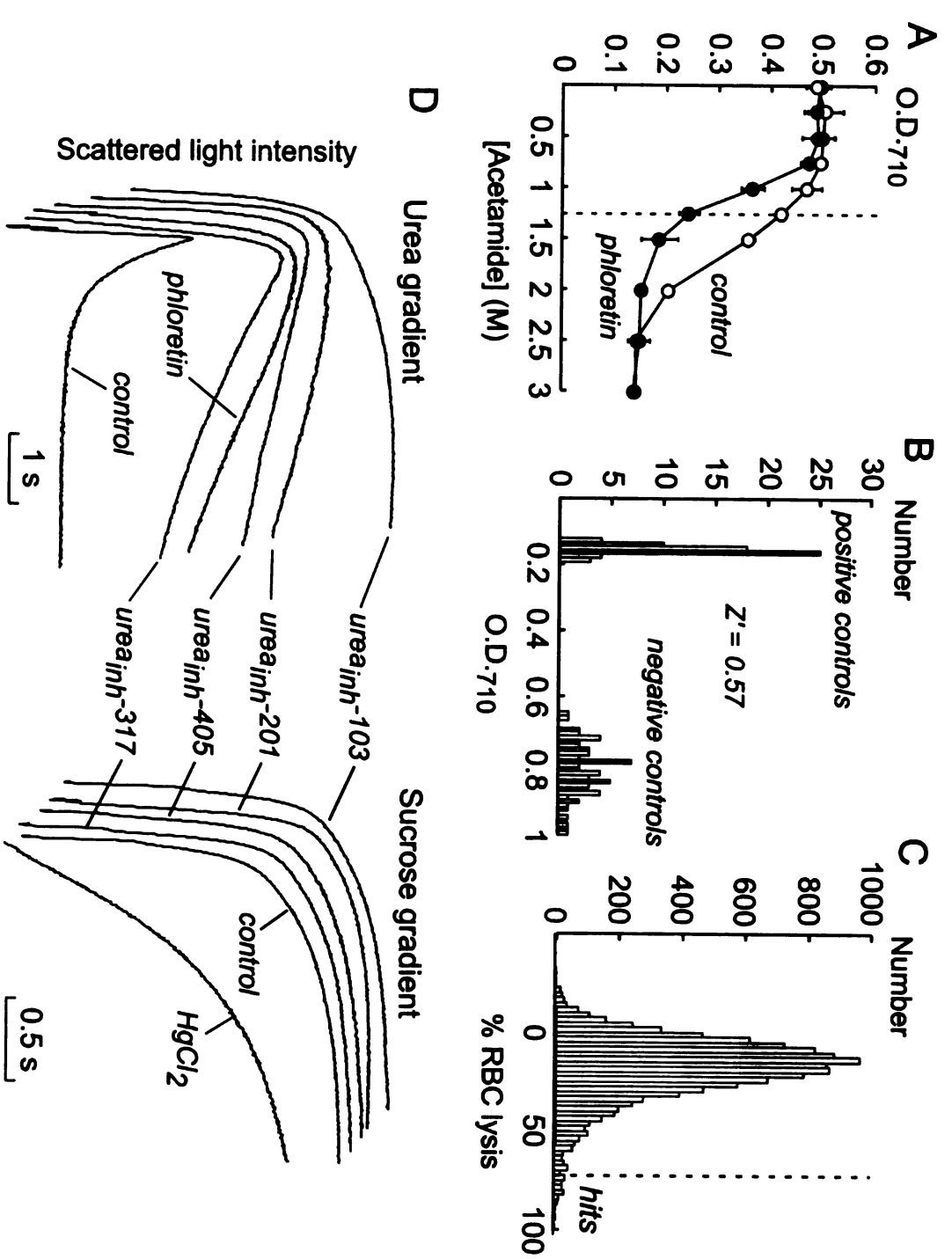


Figure 2

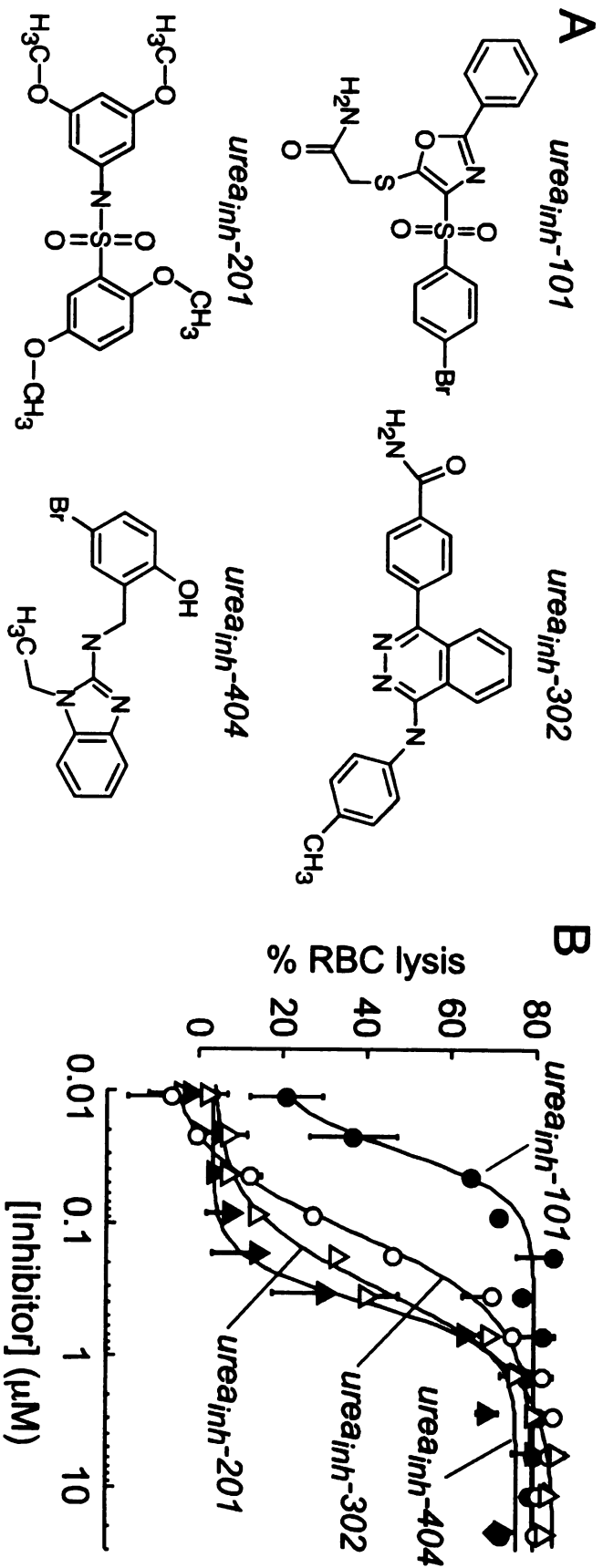


Figure 3

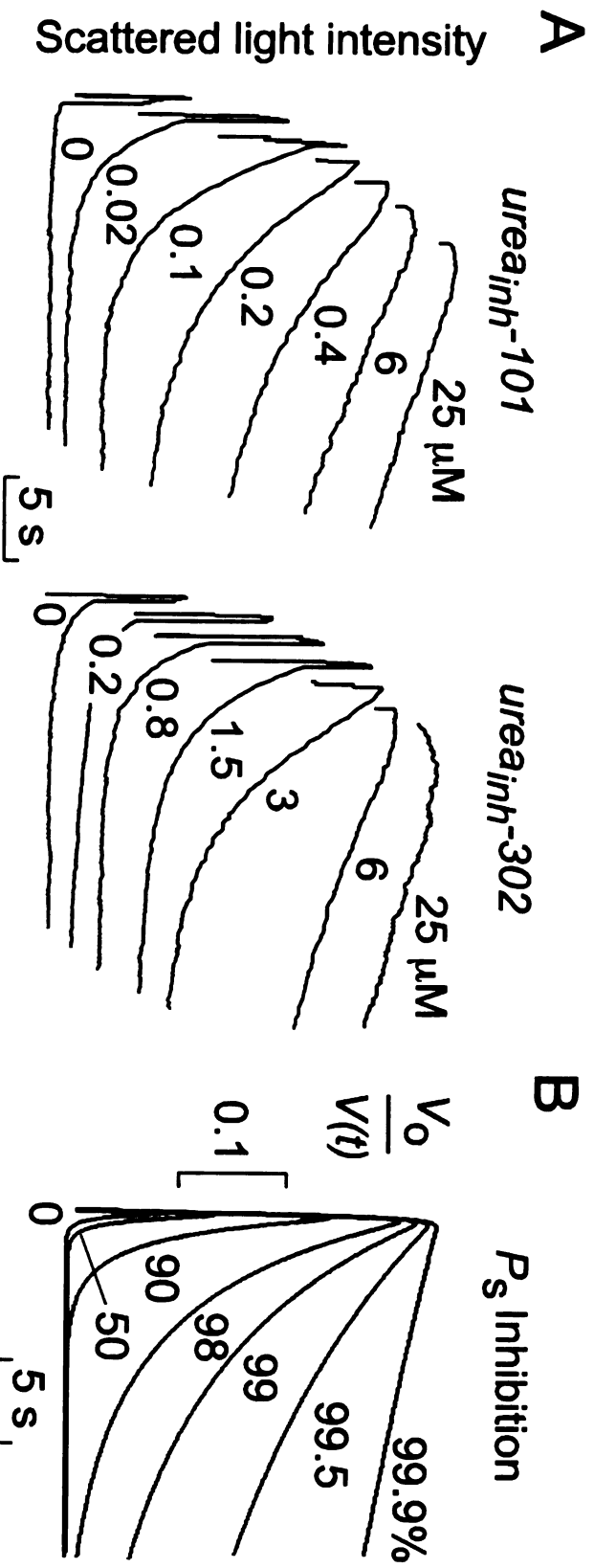
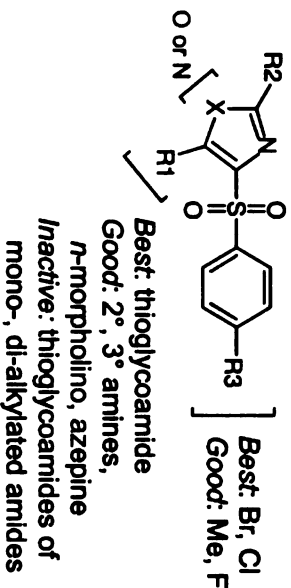


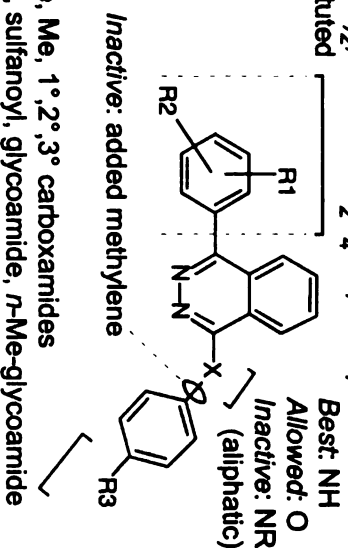
Figure 4

Best: 2-thiophene, Ph
 Good: 4-F-Ph, 4-Me-Ph, 2-furan
 Inactive: 3-, di-, tri-substituted Ph



Class 1: Phenylsulfonoxozoles

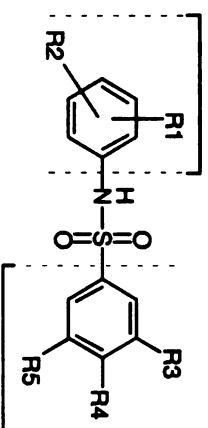
Best: 4-carboxamide, 4-OMe
 Good: 4-Me, 3-(un)substituted sulfanoyls + 4-Me
 4-CO-N(Et)₂, 4-CO-NH-C₂H₄OH, 4-OH,
 unsubstituted



Class 3: Phthalazinamines

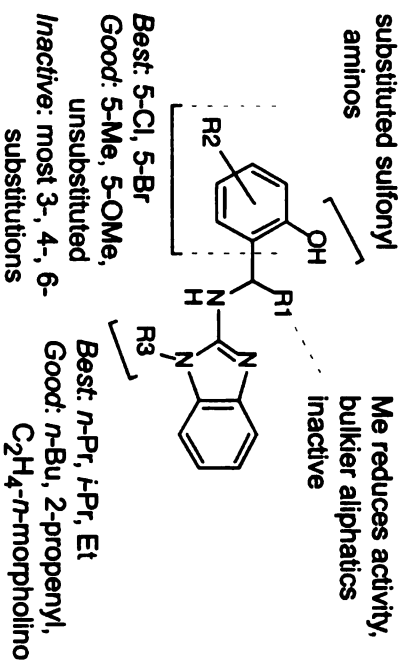
Figure 5

Best: 2,5-di-OMe
 Good: 3-O-C₂H₄-O-4
 Inactive: most 3- or 4-substitutions



Class 2: Benzenesulfonanilides

Inactive: OMe, halos,
 substituted sulfonyl
 aminos



Class 4: Aminobenzimidazoles

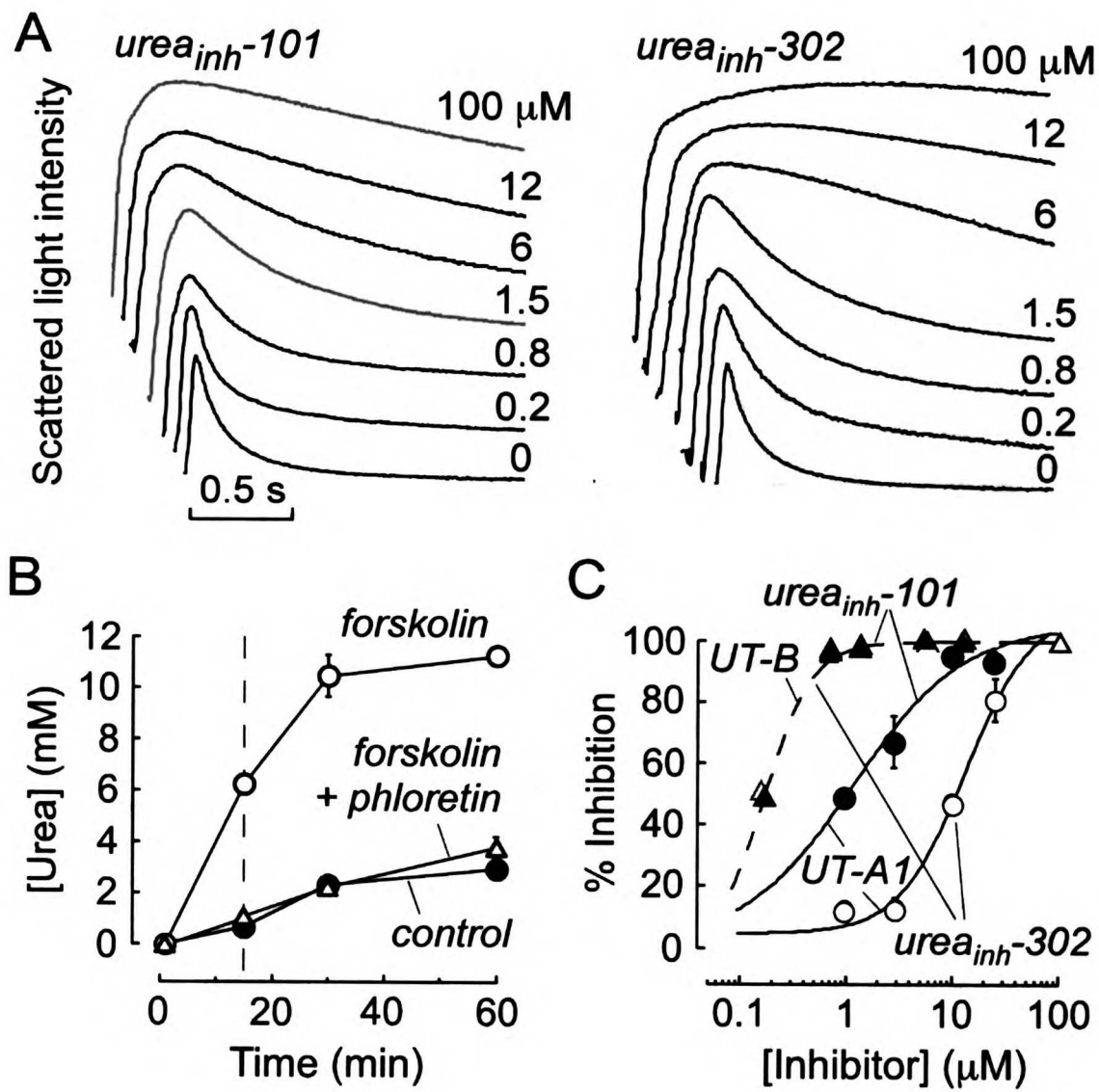


Figure 6

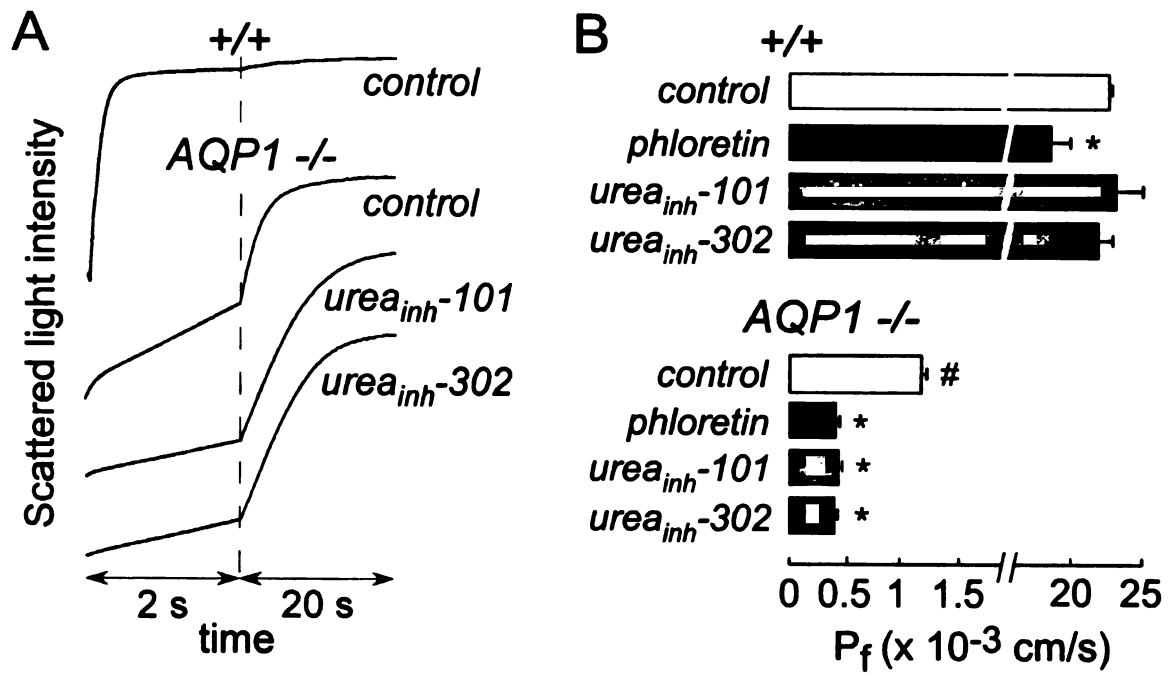


Figure 7

Figure Legends

FIGURE 1. Erythrocyte osmotic lysis assay for UT-B inhibitor discovery. **(A)** Human RBCs expressing water and urea channels (AQP1 and UT-B) are preloaded with urea or a urea analog, such as acetamide. Following replacement of the external buffer with urea/acetamide-free isosmolar solution, water entry results in cell swelling, which is limited by UT-B-mediated urea/acetamide efflux. Under optimized assay conditions, UT-B-facilitated urea/acetamide prevents osmotic lysis (*top*), whereas UT-B inhibition impairs urea/acetamide exit resulting in substantial lysis (*bottom*). **(B)** Biphasic cell volume changes in the lysis assay. Increased RBC volume beyond a threshold results in lysis. The dashed curve shows the hypothetical time course of RBC volume if lysis had not occurred.

FIGURE 2. Identification of UT-B inhibitors by high-throughput screening. **(A)** Effect of acetamide concentration on RBC osmotic lysis. Human RBC suspensions, loaded with indicated concentrations of acetamide, were diluted in acetamide-free buffer in the absence (*open circles*) or presence of 0.7 mM phloretin (*closed circles*). RBC lysis was assayed by absorbance at 710 nm (O.D.₇₁₀) (\pm SE, 4 wells per condition). The *dashed line* indicates the condition chosen for high-throughput screening. **(B)** Frequency histogram of O.D.₇₁₀ for positive and negative controls from eight 96-well plates, with *z'*-value shown. **(C)** Frequency histogram of per-cent erythrocyte lysis for the primary screen in (12,500 test wells with 4 compounds per well; 50,000 compounds total), with the *dashed line* representing the criteria chosen to define 'hits.' **(D, left)** Urea permeability measured from the kinetics of light scattering in response to a 250-mM inwardly directed urea

gradient in the absence of inhibitor (*control*) or in the presence of 0.7 mM phloretin (positive control) or 5 μM of indicated compounds. *Right*: osmotic water permeability of human RBCs measured by light scattering in response to a 250-mM inwardly directed sucrose gradient in the absence or presence of 0.3 mM HgCl_2 (positive control) or 25 μM of inhibitors.

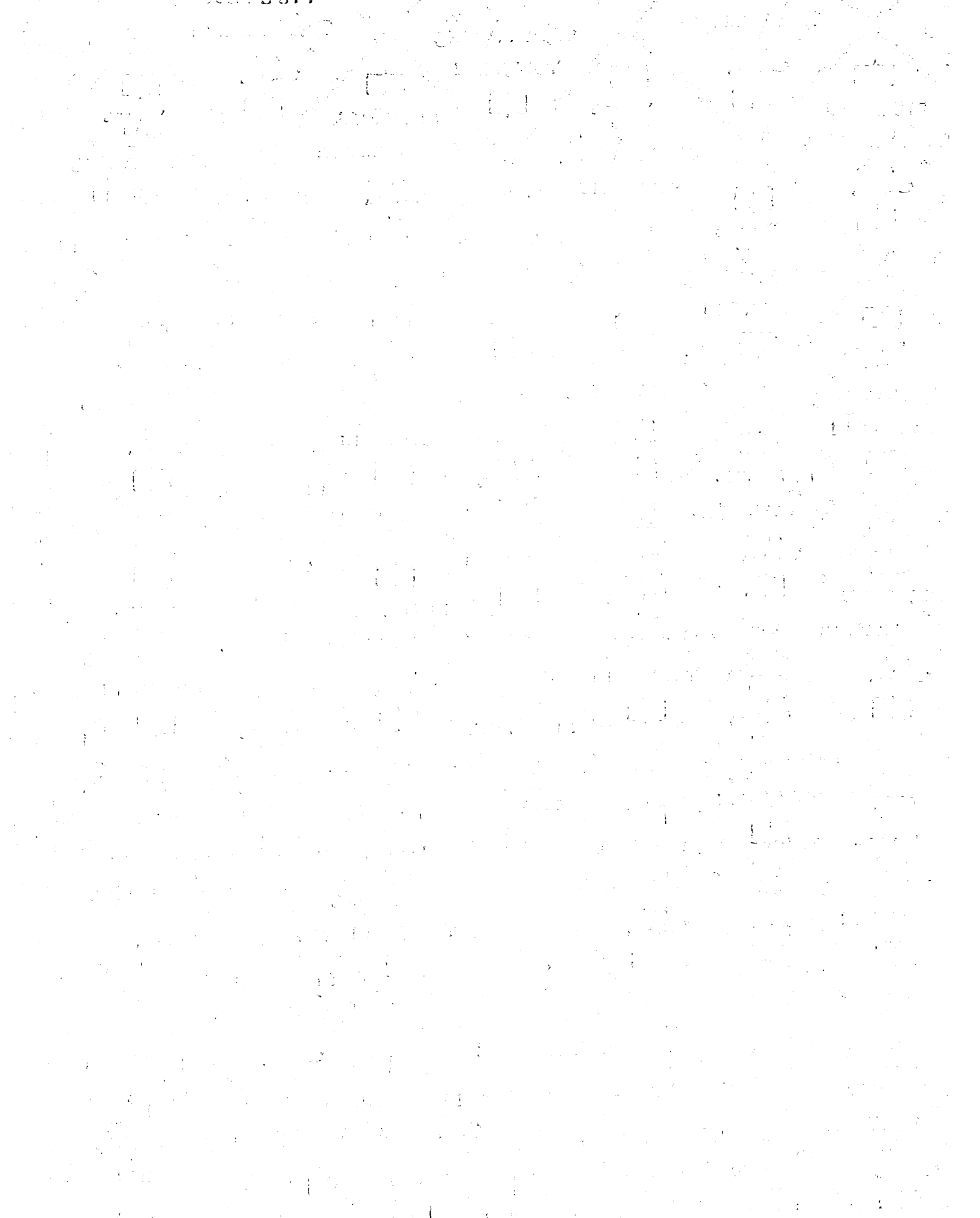
FIGURE 3. Nanomolar-potency UT-B inhibitors identified from primary high-throughput screening and assay of analogs. (A) Chemical structures of UT-B inhibitors (urea_{inh}), with one compound per class shown. (B) Dose-inhibition data for inhibitors as in (A), determined by the lysis assay in human RBCs ($\pm\text{SD}$) and fit to calculate EC_{50} (*solid lines*) as described in the Methods.

FIGURE 4. Stopped-flow measurements of urea transport in human RBCs. (A) Concentration-inhibition curves for indicated compounds (structures shown in Fig. 3) determined by light scattering in response to a 100-mM inwardly directed urea gradient. RBCs were incubated for 5 min with compounds at indicated concentrations prior to stopped-flow measurements. (B) Numerically simulated inhibitor concentration-dependence used to determine EC_{50} from stopped-flow experiments as in (A) (see Methods for details). The inverse of normalized cell volume, $V_o/V(t)$, is plotted to approximate light-scattering data at indicated percentages of urea transport inhibition.

FIGURE 5. Structure-activity analysis of phenylsulfoxyoxozoles, benzenesulfonamides, phthalazinamines and aminobenzimidazoles. General structures of UT-B inhibitors, with substitution preferences illustrated. See Tables 1–4 for lists of UT-B inhibition activities corresponding to different substitutions.

FIGURE 6. Activity of UT-B inhibitors against rodent UT-B and UT-A1. **(A)** Dose-inhibition relationships for urea_{inh}-101 (*left*) and urea_{inh}-302 (*right*) against mouse UT-B. Stopped-flow light scattering measurements done using wild-type mouse RBCs in response to a 100-mM inwardly directed gradient of *N*-methylurea. **(B)** UT-A1-mediated urea flux in stably transfected MDCK cells. Cells were treated (*open circles* and *open triangles*) or not treated (*closed circles*) with 10 μ M forskolin. Where indicated, phloretin (0.7 mM) was present (*open triangles*) (\pm SE, 3 filters per condition). The *dashed line* indicates the time chosen (15 min) to evaluate UT-A1 inhibition in **(C)**. **(C)** Concentration-dependent inhibition of mouse UT-B (*triangles*) and rat UT-A1 (*circles*) by urea_{inh}-101 (*closed symbols*) and urea_{inh}-302 (*open symbols*), determined from data such as in **(A)** and **(B)**.

FIGURE 7. UT-B-facilitated water transport demonstrated by ‘chemical UT-B knock-out’. Osmotic water permeability was measured from the time course of RBC volume in response to a 250-mM inwardly directed sucrose gradient. **(A)** Representative traces of mouse RBC water permeability done at 10°C, with genotypes and conditions indicated. Inhibitors urea_{inh}-201 and urea_{inh}-302 were used at 25 μ M. **(B)** Osmotic water permeability coefficients (P_f) from experiments as in **(A)** (\pm SE, 3–7 curves per group of RBCs pooled from 4 mice per genotype). *, $P < 0.01$ compared with no inhibitor; #, $P < 0.01$ compared with wild-type (no inhibitor).



7541918



3 1378 00754 1918

For Not to be taken
from the room.
reference

